Functionalized doubly porous polymeric materials : design and modeling

Hai Bang Ly

To cite this version:

Hai Bang Ly. Functionalized doubly porous polymeric materials : design and modeling. Materials. Université Paris-Est, 2015. English. NNT : 2015PESC1144 . tel-01308277

HAL Id: tel-01308277
https://theses.hal.science/tel-01308277

Submitted on 27 Apr 2016

THÈSE

présentée par :
Hai Bang LY

pour obtenir le titre de docteur de l'Université Paris-Est
Spécialité: Mécanique

Matériaux polymères fonctionnalisés à double porosité :

conception et modélisation

Soutenue le 02 Octobre 2015 devant un jury composé de:

Rapporteurs	
Djimédo KONDO	Professeur, Univ. Pierre et Marie Curie
Michel DUMON	Professeur, Univ. de Bordeaux
Examinateurs	
Philippe COUSSOT	Professeur, Ecole des Ponts ParisTech
Daniela BAUER	Ingénieure de recherche, IFP Energies Nouvelles
Directeurs de thèse	
Daniel GRANDE	Directeur de recherche CNRS
Vincent MONCHIET	Maître de Conférences HDR, Univ. Paris-Est Marne-la-Vallée
Invités	
Michel BORNERT	Chercheur, Ecole des Ponts ParisTech
Benjamin LE DROUMAGUET	Maître de Conférences, Univ. Paris-Est Créteil

THÈSE

présentée par :
Hai Bang LY

pour obtenir le titre de docteur de l'Université Paris-Est
Spécialité: Mécanique

Matériaux polymères fonctionnalisés à double porosité : *conception et modélisation*

Soutenue le 02 Octobre 2015 devant un jury composé de:

Rapporteurs	
Djimédo KONDO	Professeur, Univ. Pierre et Marie Curie
Michel DUMON	Professeur, Univ. de Bordeaux
Examinateurs	
Philippe COUSSOT	Professeur, Ecole des Ponts ParisTech
Daniela BAUER	Ingénieure de recherche, IFP Energies Nouvelles
Directeurs de thèse	
Daniel GRANDE	Directeur de recherche CNRS
Vincent MONCHIET	Maître de Conférences HDR, Univ. Paris-Est Marne-la-Vallée
Invités	
Michel BORNERT	Chercheur, Ecole des Ponts ParisTech
Benjamin LE DROUMAGUET	Maître de Conférences, Univ. Paris-Est Créteil

Ph.D. THESIS

presented by :
Hai Bang LY

to obtain the degree of doctor of the University of Paris-Est
Speciality: Mechanics

Functionalized Doubly Porous Polymeric Materials: *Design and Modeling*

Defended on December 02, 2015 in front of the jury constituted of:

Reviewers	
Djimédo KONDO	Professor, University Pierre et Marie Curie
Michel DUMON	Professor, University of Bordeaux
Examiners	
Philippe COUSSOT	Professor, Ecole des Ponts ParisTech
Daniela BAUER	Research Engineer, IFP Energies Nouvelles
Supervisors	
Daniel GRANDE	CNRS Senior Researcher
Vincent MONCHIET	Associate Professor, University Paris-Est Marne-la-Vallée
Invited	
Michel BORNERT	Researcher, Ecole des Ponts ParisTech
Benjamin LE DROUMAGUET	Assistant Professor, University Paris-Est Créteil

Matériaux polymères fonctionnalisés à double porosité : *conception et modélisation*

Les matériaux polymères poreux font l'objet d'intenses recherches depuis de nombreuses années et présentent certains avantages importants par rapport à leurs homologues inorganiques, comme des propriétés mécaniques modulables, une fonctionnalisation aisée et surtout un coût de production plus faible. Au cours de la dernière décennie, les matériaux à double porosité ont attiré une attention particulière de la communauté scientifique car ces matériaux offrent de nouvelles perspectives intéressantes pour l'élaboration de matériaux durables. Le rôle de chaque niveau de porosité est différent et associé à des processus de transfert de masse distincts. Les macropores (100 ţm) permettraient l'écoulement de macromolécules ou de cellules à travers le matériau, tandis qu'un réseau nanoporeux (10-100 nm) serait dédié au passage de molécules plus petites, agissant ainsi comme un deuxième mécanisme de transport, en particulier lorsque des macropores sont totalement obstrués.

La première partie de ce travail porte sur le développement d'approches polyvalentes et efficaces pour la préparation de matériaux à double porosité biocompatibles à base de poly(méthacrylate de 2-hydroxyéthyle) (PHEMA). La première approche a reposé sur l'utilisation de deux types distincts de gabarits porogènes, à savoir un macroporogène et un nanoporogène. Pour générer la macroporosité, soit des particules de NaCl ou des billes de PMMA, pouvant être fusionnées ou non, ont été utilisées afin de contrôler la morphologie l'interconnectivité des pores. Le nanoporosité a été obtenue en utilisant diverses quantités de différents solvants porogènes, générant ainsi une large gamme de distributions de tailles de pores pour ce second niveau de porosité. La seconde méthodologie a été fondée sur le procédé de séparation de phases induite thermiquement. Un mélange de co-solvants constitué de dioxane et d'eau a été utilisé pour solubiliser le PHEMA linéaire préalablement préparé, suivi par un processus de solidification par congélation du mélange de co-solvants / PHEMA, et sublimation consécutive des co-solvants pour produire les matériaux de PHEMA biporeux correspondants. Enfin, les matériaux à double porosité ont été valorisés à travers différentes réactions de fonctionnalisation en utilisant la chimie du carbonyldiimidazole, et l'immobilisation postérieure de nanoparticules d'or générées in-situ. De tels matériaux hybrides à double porosité se sont avérés être des supports catalytiques efficaces.

Dans la deuxième partie, nous avons déterminé numériquement la perméabilité des matériaux à double porosité. La méthodologie a été fondée sur une approche à double changement d'échelle dans le cadre des théories d'homogénéisation périodique et sur des calculs de cellules élémentaires. Le premier changement d'échelle a consisté à déterminer une première perméabilité associée au réseau de nanopores. A cette échelle, les pores ont été saturés par un fluide visqueux obéissant aux équations de Stokes et le problème a été résolu par une approche classiques d'éléments finis ou en utilisant des techniques plus récentes à base de la transformée de Fourier rapide. À l'échelle mésoscopique, l'écoulement du fluide a obéi aux équations de Stokes dans les macropores et aux équations de Darcy dans le solide perméable. Le problème de cellules élémentaires couplant les équations de Darcy et Stokes a été résolu par la méthode des éléments finis afin de calculer la perméabilité macroscopique finale. Dans cette optique, nous avons développé une méthode fondée sur une formulation variationnelle mixte qui a été mise en œuvre en prenant différents éléments dans les domaines de solide et fluide. Divers exemples 2D et 3D sont fournis pour illustrer la précision et la capacité des méthodes numériques proposées pour calculer la perméabilité macroscopique des matériaux biporeux.

Mots clés:
- matériaux poreux à double porosité
- approche à deux porogènes
- séparation de phases induite thermiquement
- perméabilité
- homogénéisation
- méthode des éléments finis

Functionalized Doubly Porous Polymeric Materials: *Design and Modeling*

Polymer-based porous materials have been the subject of intense research for many years and present some important advantages over their inorganic counterparts, such as tunable mechanical properties, ease to be functionalized, and especially lower production cost. Over the last decade, materials with dual porosity have attracted a particular attention from the scientific community, as these peculiar materials offer new interesting perspectives for engineering sustainable materials. The role of each porosity level is different and associated with distinct mass transfer processes. Macropores (100 ţm) would allow macromolecules and cells flow through the material, while a nanoporous network (10-100 nm) would be dedicated to the passage of smaller molecules, thus acting as a second transport mechanism, especially when macropores are totally clogged.

The first part of this work addresses the development of versatile and effective approaches to biocompatible doubly porous poly(2-hydroxyethyl methacrylate) (PHEMA)-based materials. The first approach relied on the use of two distinct types of porogen templates, i.e. a macroporogen and a nanoporogen. To generate the macroporosity, either NaCl particles or PMMA beads that could be fused or not, were used in order to control the pore morphology and interconnectivity of the materials. The nanoporosity was obtained by using various amounts of different porogenic solvents, thus generating a wide range of pore size distributions for this second porosity level. The second methodology was based on the thermally-induced phase separation process. A co-solvent mixture constituted of dioxane and water was used to solubilize previously prepared linear PHEMA, followed by a solidification process by freezing the co-solvents/PHEMA mixture, and subsequent sublimation of the co-solvents to generate the corresponding biporous PHEMA materials. Finally, advantage of doubly porous materials was taken through different functionalization reactions using carbonyldiimidazole chemistry, and further immobilization of in-situ generated gold nanoparticles. Such hybrid doubly porous materials proved to act as efficient catalytic supports.

In the second part, we numerically determined the permeability of doubly porous materials. The methodology was based on a double upscaling approach in the field of periodic homogenization theories and on unit cell calculations. The first upscaling consisted in the determination of a first permeability associated with the array of nanoscopic pores. At this scale, the pores were saturated by a viscous fluid obeying the Stokes equations and the problem was solved by means of standard Finite-Element approaches or using more recent techniques based on Fast Fourier Transform. At the mesoscopic scale, the fluid flow obeyed the Stokes equations in the macropores and the Darcy equations in the permeable solid. The unit cell problem coupling Darcy and Stokes equations was solved by the Finite Element method in order to compute the final macroscopic permeability. To this purpose, we developed a method based on a mixed variational formulation which was implemented by taking different elements in the solid and fluid regions. Various 2D and 3D examples were provided to illustrate the accuracy and the capacity of the proposed numerical methods to compute the macroscopic permeability of biporous materials.

Keywords:
- doubly porous polymeric materials
- double porogen approach
- thermally-induced phase separation
- permeability
- homogenization
- Finite Element method.

Acknowledgements

This work has benefited from a French government grant by ANR within the frame of the national program Investments for the Future ANR-11-LABX-022-01 (LabEx MMCD project). It laid within the scope of a research collaboration between the ”Mechanics” team of the Multi-Scale Modeling and Simulation laboratory (MSME) and the ”Complex Polymer Systems” team at the East-Paris Institute of Chemistry and Materials Science (ICMPE). The 3-year Ph.D. fellowship provided *via* the LabEx MMCD is gratefully acknowledged.

I would like to thank many staff members of MSME and ICMPE, Prof. Christian SOIZE, Prof. Guy BONNET, Prof. Salah NAILI, Dr. Michel LATROCHE, and Prof. Valerie LANGLOIS for fostering an outstanding research environment and for welcoming me in their respective laboratories.

I gratefully thank my supervisors, Dr. Daniel GRANDE and Dr. Vincent MONCHIET, for sparking my interest in chemical engineering and mechanical modeling, for their invaluable guidance, encouragement and their tireless efforts. They are fabulous advisors: sharp, cheery, perceptive, and mindful of things that truly matter.

I am very grateful to Prof. Michel DUMON and Prof. Djimédo KONDO for accepting to act as reviewers of my Ph.D. dissertation. Prof. Philippe COUSSOT and Dr. Daniela BAUER graciously agreed to be examiners in the jury, while Dr. Michel BORNERT and Benjamin LE DROUMAGUET accepted to participate in the jury. Let me acknowledge them.

Prof. Julien YVONNET and Prof. Christophe DESCELIERS also supported me at several points throughout my studies. My sincere thanks also goes to Séna HAMADI for the ICP analyses, Mohamed GUERROUACHE for the discussions on Raman Spectroscopy and mercury intrusion porosimetry, Rémy PIRES for Scanning Electron Microscopy analyses, Benjamin VILLEROY for SPS experiments, as well as Christian VARD for BET measurements.

Among contributors to this work are Romain POUPART, Thinh LE TIEN, Julien BABINOT, and Romain LACOMBE for many helpful discussions.

It should not go unmentioned that the people whom I have interacted with in two laboratories, such as Gaelle LE FER, Rémi CAPILLON, Olivier EZVAN, have been great and superb.

Finally, my greatest thanks go to my family: my wife, my son, my parents and my brother for their love.

All your help is sincerely appreciated.

Hai Bang LY
Paris, France
September 2015

List of Abbreviations

- **AIBN**: 2,2'-Azobis(2-methylpropionitrile)
- **ATR**: Attenuated Total Reflection
- **BET**: Brunauer-Emmett-Teller (nitrogen adsorption porosimetry)
- **CDI**: 1,1'-carbonyldiimidazole
- **DMPA**: 2,2-dimethoxy-2-phenylacetophenone
- **EGDMA**: Ethylene Glycol Dimethacrylate
- **FEM**: Finite Element Method
- **FTIR**: Fourier Transform Infrared Spectroscopy
- **FFT**: Fast Fourier Transform
- **HA**: Hydroxyapatite
- **HEMA**: 2-hydroxyethyl methacrylate
- **MIP**: Mercury Intrusion Porosimetry
- **PHEMA**: poly(2-hydroxyethyl methacrylate)
- **PMMA**: poly(methyl methacrylate)
- **SEC**: Size-Exclusion Chromatography
- **SEM**: Scanning Electron Microscopy
- **TIPS**: Thermally Induced Phase Separation

General introduction

The elaboration, the modeling, and simulation of porous materials have constituted areas of intense research and widespread interest for many years. From a synthetic point of view, a wide array of either organic or inorganic porous materials have been developed for diverse applications, such as materials for civil engineering, chromatographic supports for separation sciences, scaffolds for tissue engineering or devices for drug delivery applications. On the other hand, many studies have been devoted to the determination of effective properties of porous media *via* modeling, simulation or experimental measurements. Such investigations mainly focus on mechanical, hydraulic, or acoustic properties.

Polymer-based porous materials present some undeniable advantages over their inorganic counterparts, such as tunable mechanical properties, ease to be functionalized, and especially lower production cost. Over the last decade, doubly porous materials have attracted a particular attention from the research community. Indeed, these peculiar materials offer new interesting perspectives for the preparation of sustainable materials, the role of each porosity level being different and associated with different transfer processes. Macropores (with diameters of about 100 μm) would allow macromolecules flow through the material or seeding and proliferation of suitable cell lines within the material, while a nanoporous network (with diameters of about 100 nm) would be dedicated to the passage of smaller molecules, or play an important role regarding filtration applications, or act as a second transport mechanism to improve nutrients and wastes flow through the material, for instance, when macropores are totally clogged at the last stage of cell culture in tissue engineering applications. The modeling of doubly porous materials finds also applications in mechanical and materials engineering, *e.g.* geomaterials (concrete and rocks) in which damage by microcracking may occur due to mechanical loadings or by chemical reactions.

Throughout these highly raised demands, it actually exists a crucial need for structure and porosity optimization, depending on the specific targeted application. Therefore, it is desirable to design biporous materials with tunable structure, pore size range and morphology for fluid flow optimization or improve mechanical properties. On the other hand, investigating the physical behavior of such complex systems requires not only controlled chemical syntheses but also mechanical modeling tools. Indeed, the determination of the permeability of porous media is of fundamental importance in several practical problems related to mechanics and civil engineering (biomechanics, petroleum, flow in micro and nano systems, etc.). Further, the modeling of flow through doubly porous materials raises a number of fundamental and practical questions, such as the role of each porosity level on the macroscopic permeability, as well as the optimization of the microstructure to specific applications. The development of adapted numerical tools to simulate the fluid flow in multiporous materials then appears to be of key significance.

This Ph.D. thesis encompasses two main parts with the aim to develop the synergy between chemical engineering and mechanical modeling. This can be seen through two complementary points of view. From chemical engineering to mechanical modeling, we are able to simulate fluid flow through the biporous materials, and deduce the permeability of the synthesized materials. Conversely, from mechanical modeling to chemical engineering, by various simulations and calculations of different computed-microstructures, it is possible to pre-define the properties of mass transfer. This may be helpful for the elaboration of materials for a targeted application.

In this context, the main objectives of our work are described next. Firstly, we have engineered biporous polymeric materials with controlled pore size and connectivity. Two methods have been developed. The first approach relies on the use of two different porogens for the generation of two distinct populations of porosity, while the second strategy involves the use of a co-solvent system which generates doubly porous structures *via* thermally induced phase separation. Advantage of such doubly porous polymers has been taken through several functionalization reactions, and they have proved to be efficient supports in heterogeneous catalysis.

Secondly, in order to finely estimate the transport properties of biporous materials, the development of numerical methods has been envisioned *via* homogenization techniques. Since the problem contains two populations of highly different pore sizes, a double upscaling approach on unit cell calculations has been considered. At the lower scale, the flow through the network of nanoscopic pores is described by the Stokes equations. This allows for the computation of a mesoscopic permeability that will be used at the upper scale to determine the macroscopic permeability. Regarding the flow at the mesoscopic scale (*i.e.* that of macropores), the problem consists in solving a Darcy-Stokes coupled problem. Indeed, in the macropores the fluid flow obeys the Stokes equations, while in the permeable polymer, the flow obeys the Darcy equation to account for the presence of the nanoscopic pores.

The outlines of the Ph.D. dissertation are given below.

Chapter 1 provides an overview on the preparation methods for engineering doubly porous materials. The scope and limitations of the major approaches are highlighted. In addition, the state of the art concerning the modeling and simulation of fluid flow in doubly porous media is presented.

Chapters 2 and 3 are devoted to the synthesis of doubly porous materials. The double porogen templating approach to doubly porous PHEMA-based materials is detailed in chapter 2. To the best of our knowledge, no investigation clearly determining the different parameters that strongly influence the distinct porosity levels of biporous materials has been reported so far.

The second method based on the Thermally Induced Phase Separation (TIPS) process is investigated in chapter 3. A pre-synthesized linear PHEMA is solubilized in a co-solvent mixture of water/dioxane, then the solution is phase-separated in different temperatures in order to generate porous PHEMA with a bimodal porosity. By doing so, we have demonstrated the fabrication of doubly porous PHEMA-based materials *via* TIPS for the first time.

Chapter 4 addresses the versatile functionalization of bi-porous PHEMA-based networks obtained from the double porogen approach. Further *in-situ* generation of gold nanoparticles (GNPs), has followed for the preparation of innovative doubly porous GNP@PHEMA hybrid materials that can be used as efficient catalytic supports.

In chapters 5 and 6, we proposed a double upscaling approach to estimate the transport properties of doubly porous materials. In chapter 5, we simulate the fluid flow at the smaller porosity level, and we determine a mesoscopic permeability. To this purpose, finite element method (FEM), or iterative scheme based on Fast Fourier transform are employed to compute the permeability of 3D reconstructed porous microstructures.

In chapter 6, we determine the macroscopic permeability of doubly porous materials. At the mesoscopic scale, we determine the solution to a free fluid around a porous solid (Darcy-Stokes coupled problem). The problem is numerically solved by the FEM-based on a mixed variational formulation of the problem with the use of different interpolations in the fluid and solid regions.

Chapter 1

State of the art

The literature review chapter is organized in three sections. Section 1.1 provides a general introduction of porous media followed by general concepts associated with doubly porous materials. Section 1.2 introduces some preparation methods for doubly porous polymeric materials, and highlights the two major methods that were used in this work. Section 1.3 summarizes the present state of the art related to flow simulation and modeling concerning biporous materials.

1.1 Porous materials with double porosity

A solid matrix with interconnected voids can be defined as a porous medium. When the porosity in the medium becomes strongly heterogeneous, or there are more than two porosity levels which are distinct and separated, a multiporous medium is then considered. In the case of the fractured reservoir rocks, the first porosity level consists in pores between the grains of the matrix and the second level lies in the fractures [1–3]. In some problems related to civil engineering or soil mechanics, the first porosity level can be the interparticle voids and the second porosity level consists in the porous grains [4]. In tissue engineering, bone is considered as a multi porous medium: there are three levels of bone porosity with fluid within cortical bone (the vascular porosity), the lacunar-canalicular porosity, and the collagen-apatite porosity [5]. A doubly porous material can thus be seen as a simple model of multiporous media.

1.1.1 Polymeric materials with multiple porosity

In Nature, many materials, including marble, sandstone, clay, bones, wood, and ice, are doubly porous or even multiporous materials. Porosity can be considered as a fundamental concept that helps us to understand Nature and, to design artificial structures. Indeed, some interesting examples in Nature, such as hollow bamboo, honeycomb with hexagonal cells, and alveoli in the lungs, show an important architecture to be studied. Among these studies, porous organic [6] or inorganic materials [7] have been the subject of intense research and widespread interest for many years, mainly because of their wide range of applications. In a simple sol-gel process for the preparation of silica-based bioactive porous bone tissue scaffold [8], Almeida *et al.* presented a dual pore structure with both pores of 50-200 μm and 5-40 nm. These structures can improve performance in terms of crystallization of hydroxycarbonate apatite plus cell adhesion and proliferation, as well as vascularization. In another approach to designing bimorphous inorganic/composite structures, Onyestyak *et al.* [9], presented a composite having honeycomb structure as a new way of preparing zeolite adsorbents and catalysts. The obtained structure containing parallel channels of 20-30 μm diameters, separated by about 1-3 μm thick carbon walls, thus could increase the surface area of the material from 100 $\mathrm{cm}^2/\mathrm{cm}^3$ to 1000 $\mathrm{cm}^2/\mathrm{cm}^3$.

Polymer-based porous materials have particularly attracted much interest from the research community [6], as they possess some undeniable advantages. First, they display tunable mechanical properties in a useful range. Second, they can easily be functionalized by simple organic reactions. Last but not least, they can be engineered by processes with low production costs. Over the last decade, the preparation and analysis of doubly porous materials have particularly attracted the focus of researchers, such as for the design of biocompatible scaffolds meant for biomedical applications [10]. In this case, a hierarchical double porosity may constitute many benefits. In the area of tissue engineering, the first porosity with pore sizes higher than 100 μm may enable the seeding and proliferation of suitable cell lines within the material, while the second porosity with pore diameters lower than 1 μm should permit to improve the nutrient and waste flow though the material when the macropores are clogged at the last stage of the cell culture. For civil engineering and other applications, the larger porosity level would allow macromolecules flow through the material, while the smaller porosity level would be dedicated to the passage of smaller molecules or plays an important role in filtration applications [11]. Doubly porous materials with an open porosity can also facilitate fluid accessibility compared to an identical material with similarly lower porosity level. In the same way, introducing a bimodal mode of porosity can increase the specific surface area with regard to materials of similar macroporous network only [9].

1.1.2 Classification of doubly porous media

With a wide range of existing structures, morphologies, characteristics of porous materials, a classification of doubly porous or even multiporous materials becomes essential. Unfortunately, no such classification has been provided so far. In a more general context concerning porous media, two classifications have been proposed in the literature. They are based on the connectivity type of each constituent or refers to the storage capacity of different cavity types, for fractured reservoir problems.

The first classification of porous media was proposed in 1991 with respect to void space and solid matrix connectivity [12]. It is first necessary to recall the definition of the Representative Elementary Volume (REV), also called the Representative Volume Element (RVE), or the Unit Cell. This is the smallest volume over a domain that yield its representative value [13]. A classification of doubly porous media is based on the characteristic of void space or the solid matrix inside a Unit Cell. This unit cell is selected as it always contains both the solid phase and the fluid phase. One of the objectives of this thesis is to analyze the transport properties in porous polymeric materials, thus pore connectivity of the polymer phase is of major interest. The first classification of porous materials is summarized in Table 1.1, according to the type of different types of interconnectivity of the solid matrix and the void space.

Table 1.1: Classification of porous media with respect to void space and solid matrix connectivity. PM = porous medium, MC = single multiply connected domain only, SC = ensemble of simply connected domain only, MSC = combination of MC and SC, IP = isolated pores, and FB = fluidized bed.

		Void space		
		MSC	MC	SC
Solid matrix	MSC	PM$_1$	PM$_2$	
	MC	PM$_3$	PM$_4$	IP
	SC		FB	

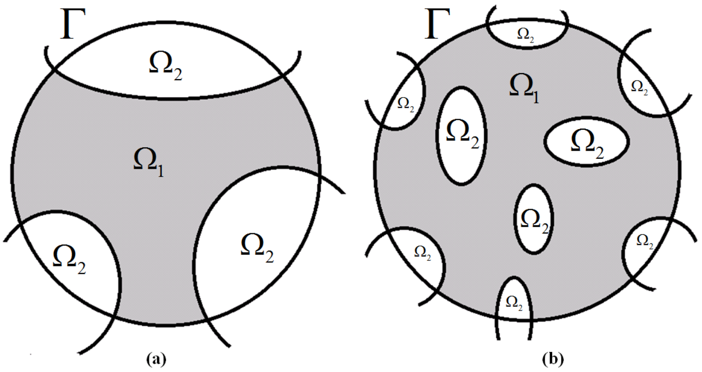

Figure 1.1: Scheme of the classification of porous media based on the connectivity of the void and solid phase.

According to Bear and Bachmat [12], a domain with a boundary Γ, is said to be connected or interconnected, if any two points belonging to it can be connected by a curve that lies completely within it (case of domain Ω_1 in Figure 1.1.a). Further, a

connected domain can be either simply- (SC) or multiply- (MC) -connected. A simply connected domain is considered if any close surface that can be placed within it can be shrunk to a point without leaving it (case of domain Ω_1 in Figure 1.1.a), and a domain is multiply connected (MC) if it is bounded from the inside by one or more disjoint closed surfaces (case of domain Ω_1 in Figure 1.1.b). Finally, a non-connected (or non-interconnected) domain is the one which is composed of a union of disjoint domains, with disjoint boundaries (case of domain Ω_2 in Figure 1.1.b).
Another classification of porous media has been proposed by Bai *et al.* in 1993, which is based on the storage capacity comparison between the fracture network and the pore matrix [14] (Figure 1.2):

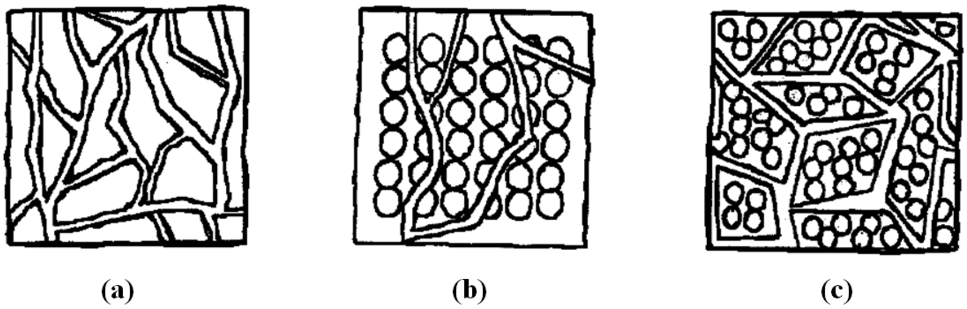

Figure 1.2: Scheme of the classification of porous media based on the storage capacity of the void and fractures: (a) fractures storage is more important, (b) smaller porosity storage is more important, and (c) the two porosity levels are equally distributed (from ref. [14]).

Figure 1.2 illustrates three configurations of porous structures that can be classified depending on the storage capacity of each porosity level. In the first case, the larger porosity (fractures) has an important role on the overall storage capacity of the media (Figure 1.2.a). The second case describes a medium in which the contribution of the smaller porosity is of considerable important to the larger one (Figure 1.2.b). The last case illustrates an averaging from the other cases, where the two porosity levels are equally distributed (Figure 1.2.c).

The two classifications above can be useful although they are usually used for fractured porous media (or rocks). We can consider the larger porosity level in doubly porous materials as fractures and the nanoporous phase as the smaller porosity level. Because of the particular morphologies of the synthesized doubly porous materials in our work, we can consider mainly a porous media of type PM_4 in the first classification, and a porous media related to Figure 1.2.b and Figure 1.2.c in the second classification.

1.1.3 General concepts associated with doubly porous polymeric materials

It is first necessary to define a terminology for doubly porous materials. With the development of studies on porous polymeric materials towards the end of 1950s, the terms macroporous and microporous were introduced [15]. According to IUPAC, macropores refer to pores which are larger than 50 nm (nanometers), mesopore size ranges from 2 nm to 50 nm and micropores are smaller than 2 nm [15]. However, macroporous networks usually have a broad pore size distribution ranging from 50 nm to several μm (microns). If the pore size is beyond 10μm, this type of hydrogel is also called a superporous hydrogel [16]. It is also well known that nanoscale refers to scales below 100 nm. In the context of the present work, to simplify these definitions and due to the two different porosity levels of the synthesized materials, the pores below 1 μm (diameter) were defined as nanopores, whereas the larger pores were defined as macropores. In some exceptional case, the definition of a ”smaller porosity” (or a ”lower porosity”) has to be used due to its pore size range higher than 1 μm. In this case, the macroporosity can be called as a ”higher porosity” or the ”upper porosity”.

A polymeric material with two different porosity levels, typically in our work macroporosity and nanoporosity, can be considered as a doubly porous material. It is interesting to note that the interconnectivity of each porosity level can be well controlled depending on the synthesis technique. This results in 4 different geometrical characteristics of the pore space within the porous materials:

- A doubly porous material with interconnected macropores, and the second porosity level comprises also an interconnected nanoporous network. In this case, fluid flow through the material may occur in both porosity levels. These common materials are widely used in tissue engineering [17–19];

- An interconnected macroporosity along with a nanoporous network which is non interconnected. In this case, the smaller porosity does not play an important role in the overall transport properties of the materials, but it could increase the specific surface area as a result of introducing a smaller porosity level. In addition to the interest of augmented surface, such a material introduces advantages in terms of chemical modification and surface functionalization compared to the materials with similar macroporosity only [20, 21];

- Another morphology of the doubly porous configuration consists in a non-interconnected macroporous network, with an interconnected nanoporous network. This type of structure might be used to decrease fluid flow due to the non interconnected macroporosity, or might be used in filtration applications;

- Finally, doubly porous materials may be constituted of non-interconnected macropores and also non interconnected nanopores. This type of material does not present a particular interest.

1.2 Preparation methods for doubly porous polymeric materials

The elaboration of porous polymers has been pursued in both applied and fundamental research for many years [6]. Porous polymers, whether they are cross-linked or not, are efficient materials used for many applications, such as chromatographic supports for separation sciences, materials for civil engineering, scaffolds for tissue engineering or devices for drug delivery applications [1–3, 10, 22–27].

According to literature studies, a typical porous polymeric material could be achieved by the following six major techniques:

- **Particle leaching**: this method is widely used to prepare porous scaffolds, mainly because of the easy operations and the accurate control of pore size and porosity. This method consists in adding salt particles to a polymer solution, then removing the salt by a corresponding solvent/diluent, thus obtaining a porous scaffold. The porosity and pore interconnectivity are well controlled by the ratio of salt particles (shape, size and coalescence level) and polymer solution [28].

- **Temperature-Induced Phase Separation (TIPS)**: a widely and common used method for the preparation of porous scaffolds is based on thermally induced phase separation. Using this technique, a homogeneous polymer solution is frozen to induce the phase separation. This phase separation mechanism may be liquid-liquid demixing, which generates polymer-poor and polymer-rich liquid phases. The subsequent growth and coalescence of the polymer-poor phase develop pores within the materials. In another case, when the quenching temperature is low enough to allow for the solution freezing, the phase separation mechanism is solid-liquid demixing, which forms frozen solvent and polymer phases. Pore size, morphology of the porous structure could be controlled by adjusting the polymer concentration, varying the solvent volume, using different solvents, or varying the cooling rate [29–31].

- **High Internal Phase Emulsions (HIPEs)**: a large variety of multiporous polymers, generally known as polyHIPEs, have been synthesized using high internal phase emulsions (HIPEs) as templates for the porous structures. HIPEs are formed by mixing two immiscible liquids in the presence of an emulsifier, usually a surfactant, such that the internal phase content is more than 74%.

PolyHIPEs are synthesized through the polymerization of monomers in the external phase. The internal phase can be evacuated through holes that develop in the polymer walls, yielding a porous polymer. Hydrophobic polymers can be synthesized within water-in-oil emulsions and hydrophilic polymers can be synthesized within oil-in-water emulsions [32–34].

- **Gas foaming**: the gas foaming technique uses high pressure gas, generally CO_2. The overall porosity and pore structure of the scaffolds depend on the amount of gas dissolved in the polymer, the rate and type of gas nucleation, and the diffusion rate of gas molecules through the polymer to the pore nuclei. Gas foaming often produces a scaffold that is too compact. In tissue engineering, to overcome this problem, this technique is often associated with salt leaching to prepare well defined interconnected macroporous structures [35, 36].

- **Electrospinning**: the electrospinning technique affords nanofibrous scaffolds from synthetic and natural polymers, with high porosity, a wide distribution of pore diameter, high surface area, and morphological similarities to natural collagen fibrils. Fiber diameters often range from several micrometers down to 10 nm. The electrospinning process is based on a fiber spinning technique driven by a high voltage electrostatic field (usually between 10-30 kV) applied between a syringe that contains a vicous polymeric solution or liquid and a collector for fiber deposition [37, 38].

- **Rapid Prototyping** (RP): this technique can be also called solid free-form fabrication (SFF), which is referred to a group of technologies that built a physical 3D object in a layer-by-layer fashion. The RP is a subset of mechanical processing techniques which allow highly complex structures to be designed as a series of thin 2D slices using a computer aided design (CAD) and computer aided manufacturing (CAM) programs. The main advantage of the technique is to allow researchers to predefine scaffolds properties such as porosity, interconnectivity, and pore size [39, 40].

In the next section, we will detail the five major techniques for the preparation of doubly porous polymeric materials as reported in the literature.

1.2.1 Double porogen approach

This strategy involves the formation of a polymeric network in the presence of two distinct porogens in the sample, followed by the subsequent extraction of the porogenic agents. A simple scheme of the doubly porogen templating approach is presented in Figure.1.3.

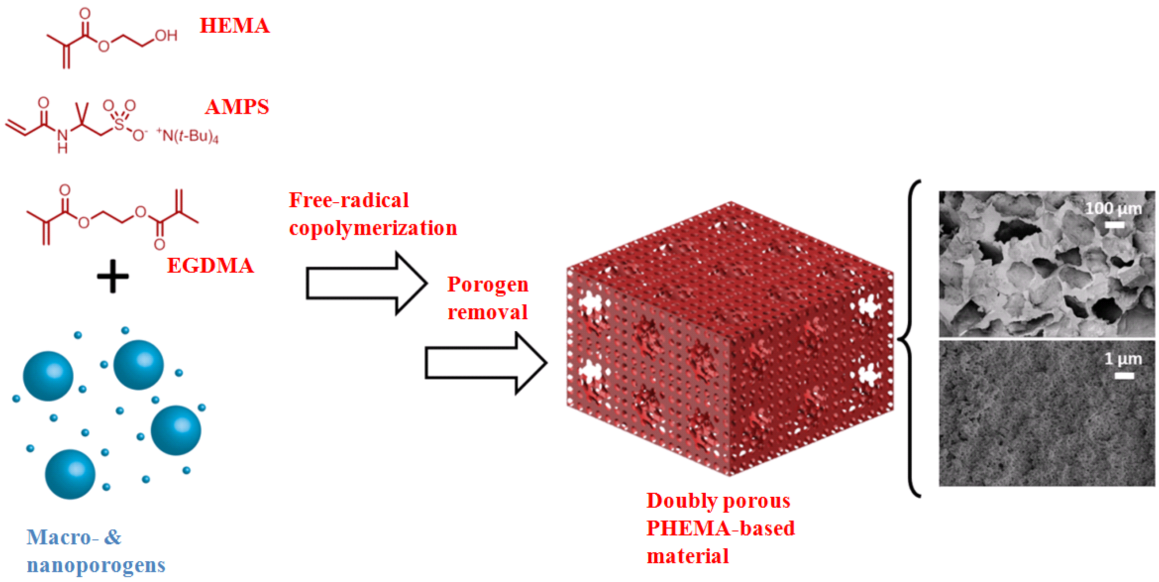

Figure 1.3: Scheme of the double porogen approach and SEM images of the porous morphology of a polymer synthesized by the double porogen approach.

It has been exploited for the preparation of dual porous PLLA- and starch-based materials [41]. In this particular case, it relies on the use of an inorganic porogen (NaCl) for macropore generation in conjunction with a macromolecular compound namely poly(ethylene oxide) (PEO) for smaller pore generation. High porosities in the 76% to 86% range were obtained along with relatively high water retention between 280% and 450%, while water uptake of pure PLLA scaffolds was about 93%. Specific surface area were not as high as 44 $m^2.g^{-1}$.

One alternative methodology of the double porogen approach relies on the use of macroporogen that, after leaching, gives rise to macropores while the smaller porosity is generated during the polymerization process by phase separation in the presence of a suitable solvent. It has been reported by Vidaurre *et al.* to prepare various copolymer-based doubly porous materials [42]. Thus, poly(2-hydroxyethyl methacrylate) (PHEMA), poly(ethyl acrylate) (PEA) and poly(ethyl acrylate-*co*-2-hydroxyethyl methacrylate) poly(EA-*co*-HEMA) with a double pore structure were prepared in the presence of poly(acrylonitrile) (PAN) fibers (of around 40 μm diameter) and ethanol as porogenic agents. In this specific case, PAN allowed for the formation of cylindrical pores with diameter in the 40 μm range while ethanol provided the nanoporous nature to the copolymer scaffolds of pore size ranging from 10 to 20 μm. Porous structures were observed to collapse upon ethanol evaporation. Porous structures of the hydrophilic scaffolds reopen when immersed into water while that of their hydrophobic counterparts did not. In the latter case, slow and progressive substitution of water by ethanol was necessary to open the pores.

Doubly porous PHEMA-based slabs were also prepared using either NaCl or $(NH_4)_2SO_4$ as macroporogens and a mixture cyclohexanol/dodecan-1-ol (CyOH/DOH

= 9/1 w/w)as nanoporogen [43]. Characterization by SEM confirmed the formation of large pores with diameters ranging from 200 to 500 μm, imprints of NaCl crystals, while smaller pores of 8 μm arose from the phase separation between the cross-linked polymer in formation and the solvent mixture. High porosities were observed (81 to 91%) and interconnection of pores in the PHEMA slabs was proved.

Bidisperse porous poly(glycidyl methacrylate-*co*-ethylene glycol methacrylate) (poly(GMA-*co*-EDMA)) frameworks have also been prepared *via* this methodology by radical suspension-polymerization method in the presence of two types of porogenic agents, *i.e.* a mixture of cyclohexanol and dodecanol (90:10 v/v) and calcium carbonate granules for micropores and macropores generation, respectively [44]. Characterization by SEM and MIP revealed that the polymeric monolith contained two types of pores, nanopores smaller than 180 nm and macropores of 500-7300 nm. The presence of such large pores in the chromatographic support allowed for high mobile phase flow rates while back pressure remained low. Moreover, the presence of epoxide functions at the surface of the stationary phase allows for the immobilization of chiral selectors such as proteins. Experimentally, BSA was thus tethered at the pore surface through a three step-strategy involving the reaction of immobilized epoxide moieties with ammonia, further reaction with 2,4,6-tricholoro-1,3,5-triazine and finally coupling with bovine serum albumin (BSA) to afford the BSA-decorated chiral stationary phase that showed some promising results regarding the separation of the two enantiomers of triptophan, even at high flow rates, indicating a possible use of these monoliths for enantiomers high speed resolution.

Shi *et al.* [45] developed biporous glycidyl methacrylate-based monoliths for separation sciences by the same methodology. The material synthesis was achieved through free-radical polymerization of GMA, triallyl isocyanurate (TAIC), divinylbenzene (DVB) in the presence of superfine sodium sulfate granules and a porogenic toluene/ n-heptane solvent mixture. Double porosity was confirmed by MIP. Macropores in the 200-3000 nm range that might serve as intraparticle flow channels along with small diffusive pores (10-150 nm) were observed. The presence of GMA repeating unit allowed for further functionalization of the monoliths with model amine, *i.e.* ethylene diamine, by nucleophilic attack of the immobilized epoxide residues. The as-obtained amine-functionalized matrices were successfully used as anion exchange chromatography supports for protein separation.

1.2.2 Combination of particle leaching and thermally induced phase separation

The combination of these particle leaching and TIPS allowed for the preparation of different dual porous materials. In this elegant methodology, the use of organic macroparticles allows for the formation of large pores after leaching of polymer beads or organic spheres, while the smaller pores are generated by a phase separation phenomenon at low temperature *via* the TIPS process.

For instance, poly(L-lactide-*co*-glycolide) (PLGA) scaffolds displaying big pores in the 75-400 μm range and small pores of less than 20 μm were obtained by using sucrose particles to generate the higher porosity and chloroform as the porogenic solvent [29]. The porosity of these materials, obtained with nearly 90% porosity, could be tuned by varying different parameters such as the polymer concentration, the freezing temperature, or the volume fraction of the porogenic solvent.

Doubly porous 3D nanofibrous gelatin (NF-gelatin) scaffolds could also be prepared using paraffin spheres of different sizes (diameter range of 150-250 μm, 250-420 μm or 420-600 μm) and a water/ethanol (1/1 : v/v) solvent mixture [46]. To increase thermal and mechanical properties of the NF-gelatine-based porous materials, a final cross-linking reaction with 1-ethyl-3-(3-dimethylaminopropyl) carbodiimide (EDC) was necessary. This reaction step was realized in a acetone/water solvent mixture (90/10 : v/v) in order for the polymeric scaffold not to swell and to retain its nanofibrous morphology. The as-obtained frameworks possess surface areas higher than 32 $m^2.g^{-1}$, high porosities (higher than 96%), well-connected macropores, nanofibrous pore wall structures along with good mechanical properties. The porous features of these materials, such as shape and size, interpores connectivity and pore wall morphology could be advantageously controlled by tuning the diameter of paraffin spheres, the assembly conditions (time and temperature of heat treatment), phase separation and post-treatment parameters, respectively. It was also observed that the mechanical properties of these porous NF-gelatin scaffolds were highly influenced by polymer concentration and cross-linking density. The authors notably demonstrated that this novel materials have significantly higher compressive modulus than SW-gelatin scaffolds but especially 10 times higher than the commercial available Gelfoam materials. More interestingly, after seeding and growing of MC3T3-E1 pre-osteoblasts cell culture, the NF-gelatin material retained its original diameter while that of the Gelfoam/cell construct shrunk to about 50% and 40% of its original size after 2 and 4 weeks of cell culture, respectively. This last result notably demonstrated the adequate mechanical strength of NF-gelatin scaffolds to maintain the 3D geometry required for cell in-growth and matrix production until later neotissue formation during tissue engineering process.

Recently, the possibility to prepare dual porous poly(L-lactic acid) (PLLA) scaffolds was also investigated by Santamaria *et al.* [30]. The higher porosity level arised from the leaching of poly(ethyl methacrylate) (PEMA) beads having diameters ranging from 120 to 200 μm while the small pores were obtained from TIPS process using dioxane as porogenic solvent. The authors demonstrated that PLLA to dioxane ratio controls micropore size and volume fraction of micropores and has also a certain influence on the macropore size due to the ability of dioxane to swell macroporogen particles. They also showed that the amount of macroporogen mixed with the PLLA solution allows modulating the size of pore throats interconnecting the macropores. The variation of these latter structural parameters allowed for modulating mechanical response and also permeability of the polymeric scaffold.

Chen *et al.* proposed the preparation of nanofibrous poly(L-lactic acid) (PLLA) doubly porous scaffolds through the use of thermally-interconnected paraffin spheres as macroporogen and a mixture dioxane/ pyridine used as porogenic solvent [31]. This methodology allowed for the synthesis of fibrous PLLA frameworks with interconnected macropores and nanopores lining the macropore walls.

1.2.3 High internal phase emulsions

High internal phase emulsion (HIPE) polymerization approaches have been applied to the synthesis of macroporous polymers [47]. This technique has been known for many years and finds applications in areas such as food preparation, fuels, oil recovery and cosmetics [48]. Figure 1.4 illustrates a scheme of typical polyHIPE synthesis [49].

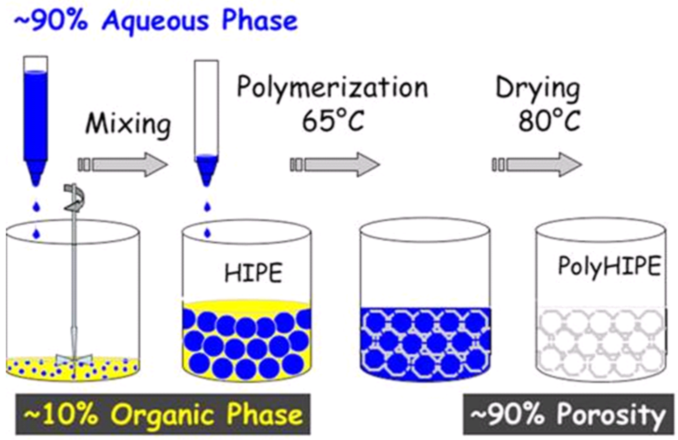

Figure 1.4: Schematic illustration of HIPE formation and polyHIPE synthesis within a water-in-oil HIPE that contains an aqueous internal phase dispersed within a hydrophobic monomer external phase. Based on ref [49].

One application of HIPEs that has found considerable use in materials science is as templates to create highly porous structures [32, 50]. This materials, formed by curing the continuous, or non-droplet, phase of the emulsion, are known as polyHIPEs. Following solidification of the continuous phase, the emulsion droplets are embedded in the resulting material. Under the correct conditions (vide infra), small interconnecting windows are formed between adjacent emulsion droplets allowing the droplet phase to be removed by drying. Typically, polyHIPEs are synthesized using conventional free radical polymerization in surfactant-stabilized water-in-oil (w/o) HIPEs. However, other polymerization methods (*e.g.* step-growth, atom transfer radical polymerization (ATRP), ring opening metathesis polymerization (ROMP)), other HIPE stabilization techniques (*e.g.* the particle-based stabilization in Pickering HIPEs), and other types of HIPEs (*e.g.* oil-in-water (o/w)) have also been investigated [34]. The types of polyHIPE systems developed include copolymers, interpenetrating polymer networks, biodegradable polymers, bicontinuous polymers, organic-inorganic hybrids, porous inorganics, and nanocomposites [34]. A typical polyHIPE can be produced through the copolymerization of styrene and divinylbenzene *via* a water in oil HIPE (at 90% internal phase) [51]. Styrene is a water-immiscible liquid, therefore water-in-oil HIPEs are used to creat polystyrene polyHIPEs. These porous material have two types of porous structure, a larger one contains pores of 10-20 μm, and on the wall of the larger porosity located a smaller porosity of about 1-3 μm. This type of porous structure had the ability to rapidly absorb large quantities of liquids through capillary action. This work on polyHIPE has also developed theoretical models to describe the relationships between the void size and the mechanical behavior. Many others hydrophobic monomers have been used to creat polyHIPEs from water-in-oil emulsions such as 2-ethylhexyl acrylate (EHA) and methacrylate (EHMA) [33, 52], butylacrylate (BA) [52] and isobornyl acrylate (IBA) [53]. PolyHIPEs can have complex morphologies. They possess spherical cavities, known as voids, and windows that interconnect these spherical voids. Furthermore, a much finer porous texture within the walls of the base material can be created [47]. Furthermore, the dimensions of the porous materials can be varied from thin membranes to large monolithic articles.

1.2.4 Gas foaming process

The gas foaming process consists in three principal steps: saturation, desorption, and foaming. A polymer is introduced into a pressure vessel under a controlled gas pressure and temperature, in the first step. The gas then diffuses into the polymer, occupying the free spaces between the polymer chains [54, 55]. In the second step, gas pressure is released and the sample enters into a supersaturated state. The polymer starts to release the excess of gas by diffusion to the outside or by the formation of discontinuities/voids inside the matrix. These voids will acts as nuclei for the cells formation [56, 57]. In the last step, when the saturated sample reaches a temperature close (or over) to its glass transition temperature (T_g) the nuclei previously formed can grow into cells. Cell growing is promoted by the pressure difference between the gas inside the sample and the external pressure. Final cell size is controlled by the magnitude of the pressure inside the sample, and the viscoelastic properties of the polymer matrix at the foaming temperature. Nevertheless, the gas foaming technique could only produce a monoporous polymer structure. A simple scheme of such technique is presented in Figure 1.5

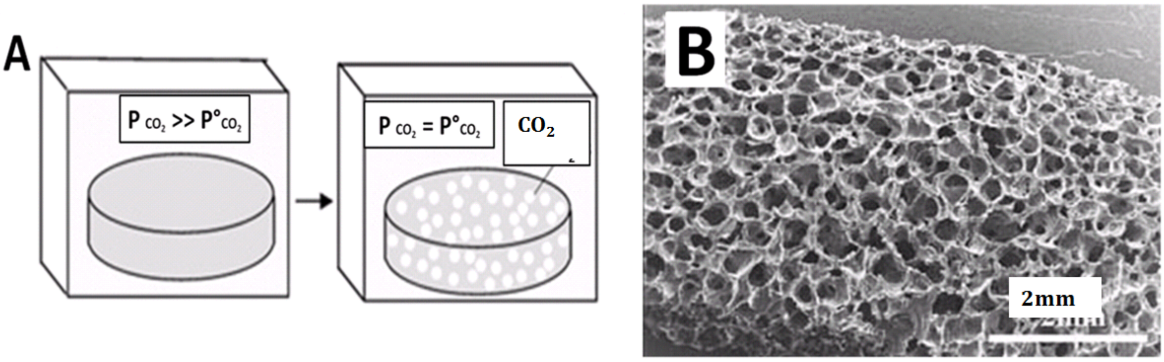

Figure 1.5: (a) A simple scheme of the gas foaming process and, (b) SEM image of the morphology of a porous polylactic acid (PLA) polymer foam (from ref. [58]).

Gas foaming was used to produce microcellular polymer system [59, 60], then it was developed as a technique to fabricate highly porous macrocelullar foams from copolymers of lactic and glycolic acid using high pressure CO_2 gas processing [61]. Researchers used gas foaming process combined with temperature-induced phase separation in order to generate a dual porosity within polymeric materials. It has been notably developed for the preparation of PLLA- and PLGA-based materials presenting a double porosity, namely large pores in the 200-300 μm range and small ones in the 5-20 μm range, with an interconnected structure [62]. Experimentally, poly(lactic acid) (PLLA) or poly(lactic-*co*-glycolic acid)PLGA was dissolved in a dioxane/water solvent mixture at different ratios. The resulting PLLA/PLGA solutions were supplemented with sodium bicarbonate and freeze-dried to generate the dual porosity. Two parameters, namely the freeze-drying temperature (FDT) and the water content were tuned. Whereas FDT did not show any significant influence on the properties (porosity, mechanical) of the obtained polymeric frameworks, the compressive strength of the materials was diluted with the water content of the polymer solution before freeze-drying. It is good to notice that high porosity level (92% to 98%) were obtained with this methodology. This polymeric scaffold, because of all these characteristics, could find a promising application in the tissue engineering area. With another approach dedicated to fabricate scaffolds for tissue engineering, Harris *et al.* proposed a combination of gas foaming approach and salt leaching technique [63]. Indeed, gas foaming approach typically yield a closed pore structure, which is disadvantageous in many applications of cell transplantation. In addition, a solid skin of polymer results on the exterior surface of the foamed matrix [60] and this is often undesirable. A coupling approach with salt leaching technique could enable the fabrication of highly porous matrices with levels of pore connectivity between predominantly interconnected and closed. Precisely, disks comprised of poly (D,L-lactic-*co*-glycolic acid) and sodium chloride (NaCl) particles were compression molded at room temperature and subsequently allowed to equilibrate with high pressure CO_2 gas at 800 psi. Creation of a thermodynamic instability led to the nucleation and growth of gas pores in the polymer particles, resulting in the expansion of the polymer particles. The polymer particles fused to form a continuous matrix with entrapped salt particles. The NaCl particles subsequently were leached to yield macropores within the polymer matrix. The main advantage of the gas foaming process is to fabricate the porous matrix without the use of organic solvents. Indeed, residues of organic solvents, which can remain in polymers after processing, may damage transplanted cells and nearby tissue and inactivate many biologically active factors (*e.g.,* growth factors) that one might wish to incorporate into the polymer matrix for controlled release. Several works have also reported the effectiveness of the coupling process of gas foaming with another approach, mainly for the fabrication of biodegradable PLLA porous scaffolds [64, 65], which is a common polymer for tissue engineering.

1.2.5 Electrospinning

The ”electrospinning” technique is based on a well-known principle. In 1882, Lord Rayleigh worked on the number of loads required to overcome the surface tension forces phenomena [66]. Thereafter, the first devices generating a spray from a liquid by applying electrostatic charges were patented by Cooley and Morton in 1902 and 1903 [67, 68]. The first patent that actually described a device capable of generating synthetic fibers by applying electrostatic charges appeared in 1934, and was introduced by Formhals at the University of Mainz [69]. Despite these early discoveries, the process has only been used commercially until 1991 for the manufacture of filters within the textile industry. Since the 1990s, ”electrospinning” has arisen more and more interest in both academia and industry. In particular, Reneker and his collaborators at the University of Akron who developed the production of very fine fibers from a broad range of organic polymers [70, 71]. Figure 1.6 shows a simple scheme of the electrospinning process and a SEM image of a typical polymer fabricated by electrospinning.

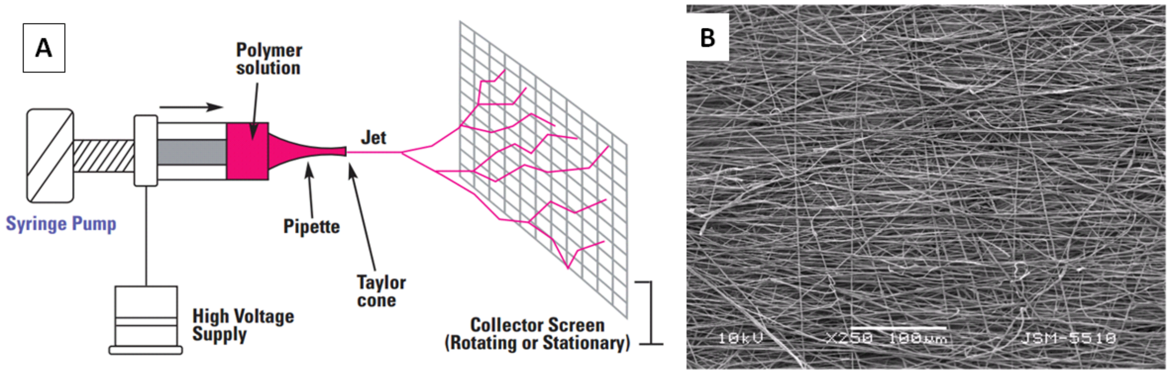

Figure 1.6: (a) A simple scheme of the electrospinning process and, (b) SEM image of the porous morphology of a polymer fabricated by electrospinning.

Doubly porous materials fabricated by electrospinning have not been well developed in the literature, except in one case where the fibers are porous [72]. The first porosity level can be considered by the spaces between the fibers, and the second porosity level is located within the porous fibers. The surface area of a nanofiber can be greatly increased when its structure is switched from a solid to a porous one. Increase in surface areas is beneficial to many applications that include catalysis, filtration, absorption, fuel cells, solar cells, batteries, and tissue engineering. Two slightly different approaches have been reported for introducing a porous structure into the bulk of an electrospun nanofiber [38]. One of them was based on the selective removal of a component from nanofibers made of a composite or blend material. The other one involved the use of phase separation of different polymers during electrospinning under the application of proper spinning parameters. Wendorff and co-workers investigated the structural changes for fibers consisting of a PLA/PVP blend when one of the two components was selectively removed [73]. It was found that the fibers became highly porous in structure when equal amounts of the two polymers were loaded into the electrospinning solution. If the amount of one polymer was much higher than the other one, the fibers remained compact in structure after one of the polymer phases had been removed. The same group also found that porous fibers of PLA and polycarbonates (PC) could be directly obtained if the spinning parameters and the solvent system were judiciously selected [74]. Rabolt and co-workers have also observed the formation of pores in the electrospinning of other polymers such as PC,poly(methyl methacrylate) (PMMA), and polystyrene (PS).They found that the solvent vapor pressure and the humidity in atmosphere strongly affected the formation of pores [75, 76]. Recently, Xia and Li demonstrated that porous ceramic nanofibers could be fabricated by electrospinning with the use of a coaxial, double-capillary system [77]. In this case, the PS solution in a mixture of DMF and tetrahydrofuran (THF) was used as the core liquid and a PVP/Ti(OiPr)$_4$ solution in ethanol was used as the sheath liquid. Although the two polymers (PS and PVP) are immiscible, the solvents are miscible. It was found that these two liquids could be partially mixed in the electrospinning process because the mutual diffusion of the two solvents could bring PS and PVP/Ti(OiPr)$_4$ together to form a more or less homogeneous mixture in certain regions of each liquid jet. As the solvents evaporated quickly in the next steps, these two polymer phases were separated to generate nanoscale domains of PS embedded in a continuous TiO$_2$/PVP matrix. Once the PS phase had been removed by calcination (along with the PVP phase), the resultant fibers became highly porous in the PS-rich regions.

1.2.6 Other techniques

Emulsion and beads sintering

Another methodology involving emulsion and beads sintering has recently been reported by Luciani *et al.* [78] for the preparation of biporous materials for sustained protein (BSA) delivery. Thus, poly(ϵ-caprolactone) (PCL, Mn = 65 kg.mol^{-1}) was emulsified in presence of poly(vinyl alcohol) (PVA) as a surfactant in a water/dichloromethane mixture. After extraction of the solvent, beads displaying average diameter of tens of micrometers were obtained. In a last step, sintering of PCL microspheres of a selected size range was achieved at 60 °C for 1 hour in molds. In this way, the second higher porosity was easily generated in these materials. It is noteworthy that the incorporation of BSA in such PCL doubly porous materials necessitate a double emulsion process during the first step of this methodology in order to encapsulate BSA protein within the core of PCL microspheres.

Double emulsification approach

Biporous materials can also be prepared by double emulsification and UV-irradiated polymerization. This strategy is based on the use of an aqueous suspension of an superfine granule and an equivalent organic solvent as porogenic agents to creat different type of pores [79]. In this study, super-fin calcium carbonate were first suspended in a Triton X-114 solution, then recovered by centrifugation and resuspended into deionized water. Cyclohexanol and dodecanol were used as the organic porogenic solvents. The two phase system, after being homogenized, were used to prepare the water-in-oil emulsion (first emulsification), and then immediately poured into a reactor for the second emulsification. The beads were then collected, washed, and analyzed. Mercury intrusion porosimetry gives the average diameter of calcium carbonate beads 46.3 μm, and possess two types of pores between 20-200 nm and 500-5300 nm.

1.3 Mass transfer properties in doubly porous materials

Due to a vast domain of applications of doubly porous materials, the properties of mass transfert have been long far studied *via* experimental measurements, theoretical modeling and simulations. Such investigations focus on mechanical, hydraulic, and acoustic properties for applications in civil engineering or soil mechanics, for instance. Indeed, investigating the physical behavior of such complex systems requires not only controlled chemical syntheses but also mechanical modeling tools. The determination of the permeability is of fundamental importance in several practical problems related to mechanics and civil engineering (biomechanics, petroleum, flow in micro and nano systems, etc..). Further, the modeling of flow through doubly porous materials raises a number of fundamental and practical questions, such as the role of each porosity level on the macroscopic permeability, as well as the optimization of the microstructure to specific applications.

Two main morphologies can be envisioned depending on the interconnectivity of the porous media: macropores may be either interconnected to each other or non-interconnected to each other but interconnected through the nanoporous network. The development of adapted numerical which account for the porous microstructures then appears to be of key importance. The determination of the permeability in connection with the microstructure geometry has been addressed with homogenization techniques based either on asymptotic expansions [80, 81], or on volume average methods applied to random microstructures [82]. These approaches provide the elementary cell problem which has to be solved to determine the macroscopic permeability. For instance, the computation of permeability of monoporous materials has been performed using expansions along eigenfunctions [83–87]. However, these studies generally reduce their analysis to some simple geometrical configurations, such as the flow through regular arrays of cylinders or spheres. In the case of more complex microstructures, the Finite Element Method (FEM) can be used for computing the permeability of porous media [88–91]. An alternative method based on Fast Fourier transform (FFT) has been recently proposed by Monchiet *et al.* [92, 93]. It extends an original method proposed for elastic composites [94–97] and showed many advantages over FEM, particularly in reducing the computer memory occupancy. The homogenization approaches have then been extended to the case of doubly porous media [98]. Particularly, Auriault and Boutin [1–3], Royer *et al.* [99], Boutin *et al.* [4], Olny and Boutin [100], have considered the fluid flow in granular aggregates for which grains are also porous, *i.e.* contain a network of smaller interconnected pores. In such a situation, there is a dominant flow at the larger pore level, and the fluid flow at the lower pore level only introduce a small correction to the macroscopic permeability. Furthermore, the grains seem to be impervious when the nanopores are much smaller than the macropores, and could thus be not considered in the calculation of permeability [1, 4]. However, for porous materials constituted of isolated macropores in a nanoporous solid, the role of nanopores may be crucial in the calculation of macroscopic permeability. Between these two limit cases, there is a wide range of various situations for which both the nanopores and the macropores have an important role on the macroscopic filtration law. Note that in the works of Auriault and Boutin [1–3], the results for the computation of macroscopic static permeability is applicable to arbitrary morphology, including the case of isolated macropores.

Doubly porous materials contains three separated scale:

- that of the smaller pores or nanopores, this scale is thereafter called ”nanoscale”,
- that of the larger pores or macropores. This intermediate scale is thereafter called ”mesoscale”, and
- the macroscopic scale at which the pressure gradient is applied.

Due to the occurrence of three scales, the effective permeability is determined by a consecutive double homogenization procedure (Fig. 1.7). In a first step, the mesoscopic permeability $\boldsymbol{K}_{\text{meso}}$ is obtained by homogenization of the lower scale. At this scale, the fluid flow is described by the Stokes equation with an adherence condition at the surface of the solid. At the mesoscopic scale (that of the macropores), the flow in the macropore is described by the Stokes equation while in the solid region, the fluid flow is described by the Darcy equation. A Darcy-Stokes problem may then be solved to compute the macroscopic permeability. The development of numerical methods for computing the macroscopic permeability of doubly porous materials remains quite challenging since the resolution of Darcy-Stokes problem need the consideration of specific variational formulation and interpolation which have been evaluated mainly for some simple 2D examples with rectangular domains.

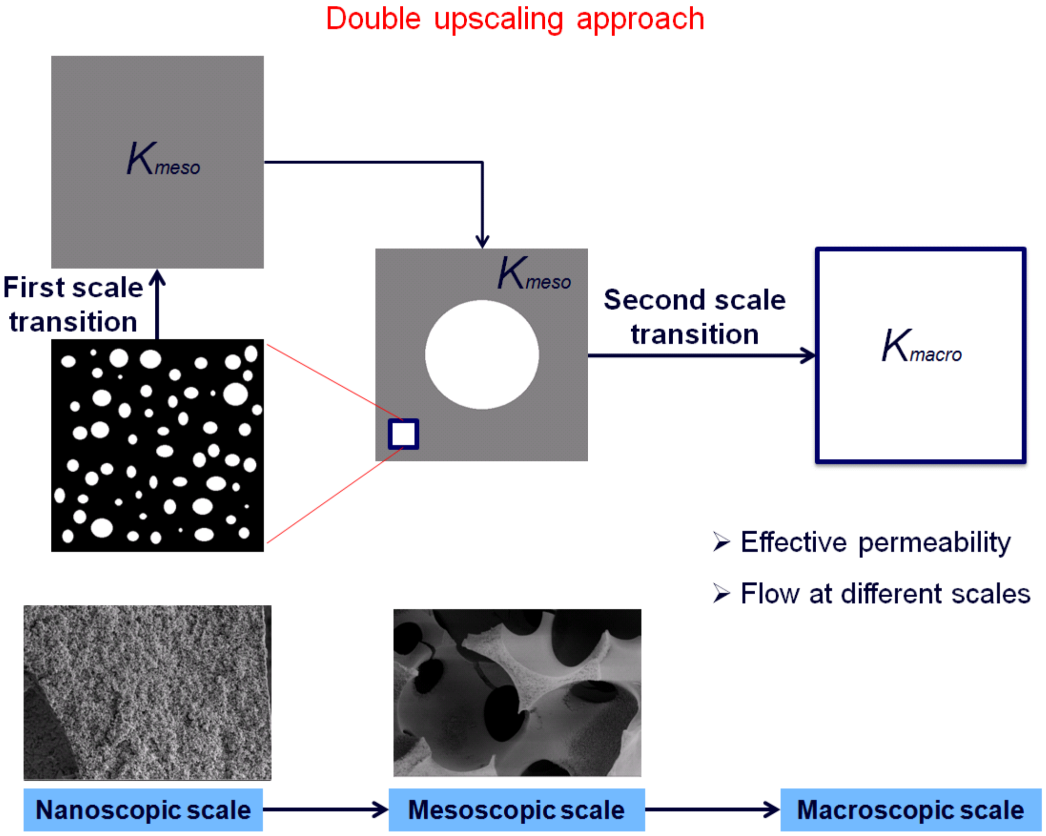

Figure 1.7: Scheme of the double upscaling approach proposed.

1.3.1 Flow through the lower porosity level: Solving the Stokes equations

The Stokes equations govern the incompressible flow of viscous fluids, and are similar to that of incompressible elasticity. The Stokes equations are a particular case of more complicated equation such that Navier-Stokes ones. Consequently, the numerical solution of many engineering problems is basically solved *via* the Stokes equations. Thus, a large number of works focus on the ability to solve the Stokes equations.

In finite element problems, the classical Galerkin/variational formulation of the Stokes problem has been first proposed by Herrmann [101] and can be viewed as a particular case of the mixed variational formulation of Hellinger-Reissner [102]. Incompressible fluid flow problems, otherwise the Stokes equations, generally contain velocity and pressure as the unknown variables and fall in the category of mixed formulations [103]. It was recognized by the formulation of this type that, the solutions were strongly depended upon the particular pair of velocity and pressure interpolations employed. Otherwise, natural combinations produced violently oscillating pressures. The mathematical works for understanding the behavior of mixed methods for the Stokes problem was provided by Babuska [104], Brezzi [105] and later by Ladyzhenskaya [106] for the first rigorous proofs of the convergence of a finite difference method for this problem. The spaces of discretization must satisfy the inf-sup condition or the Ladyhenskaya-Babuska-Brezzi (LBB) condition. The inf-sup condition limits the choice of subspaces for the discretization of the velocity and pressure fields, so the chosen mixed finite elements should satisfy this stability crition to yield convergent solutions. Many different techniques to deal with this problem can be found in the literature, mainly based on two choices: an equal-order interpolations or an unequal-order interpolations.

1.3.1.1 Unequal-order interpolations of Stokes problem

The MINI elements [107], Taylor-Hood [108] or Crouzeix-Raviart elements families provide unequal order interpolations for the velocity and the pressure which satisfy the LBB condition. For the sake of simplicity, we focus on the implementation of these families of elements, which are detailed below. If we take an example of the pair (for the velocity field and the pressure field) $P_{n\geq 1}/P_{n\geq 1}$, and P_1/P_0 (P_n being the interpolation polynomial of degree n in a triangular element), they are well known to be unstable. It means that the spaces built on these finite element pairs do not satisfy the inf-sup condition. The next part will be dedicated to give some examples of stable pairs of finite elements for Stokes problem.

MINI element: These elements use the bubble functions to satisfy the inf-sup condition. The MINI element has been introduced by Arnold, Brezzi and Fortin [107]. The idea of the so-called MINI element is to add bubble functions to the velocity space to stabilize the unstable pair P1/P1. The MINI element is the stable pair P1+/P1 (where "+" denotes the bubble functions), and represent the most economic stable element for solving the Stokes equations. Bai [109] proposed a new version of the MINI element based on bilinear velocity and bilinear continuous pressure that can also satisfy the inf-sup condition. Baiocchi *et al.* [110] first establish the equivalence that exists between the stabilization schemes such as Galerkin least squares formulation and the standard Galerkin method based on the use of bubble functions. The relation

between the Galerkin method enriched with bubbles and stabilized methods has been extended to the advection-diffusion equation by Brezzi *et al.* [111]. Later, Hughes [112] established the relationship between the bubble functions and the stabilized methods in an approach developed for deriving variational methods capable of representing multiscale phenomena.
P1+/P1 has 11 degrees of freedom in 2D (8 for velocity and 3 for pressure), and 19 degrees of freedom in 3D (15 for velocity and 4 for pressure). The detailed basis functions of the P1+/P1 element will be presented in chapter 4 for 2D and 3D cases.

Taylor-Hood elements: The Taylor-Hood elements [108] have the Lagrangian finite element spaces K_l which are defined by:

$$K_l = \begin{cases} P_l \text{ if the elements are triangles or tetrahedron} \\ Q_l \text{ if the elements are quadrilaterals or hexahedrons} \end{cases} \tag{1.1}$$

where P_l are polynomial of order l and Q_l are quadratics of order l. The Taylor-Hood elements satisfy to the inf-sup conditions. The most popular/economic element in the Taylor-Hood families ($\mathrm{P}_l/\mathrm{P}_{l-1}$) is the P2/P1 element and is the lowest order element in the Taylor-Hood family. It has 15 degrees of freedom (DOFs) in 2D (12 for velocity and 3 for pressure) and 34 degrees of freedom in 3D (30 for velocity and 4 for pressure). It is more expensive in memory space and CPU time than the MINI element.

Taylor-Hood elements are often considered for two-dimensional finite element simulation of laminar flame propagation [113], mixed convection within a porous heat generating horizontal annulus [114], effective boundary conditions for buoyancy-driven flows and heat transfer in fully open-ended two-dimensional enclosures [115], numerical simulation of the sedimentation of a tripole-1ike body in an incompressible viscous fluid [116], modeling of mass transfer from falling droplets [117], or 3D finite element modeling of hydrodynamics of a hydrocyclone [118] used the Taylor Hood elements. All these results demonstrated the successful application of the Taylor-Hood families in finite element modeling of industrial flow problems.The detailed basis functions of the P2/P1 element will be presented in chapter 4 for 2D and 3D cases.

Other elements: Besides, there is a long list of elements found in the literature which can be used for the discretization of Stokes problems. For exemple, the reader could find below some examples:

- The Nédélec elements [119,120], which introduce tangential velocity on the edges as the DOFs (Figure 1.8),

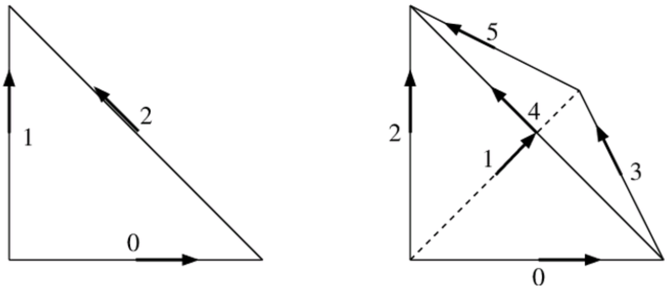

Figure 1.8: The Nedelec elements in 2D and 3D

- the Q_{k+1}-Q_k element on box grids for k $\geqslant$ 2, with Q_k are polynomial approximation of degree k on quadrangle element.

1.3.1.2 Equal-order interpolations of Stokes problem

Various stabilization schemes have been proposed in order to use equal-order interpolations of the velocity and the pressure fields. Such schemes can be listed as: the Brezzi-Pitkaranta scheme [121], the Galerkin least-squares approach [122], the variational multiscale method [123], and the polynomial pressure projection (PPP) technique [124, 125]. Successful application of these stabilization schemes has been reported for poromechanics of single porosity media [126–128].

The least-squares Galerkin finite element method is based on the use of continuous C(1) Hermite elements. These elements, however, are limited in flexibility and requires implementation effort due to the calculation of the second order derivatives [129].

On the other hand, augmented Galerkin or stabilization techniques based on either the modification of the weight functions, or on the modification of interpolation functions for velocity and pressure fields have also been proposed [122, 130–133].

Hughes and De Sampaio proposed similar formulations which consists with additional terms in the continuity equation, thus yield the results independently from oscillations. Precisely, Hughes *et al.* [122] proposed a finite element formulation, or the Petrov-Galerkin method, *via* the incorporation of the additional terms in the continuity equation containing modified weight functions. Later, De Sampaio [130] developed an approach by applying the Galerkin method to the steady state continuity equation and the least squares method to the time discretized momentum balance equation, which was extended from the work of Jiang [134], to solve the Navier-Stokes equations.

Douglas and Wang [135] proposed a modification of the method introduced by Hughes *et al.* [122]. This method is called ”an absolute stabilized finite element method for Stokes problem”. The authors assume that the velocity on the boundary should only respect the compatibility condition. Douglas and Wang modify also the method proposed by Hughes *et al.* [122] to deal with non continuity of pressure interpolation and by introducing a jump operator.

Zienkiewicz and Wu [131] suggested a new fomulation for Stokes and Navier-Stokes equations by introducing an additional term for artificial compressibility in the continuity equation. Extended to the Navier-Stokes problem, they used different time stepping operators (*i.e.* simple predictor-corrector, operator splitting (velocity correction) and the Runge-Kutta-Galerkin schemes) for the temporal discretization of the flow governing equations and obtained stable and accurate solutions.

Another methods existing in the literature, are the multiscale methods. They are different from the penalized and residual methods: they use stabilization terms provided by the effect of a fine scale which is not captured by the above methods. A theoretical formulation for this multiscale method can be found in the homogenization approach of [136] and its finite element implementation is presented by Hou and Wu [137]. In this works, the standard finite element basis functions are replaced by new ones which contain fine scale structure. These new functions are calculated by solving local fine scale problems. Lately, Aarnes *et al.* [138] have extended this method to the mixed problems. There are two essential types of Multiscale Methods: the Variational Multiscale Methods (VMS) and the Adaptive Variational Multiscale Methods (AVMS). The The Variational MultiScale method (VMS) is widely used in stabilizing the Stokes equations. The VMS is based on the idea of splitting the finite element spaces into a coarse and a fine parts. The coarse space is a standard finite element space but the fine space is an infinite dimensional space. Hughes suggests that the fine scale solution could be solved by analytical approximation on each coarse element in terms of the solutions calculated directly in the coarse space. In the literature, we can find two important Variational Multiscale Methods: Hughes Variational Method (HVM) developed in the works of Nakshatrala *et al.* [139], used for stabilizing the Stokes equations (and can also be applied to the Darcy equations), and another type of method which introduces operators of projection onto the fine scale spaces, the Algebraic SubGrid Scale (ASGS) and Orthogonal SubGrid Scale (OSGS) [140].

1.3.2 Flow through doubly porous materials: Solving the Darcy-Stokes coupled problems

Coupling free fluid flow with porous media has various practical applications such as hydrological systems in which surface water percolates through rocks and sand, or physiological phenomena like the blood motion in the vessels, solidification of metals in casting industries, spontaneous ignition of coal stockpiles [141], a model of lung alveolar sheet [142], insulation by permeable materials [143], porous bearings or spheres [144, 145], packed bed of particles [146–148], other important convection related problems [149–152], and in modeling of liquid infusion into fibrous media undergoing compaction

[153].

There are two approaches for modeling fluid flow in doubly porous media. The first approach is based on the use of Brinkman equation to describe the flow in doubly porous media [154]. The Brinkman equation couples the Darcy and Stokes equations, and consider the continuity of the velocity and the pressure. However, Brinkman's equation is only applicable to media of high permeability [155].

The second approach is based on the use of Stokes equations in free domain, Darcy equation in the porous solid, and the imposition of a slip-wall boundary conditions at the free/porous interface. The Beavers-Joseph (BJ) interface conditions have been often considered in the literature [156]. This model involves continuity of the normal velocity but the tangential component, and the pressure are discontinuous. Saffman [157] extends the Beavers and Joseph model by applying it to a non-homogenous porous medium *via* a statistical approach (BJS). Later, Jager and Mikelic [158] provide some mathematical justification for Saffman's form of the Beavers and Joseph conditions. In spite of all such works, the use of Beavers and Joseph approach poses an unresolved problem because it depends on the evaluation of a slip coefficient at the free/porous interface. The value of this coefficient depends on many physical parameters such as the geometry of the interface, or the nature of the fluid, making it nearly impossible to measure experimentally. Therefore, studies in coupling Darcy and Stokes equations with BJS interface conditions have received considerable attention in the last decades. The main challenge is to construct a sound mathematical formulation and the selection of appropriate approximating function spaces for the numerical solution of these equations, which guarantee stability of the solutions, is not straightforward [159, 160].

The discretization of the Darcy-Stokes coupled problem with BJS interface conditions has been the subject of many researches in the literature. Among the different methods, two main strategies have been developed: an "unified" or a "decoupled" one. Decoupled strategies use different discretization spaces for Stokes and Darcy. The main decoupled strategy used in the literature for coupling Stokes-Darcy are in the work of Discacciati [161], Layton [159] or Celle [153]. In an unified approach, the finite element discretization is based on the same finite element spaces (or elements) for both region. Such method are based on the use of the "robust" elements, or modified variational formulation of the coupled problem [162–165].

1.3.2.1 Decoupled approach

The decoupled strategy is based on the use of two matching meshes and two finite element spaces for discretizing the Stokes-Darcy coupled system. This approach has been considered for various applications. For instance, Salinger *et al.* [141] study coal stockpile ignition problem in which they consider the reaction, transport and flows within and around a porous coal stockpile in shape of a frustum sitting on the ground and surrounded by atmosphere. They have also shown the sensitivity of the results with the value of the slip coefficient in the BJS model. Discacciati *et al.* [166], Miglio *et al.* [167] study the coupling of Navier-Stokes and Darcy equations for groundwater flow. Also, Gartling *et al.* [168] investigate the coupling of Navier-Stokes and Darcy equations for studying metal processing alloy solidification problems.

Below are given the elements usually used for Darcy problem and for the decoupled approach of Darcy-Stokes problem.

Stable elements for Darcy:

- The Raviart-Thomas (RT) elements are well-known stable elements for the discretization of Darcy problem [108]. Contrarily to the classic interpolation which uses the velocity at the nodes as DOFs, the Raviart-Thomas elements introduce the moments of the normal component of the velocity on each edge as DOFs (see figure 1.9). The Raviart-Thomas approximation is applicable to triangular element, and the approximation RTn then introduces the normal component at n+1 points per edge. In the case $n = 0$ the RT element are associated with constant normal velocity field on each edge.

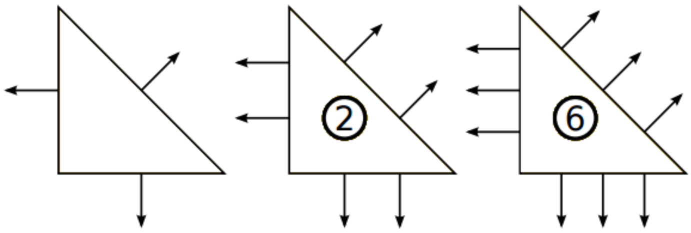

Figure 1.9: The zeroth order (n=0), linear (n=1) and quadratic (n=2) Raviart-Thomas element for triangles.

The Raviart-Thomas element is also applicable to rectangles and boxes (see figure 1.10).

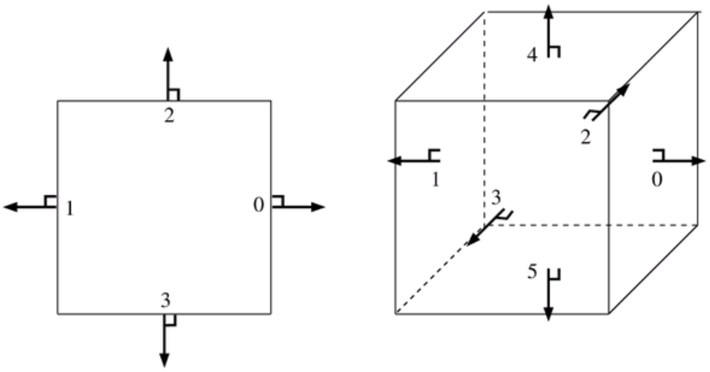

Figure 1.10: The Raviart-Thomas element for rectangles and boxes.

- The Brezzi-Douglas-Marini (BDM) elements are also well-known a stable element for the discretization of Darcy problem [169]. The degrees of freedom for the BDM elements also include the normal component on each edge, but are based on augmenting the space of vector polynomials.

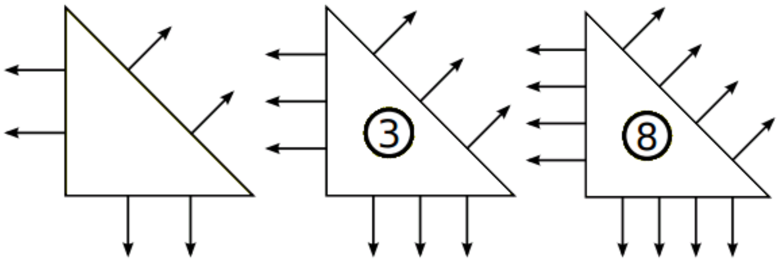

Figure 1.11: The linear, quadratic and cubic Brezzi-Douglas-Marini for triangles.

Decoupled elements for Stokes-Darcy: As introduced, decoupled finite elements used in the literature for coupling Stokes-Darcy can be

- Taylor-Hood for Stokes with C0 Lagrangian for Darcy [161]
- Taylor-Hood or MINI elements for Stokes, coupling with Raviart-Thomas or Brezzi-Douglas-Marini elements for Darcy [159]

1.3.2.2 Unified approach

The unified strategy consist in defining one mesh and one finite element space for discretizing both Darcy and Stokes region.

In the paper of Arbogast and Brunson [162], the authors claim that the finite element discretization based on the same finite element spaces for Darcy and Stokes regions is more advantageously for its implementation, but also raises some problems. Indeed, they argued most of the stable Stokes elements are not stable in the Darcy region while most of the stable Darcy elements are not convergent for the Stokes problem. In [162], it is suggested to use a C0-element of Fortin [170] and higher order generalizations provided by Arbogast and Wheeler [171], to overcome work simultaneously with Darcy and Stokes equations. Since the tangential velocity field is discontinuous across the interface between Darcy and Stokes region, a minor modification of the discretization space is provided but shown to be easily implemented in a self-made FE code. These robusts elements are rectangular in which the velocity belongs to a 12 dimensional space of reduced quadratics, while the pressure is approximated by piecewise constants (see also [172] for the use of rectangular robusts elements). A possible disadvantage of this discretization is that the real microstruture is replaced by an array of pixels which belongs to Darcy or Stokes region. By doing so, the interface is approximated by a succession of horizontal and vertical edges.

In the recent years, considerable effort have been made to provide unified approaches for the discretization of Darcy-Stokes problem. For instance, some authors develop modified variational formulation of the Darcy-Stokes problem such that the same finite element spaces must be used in throughout the entire domain, see for instance Urquiza *et al.* [173], Karper *et al.* [165], Correa and Loula [164]. Particularly, in [165] the coupled problem is solved by using standard Stokes elements like the MINI element or the Taylor-Hood element in the entire domain.

Nafa [174] takes the same variational formulation for the coupled Darcy-Stokes problem and discretize by standard equal-order finite elements enriched with bubbles functions and use local projection stabilization technique. To overcome the difficulty related to the use of the Beavers and Joseph interface condition, more recently Burman and Hansbo [160] proposed a unified approach for the solution of the coupled Stokes/Darcy problem using an edge stabilization technique in conjunction with the use of mixed P/P0 finite elements. The edge stabilization involves the splitting of the viscous stress term into its normal and tangential components at the free/porous interface. The normal stress component is then equated to the pressure differential across the free/porous interface. The method is mathematically complicated for their suitability to practical situations where the interface may have complex geometrical shapes.

1.4 Conclusions

As a conclusion for the elaboration of doubly porous materials: among the methods presented, the phase separation technique, and the gas foaming technique usually form a monoporous scaffold, with pore size ranging at least on the micron scale. Researchers usually couple these techniques with a porogen leaching process to obtain a scaffolds with doubly porosity, thus facilitating cell seeding and proliferation, for example. The particle leaching technique provides a large range of scaffolds but it is limited by particles size, thus this method can only produce polymers with large pores. The use of smaller particles as porogens is not easy in terms of controlling interconnectivity of the polymer scaffolds. The electrospinning technique limited the structures to a fibrous morphology with low diameter (under several microns). With polymer scaffolds synthesized from HIPE techniques, the production of hydrophilic ”reversed” polyHIPEs from oil-in-water HIPE systems is hampered by their relatively poor stability and relatively limited synthesis windows, as only materials with relatively low porosities and/or rather poor interconnectivities have effectively been engineered so far. Finally, the use of rapid prototyping is limited to the resolution of the 3D printers, which is in general several hundreds of nanometers only.

In this work, we propose the use of two technique, the double porogen approach and Thermally Induced Phase Separation, for the fabrication of doubly porous polymeric materials. Our main motivation of the use of these two techniques is the facility to manipulate, and it requires no specific or complicated process. Moreover, no systematic investigation was further studied in the literature for the double porogen approach, mainly on the influence and controlled pore size, morphology of the two porosity levels in doubly porous materials. This is our main goal for the use of the first technique of synthesis. For the preparation of doubly porous materials *via* Thermally Induced Phase Separation, to the best of our knowledge, no PHEMA-based porous materials has ever been synthesized before. We herein propose for the first time the use of this technique for the fabrication of doubly porous PHEMA-based materials with only a co-solvent mixture for the generation of a bimodal porosity within the framework.

Secondly, for the sake of simplicity of implementation, we use an unequal-order interpolations for the discretization of the Stokes equations. Numerical tools based on Finite Element Method for the discretization of Stokes equations are developed, and these results are compared with data provided in the literature. The main objective is to demonstrate the effectiveness and advantages of the use of Fast Fourier Transform based numerical tool to solve the Stokes equations for microstructures with complex geometries.

The coupling of Stokes and Darcy problem is discretized using two different approaches, which were highlighted above. For decoupled approach, we develop the classical approach using stable elements for Stokes (MINI elements), along with stable element in Darcy (Raviart-Thomas elements). The use of MINI element with Raviart-Thomas elements is motivated because they are the most economic elements, and gives an undeniable advantage when treating high dimensional problem. For unified approach, we apply the Arbogast robust elements as the theoretical background of such elements is well-documented in the literature by the authors.

References

[1] J. Auriault and C. Boutin, "Deformable porous media with double porosity. quasi-statics. i: Coupling effects," *Transport in Porous Media*, vol. 7, pp. 63–82, 1992.

[2] J. Auriault and C. Boutin, "Deformable porous media with double porosity. quasi-statics. ii: Memory effects," *Transport in Porous Media*, vol. 10, pp. 153–169, 1993.

[3] J. Auriault and C. Boutin, "Deformable porous media with double porosity iii: Acoustics," *Transport in Porous Media*, vol. 14, pp. 143–162, 1994.

[4] C. Boutin, P. Royer, and J. Auriault, "Acoustic absorption of porous surfacing with dual porosity," *International Journal of Solids and Structures*, vol. 35, pp. 4709–4737, 1998.

[5] S. C. Cowin, *Bone Mechanics Handbook*. Boca Raton, Florida: CRC Press, 2001.

[6] D. Wu, F. Xu, B. Sun, R. Fu, H. He, and K. Matyjaszewski, "Design and preparation of porous polymers," *Chemical Reviews*, vol. 112, pp. 3959–4015, 2012.

[7] C. J. Brinker, "Porous inorganic materials," *Current Opinion in Solid State and Materials Science*, vol. 1, pp. 798–805, 1996.

[8] R. Almeida, A. Gama, and Y. Vueva, "Bioactive sol-gel scaffolds with dual porosity for tissue engineering," *Journal of Sol-gel Science and Technology*, vol. 57, pp. 336–342, 2011.

[9] G. Onyestyak, J. Valyon, and K. Papp, "Novel biomorphous zeolite/carbon composite having honeycomb structure," *Materials Science and Engineering: A*, vol. 412, pp. 48–52, 2005.

[10] X. H. Liu and P. X. Ma, "Polymeric scaffolds for bone tissue engineering," *Annals of Biomedical Engineering*, vol. 32, pp. 477–486, 2004.

[11] I. Tokarev and S. Minko, "Stimuli-responsive porous hydrogels at interfaces for molecular filtration, separation, controlled release, and gating in capsules and membranes," *Advanced Materials*, vol. 22, pp. 3446–3462, 2010.

[12] J. Bear and Y. Bachmat, *Introduction to modelling phenomena of transport in porous media.* Netherlands: Springer Netherlands, 1991.

[13] R. Hill, "Elastic properties of reinforced solids: some theoretical principles," *Journal of the Mechanics and Physics of Solids*, vol. 11, pp. 357–372, 1963.

[14] M. Bai, D. Elsworth, and J.-C. Roegiers, "Modeling of naturally fractured reservoirs using deformation dependent flow mechanism," vol. 30, pp. 1185–1191, 1993.

[15] O. Okay, "Macroporous copolymer networks," *Progress in Polymer Science*, vol. 25, pp. 711–779, 2000.

[16] M. N. R. Kumar, N. Kumar, A. Domb, and M. Arora, *Pharmaceutical polymeric controlled drug delivery systems*, pp. 45–117. Springer, 2002.

[17] K. M. Woo, V. J. Chen, and P. X. Ma, "Nano-fibrous scaffolding architecture selectively enhances protein adsorption contributing to cell attachment," *Journal of Biomedical Materials Research Part A*, vol. 67, pp. 531–537, 2003.

[18] V. J. Chen, L. A. Smith, and P. X. Ma, "Bone regeneration on computer-designed nano-fibrous scaffolds," *Biomaterials*, vol. 27, pp. 3973–3979, 2006.

[19] J. Hu, X. Liu, and P. X. Ma, "Induction of osteoblast differentiation phenotype on poly (l-lactic acid) nanofibrous matrix," *Biomaterials*, vol. 29, pp. 3815–3821, 2008.

[20] A. Barbetta and N. R. Cameron, "Morphology and surface area of emulsion-derived (polyhipe) solid foams prepared with oil-phase soluble porogenic solvents: Three-component surfactant system," *Macromolecules*, vol. 37, pp. 3202–3213, 2004.

[21] A. Barbetta and N. R. Cameron, "Morphology and surface area of emulsion-derived (polyhipe) solid foams prepared with oil-phase soluble porogenic solvents: Span 80 as surfactant," *Macromolecules*, vol. 37, pp. 3188–3201, 2004.

[22] R. Langer and J. P. Vacanti, "Tissue engineering," *Science*, vol. 260, pp. 920–926, 1993.

[23] L. S. Nair and C. T. Laurencin, "Biodegradable polymers as biomaterials," *Progress in Polymer Science*, vol. 32, pp. 762–798, 2007.

[24] M. R. Kreitz, J. A. Domm, and E. Mathiowitz, "Controlled delivery of therapeutics from microporous membranes. ii. in vitro degradation and release of heparin-loaded poly(d,l-lactide-*co*-glycolide)," *Biomaterials*, vol. 18, pp. 1645–1651, 1997.

[25] Y. Y. Yang, T. S. Chung, and N. P. Ng, "Morphology, drug distribution, and in vitro release profiles of biodegradable polymeric microspheres containing protein fabricated by double-emulsion solvent extraction/evaporation method," *Biomaterials*, vol. 22, pp. 231–241, 2001.

[26] V. R. Patel and M. M. Amiji, "Preparation and characterization of freeze-dried chitosan-poly(ethylene oxide) hydrogels for site-specific antibiotic delivery in the stomach," *Pharmaceutical Research*, vol. 13, pp. 588–593, 1996.

[27] S. H. Lee and H. Shin, "Matrices and scaffolds for delivery of bioactive molecules in bone and cartilage tissue engineering," *Advanced Drug Delivery Reviews*, vol. 59, pp. 339–359, 2007.

[28] K. Rezwan, Q. Chen, J. Blaker, and A. R. Boccaccini, "Biodegradable and bioactive porous polymer/inorganic composite scaffolds for bone tissue engineering," *Biomaterials*, vol. 27, pp. 3413–3431, 2006.

[29] Y. Yang, J. Zhao, Y. Zhao, L. Wen, X. Yuan, and Y. Fan, "Formation of porous plga scaffolds by a combining method of thermally induced phase separation and porogen leaching," *Journal of Applied Polymer Science*, vol. 109, pp. 1232–1241, 2008.

[30] V. A. Santamaria, H. Deplaine, D. Mariggio, A. Villanueva-Molines, J. Garcia-Aznar, J. G. Ribelles, M. Doblaré, G. G. Ferrer, and I. Ochoa, "Influence of the macro and micro-porous structure on the mechanical behavior of poly (l-lactic acid) scaffolds," *Journal of Non-Crystalline Solids*, vol. 358, pp. 3141–3149, 2012.

[31] V. J. Chen and P. X. Ma, "Nano-fibrous poly (l-lactic acid) scaffolds with interconnected spherical macropores," *Biomaterials*, vol. 25, pp. 2065–2073, 2004.

[32] N. Cameron and D. Sherrington, *High internal phase emulsions (HIPEs)-Structure, properties and use in polymer preparation*, pp. 163–214. Springer, 1996.

[33] N. Cameron and D. Sherrington, "Preparation and glass transition temperatures of elastomeric polyhipe materials," *Journal of Materials Chemistry*, vol. 7, pp. 2209–2212, 1997.

[34] M. S. Silverstein and N. R. Cameron, “Polyhipes-porous polymers from high internal phase emulsions,” *Encyclopedia of Polymer Science and Technology*, 2010.

[35] J. A. R. Ruiz, M. Pedros, J.-M. Tallon, and M. Dumon, “Micro and nano cellular amorphous polymers (pmma, ps) in supercritical co 2 assisted by nanostructured co 2-philic block copolymers–one step foaming process,” *The Journal of Supercritical Fluids*, vol. 58, pp. 168–176, 2011.

[36] J. A. R. Ruiz, J. Marc-Tallon, M. Pedros, and M. Dumon, “Two-step micro cellular foaming of amorphous polymers in supercritical co 2,” *The Journal of Supercritical Fluids*, vol. 57, pp. 87–94, 2011.

[37] Z.-M. Huang, Y.-Z. Zhang, M. Kotaki, and S. Ramakrishna, “A review on polymer nanofibers by electrospinning and their applications in nanocomposites,” *Composites Science and Technology*, vol. 63, pp. 2223–2253, 2003.

[38] D. Li and Y. Xia, “Electrospinning of nanofibers: reinventing the wheel?,” *Advanced Materials*, vol. 16, pp. 1151–1170, 2004.

[39] S. Yang, K.-F. Leong, Z. Du, and C.-K. Chua, “The design of scaffolds for use in tissue engineering. part ii. rapid prototyping techniques,” *Tissue Engineering*, vol. 8, pp. 1–11, 2002.

[40] W.-Y. Yeong, C.-K. Chua, K.-F. Leong, and M. Chandrasekaran, “Rapid prototyping in tissue engineering: challenges and potential,” *TRENDS in Biotechnology*, vol. 22, pp. 643–652, 2004.

[41] S. Ghosh, J. Viana, R. Reis, and J. Mano, “The double porogen approach as a new technique for the fabrication of interconnected poly (l-lactic acid) and starch based biodegradable scaffolds,” *Journal of Materials Science: Materials in Medicine*, vol. 18, pp. 185–193, 2007.

[42] A. Vidaurre, I. C. CortÃązar, and J. G. Ribelles, “Polymeric scaffolds with a double pore structure,” *Journal of Non-Crystalline Solids*, vol. 353, pp. 1095–1100, 2007.

[43] D. Horak, H. Hlidkova, J. Hradil, M. Lapcikova, and M. Slouf, “Superporous poly(2-hydroxyethyl methacrylate) based scaffolds: Preparation and characterization,” *Polymer*, vol. 49, pp. 2046–2054, 2008.

[44] Y. Li, Q.-H. Shi, and Y. Sun, “Rapid chiral separation by flow-through chromatography with a biporous stationary phase,” *Chromatographia*, vol. 61, pp. 213–217, 2005.

[45] Y. Shi, X.-Y. Dong, and Y. Sun, “Development of rigid biporous polymeric adsorbent for protein chromatography,” *Chromatographia*, vol. 55, pp. 405–410, 2002.

[46] X. Liu and P. X. Ma, “Phase separation, pore structure, and properties of nanofibrous gelatin scaffolds,” *Biomaterials*, vol. 30, pp. 4094–4103, 2009.

[47] N. R. Cameron, “High internal phase emulsion templating as a route to well-defined porous polymers,” *Polymer*, vol. 46, pp. 1439–1449, 2005.

[48] K. J. Lissant, *Emulsions and emulsion technology.* Dekker New York, 1974.

[49] N. R. Cameron, P. Krajnc, and M. S. Silverstein, *Colloidal templating.* John Wiley & Sons, 2011.

[50] F. Svec, T. B. Tennikova, and Z. Deyl, *Monolithic materials: preparation, properties and applications.* Amsterdam: Elsevier, 2003.

[51] G. Ceglia, L. Mahéo, P. Viot, D. Bernard, A. Chirazi, I. Ly, O. Mondain-Monval, and V. Schmitt, “Formulation and mechanical properties of emulsion-based model polymer foams,” *The European Physical Journal E: Soft Matter and Biological Physics*, vol. 35, pp. 1–11, 2012.

[52] C. J. C. Edwards, D. P. Gregory, and M. Sharples, "Low density porous elastic cross-linked polymeric materials and their preparation," 1988.

[53] K. Thunhorst, M. Gehlsen, R. Wright, E. Nelson, S. Koecher, and D. Gold, "Foams made by photopolymerization of emulsions," 2001.

[54] J. Crank, "The mathematics of diffusion," *London: Oxford Univ. Press*, 1956.

[55] W. Vieth and K. Sladek, "A model for diffusion in a glassy polymer," *Journal of Colloid Science*, vol. 20, pp. 1014–1033, 1965.

[56] J. S. Colton and N. P. Suh, "Nucleation of microcellular foam: theory and practice," *Polymer Engineering and Science*, vol. 27, pp. 500–503, 1987.

[57] S. K. Goel and E. J. Beckman, "Generation of microcellular polymeric foams using supercritical carbon dioxide. i: Effect of pressure and temperature on nucleation," *Polymer Engineering and Science*, vol. 34, pp. 1137–1147, 1994.

[58] R. A. Quirk, R. M. France, K. M. Shakesheff, and S. M. Howdle, "Supercritical fluid technologies and tissue engineering scaffolds," *Current Opinion in Solid State and Materials Science*, vol. 8, pp. 313–321, 2004.

[59] C. B. Park, D. F. Baldwin, and N. P. Suh, "Effect of the pressure drip rate on cell nucleation in continuous processing of microcellular polymers," *Polymer Engineering and Science*, vol. 35, pp. 432–440, 1995. Park, cb baldwin, df suh, np.

[60] D. F. Baldwin, M. Shimbo, and N. P. Suh, "The role of gas dissolution and induced crystallization during microcellular polymer processing - a study of poly(ethylene-terephthalate) and carbon-dioxide systems," *Journal of Engineering Materials and Technology-Transactions of the Asme*, vol. 117, pp. 62–74, 1995. Baldwin, df shimbo, m suh, np.

[61] D. J. Mooney, D. F. Baldwin, N. P. Suh, J. P. Vacanti, and R. Langer, "Novel approach to fabricate porous sponges of poly (d, l-lactic-co-glycolic acid) without the use of organic solvents," *Biomaterials*, vol. 17, pp. 1417–1422, 1996.

[62] K. Park, H. J. Jung, J. S. Son, K. D. Park, J.-J. Kim, K.-D. Ahn, and D. K. Han, "Preparation of biodegradable polymer scaffolds with dual pore system for tissue regeneration," *Macromolecular Symposia*, vol. 249, pp. 145–150, 2007.

[63] L. D. Harris, B. S. Kim, and D. J. Mooney, "Open pore biodegradable matrices formed with gas foaming," *Journal of Biomedical Materials Research*, vol. 42, pp. 396–402, 1998. Harris, LD Kim, BS Mooney, DJ.

[64] H. J. Jung, K. Park, J.-J. Kim, J. H. Lee, K.-O. Han, and D. K. Han, "Effect of rgd-immobilized dual-pore poly (l-lactic acid) scaffolds on chondrocyte proliferation and extracellular matrix production," *Artificial Organs*, vol. 32, pp. 981–989, 2008.

[65] Y. S. Nam, J. J. Yoon, and T. G. Park, "A novel fabrication method of macroporous biodegradable polymer scaffolds using gas foaming salt as a porogen additive," *Journal of Biomedical Materials Research*, vol. 53, pp. 1–7, 2000. Nam, YS Yoon, JJ Park, TG.

[66] L. Rayleigh, "Xx. on the equilibrium of liquid conducting masses charged with electricity," *The London, Edinburgh, and Dublin Philosophical Magazine and Journal of Science*, vol. 14, pp. 184–186, 1882.

[67] W. J. Morton, "Method of dispersing fluids," 1902.

[68] J. F. Cooley, "Rotary fluid-motor," 1903.

[69] F. Anton, “Process and apparatus for preparing artificial threads,” 1934.

[70] D. H. Reneker and I. Chun, “Nanometre diameter fibres of polymer, produced by electrospinning,” *Nanotechnology*, vol. 7, p. 216, 1996.

[71] D. H. Reneker and A. L. Yarin, “Electrospinning jets and polymer nanofibers,” *Polymer*, vol. 49, pp. 2387–2425, 2008.

[72] P. Dayal, J. Liu, S. Kumar, and T. Kyu, “Experimental and theoretical investigations of porous structure formation in electrospun fibers,” *Macromolecules*, vol. 40, pp. 7689–7694, 2007.

[73] M. Bognitzki, T. Frese, M. Steinhart, A. Greiner, J. H. Wendorff, A. Schaper, and M. Hellwig, “Preparation of fibers with nanoscaled morphologies: electrospinning of polymer blends,” *Polymer Engineering and Science*, vol. 41, pp. 982–989, 2001.

[74] M. Bognitzki, W. Czado, T. Frese, A. Schaper, M. Hellwig, M. Steinhart, A. Greiner, and J. H. Wendorff, “Nanostructured fibers via electrospinning,” *Advanced Materials*, p. 70, 2001.

[75] C. L. Casper, J. S. Stephens, N. G. Tassi, D. B. Chase, and J. F. Rabolt, “Controlling surface morphology of electrospun polystyrene fibers: effect of humidity and molecular weight in the electrospinning process,” *Macromolecules*, vol. 37, pp. 573–578, 2004.

[76] S. Megelski, J. S. Stephens, D. B. Chase, and J. F. Rabolt, “Micro-and nanostructured surface morphology on electrospun polymer fibers,” *Macromolecules*, vol. 35, pp. 8456–8466, 2002.

[77] D. Li and Y. Xia, “Direct fabrication of composite and ceramic hollow nanofibers by electrospinning,” *Nano letters*, vol. 4, pp. 933–938, 2004.

[78] A. Luciani, V. Coccoli, S. Orsi, L. Ambrosio, and P. A. Netti, “Pcl microspheres based functional scaffolds by bottom-up approach with predefined microstructural properties and release profiles,” *Biomaterials*, vol. 29, pp. 4800–4807, 2008.

[79] G.-Y. Sun, Z. Yang, X.-Y. Dong, and Y. Sun, “Biporous polymeric beads fabricated by double emulsification for high-speed protein chromatography,” *Journal of Applied Polymer Science*, vol. 103, pp. 17–23, 2007.

[80] J.-L. Auriault and E. Sanchez-Palencia, “Etude du comportement macroscopique d’un milieu poreux saturé déformable,” *Journal de Mécanique*, vol. 16, pp. 575–603, 1977.

[81] E. Sanchez-Palencia, “Non-homogeneous media and vibration theory,” in *Non-homogeneous media and vibration theory*, vol. 127, 1980.

[82] S. Whitaker, “Diffusion and dispersion in porous media,” *AIChE Journal*, vol. 13, pp. 420–427, 1967.

[83] C. Wang, “Stokes flow through an array of rectangular fibers,” *International Journal of Multiphase Flow*, vol. 22, pp. 185–194, 1996.

[84] C. Wang, “Stokes flow through a rectangular array of circular cylinders,” *Fluid Dynamics Research*, vol. 29, pp. 65–80, 2001.

[85] C. Wang, “Stokes slip flow through square and triangular arrays of circular cylinders,” *Fluid Dynamics Research*, vol. 32, pp. 233–246, 2003.

[86] A. Sangani and A. Acrivos, “Slow flow past periodic arrays of cylinders with application to heat transfer,” *International Journal of Multiphase Flow*, vol. 8, pp. 193–206, 1982.

[87] A. Sangani and A. Acrivos, “Slow flow through a periodic array of spheres,” *International Journal of Multiphase Flow*, vol. 8, pp. 343–360, 1982.

[88] J. Barrere, J.-P. Caltagirone, and O. Gipouloux, “Détermination numérique de la perméabilité en milieu poreux périodique tridimensionnel,” *Comptes Rendus de l’Académie des Sciences. Série 2, Mécanique, Physique, Chimie, Sciences de l’Univers, Sciences de la Terre*, vol. 310, pp. 347–352, 1990.

[89] D. Cioranescu, P. Donato, and H. I. Ene, “Homogenization of the stokes problem with nonhomogenous slip boundary conditions,” *Mathematical Methods in the Applied Sciences*, vol. 19, pp. 857–881, 1996.

[90] F. Alcocer, V. Kumar, and P. Singh, “Permeability of periodic porous media,” *Physical Review E*, vol. 59, p. 711, 1999.

[91] F. Alcocer and P. Singh, “Permeability of periodic arrays of cylinders for viscoelastic flows,” *Physics of Fluids*, vol. 14, pp. 2578–2581, 2002.

[92] V. Monchiet, G. Bonnet, and G. Lauriat, “A fft-based method to compute the permeability induced by a stokes slip flow through a porous medium,” *Comptes Rendus Mécanique*, vol. 337, pp. 192–197, 2009.

[93] T.-K. Nguyen, V. Monchiet, and G. Bonnet, “A fourier based numerical method for computing the dynamic permeability of periodic porous media,” *European Journal of Mechanics-B/Fluids*, vol. 37, pp. 90–98, 2013.

[94] H. Moulinec and P. Suquet, “A fast numerical method for computing the linear and nonlinear mechanical properties of composites,” *Comptes Rendus de l’Académie des Sciences. Série II, Mécanique, Physique, Chimie, Astronomie*, vol. 318, pp. 1417–1423, 1994.

[95] J. Michel, H. Moulinec, and P. Suquet, “A computational scheme for linear and non-linear composites with arbitrary phase contrast,” *International Journal for Numerical Methods in Engineering*, vol. 52, pp. 139–160, 2001.

[96] G. Bonnet, “Effective properties of elastic periodic composite media with fibers,” *Journal of the Mechanics and Physics of Solids*, vol. 55, pp. 881–899, 2007.

[97] V. Monchiet and G. Bonnet, “A polarization-based fft iterative scheme for computing the effective properties of elastic composites with arbitrary contrast,” *International Journal for Numerical Methods in Engineering*, vol. 89, pp. 1419–1436, 2012.

[98] M. Quintard and S. Whitaker, “Single phase flow in porous media: the effect of local heterogeneities,” *Collection Colloques et Séminaires-Institut Francais du Pétrole*, pp. 473–486, 1987.

[99] P. Royer, J. Auriault, and C. Boutin, “Macroscopic modeling of double-porosity reservoirs,” *Journal of Petroleum Science and Engineering*, vol. 16, pp. 187–202, 1996.

[100] X. Olny and C. Boutin, “Acoustic wave propagation in double porosity media,” *The Journal of the Acoustical Society of America*, vol. 114, pp. 73–89, 2003.

[101] L. R. Herrmann, “Elasticity equations for incompressible and nearly incompressible materials by a variational theorem.,” *AIAA Journal*, vol. 3, pp. 1896–1900, 1965.

[102] E. Reissner, “On a variational theorem in elasticity,” *J. Math. Phys*, vol. 29, pp. 90–95, 1950.

[103] O. C. Zienkiewicz, R. L. Taylor, O. C. Zienkiewicz, and R. L. Taylor, *The finite element method*, vol. 3. McGraw-hill London, 1977.

[104] I. Babuška, “Error-bounds for finite element method,” *Numerische Mathematik*, vol. 16, pp. 322–333, 1971.

[105] F. Brezzi, "On the existence, uniqueness and approximation of saddle-point problems arising from lagrangian multipliers," *Revue française d'automatique, informatique, recherche opérationnelle. Analyse numérique*, vol. 8, pp. 129–151, 1974.

[106] O. A. Ladyzhenskaya and R. A. Silverman, *The mathematical theory of viscous incompressible flow*, vol. 76. Gordon and Breach New York, 1969.

[107] D. N. Arnold, F. Brezzi, and M. Fortin, "A stable finite element for the stokes equations," *Calcolo*, vol. 21, pp. 337–344, 1984.

[108] C. Taylor and P. Hood, "A numerical solution of the navier-stokes equations using the finite element technique," *Computers & Fluids*, vol. 1, pp. 73–100, 1973.

[109] W. Bai, "The quadrilateral 'mini' finite element for the stokes problem," *Computer Methods in Applied Mechanics and Engineering*, vol. 143, pp. 41–47, 1997.

[110] B. Claudio and B. Franco, "Virtual bubbles and galerkin-least-squares type methods [j]," *Comput Methods Appl Mech Engrg*, vol. 105, pp. 125–141, 1993.

[111] F. Brezzi, M.-O. Bristeau, L. P. Franca, M. Mallet, and G. Rogé, "A relationship between stabilized finite element methods and the galerkin method with bubble functions," *Computer Methods in Applied Mechanics and Engineering*, vol. 96, pp. 117–129, 1992.

[112] T. J. Hughes, "Multiscale phenomena: Green's functions, the dirichlet-to-neumann formulation, subgrid scale models, bubbles and the origins of stabilized methods," *Computer Methods in Applied Mechanics and Engineering*, vol. 127, pp. 387–401, 1995.

[113] B. Michaelis and B. Rogg, "Fem-simulation of laminar flame propagation. i: Two-dimensional flames," *Journal of Computational Physics*, vol. 196, pp. 417–447, 2004.

[114] K. Khanafer and A. J. Chamkha, "Mixed convection within a porous heat generating horizontal annulus," *International Journal of Heat and Mass Transfer*, vol. 46, pp. 1725–1735, 2003.

[115] K. Khanafer and K. Vafai, "Effective boundary conditions for buoyancy-driven flows and heat transfer in fully open-ended two-dimensional enclosures," *International Journal of Heat and Mass Transfer*, vol. 45, pp. 2527–2538, 2002.

[116] L. H. Juárez, R. Glowinski, and B. M. Pettitt, "Numerical simulation of the sedimentation of a tripole-like body in an incompressible viscous fluid," *Applied Mathematics Letters*, vol. 15, pp. 743–747, 2002.

[117] J. Petera and L. Weatherley, "Modelling of mass transfer from falling droplets," *Chemical Engineering Science*, vol. 56, pp. 4929–4947, 2001.

[118] A. Nowakowski, W. Kraipech, R. Williams, and T. Dyakowski, "The hydrodynamics of a hydrocyclone based on a three-dimensional multi-continuum model," *Chemical Engineering Journal*, vol. 80, pp. 275–282, 2000.

[119] J.-C. Nédélec, "A new family of mixed finite elements in r 3," *Numerische Mathematik*, vol. 50, pp. 57–81, 1986.

[120] J.-C. Nédélec, "Mixed finite elements in r3," *Numerische Mathematik*, vol. 35, pp. 315–341, 1980.

[121] F. Brezzi and J. Pitkäranta, *On the stabilization of finite element approximations of the Stokes equations.* Springer, 1984.

[122] T. J. Hughes, L. P. Franca, and M. Balestra, "A new finite element formulation for computational fluid dynamics: V. circumventing the babuška-brezzi condition: A stable petrov-galerkin formulation of the stokes problem accommodating equal-order interpolations," *Computer Methods in Applied Mechanics and Engineering*, vol. 59, pp. 85–99, 1986.

[123] T. J. Hughes, G. R. Feijóo, L. Mazzei, and J.-B. Quincy, "The variational multiscale method-a paradigm for computational mechanics," *Computer methods in applied mechanics and engineering*, vol. 166, pp. 3–24, 1998.

[124] P. B. Bochev, C. R. Dohrmann, and M. D. Gunzburger, "Stabilization of low-order mixed finite elements for the stokes equations," *SIAM Journal on Numerical Analysis*, vol. 44, pp. 82–101, 2006.

[125] C. R. Dohrmann and P. B. Bochev, "A stabilized finite element method for the stokes problem based on polynomial pressure projections," *International Journal for Numerical Methods in Fluids*, vol. 46, pp. 183–201, 2004.

[126] W. Sun, J. T. Ostien, and A. G. Salinger, "A stabilized assumed deformation gradient finite element formulation for strongly coupled poromechanical simulations at finite strain," *International Journal for Numerical and Analytical Methods in Geomechanics*, vol. 37, pp. 2755–2788, 2013.

[127] A. Truty and T. Zimmermann, "Stabilized mixed finite element formulations for materially nonlinear partially saturated two-phase media," *Computer Methods in Applied Mechanics and Engineering*, vol. 195, pp. 1517–1546, 2006.

[128] J. A. White and R. I. Borja, "Stabilized low-order finite elements for coupled solid-deformation/fluid-diffusion and their application to fault zone transients," *Computer Methods in Applied Mechanics and Engineering*, vol. 197, pp. 4353–4366, 2008.

[129] V. Nassehi and J. Petera, "A new least-squares finite element model for combined navier–stokes and darcy flows in geometrically complicated domains with solid and porous boundaries," *International Journal for Numerical Methods in Engineering*, vol. 37, pp. 1609–1620, 1994.

[130] P. De Sampaio, "A petrov–galerkin formulation for the incompressible navier–stokes equations using equal order interpolation for velocity and pressure," *International Journal for Numerical Methods in Engineering*, vol. 31, pp. 1135–1149, 1991.

[131] O. Zienkiewicz and J. Wu, "Incompressibility without tearsâĂŤhow to avoid restrictions of mixed formulation," *International Journal for Numerical Methods in Engineering*, vol. 32, pp. 1189–1203, 1991.

[132] F. Brezzi and M. Fortin, *Mixed and hybrid finite element methods*, vol. 15. Springer Science & Business Media, 2012.

[133] L. P. Franca and S. L. Frey, "Stabilized finite element methods: Ii. the incompressible navier-stokes equations," *Computer Methods in Applied Mechanics and Engineering*, vol. 99, pp. 209–233, 1992.

[134] B.-N. Jiang and G. F. Carey, "A stable least-squares finite element method for non-linear hyperbolic problems," *International Journal for Numerical Methods in Fluids*, vol. 8, pp. 933–942, 1988.

[135] J. Douglas and J. P. Wang, "An absolutely stabilized finite element method for the stokes problem," *Mathematics of Computation*, vol. 52, pp. 495–508, 1989.

[136] J. H. Bramble and J. Xu, "A local post-processing technique for improving the accuracy in mixed finite-element approximations," *SIAM Journal on Numerical Analysis*, vol. 26, pp. 1267–1275, 1989.

[137] T. Y. Hou and X.-H. Wu, "A multiscale finite element method for elliptic problems in composite materials and porous media," *Journal of Computational Physics*, vol. 134, pp. 169–189, 1997.

[138] J. Aarnes, T. Gimse, and K. Lie, "An introduction to the numerics of flow in porous media using matlab, geometrical modelling numerical simulation and optimization, industrial mathematics at sintef," 2005.

[139] K. Nakshatrala, D. Turner, K. Hjelmstad, and A. Masud, "A stabilized mixed finite element method for darcy flow based on a multiscale decomposition of the solution," *Computer Methods in Applied Mechanics and Engineering*, vol. 195, pp. 4036–4049, 2006.

[140] S. Badia and R. Codina, "Stabilized continuous and discontinuous galerkin techniques for darcy flow," *Computer Methods in Applied Mechanics and Engineering*, vol. 199, pp. 1654–1667, 2010.

[141] A. G. Salinger, R. Aris, and J. J. Derby, "Modeling the spontaneous ignition of coal stockpiles," *AIChE journal*, vol. 40, pp. 991–1004, 1994.

[142] H. Tang and Y. Fung, "Fluid movement in a channel with permeable walls covered by porous media: a model of lung alveolar sheet," *Journal of Applied Mechanics*, vol. 42, pp. 45–50, 1975.

[143] T. MASUOKA, "Convective currents in a horizontal layer divided by a permeable wall," *Bulletin of JSME*, vol. 17, pp. 225–232, 1974.

[144] D. D. Joseph and L. Tao, "Lubrication of a porous bearing-stokes' solution," *Journal of Applied Mechanics*, vol. 33, pp. 753–760, 1966.

[145] I. Jones, "Low reynolds number flow past a porous spherical shell," in *Mathematical Proceedings of the Cambridge Philosophical Society*, vol. 73, pp. 231–238, Cambridge Univ Press, 1973.

[146] T. S. Lundgren, "Slow flow through stationary random beds and suspensions of spheres," *Journal of Fluid Mechanics*, vol. 51, pp. 273–299, 1972.

[147] G. Neale, N. Epstein, and W. Nader, "Creeping flow relative to permeable spheres," *Chemical Engineering Science*, vol. 28, pp. 1865–1874, 1973.

[148] G. H. Neale and W. K. Nader, "Prediction of transport processes within porous media: creeping flow relative to a fixed swarm of spherical particles," *AIChE Journal*, vol. 20, pp. 530–538, 1974.

[149] C. Beckermann, S. Ramadhyani, and R. Viskanta, "Natural convection flow and heat transfer between a fluid layer and a porous layer inside a rectangular enclosure," *Journal of Heat Transfer*, vol. 109, pp. 363–370, 1987.

[150] C. Beckermann, R. Viskanta, and S. Ramadhyani, "Natural convection in vertical enclosures containing simultaneously fluid and porous layers," *Journal of Fluid Mechanics*, vol. 186, pp. 257–284, 1988.

[151] D. Poulikakos and M. Kazmierczak, "Forced convection in a duct partially filled with a porous material," *ASME J. Heat Transfer*, vol. 109, pp. 653–662, 1987.

[152] M. Taslim and U. Narusawa, "Thermal stability of horizontally superposed porous and fluid layers," *Journal of Heat Transfer*, vol. 111, pp. 357–362, 1989.

[153] P. Celle, S. Drapier, and J.-M. Bergheau, "Numerical modelling of liquid infusion into fibrous media undergoing compaction," *European Journal of Mechanics-A/Solids*, vol. 27, pp. 647–661, 2008.

[154] H. Brinkman, "A calculation of the viscous force exerted by a flowing fluid on a dense swarm of particles," *Applied Scientific Research*, vol. 1, pp. 27–34, 1947.

[155] S. Kim and W. B. Russel, "Modelling of porous media by renormalization of the stokes equations," *Journal of Fluid Mechanics*, vol. 154, pp. 269–286, 1985.

[156] G. S. Beavers and D. D. Joseph, "Boundary conditions at a naturally permeable wall," *Journal of Fluid Mechanics*, vol. 30, pp. 197–207, 1967.

[157] P. G. Saffman, "Boundary condition at surface of a porous medium," *Studies in Applied Mathematics*, vol. 50, p. 93, 1971.

[158] A. Mikelic and W. Jäger, "On the interface boundary condition of beavers, joseph, and saffman," *SIAM Journal on Applied Mathematics*, vol. 60, pp. 1111–1127, 2000.

[159] W. J. Layton, F. Schieweck, and I. Yotov, "Coupling fluid flow with porous media flow," *SIAM Journal on Numerical Analysis*, vol. 40, pp. 2195–2218, 2003.

[160] E. Burman and P. Hansbo, "A unified stabilized method for stokes' and darcy's equations," *Journal of Computational and Applied Mathematics*, vol. 198, pp. 35–51, 2007.

[161] M. Discacciati, A. Quarteroni, and A. Valli, "Robin-robin domain decomposition methods for the stokes-darcy coupling," *SIAM Journal on Numerical Analysis*, vol. 45, pp. 1246–1268, 2007.

[162] T. Arbogast and D. S. Brunson, "A computational method for approximating a darcy–stokes system governing a vuggy porous medium," *Computational Geosciences*, vol. 11, pp. 207–218, 2007.

[163] X. Xie, J. Xu, and G. Xue, "Uniformly-stable finite element methods for darcy-stokes-brinkman models," *Journal of Computational Mathematics-International Edition*, vol. 26, p. 437, 2008.

[164] M. Correa and A. Loula, "A unified mixed formulation naturally coupling stokes and darcy flows," *Computer Methods in Applied Mechanics and Engineering*, vol. 198, pp. 2710–2722, 2009.

[165] T. Karper, K.-A. Mardal, and R. Winther, "Unified finite element discretizations of coupled darcy–stokes flow," *Numerical Methods for Partial Differential Equations*, vol. 25, pp. 311–326, 2009.

[166] M. Discacciati, E. Miglio, and A. Quarteroni, "Mathematical and numerical models for coupling surface and groundwater flows," *Applied Numerical Mathematics*, vol. 43, pp. 57–74, 2002.

[167] E. Miglio, A. Quarteroni, and F. Saleri, "Coupling of free surface and groundwater flows," *Computers & Fluids*, vol. 32, pp. 73–83, 2003.

[168] D. Gartling, C. Hickox, and R. Givler, "Simulation of coupled viscous and porous flow problems," *International Journal of Computational Fluid Dynamics*, vol. 7, pp. 23–48, 1996.

[169] F. Brezzi, J. Douglas Jr, and L. D. Marini, "Two families of mixed finite elements for second order elliptic problems," *Numerische Mathematik*, vol. 47, pp. 217–235, 1985.

[170] M. Fortin, "Old and new finite elements for incompressible flows," *International Journal for Numerical Methods in Fluids*, vol. 1, pp. 347–364, 1981.

[171] T. Arbogast and M. F. Wheeler, "A family of rectangular mixed elements with a continuous flux for second order elliptic problems," *SIAM Journal on Numerical Analysis*, vol. 42, pp. 1914–1931, 2005.

[172] K. A. Mardal, X.-C. Tai, and R. Winther, "A robust finite element method for darcy–stokes flow," *SIAM Journal on Numerical Analysis*, vol. 40, pp. 1605–1631, 2002.

[173] J. Urquiza, D. N'dri, A. Garon, and M. Delfour, "Coupling stokes and darcy equations," *Applied Numerical Mathematics*, vol. 58, pp. 525–538, 2008.

[174] K. Nafa, "Equal order approximations enriched with bubbles for coupled stokes–darcy problem," *Journal of Computational and Applied Mathematics*, vol. 270, pp. 275–282, 2014.

Chapter 2

Facile fabrication of doubly porous polymeric materials with controlled nano- and macro-porosity

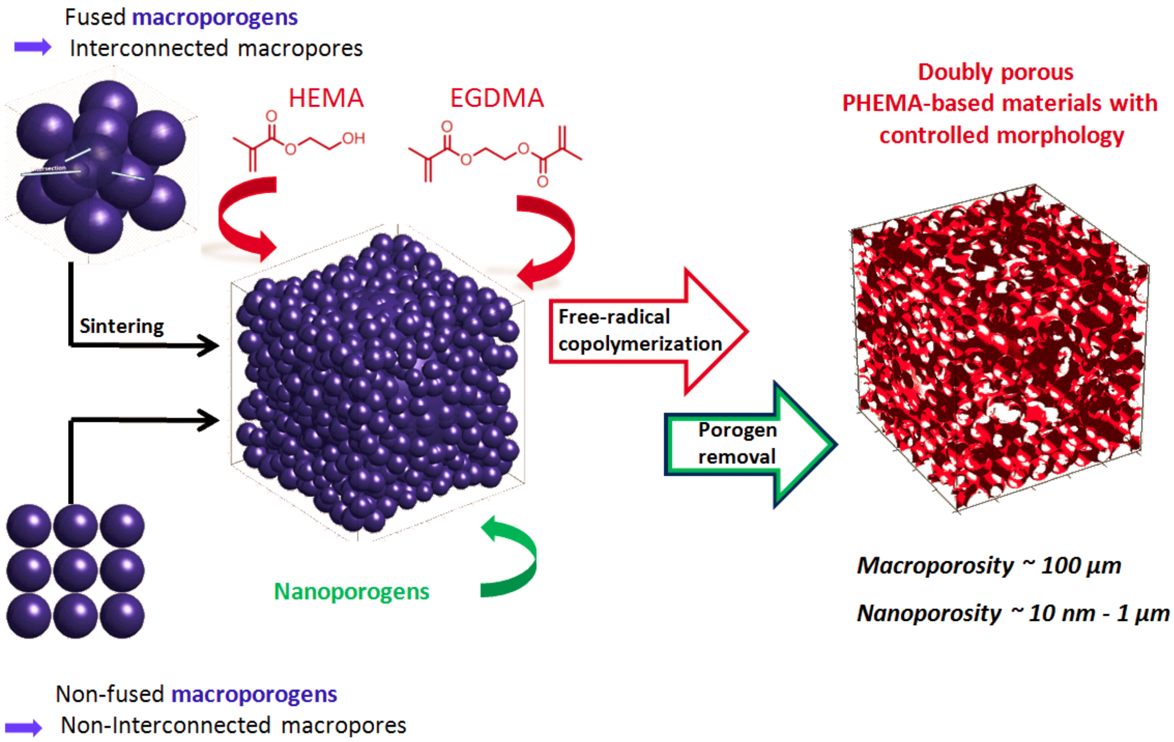

The work developed in this chapter has been published in 5 different papers:

- B. Le Droumaguet, R. Lacombe, H.B. Ly, M. Guerrouache, B. Carbonnier, D. Grande: Engineering functional doubly porous PHEMA-based materials, *Polymer* 55, 373 (2014).
- B. Le Droumaguet, R. Lacombe, H.B. Ly, B. Carbonnier, D. Grande: Novel Polymeric Materials with Double Porosity: Synthesis and Characterization, *Macromol. Symp.* 304, 18 (2014).
- H.B. Ly, B. Le Droumaguet, V. Monchiet, D. Grande: Designing and modeling doubly porous polymeric materials, *Eur. Phys. J. Special Topics* 224, 1689-1706 (2015).
- H.B. Ly, B. Le Droumaguet, V. Monchiet, D. Grande: Facile fabrication of doubly porous polymeric materials with controlled nano- and macro-porosity, submitted as a regular article to *Polymer*.
- H.B. Ly, L. Halbardier, D. Grande: Biporous cross-linked polymers with controlled pore size and connectivity, submitted as a regular article to *Macromol. Symp.*

2.1 Introduction

The elaboration of well-defined porous polymeric materials has been the subject of intense research over the past decade. It has notably focused on the preparation of materials for civil engineering, chromatographic supports for separation sciences [1–3], scaffolds for tissue engineering [4] or devices for drug delivery applications [5], to cite but a few. Throughout these highly raised demands, it actually exists a crucial need for structure and porosity optimization, depending on the specific targeted application. In this context, doubly porous materials have attracted a particular attention from the research community. For instance, in the area of tissue engineering, the first porosity level with pore size higher than 100 μm may facilitate cell seeding and proliferation within a biocompatible material, while the second porosity level with pore size lower than 1 μm could improve the nutrient or waste flow through the material. In the case of civil engineering and other mechanical applications, the larger porosity level would allow macromolecules flow through the material, while the smaller porosity level would be dedicated to the passage of smaller molecules or play an important role regarding filtration applications [6–8]. Therefore, it is desirable to design such materials with tunable structure, pore size and morphology for fluid flow optimization, improved mechanical properties or optimized cell proliferation.

Over the last years, miscellaneous studies have reported on the implementation of biporous polymeric frameworks relying on different synthetic strategies. Temperature-induced phase separation (TIPS) in combination with particle leaching has recently been reported by different research groups for the design of poly(L-lactide)- [9], gelatin- [10] or poly(lactide-*co*-glycolide)- [11] based scaffolds. Macropores were generated *via* templating by using poly(ethyl methacrylate), paraffin, and sucrose spheres (with different diameter ranges), while dioxane, ethanol/water or chloroform permitted the formation of a smaller pore range during the TIPS process. Moreover, methodologies based on the use of two different porogens have been reported. They typically include a porogenic solvent as a nanoporogen and inorganic particles as macroporogens, such as sodium chloride (NaCl) [12–14], calcium carbonate ($CaCO_3$) [15] or ammonium sulfate ($(NH_4)_2SO_4$) [16]. Different research groups have focused on the influence of various porogenic solvent mixtures, and especially 9/1 (v/v) cyclohexanol/dodecan-1-ol solvent system, on the porosity of poly(2-hydroxyethyl methacrylate)-based porous frameworks [16, 17]. The preparation of diverse monolithic polymers, including poly(2-hydroxyethyl methacrylate) (PHEMA), *via* the use of (co)porogens such as methanol, ethanol, THF or hexane, has also been well-documented in the literature [3]. Additionally, Okay *et al.* have prepared poly(2-hydroxyethyl methacrylate-*co*-ethylene glycol dimethacrylate) (poly(HEMA-*co*-EGDMA) porous beads in the presence of cyclohexanol or toluene as the porogenic solvents [18]. Last but not least, a hierarchically-structured porosity was obtained in PHEMA-based materials by High Internal Phase Emulsion (HIPE) templating [19–21]. The first porosity arose from the removal of an organic porogenic solvent, while the second one resulted from interconnections between adjacent pores. However, the production of hydrophilic "reversed" polyHIPEs from oil-in-water HIPE systems is hampered by their relatively poor stability and relatively limited synthesis windows, as only materials with relatively low porosities and/or rather poor interconnectivities have effectively been engineered so far.

In this context, to the best of our knowledge, no investigation clearly determining the different parameters that strongly influence the distinct porosity levels of polymeric materials has been reported so far. In order to improve such biporous polymeric systems, a thorough analysis of the parameters influencing their porous features may be required. Based on doubly porous PHEMA-based biocompatible materials, we herein propose a detailed analysis of the different parameters that permit to finely tune the nanoporosity but also to increase the macropore interconnectivity of such biporous materials through novel approaches revisiting the use of two types of porogens, namely a macroporogen in combination with a nanoporogen. In order to generate the macroporosity, either fused or not NaCl particles with size in the 125-200 μm range, or fused PMMA beads with size in the 200 μm range are used as the macroporogenic template, while the second porosity level is generally obtained by using different porogenic solvents through phase separation during the materials formation by free-radical copolymerization. Such methodologies enable the effective and straightforward preparation of doubly porous PHEMA-based materials with controlled morphology. The porosity of the as-obtained porous frameworks is carefully examined by means of scanning electron microscopy (SEM), mercury intrusion porosimetry (MIP), and nitrogen sorption porosimetry so as to elucidate the critical parameters regarding the features of both nano- and macroporosity.

2.2 Experimental

2.2.1 Materials

2-hydroxyethyl methacrylate (HEMA, 97%), ethylene glycol dimethacrylate (EGDMA, 98%), 2,2-dimethoxy-2-phenylacetophenone (DMPA), dodecanol (DOH, 98%), hydroxyapatite (HA, $\sim$ 200 nm) and 2,2'-Azobis(2-methylpropionitrile) (AIBN, 98%) were purchased from Aldrich. AIBN was recrystallized from methanol (MeOH) prior to use. Sodium chloride (NaCl) of 50-500 μm particle size was purchased from Prolabo. Poly(methyl methacrylate) (PMMA) beads (200 μm average diameter, dispersity index: 3.0) were supplied by Polysciences, Inc. Calcium carbonate ($CaCO_3$, Mikhart 130, particle size ranging from 60 to 400 μm) was kindly provided by

Provencale SA, France. All the particles were sieved and stored in moisture-free conditions prior to PHEMA-based network synthesis. Methanol (MeOH, Carlo Erba), absolute ethanol (EtOH, 99%, SDS), propan-1-ol (*n*-PrOH, 99.5%, Carlo Erba), propan-2-ol (*i*-PrOH, for analysis-ACS-Reag.Ph.Eur, Carlo Erba), cyclohexanol (CyOH, 98%, Carlo Erba), dichloromethane (CH_2Cl_2, 99.9%, Carlo Erba), and tetrahydrofuran (THF, 99.9%, SDS) were supplied by Carlo Erba. All reagents and solvents were used without any further purification procedure.

2.2.2 Preparation of nanoporous PHEMA-based materials

The polymerization mixtures constituted of HEMA, EGDMA (varying molar ratios: 95/5, 90/10, 80/20, 70/30 and 60/40 mol. %) and DMPA (2 wt. % with respect to the total comonomer amount) were homogenized with the solvent (various comonomers/porogenic solvent volume ratios: 40/60, 30/70, 25/75, 20/80 and 10/90 vol. %) before being transferred into glass vials. The latters were placed in a spectrolinker XL-1500 UV oven (Spectronics, Westburry, NY, USA) equipped with six lamps (6 × 15 W) for 4 h under irradiation at 365 nm so as to trigger the photo-induced free-radical copolymerization. The as-obtained materials were then subjected to porogen extraction by immersing them in deionized water (or in EtOH when CyOH or DOH was used as a nanoporogen), at room temperature for 2 days. The extraction solution was renewed every 12 h. After porogen extraction, the nanoporous PHEMA samples were abundantly washed with deionized water, and dried at room temperature under vacuum. Gravimetric analysis confirmed complete removal of the porogens.

2.2.3 Preparation of doubly porous PHEMA-based materials

Initially, 125-200 μm sieved NaCl particles were introduced into a crucible and sintered in a DJ5S R. Renat oven (maximum power of 2.5 kW and maximum temperature of 1200°C) for 3 h at 730°C to allow for the formation of an interconnected NaCl phase. Alternatively, previously sieved NaCl particles were submitted to a Spark Plasma Sintering (SPS) treatment so as to obtain a fused NaCl particle phase. A Sumitomo Dr. Sinter Lab 515S SPS machine from Fuji Electronic Industrial was used. Experimentally, NaCl particles were introduced into a graphite die and heated from room temperature to 100°C at a heating rate of 50°C.min^{-1}, while applying a 3 kN force onto the sample under inert atmosphere. After 20 min at 100°C, the sintered sample was cooled to room temperature at a rate of 50°C.min^{-1}. The mixture consisting of HEMA, EGDMA (with different molar ratios: 95/5, 90/10, 80/20, 70/30, and 60/40 mol. %), DMPA (2 wt.% with respect to the comonomers), and the solvents (with various volume percentages) was added to the NaCl particles (either fused or not), and the polymerization was conducted in a UV oven for 4 h at

365 nm. When NaCl particles were non-interconnected, they were removed by extraction with deionized water for 3 days (water was changed every 24 h), while NaCl removal took 1 day for the materials with fused particles. After this step, the samples were washed abundantly with the extracting solvent, and dried at room temperature under vacuum. Gravimetric analysis was also used to confirm the complete removal of NaCl particles and different solvents.

2.2.4 Instrumentation

SEM investigation of the materials was performed on a MERLIN microscope from Zeiss equipped with InLens and SE2 detectors using a low accelerating tension (2-3 kV) with a diaphragm aperture of 30 μm. The samples were first cryofractured and coated with a 4 nm layer of palladium/platinum alloy in a Cressington 208 HR sputter-coater. Average pore diameters were determined using the ImageJ 1.47v software.

The porosity ratios, pore volumes, and pore size distributions of the materials were determined by MIP using an AutoPore IV 9500 porosimeter from Micromeritics. The determination of the porosity features was based on the Washburn equation between the applied pressure (from 1.03 to 206.8 MPa) and the pore diameter into which mercury intruded.

The nitrogen sorption measurements were carried out at 77 K with a Quantachrome Autosorb iQ analyzer. The specific surface area values for the investigated porous polymers were quantified using the BET method at relative pressure (P/P_0) values ranging from 0.05 to 0.3.

2.3 Results and discussion

In order to develop biocompatible doubly porous materials, 2-hydroxyethyl methacrylate (HEMA) was selected as the monomer of reference, as it has been so far mainly devoted to the preparation of scaffolds for tissue engineering or the production of drug delivery devices. PHEMA-based materials have notably been used as hydrogels to develop soft contact and intraocular lenses, implants, wound dressings, drug delivery systems, and carriers for immobilization of enzymes, antibodies, or cells [22]. On the other hand, hydroxyl groups in such materials are available for further modifications to promote cell attachment, proliferation, differentiation, and migration in biomedical applications [23–25]. EGDMA was chosen as the cross-linking agent as its use in combination with HEMA has been well reported.

In addition, tiny quantities (1 mol% with respect to monomer and cross-linker) of a charged comonomer, *i.e.* 2-acrylamido-2-methylpropane sulfonic acid tetrabutylammonium salt (AMPS-TBA), were used as it would allow for the decoration of the pore surface with charges for potential further functionalization or even for the generation of an electro-osmotic flow (EOF) through the polymeric frameworks, which could be of interest for the design of specific bioreactors [26, 27].

2.3.1 Preliminary results

2.3.1.1 Preparation of biporous PHEMA-based material using $CaCO_3$ and HA as porogens

As a starting point for the design of materials with double porosity, $CaCO_3$ particles with size ranging from 125 to 160 μm were used to generate the macroporosity as they have recently been demonstrated to allow for the formation of porous hydrogels through particle templating [28–30]. In addition, HA nanoparticles, with an average diameter of 200 nm, were selected as nanoporogenic agents for the first time, because they can easily be removed under the same hydrolytic conditions as those used for $CaCO_3$ removal. A mixture of HEMA, EGDMA, and AMPS-TBA was copolymerized *via* AIBN-induced free-radical polymerization in presence of the pair of porogens, *i.e.* $CaCO_3$ and HA. After polymerization at 70°C for 4 h, the resulting materials were subjected to a hydrolysis in a 3M HCl aqueous solution for 1 week. The complete removal of the porogenic templates was verified by FTIR spectroscopy through the total disappearance of the characteristic bands of HA at ~1020 cm^{-1} and $CaCO_3$ at ~1400 cm^{-1}, respectively (Figure 2.1).

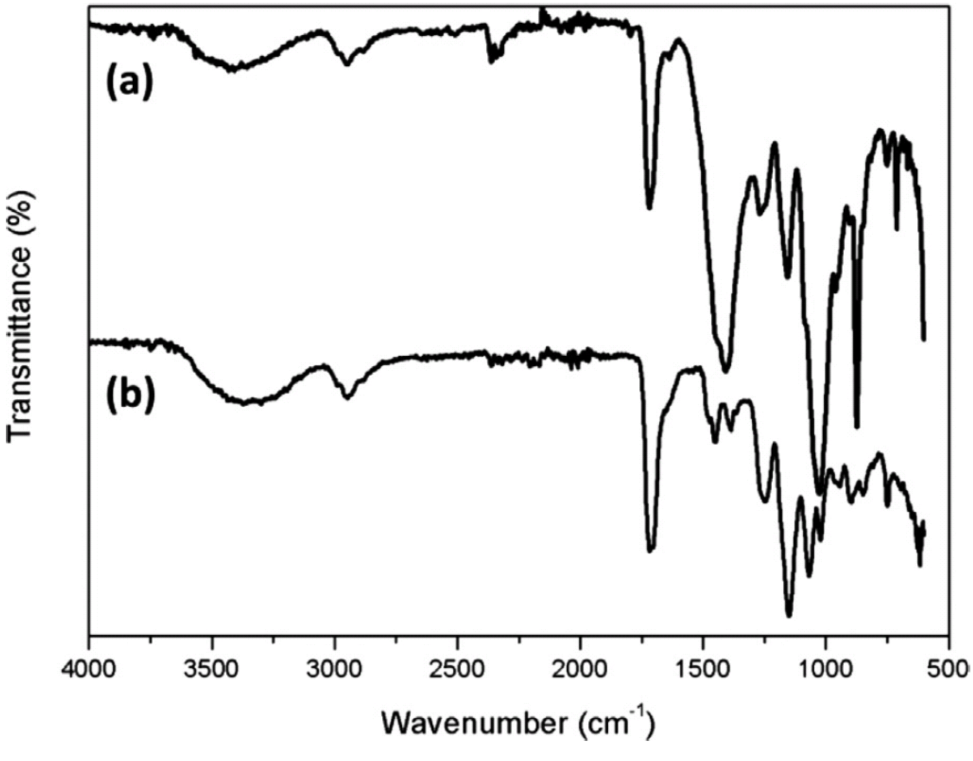

Figure 2.1: ATR-FTIR spectra of PHEMA-based material before (a) and after (b) hydrolysis of the porogenic agents ($CaCO_3$ and HA).

FTIR confirmed that the hydrolysis, carried out in rather harsh acidic conditions, did not affect the material chemical structure. Indeed, the C=O stretching band intensity at 1720 cm^{-1} from the PHEMA network did not show any significant decrease after porogen removal. The porosity was characterized by MIP (Figure 5.16) and SEM (Figure 6.13).

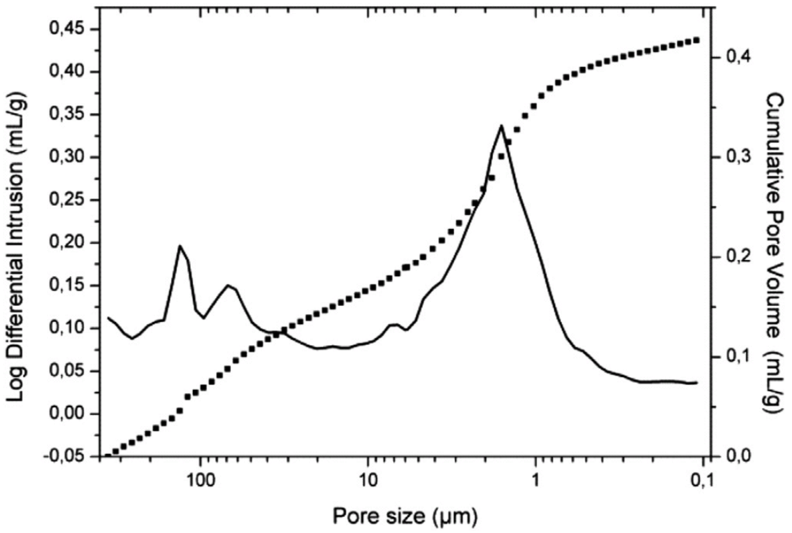

Figure 2.2: MIP profile of doubly porous PHEMA-based material obtained upon hydrolysis of $CaCO_3$ and HA by aqueous HCl solution.

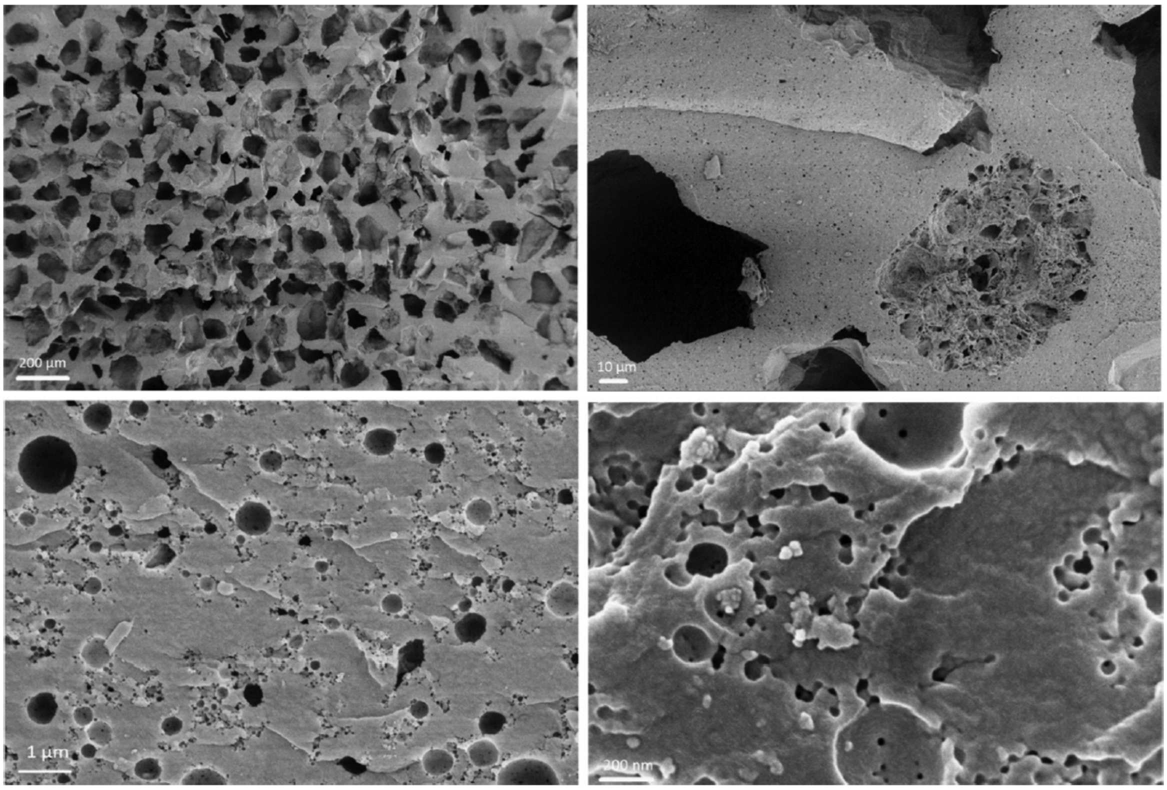

Figure 2.3: SEM micrographs of doubly porous PHEMA-based material obtained upon hydrolysis of $CaCO_3$ and HA by aqueous HCl solution.

MIP evidenced the presence of a bimodal porosity, the macroporosity being centered around 100 μm, while the smaller porosity was found to be centered around 1.5 μm. It was thus assumed that the porosity centered on 1.5 μm, arising from the hydrolysis of the 200 nm HA particles, was due to HA cluster formation during the polymerization process, giving rise to a higher average pore size than that expected. SEM observation of this porous material corroborated MIP analysis. Indeed, macropores with an average diameter around 120 μm were observed along with a smaller porosity centered around 1.05 μm.

2.3.1.2 Discussions on the preliminary results

These preliminary studies on the design of PHEMA-based doubly porous materials *via* the double porogen templating approach through the use of two types of particles clearly showed some limitations in controlling the porosity, especially the nanoporous phase interconnectivity and the nanopore size range, likely due to HA particle cluster formation before porogen removal. Additionally, low porosity ratios from 30 to 40 % were observed. In order to control the overall interconnectivity of the porous structure *via* particle templating, such inorganic templates should be partially fused. However, due to different glass transition temperatures of macro- and nanoparticles, one such process may not be achieved easily. Further, to prevent the nanoparticles cluster formation phenomenon, the polymerization mixtures should diffuse homogeneously through the particle template by applying high pressure so as to ensure the polymerization solution penetration into the narrow interstitial voids of the sacrificial template. Finally, from an economic point of view, the use of rather expensive HA nanoparticles seems inappropriate if one considers future potential industrial production costs.

In order to circumvent these limitations, a more common nanoporogen was selected, *i.e.* a porogenic solvent. Indeed, the strategy using a porogenic solvent and a macroporogen template to prepare biporous materials has an undeniable advantage over others. This approach implies the formation of the two different levels of porosity *via* distinct and independent processes. The nanoporous phase was developed within the polymeric network through a phase separation process induced during free-radical polymerization. The nanoporosity may greatly be influenced by different key parameters, such as the nature of the porogenic solvent used, its proportion with respect to the comonomers total volume, but also by the cross-link density of polymer networks [3, 18, 31]. On the other hand, the macroporogen was incorporated into the comonomers/solvent(s) prior to the polymerization step, and by a simple post-polymerization removal with a suitable solvent, the macroporosity was generated within the polymer matrix. The macroporous phase formation depends on different critical parameters, such as particle shape and particle packing. Indeed, macropores can be either interconnected, if the particles are fused, or non-interconnected if they are not. Therefore, this factor governs the overall interconnectivity associated with the porous materials and has a great importance over the specific surface area of the resulting materials [32].

Prior to the rational design of doubly porous PHEMA-based materials, a complete analysis of the formation of the nanopore size distribution was carried out in a first stage. Due to the independent formation of both porosity levels, we indeed considered only the development of a nanoporous network with an emphasis on the porosity, average pore size, and pore interconnectivity. The effects of the porogenic solvent structure and its proportion were carefully investigated. Furthermore, the cross-linker proportion in the comonomer mixture was varied and its influence on the nanoporosity was also analyzed. Doubly porous PHEMA materials were then designed by resorting to 200-250 μm sieved NaCl particles or 160-200 μm sieved PMMA beads in conjunction with a porogenic solvent, and all the experiments realized in the previous stages were taken into account to strengthen the proof of concept that the formation of both porosity levels could be controlled independently.

2.3.2 Effect of porogenic solvent on porous PHEMA-based materials

Porous structures can only be prepared when the amounts of porogenic solvent and cross-linking agent are higher than certain threshold values [31]. Pore size distributions in nanoporous networks can be finely tuned by changing the solvent nature and proportion in the initial polymerization feed. First of all, different solvents were assessed to investigate the effect of the solvent structure on the porous characteristics of the resulting nanoporous networks. Based on their solubility parameters, the different alcohols used, namely methanol (MeOH), ethanol (EtOH), *n*-propanol (*n*-PrOH), *i*-propanol (*i*-PrOH), cyclohexanol (CyOH) and dodecanol (DOH), were miscible with the comonomer mixture before polymerization. Nanoporous networks could thus be obtained through a phase separation process after complete removal of the solvents after polymerization. MIP profiles of the resulting PHEMA samples are shown in Figure 6.14. As expected from the solvent nature, the more hydrophobic the solvent, the larger the average pore size of the resulting PHEMA-based materials. The porous features of the as-obtained materials could notably be correlated to some basic parameters of the solvents used, *i.e.* solubility parameters and dielectric constants as illustrated in Table 2.1. More precisely, the use of polar solvents, such as MeOH or EtOH, as nanoporogens gave a unimodal and rather narrow pore size distribution curve. A nanoporous network with pore size ranging from 30 nm up to 1 μm, centered at 160 nm, was observed when using MeOH as a porogenic solvent, while a distribution ranging from 30 nm to 10 μm, centered at 180 nm, was obtained when using EtOH.

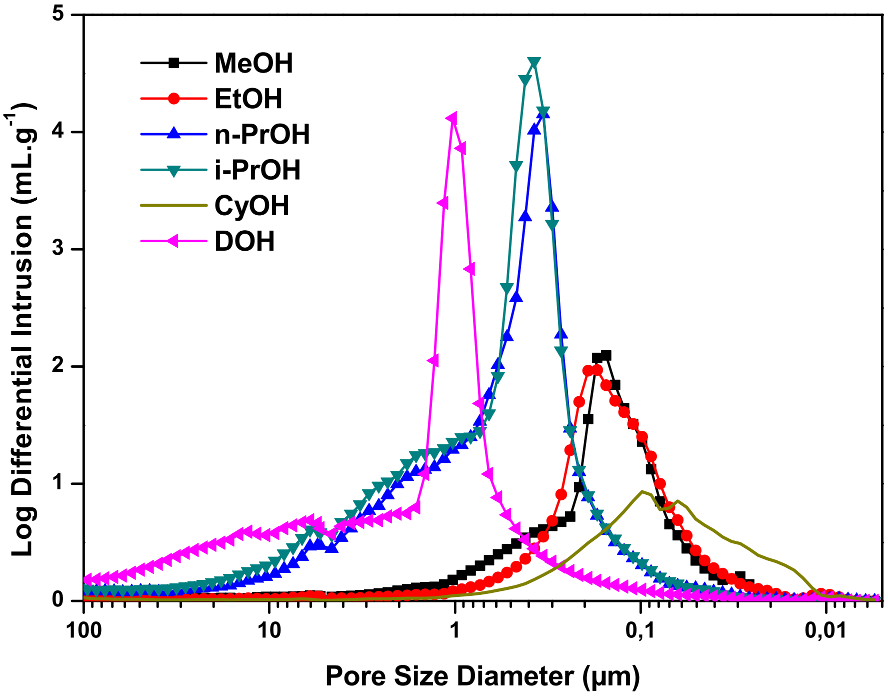

Figure 2.4: Mercury intrusion porosimetry profiles of various monoporous PHEMA networks depending on the structure of the porogenic solvent used. The polymerization mixture was constituted of 70/30 mol. % HEMA/EGDMA in the presence of 80 vol. % of the porogenic solvent.

The 62% porosity ratio of the as-obtained material with MeOH was rather weak when compared to the 80 vol.% (with respect to the total volume of comonomers) of solvent initially added to the polymerization feed. This could be likely attributed to some non-interconnected nanosized porosity within the polymeric material or to a lack of separation phase due to the solvent nature. In the case of EtOH as the porogenic solvent, the 74% porosity observed by MIP was in good agreement with the 80 vol.% EtOH to comonomers volume ratio initially present in the polymerization feed. Using a less polar alcohol, such as *n*-PrOH or *i*-PrOH, allowed for the preparation of porous networks with higher average diameter centered at 360 nm and 380 nm, respectively. In these cases, the pore size distribution curves were broader. Accordingly, higher pore volumes were observed, *i.e.* 2.78 mL.g^{-1} and 3.11 mL.g^{-1} for *n*-PrOH and *i*-PrOH, respectively. Porosity ratios determined by MIP were also in good agreement with the volume of the corresponding porogenic solvents (*i.e.* 77% for both *n*-PrOH and *i*-PrOH). With DOH as a porogen, the porous PHEMA sample had a macro-range average pore size of about 1 μm, and also a better agreement between the porosity (73%) and the volume of porogen initially present in the copolymerization mixture (80 vol.%).

Table 2.1: Porous features of monoporous PHEMA networks synthesized using various solvents as porogenic agents. The HEMA/EGDMA molar ratio was fixed at 70/30 mol. % and the volume ratio of comonomers/solvent was equal to 20/80 vol. %.

Solvent	Porosity ratio[a] (%)	Total pore volume[a] ($mL.g^{-1}$)	$D_p{}^a$ (nm)	S^b_{BET} ($m^2.g^{-1}$)	δ^c ($MPa^{0.5}$)	ε^d
MeOH	62	1.32	160	57	29.7	32.7
EtOH	74	2.48	190	40	26.0	24.5
n-PrOH	77	2.78	330	47	24.3	20.1
i-PrOH	77	3.11	380	30	23.5	17.9
CyOH	51	0.92	97	-	23.3	15.0
DOH	73	2.28	1000	44	20.5	6.5

[a] Values as determined by MIP.

[b] Specific surface area values as determined by N_2 sorption measurements (BET method).

[c] Solubility parameters cited from literature [33].

[d] Dielectric constants cited from literature [34].

An unusual behavior of the HEMA/EGDMA polymerization mixture was observed when using CyOH as a porogenic solvent for the formation of the nanoporous network. The polarity of CyOH lies in the middle range of that associated with the solvents in this study (*i.e.*, ε(DOH) < ε(CyOH) < ε(*n*-PrOH) < ε(EtOH) < ε(MeOH)). Surprisingly, an average pore size ranging in the ~100 nm order of magnitude was observed, while only 51% of porosity, and a rather low pore volume (*i.e.* 0.92 $mL.g^{-1}$) were found. We assumed that this particular porous feature using CyOH was likely due to rather bad solvating conditions of the growing cross-linked copolymer, leading to an early phase separation of the solvent from the copolymer network, and thus to very low porosity.

Second, the effect of the solvent proportion on the HEMA/EGDMA nanoporous system was analyzed by varying the volume percentage of EtOH in the polymerization feed. EtOH was fixed as a reference solvent, and a polymerization mixture constituted of 70/30 mol.% HEMA/EGDMA and DMPA (2 wt.% with respect to comonomers amount) was kept constant. The final comonomers/EtOH volume ratio was varied from 10/90 to 40/60 vol.%. MIP measurements were used to analyze the effect of the solvent amount on the porosity of the as-obtained (nano)porous polymers (Figure 6.15). A dramatic increase in average pore size was observed with increasing EtOH vol.%. With 60 vol.% EtOH, meso- and macroporosity were obtained ranging from 10 to 100 nm as evidenced by the MIP profile, the average pore size diameter being centered at 25 nm. At 75 and 80 vol.% of EtOH, larger macropores centered at 70 nm and 190 nm, respectively, were observed. At higher vol.% of EtOH, *i.e.* 85 and 90 vol.%, well-interconnected porous polymeric frameworks were obtained with 80% and 88% porosity, respectively, and the pore size distribution curves were centered at 1.3 μm and 11.5 μm. The porosity ratios of the porous polymers, *i.e.* 74%, 80%, and 88%, were in good agreement with the initial volumes of EtOH added, *i.e.* 80%, 85%, and 90%, thus demonstrating a good interconnectivity of the porous polymers. Samples with 60% and 75% vol.% EtOH could eventually show some closed pore structures as evidenced by their relatively low porosity ratios, *i.e.* 36% and 63%, respectively. Total pore volumes of the as-obtained porous materials were also determined *via* MIP (Table 2.2). It is noteworthy that increasing amounts of porogenic solvent could be associated with increasing pore volumes. Moreover, the pore volume seemed to increase linearly with the solvent proportion (from 0.44, 1.35, 2.49, and 3.30 to 6.38 mL.g^{-1} for samples with 60, 75, 80, 85, and 90 vol.% of EtOH, respectively). SEM micrographs of the sample with 80 vol.% EtOH are presented in Figure 2.6. Nitrogen sorption measurements were effected in order to give information on the surface area of the nanoporous materials. Values ranging from 30 to 70 m^2.g^{-1} were determined in most cases.

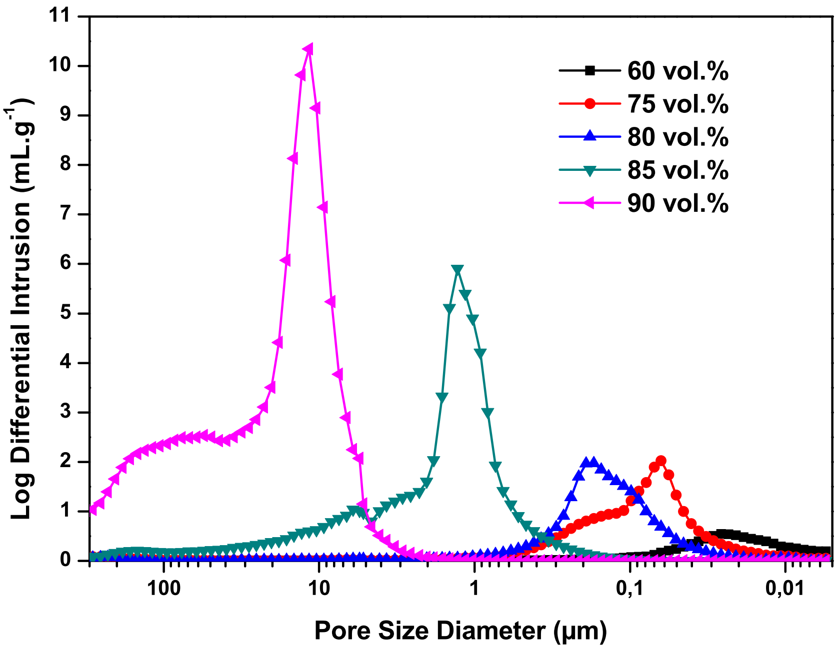

Figure 2.5: Mercury intrusion porosimetry profiles of various monoporous PHEMA networks depending on the volume proportion of EtOH as the porogenic solvent. The polymerization mixture was constituted of 70/30 mol.% HEMA/EGDMA.

Table 2.2: Porous features of monoporous PHEMA networks synthesized using various volume proportions of porogenic solvent (EtOH). The HEMA/EGDMA molar ratio was fixed at 70/30 mol.%.

Porogenic Solvent (vol. %)	Porosity ratio[a] (%)	Total pore volume[a] (mL.g^{-1})	D_p[a] (nm)	S^b_{BET} (m^2.g^{-1})
60	36	0.44	25	48
75	63	1.35	65	70
80	74	2.48	190	40
85	80	3.29	1270	62
90	88	6.38	11500	158

[a] Values as determined by MIP.

[b] Specific surface area values as determined by N_2 sorption measurements (BET method).

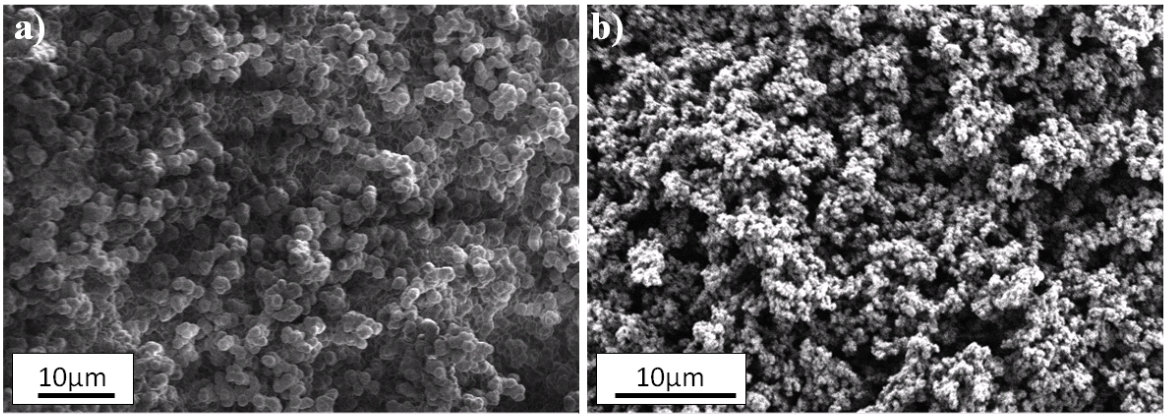

Figure 2.6: SEM micrographs of monoporous PHEMA-based materials prepared from: (a) 60/40 mol.% HEMA/EGDMA and 80 vol.% *i*-PrOH with respect to the total volume of comonomers; (b) 70/30 mol.% HEMA/EGDMA and 80 vol.% EtOH with respect to the total volume of comonomers.

2.3.3 Effect of cross-linker concentration on porous PHEMA-based materials

It is well known that the nature of cross-linker and its concentration in the initial polymerization feed can also affect the pore size distribution of resulting porous networks. In this paper, we focused our attention on EGDMA as the cross-linking agent and carefully analyzed the influence of its molar proportion (when compared to the functional HEMA monomer) on the pore size distribution range. EGDMA was chosen not only because of its common use in polymeric porous materials, but also because it gives rise to a higher modulus of elasticity for the resulting networks, when compared to diethylene glycol dimethacrylate (DEGDMA) or triethylene glycol methacrylate (TEGDMA) [35]. Polymerization mixtures constituted of various HEMA/EGDMA molar ratios, *i.e.* 95/5, 90/10, 80/20, 70/30 and 60/40 mol.%, and DMAP (2 wt.% with respect to total comonomers amount) were homogenized with a constant volume of *i*-PrOH, namely 80 vol.%. The porous features of the resulting PHEMA frameworks are gathered in Table 2.3, and the corresponding MIP profiles are presented in Figure 6.16. At low EGDMA concentration (*i.e.* 5 mol.%), the porous structure was not well-developed and mechanically unstable, likely due to a too high amount of porogenic solvent added (*i.e.* 80 vol.% *i*-PrOH) and a too low cross-link degree of the resulting network. The PHEMA-based porous material was nicely formed when using 10 mol.% EGDMA but resulted in only 19% porosity, as observed by MIP. Additionally, an average pore size diameter of 9 nm was obtained. The low value of porosity ratio demonstrated a large amount of inaccessible pores during MIP analysis or an underestimation of the pore volume due to the pressure applied to a fragile material [36]. It is noteworthy that the synthesis of mechanically stable porous structures could be achieved when using a low EGDMA proportion. In one such case, it was necessary to decrease the percentage of the porogenic solvent in the copolymerization mixture down to 50 vol.% [3, 17, 18].

Table 2.3: Porous features of monoporous PHEMA networks synthesized using various EGDMA molar concentrations. The volume proportion of porogenic solvent (*i*-PrOH) was equal to 80 vol.% with respect to the total volume of comonomers.

EGDMA (mol. %)	Porosity ratio^a (%)	Total pore volume^a (mL.g^{-1})	$D_p{}^a$ (nm)	S$^b_{BET}$ (m^2.g^{-1})
10	19	0.18	95	90
20	65	1.57	190	87
30	77	3.11	380	46
40	80	3.68	3400	50

[a] Values as determined by MIP.

[b] Specific surface area values as determined by N_2 sorption measurements (BET method).

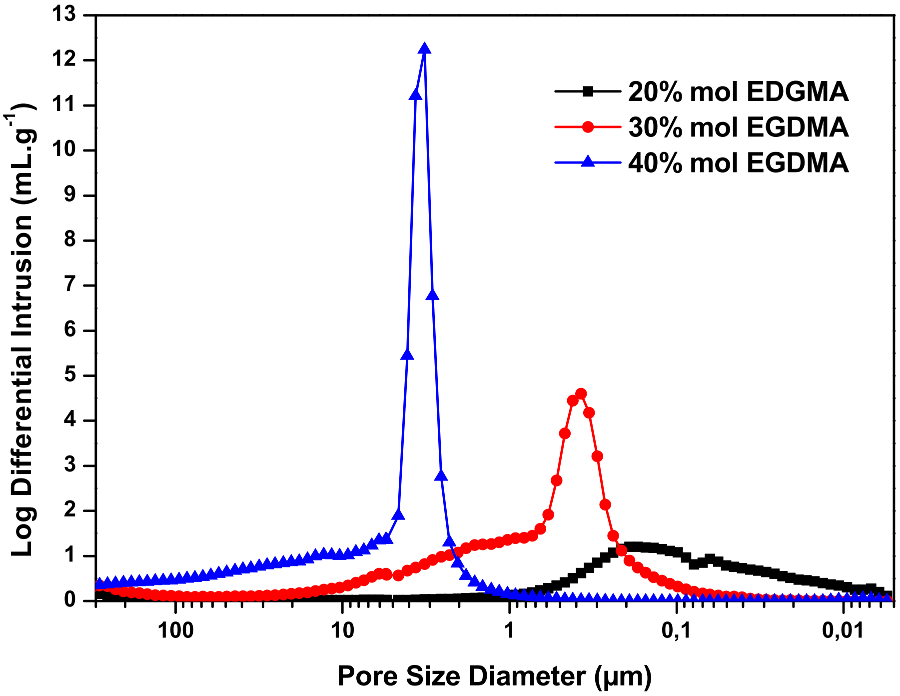

Figure 2.7: Mercury intrusion porosimetry profiles of monoporous PHEMA-based samples prepared from various EGDMA molar concentrations. The polymerization mixture was constituted of HEMA/EGDMA in the presence of 80 vol.% *i*-PrOH as a porogenic solvent.

At 20 mol.% EGDMA, the pore size distribution was found to be much broader, varying from 5 nm to 1 μm, and centered around 190 nm. In this case, the porosity ratio was in better agreement with the amount of *i*-PrOH added (65% porosity vs. 80 vol.% *i*-PrOH with respect to the total comonomer volume). A good interconnectivity was observed when increasing the EGDMA molar ratio up to 30 mol.% and 40 mol.%. Indeed, the porosity of the resulting PHEMA materials increased up to 77% and 80%, respectively. Average pore size was centered at 380 nm for 30 mol.% EGDMA, and at 40 mol.% EGDMA, the distribution curve was rather broad and centered at 3.4 μm. Reproducible and regular porous structures could be obtained when high HEMA molar ratio were used in the polymerization feed. This was also confirmed by SEM: highly regular globular structures were indeed observed (see Figure 2.6).

Further, we do believe that other parameters could play a key role over the pore size range obtained, such as the polymerization temperature or the radical initiator type [31, 37], but these parameters have not been fully analyzed yet and will not be reported in this study.

2.3.4 Comparison of thermally-induced and photo-initiated polymerizations of HEMA

The difference between thermally-induced and photo-initiated copolymerization of HEMA and EGDMA may probably have a crucial role over the porous features of PHEMA-based materials as well [38]. Thus, we herein propose to analyze the effect of the polymerization conditions on the HEMA/EGDMA nanoporous system, by varying the temperature of thermally-initiated polymerization or by resorting to a photo-initiated process. *i*-PrOH was fixed as a reference solvent and the volume ratio of comonomers (constituted of 70/30 mol.% of HEMA/EGDMA)/solvent was equal to 15/85 vol.%. For photo-initiated polymerization, DMPA was chosen as a photo-initiator, and the polymerization was conducted in a UV oven for 4 h. For thermally-initiated polymerization, AIBN was chosen as the initiator and the vial constituted a polymerization mixture was placed in an oil bath at 65 or 70 °C for 20 h. MIP measurements were used to examine the porosity of the as-obtained (nano)porous polymers (Figure 2.8).

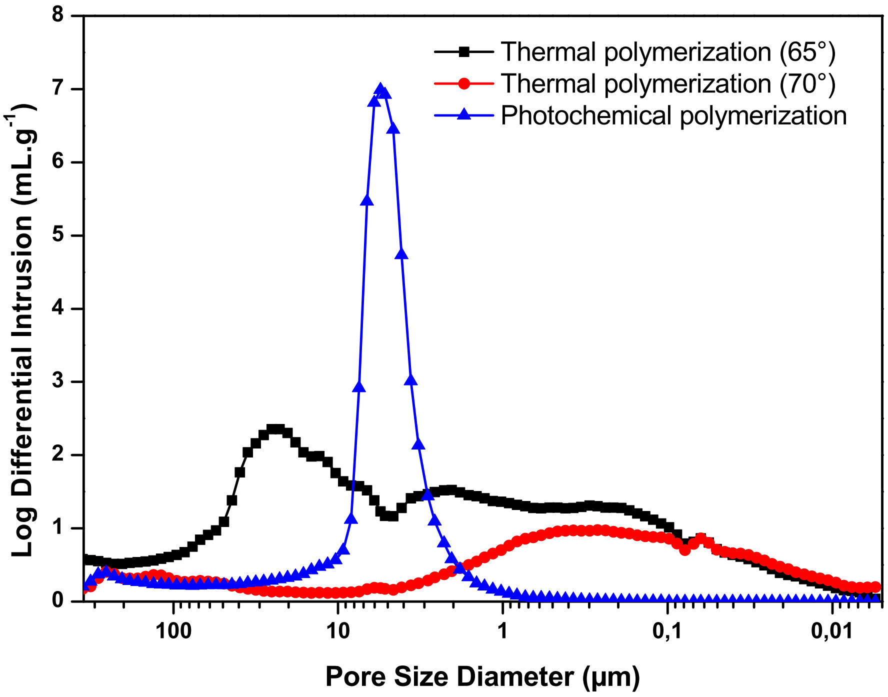

Figure 2.8: Mercury intrusion porosimetry profiles of monoporous PHEMA-based samples prepared from thermally-induced and photo-initiated polymerization processes. The polymerization mixture was constituted of 70/30 mol.% HEMA/EGDMA in the presence of 85 vol.% *i*-PrOH as a porogenic solvent.

The thermally-initiated polymerization at 75 °C was not successful because this temperature was too close to the boiling point of *i*-PrOH (*i.e.* 82 °C), thus leading to porous structure collapse. When the polymerization temperature was between 65 and 70 °C, stable porous frameworks were successfully synthesized. At the lower temperature (*i.e.* 65°C), meso-, nano- and macro-porosity were obtained ranging from 10 nm to 60 μm, as evidenced by the MIP profile. The pore size distribution curve was very broad in this case. At a higher temperature (*i.e.* 70°C), a narrower pore size distribution was observed, ranging from 10 nm to 5 μm and centered around 300 nm . With similar mixture of HEMA/EGDMA/*i*-PrOH, photo-initiated polymerization gave a distribution curve much narrower than the two previous cases. Macroporosity was observed between 1 and 10 μm and centered around 5 μm. These monoporous PHEMA-based materials presented 82, 71 and 74 % porosity corresponding to the samples prepared at 65°C, 70°C and photo polymerization, respectively. A higher pore volume was observed in the case of the thermal polymerization at 65°C (4.61 mL.g^{-1}), whereas it was equal to 2.24 mL.g^{-1} and 2.88 mL.g^{-1} for samples obtained at 70°C and by photo-polymerization, respectively.

As a matter of fact, AIBN decomposition and monomer propagation at 65°C were slower than those at 70°C. This resulted in larger pores, and a rather inhomogeneous porous structure. When comparing between thermally- and photo-initiated polymerization, the porous structure in the latter case was much more homogeneous than thermal polymerization. The photo-initiator decomposition was faster than the thermal-initiator, thus the polymerization was more efficient. A photochemical process is well-known to be faster and more efficient than a classical thermal polymerization. Therefore, it is more appropriate for the generation of porous materials with controlled morphology.

2.3.5 Effect of macroporogen structure on doubly porous materials

2.3.5.1 Use of PMMA beads for macropore generation

The first strategy developed to generate doubly porous polymeric scaffolds was adapted from a previously published work from LaNasa *et al.* and Diego *et al.* [39,40], in which fused PMMA beads were used to generate an interconnected macroporous network within PHEMA hydrogels. Prior to the formation of the PHEMA network, PMMA beads displaying an average diameter of 200 μm were sieved because of their broad particle size distribution. Depending on the bead average diameter, different fractions were isolated, and the fraction comprising beads with diameters ranging from 160 to 200 μm was used for further experiments. PMMA beads were then sintered for 4 h at 140 °C, *i.e.* a temperature higher than their glass transition temperature (T_g = 105 °C). Sintering of PMMA beads was carried out in a Solvis LAB VC-20 vacuum oven from Penggli coupled with a CIT Alcatel pump type 2002A. The formation of the

PMMA beads template was monitored by SEM (Figure 2.9).

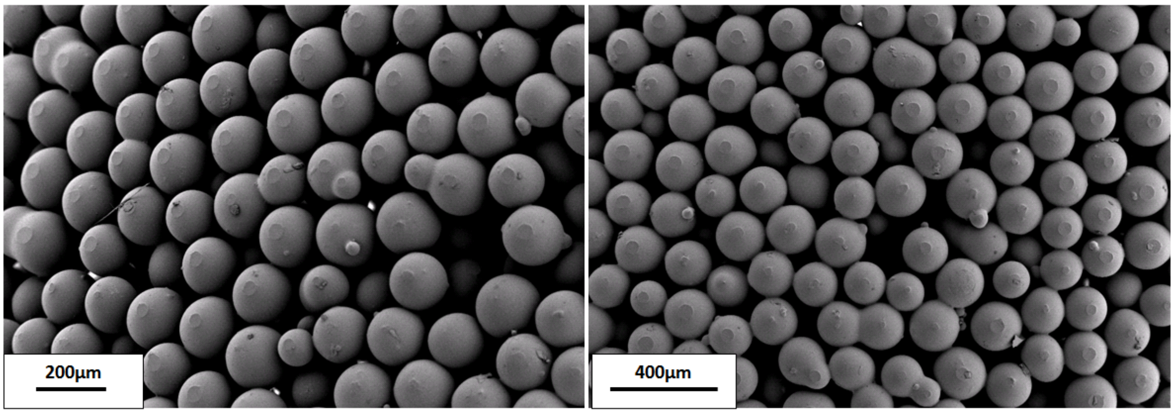

Figure 2.9: SEM micrographs of PMMA beads after sintering for 4 h at 140 °C.

As expected, a partial coalescence of PMMA spheres was obtained, thus giving rise to a continuous phase that should further lead to interconnected pores after PHEMA network synthesis, followed by PMMA beads extraction. The main difference with previous works lied in the generation of another level of porosity within the same material. The vial containing the PMMA beads template was filled with the polymerization feed supplemented with ethanol. The free-radical copolymerization of HEMA and EGDMA was carried out under UV irradiation for 1 h and subsequently at 70 °C for 4 h in an oil bath. After extraction of ethanol and PMMA beads with a suitable solvent (THF), the complete extraction of the porogenic agents was confirmed by gravimetry. The resulting porous materials were characterized by MIP (Figure 2.10) and SEM (Figure 2.11).

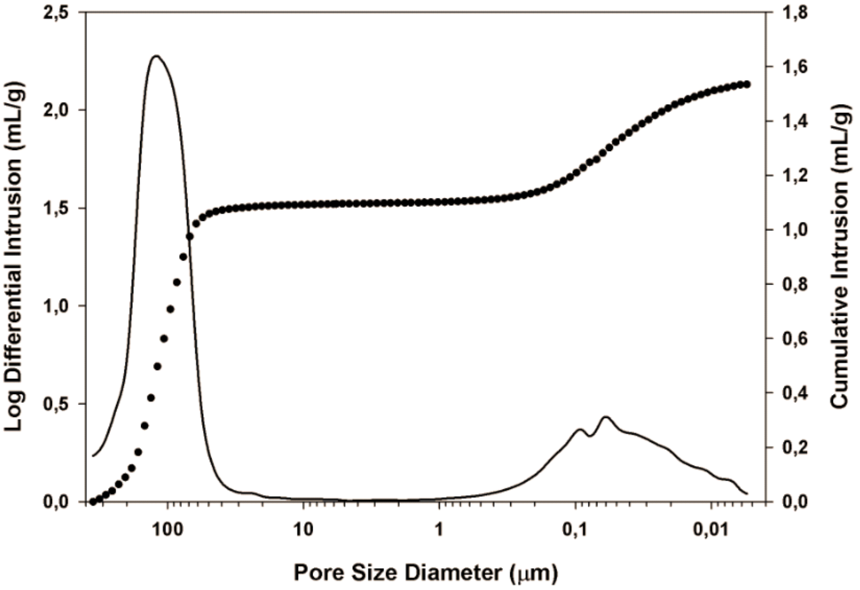

Figure 2.10: MIP profile of doubly porous PHEMA-based material obtained upon extraction of PMMA beads and ethanol with THF.

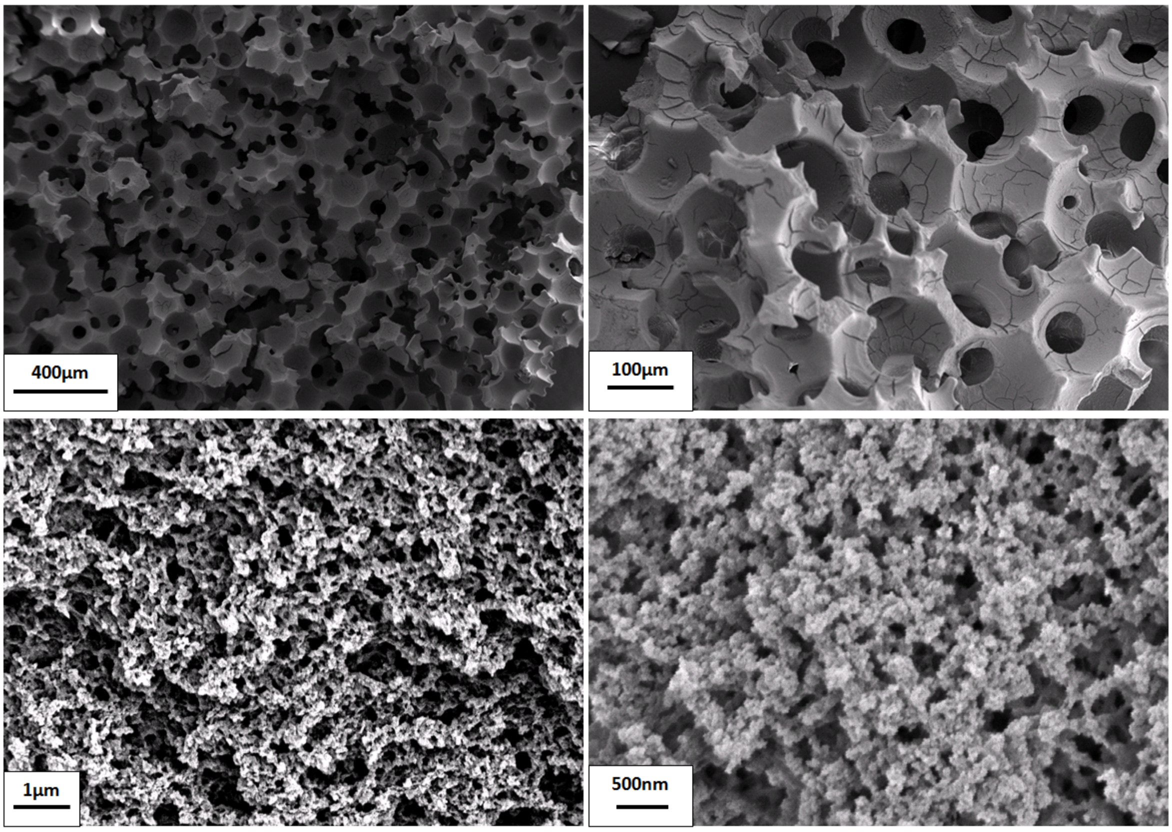

Figure 2.11: SEM micrographs of doubly porous PHEMA-based material obtained upon extraction of PMMA beads and ethanol with THF.

It is noteworthy that the use of highly polar solvents was detrimental to the robustness of PHEMA-based materials, likely due to an important swelling of the polymeric scaffold that physically destroyed the structure of the as-obtained materials. However, the use of THF as an extracting solvent for PMMA beads allowed for the preparation of much more stable materials. MIP analysis of the as-obtained polymeric scaffolds showed a well-defined macroporosity centered around 120 μm, while a second level of porosity was found around 60 nm (Table 2.4). These original biporous PHEMA-based materials presented a 65 % porosity ratio, and a macropores to nanopores ratio equal to 66/33 vol.%. The SEM observation confirmed the presence of a bimodal porosity: macropores with an average diameter of about 165 μm (as expected according to PMMA beads diameter) and interconnecting voids of about 50 μm were observed, while nanopores of about 260 nm diameter were found. It is worth mentioning that the significant difference between the results obtained from the two characterization techniques might be attributable to the pressure applied on these soft materials during MIP analysis (due to Hg penetration under high pressure) that could lead to partial collapse of the porosity, and thus to underestimation and inaccuracy in the determination of pore size distributions [36]. Again, the biporous polymeric material displayed a much higher specific surface area (*i.e.* 140 $m^2.g^{-1}$) than that of the corresponding macroporous specimen (*i.e.* 66

$m^2.g^{-1}$), thus demonstrating the significant role of nanopores in increasing the specific surface area in biporous materials.

Table 2.4: Porous features of PHEMA-based materials obtained using NaCl particles or PMMA beads as macroporogens.

Porogens	Porosity ratio[a] (%)	Total pore volume[a] ($mL.g^{-1}$)	$D_p{}^a$ (μm)	$D_p{}^b$ (μm)	Specific surface area[c] ($m^2.g^{-1}$)
NaCl	64	2.69	132/0	248/0	110
NaCl/EtOH	64	1.71	165/0.03	200/0.09	239
PMMA	60	1.27	130/0	172/0	66
PMMA/EtOH	65	1.53	120/0.06	165/0.26	140

[a] results as obtained by MIP

[b] average pore diameters as determined by SEM

[c] results as obtained by nitrogen sorption measurements using the BET method.

2.3.5.2 Use of NaCl particles for macropore generation

NaCl particles have been demonstrated to enable the formation of macroporous materials through particle templating associated with a straightforward macroporogen removal [41–44]. In the present paper, native cubic NaCl inorganic particles were chosen as a template of choice for the generation of macropores within doubly porous PHEMA-based materials. Two different macropore connectivities for the doubly porous materials could be obtained using NaCl particles: indeed, macropores could be either interconnected between them or non-interconnected. In the latter case, macropores were interconnected *via* the nanoporous framework developed within the macropore walls. The nanoporosity was derived from the phase separation occurring during the free-radical copolymerization of a comonomer mixture in the presence of a porogenic solvent. For the formation of interconnected macropores, two types of NaCl templates could be employed depending on the sintering method. The first one relied on the classical sintering of NaCl particles in an oven for 3 h at 730°C. The formation of the resulting 3-D NaCl phase was monitored by SEM (Figures 6.18.a and 6.18.b). Fused NaCl particles were thus observed. The second method implied the use of a NaCl template prepared *via* Spark Plasma Sintering (SPS). Again, a properly interconnected physical inorganic network was obtained, as observed in Figures 6.18.c and 6.18.d by SEM.

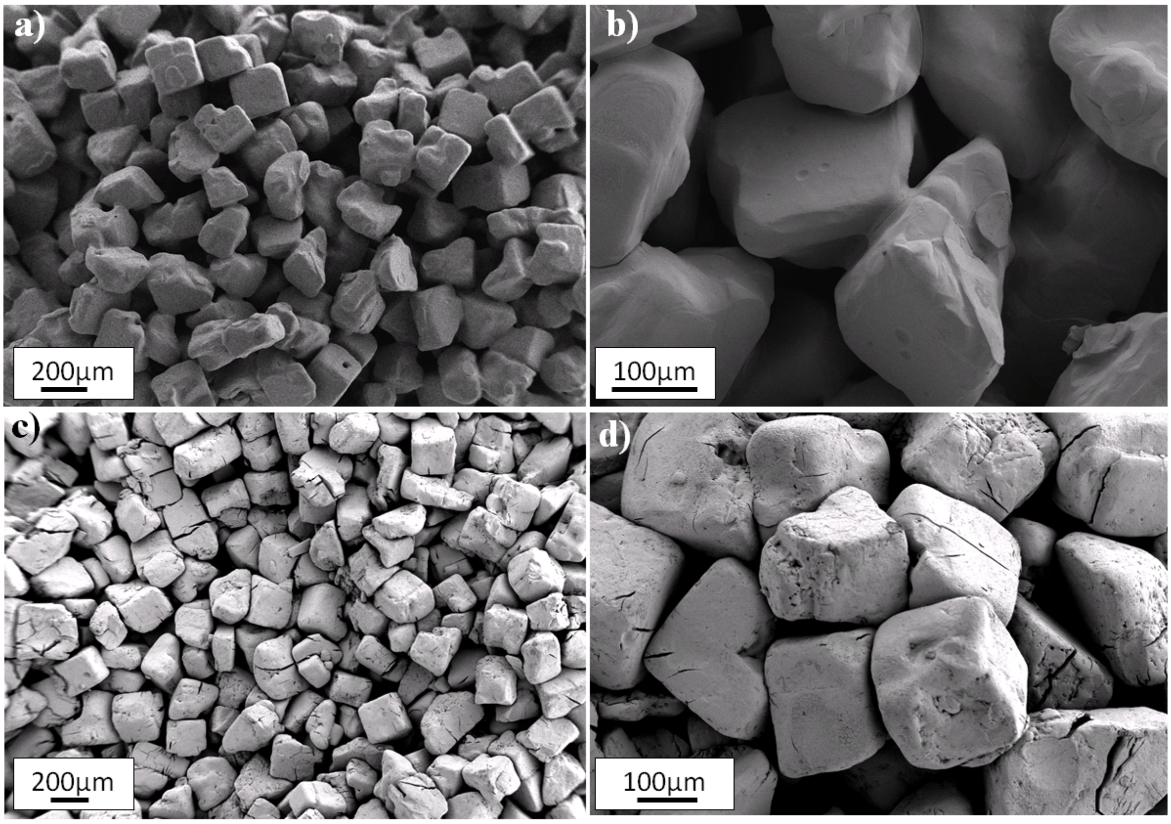

Figure 2.12: SEM micrographs of NaCl 3-D templates after sintering: (a,b) sintering at 730°C for 3 h; (c,d) Spark Plasma Sintering treatment.

The originality of our approach, namely an independent control over the nanoporosity and the macroporosity, was demonstrated in this series of experiments. First, the vials containing non-fused NaCl particles were filled with the HEMA/EGDMA/EtOH mixtures and the polymerization was conducted for 4 h *via* photo-initiated free-radical copolymerization at 365 nm. After subsequent removal of NaCl particles and porogenic solvent by extraction with deionized water for a suitable time, the as-obtained doubly porous materials were dried under vacuum. The complete extraction of the macro/nano-porogenic agents was confirmed by gravimetry. The resulting biporous PHEMA-based materials with non-interconnected macropores were analyzed by SEM and MIP, as shown in Figure 2.13.a,b and Figure 2.14, respectively. 75 vol. % EtOH and 30 mol. % EGDMA were kept constant in this case. A bimodal porous distribution was evidenced by means of SEM observation. The presence of macropores with an average diameter of about 165 μm (which closely corresponded to the NaCl particle diameter used) and nanopores observable on the macropore walls of about 90 nm diameter was demonstrated. MIP analyses confirmed the presence of a well-defined bimodal porosity, the macroporosity being centered around 120 μm, while the nanoporosity was found to be centered at 80 nm. Such analyses clearly pointed out the possibility of easily generating biporous materials with controlled porosity *via* the double porogen templating approach.

When comparing the latter biporous structure with a monoporous material prepared from the same polymerization mixture but in the absence of NaCl particle template Figure 2.13.c, it is readily observed that nanopores with sizes in the same order of magnitude were found: indeed, a pore size distribution ranging from 30 nm to 70 nm was determined by MIP for the nanoporous sample Figure 2.14. Finally, the biporous material presented a rather low 64% porosity ratio, most probably because macropores were not fully interconnected each other, with a macropore to nanopore volume ratio of about 70/30 vol. %. The significant advantage of this biporous material was that it exhibited a much higher specific surface area, *i.e.* S_{BET} = 239 $m^2.g^{-1}$, than that of its monoporous counterpart (S_{BET} = 110 $m^2.g^{-1}$), as measured from nitrogen sorption porosimetry (Table 2.4).

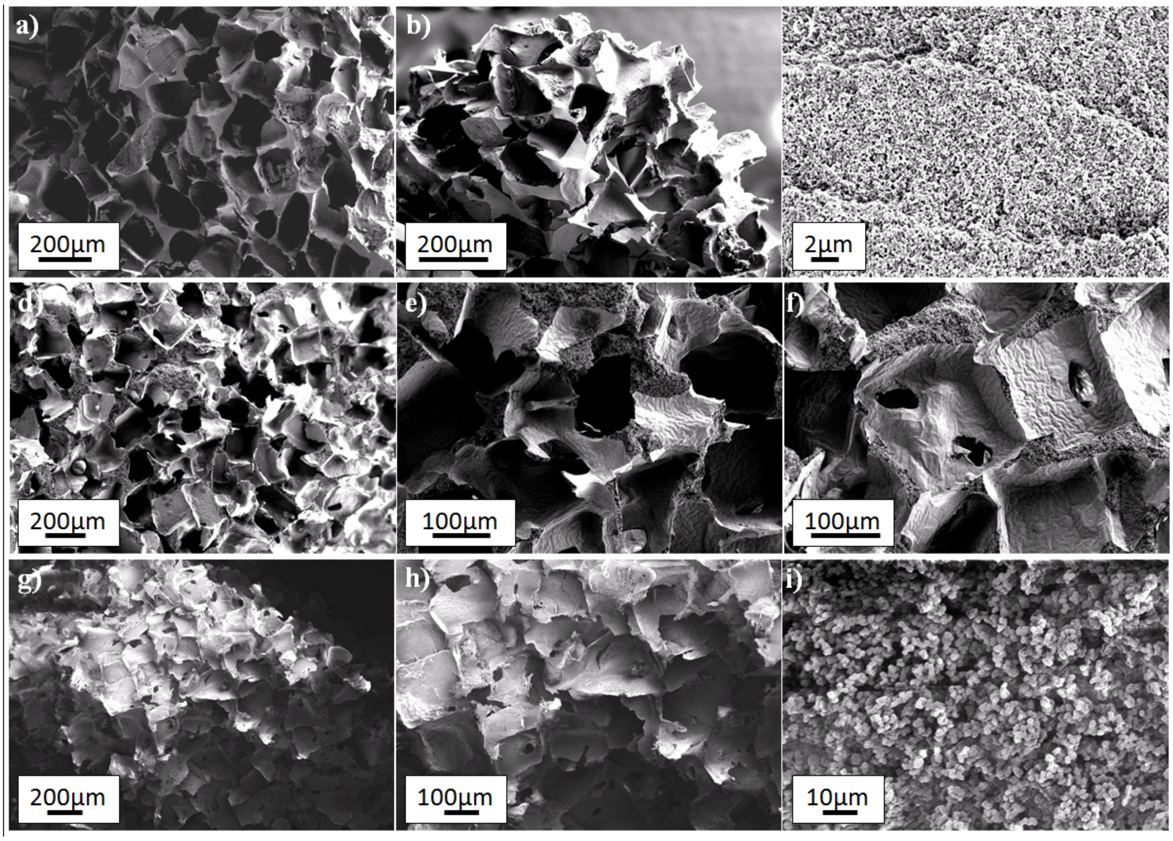

Figure 2.13: SEM micrographs of porous PHEMA-based materials: (a,b) doubly porous sample with non-interconnected macropores (70/30 mol. % HEMA/EGDMA and 75 vol. % EtOH with respect to the comonomers), (c) corresponding nanoporous network; (d,e,f) biporous sample with interconnected macropores by using NaCl template sintered at 730°C (70/30 mol. % HEMA/EGDMA and 70 vol. % *i*-PrOH); (g,h) biporous sample with interconnected macropores by using NaCl template derived from SPS treatment (70/30 mol. % HEMA/EGDMA and 80 vol. % *i*-PrOH), (i) corresponding nanoporous network.

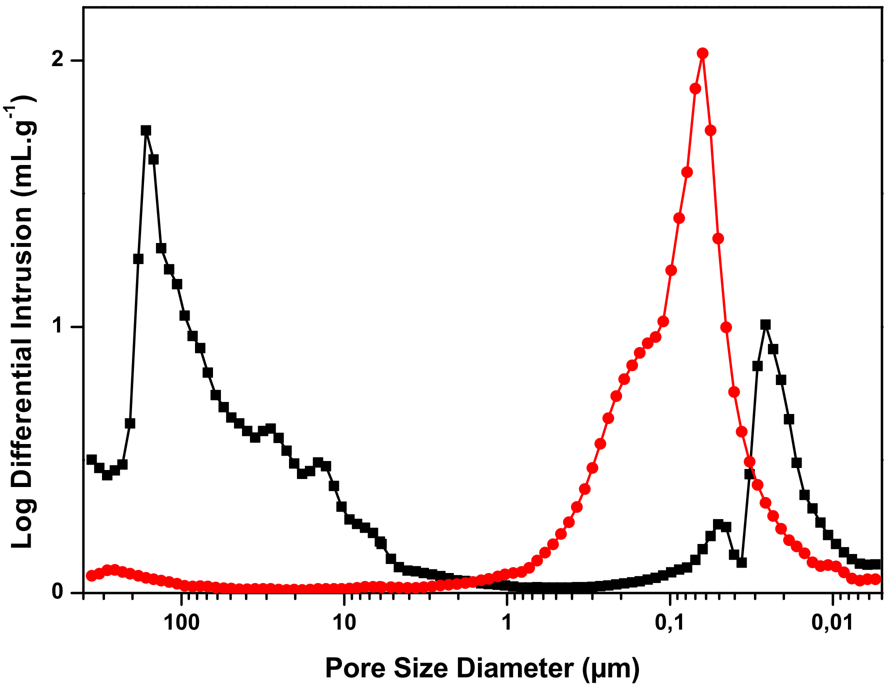

Figure 2.14: Mercury intrusion porosimetry profile of biporous PHEMA material with non-interconnected macropores prepared using NaCl particles and 75 vol. % EtOH with respect to the total volume of comonomers (HEMA/EGDMA: 70/30 mol. %). The curve associated with the biporous material was plotted (squares) along with that corresponding to the monoporous counterpart (circles).

In a second stage of the investigation of the effect of macroporogens on biporous polymeric materials, PHEMA-based materials with interconnected macropores were also analyzed by SEM (Figure 2.13.d,e,f) and MIP (Figure 2.15). As expected, the coalescence of NaCl particles gave rise to an interconnected macroporous structure after their removal. Macropores with an average diameter of about 140 μm and interconnecting voids from 5 μm to 60 μm were observed by SEM. A porogenic solvent was used, *i.e.* 70 vol. % *i*-PrOH with respect to the total comonomers volume, for the formation of the nanoporous network with pores of about 80 nm. MIP profiles corroborated the occurrence of a bimodal porosity in such materials: macropore diameter was centered at about 120 μm, while a second porosity level was found around 80 nm. These results were logical compared to those previously obtained for monoporous materials (see previous section). The original biporous material presented an 80% porosity ratio, and a macropore to nanopore volume ratio equal to 75/25 vol. %. Therefore, the higher porosity value arose not only from the use of *i*-PrOH (*i.e.* 80 % compared to 64 % with EtOH), but also from the more significant contribution of the interconnected macroporous network -due to closer particle packing- (*i.e.* 75 % compared to 70 % with EtOH).

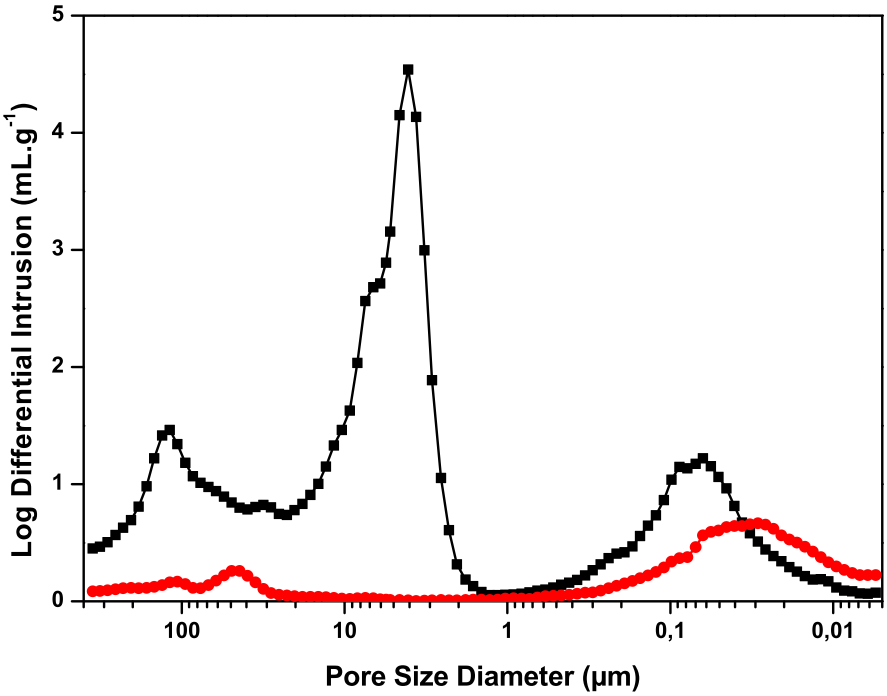

Figure 2.15: Mercury intrusion porosimetry profile of biporous PHEMA material with interconnected macropores prepared using fused NaCl template. The polymerization mixture was constituted of 70/30 mol. % HEMA/EGDMA and 70 vol. % *i*-PrOH with respect to the total volume of comonomers. The curve associated with the biporous material was plotted (squares) along with that corresponding to the monoporous counterpart (circles).

More interestingly, the MIP profile indicated some interconnectivity with a ”threshold diameter” [45] of around 5 μm (Figure 2.15), thus clearly demonstrating that one such doubly porous PHEMA material possessed interconnected macropores [46]. This is an essential point that distinguishes the interconnected macroporous materials from the non-interconnected counterparts. Such a biporous material displayed a nanoporosity in the 60-90 nm range, and it was found to be in good agreement with that of its monoporous counterpart, *i.e.* ranging from 30 to 80 nm (Figure 2.15). Again, this study demonstrated that the formation of both porosity levels was independent in the doubly porous materials, and thus highlighted the benefit of the double porogen approach using inorganic particles in conjunction with porogenic solvents.

It is worth mentioning that the fusion of NaCl cubic particles has many contact/fusion modes, namely face to face, side to side, point to point mode, etc., thus giving rise to a polymodal fused inorganic template [14]. On the contrary, the use of spherical NaCl particles or organic PMMA beads only allows for one fusion mode [39–41], so that the interconnectivity between adjacent macropores might be better controlled. Therefore, NaCl particle packing could also be an important factor to take into consideration regarding its influence on the macroporosity. Random NaCl particle packing might decrease the final macroporosity compared to packing after a simple treatment under ultrasonication that might indeed allow for a better particle compaction, thus generating less interstitial voids between adjacent particles and, as a consequence, a lower porosity ratio in the resulting PHEMA materials. Another possibility to better control the macroporosity features relies on the control of the NaCl particle dispersity. A narrow particle dispersity in the NaCl template may indeed increase the interparticular voids in comparison with a broad particle dispersity [47].

In order to investigate the effect of the macroporogen packing effect, we proposed a new approach to the sintering of NaCl particles through the use of Spark Plasma Sintering (SPS). The polymerization mixture was constituted of HEMA/EGDMA at 70/30 mol. % in conjunction with 80 vol. % *i*-PrOH with respect to the comonomers volume. SEM micrographs of the as-obtained doubly porous material are featured in Figure 2.13.g,h,i, and its MIP profile is plotted in Figure 6.19. This original biporous material displayed a macroporosity with a pore size of around 50 μm and a nanoporosity with a pore size of around 400 nm. Again, we observed an excellent agreement with the pore size of the corresponding nanoporous material prepared from the same polymerization mixture, *i.e.* centered at ∼400 nm. It is noteworthy that the pore size distribution curve presented only a bimodal distribution even though the macroporosity was interconnected. This behavior could easily be explained *via* the threshold size theory that was reported in the literature regarding MIP measurements for cement-based materials [45]. The main reason laid in the existence of the thresholds also known as interconnectivity paths. When NaCl were merely fused at 730°C, the threshold size was of about 5-10 μm: mercury flowed from the exterior of the sample to the interior, but could only deeply penetrate into the material at a reached corresponding pressure. The threshold size of the material could represent the ”point to face”, or ”point to point” sintering mode of NaCl cubic shape particles, as detailed above. In the case of SPS-mediated NaCl sintering, the threshold size of such material was much higher, likely due to the closer NaCl particle compaction resulting from the high pressure employed. The NaCl particles could then be fused within the ”face to face” or ”edge to face” sintering mode. Due to the larger threshold size, mercury fully penetrated into the material easier, thus giving only a bimodal porous distribution. Nevertheless, the MIP profile of such a material presented an underestimated average value of the macropore size. This phenomenon was also observed when working with sacrificial fused PMMA beads as macroporogens with interconnectivity or threshold diameter of about 65 μm [32]. Similar MIP profiles were also observed with polyHIPE-based porous materials in which average pore diameters were usually underestimated when compared to results obtained from SEM images [48], due to the threshold size theory.

The significant influence of the physical network constituted of SPS-compacted NaCl particles laid in the porosity of this very original biporous PHEMA material, *i.e.* 91 % porosity compared to 80 % porosity with the material obtained with classically fused NaCl particles. In addition, the contribution of the macroporosity to the overall porosity was more important than in the previous case, *i.e.* 85 % compared to 75 %.

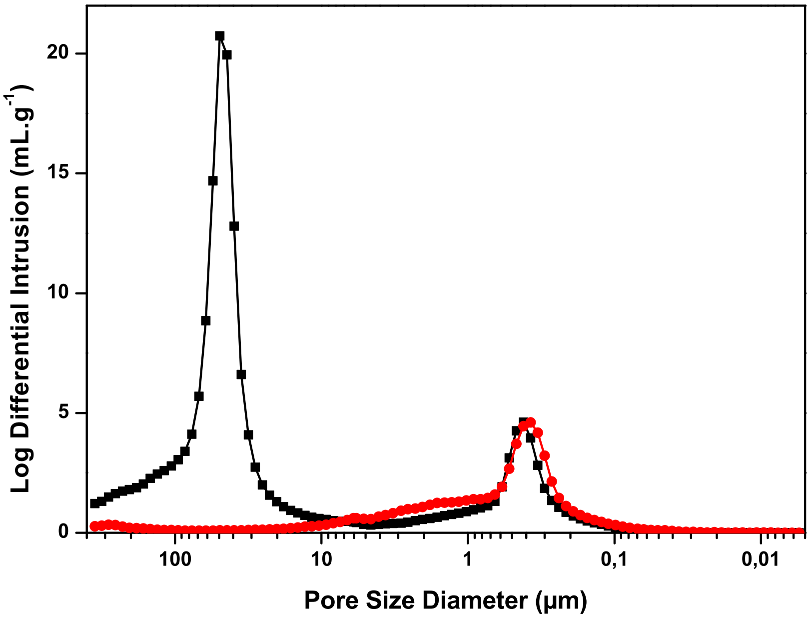

Figure 2.16: Mercury intrusion porosimetry profile of biporous PHEMA material with interconnected macropores prepared using the NaCl template resulting from SPS. The polymerization mixture was constituted of 70/30 mol. % HEMA/EGDMA and 80 vol. % *i*-PrOH with respect to the total volume of comonomers. The curve associated with the biporous material was plotted (squares) along with that corresponding to the monoporous counterpart (circles).

2.4 Conclusions

This chapter demonstrates the effectiveness and versatility of the double porogen templating approach as a facile route to control pore size, morphology and interconnectivity of doubly porous PHEMA-based materials. Such original biporous materials could successfully be engineered through the use of NaCl particles or PMMA beads as macroporogens in conjunction with a solvent as a nanoporogen. Through this approach, it is thus possible to finely tune in an independent manner nanoporosity and macroporosity. Upon removal of the porogenic agents, polymeric frameworks with double porosity were indeed obtained, and such dual porosity was confirmed by SEM and MIP characterization.

The two porosity levels could make these materials suitable for miscellaneous applications in the biomedical area in particular. These porous materials could thus constitute attractive scaffolds for tissue engineering applications as long as bioactive molecules, such as proteins or growth factors, are tethered to the pore surface. The possibility to functionalize the pore surface will be investigated so that the resulting materials might be used as potential bioreactors.

References

[1] T.-X. Lav, B. Carbonnier, M. Guerrouache, and D. Grande, “Porous polystyrene-based monolithic materials templated by semi-interpenetrating polymer networks for capillary electrochromatography,” *Polymer*, vol. 51, pp. 5890–5894, 2010.

[2] T.-X. Lav, D. Grande, C. Gaillet, M. Guerrouache, and B. Carbonnier, “Porous poly (styrene-co-divinylbenzene) neutral monolith: From design and characterization to reversed-phase capillary electrochromatography applications,” *Macromolecular Chemistry and Physics*, vol. 213, pp. 64–71, 2012.

[3] C. Yu, M. Xu, F. Svec, and J. M. Fréchet, “Preparation of monolithic polymers with controlled porous properties for microfluidic chip applications using photoinitiated free-radical polymerization,” *Journal of Polymer Science Part A: Polymer Chemistry*, vol. 40, pp. 755–769, 2002.

[4] R. Langer and J. P. Vacanti, “Tissue engineering,” *Science*, vol. 260, pp. 920–926, 1993.

[5] L. S. Nair and C. T. Laurencin, “Biodegradable polymers as biomaterials,” *Progress in Polymer Science*, vol. 32, pp. 762–798, 2007.

[6] X. Liu and P. X. Ma, “Polymeric scaffolds for bone tissue engineering,” *Annals of Biomedical Engineering*, vol. 32, pp. 477–486, 2004.

[7] J. Auriault and C. Boutin, “Deformable porous media with double porosity. quasi-statics. i: Coupling effects,” *Transport in Porous Media*, vol. 7, pp. 63–82, 1992.

[8] C. Boutin, P. Royer, and J. Auriault, “Acoustic absorption of porous surfacing with dual porosity,” *International Journal of Solids and Structures*, vol. 35, pp. 4709–4737, 1998.

[9] V. A. Santamaría, H. Deplaine, D. Mariggió, A. Villanueva-Molines, J. García-Aznar, J. G. Ribelles, M. Doblaré, G. G. Ferrer, and I. Ochoa, “Influence of the macro and micro-porous structure on the mechanical behavior of poly (l-lactic acid) scaffolds,” *Journal of Non-Crystalline Solids*, vol. 358, pp. 3141–3149, 2012.

[10] X. Liu and P. X. Ma, “Phase separation, pore structure, and properties of nanofibrous gelatin scaffolds,” *Biomaterials*, vol. 30, pp. 4094–4103, 2009.

[11] Y. Yang, J. Zhao, Y. Zhao, L. Wen, X. Yuan, and Y. Fan, “Formation of porous plga scaffolds by a combining method of thermally induced phase separation and porogen leaching,” *Journal of Applied Polymer Science*, vol. 109, pp. 1232–1241, 2008.

[12] S. Ghosh, J. Viana, R. Reis, and J. Mano, “The double porogen approach as a new technique for the fabrication of interconnected poly (l-lactic acid) and starch based biodegradable scaffolds,” *Journal of Materials Science: Materials in Medicine*, vol. 18, pp. 185–193, 2007.

[13] K. A. Gross and L. M. Rodriguez-Lorenzo, *Thermally sprayed scaffolds for tissue engineering applications*, vol. 254-2 of *Key Engineering Materials*, pp. 961–964. 2004.

[14] K. A. Gross and L. M. Rodrıguez-Lorenzo, “Biodegradable composite scaffolds with an interconnected spherical network for bone tissue engineering,” *Biomaterials*, vol. 25, pp. 4955–4962, 2004.

[15] K. Park, H. J. Jung, J. S. Son, K. D. Park, J.-J. Kim, K.-D. Ahn, and D. K. Han, “Preparation of biodegradable polymer scaffolds with dual pore system for tissue regeneration,” *Macromolecular Symposia*, vol. 249, pp. 145–150, 2007.

[16] D. Horák, H. Hlídková, J. Hradil, M. Lapčíková, and M. Šlouf, “Superporous poly (2-hydroxyethyl methacrylate) based scaffolds: preparation and characterization,” *Polymer*, vol. 49, pp. 2046–2054, 2008.

[17] J. Hradil and D. Horák, “Characterization of pore structure of phema-based slabs,” *Reactive and Functional Polymers*, vol. 62, pp. 1–9, 2005.

[18] O. Okay and Ç. Gürün, “Synthesis and formation mechanism of porous 2-hydroxyethyl methacrylate–ethylene glycol dimethacrylate copolymer beads,” *Journal of Applied Polymer Science*, vol. 46, pp. 401–410, 1992.

[19] S. Kovacic, D. Štefanec, and P. Krajnc, “Highly porous open-cellular monoliths from 2-hydroxyethyl methacrylate based high internal phase emulsions (hipes): preparation and void size tuning,” *Macromolecules*, vol. 40, pp. 8056–8060, 2007.

[20] O. Kulygin and M. S. Silverstein, “Porous poly (2-hydroxyethyl methacrylate) hydrogels synthesized within high internal phase emulsions,” *Soft Matter*, vol. 3, pp. 1525–1529, 2007.

[21] N. R. Cameron, “High internal phase emulsion templating as a route to well-defined porous polymers,” *Polymer*, vol. 46, pp. 1439–1449, 2005.

[22] N. A. Peppas *et al.*, *Hydrogels in medicine and pharmacy*, vol. 3. CRC press Boca Raton, FL, 1987.

[23] J. Yang, P. Zhang, L. Tang, P. Sun, W. Liu, P. Sun, A. Zuo, and D. Liang, “Temperature-tuned dna condensation and gene transfection by pei-g-(pmeo 2 ma-b-phema) copolymer-based nonviral vectors,” *Biomaterials*, vol. 31, pp. 144–155, 2010.

[24] K. Yamada, Y. Iizawa, J.-i. Yamada, and M. Hirata, “Retention of activity of urease immobilized on grafted polymer films,” *Journal of Applied Polymer Science*, vol. 102, pp. 4886–4896, 2006.

[25] S. L. McArthur, M. W. Halter, V. Vogel, and D. G. Castner, “Covalent coupling and characterization of supported lipid layers,” *Langmuir*, vol. 19, pp. 8316–8324, 2003.

[26] T. Lemaire, J. Kaiser, S. Naili, and V. Sansalone, “Modelling of the transport in electrically charged porous media including ionic exchanges,” *Mechanics Research Communications*, vol. 37, pp. 495–499, 2010.

[27] T. Lemaire, S. Naili, and V. Sansalone, “Multiphysical modelling of fluid transport through osteo-articular media,” *Anais da Academia Brasileira de Ciências*, vol. 82, pp. 127–144, 2010.

[28] M. Behra, S. Schmidt, J. Hartmann, D. V. Volodkin, and L. Hartmann, “Synthesis of porous peg microgels using caco3 microspheres as hard templates,” *Macromolecular Rapid Communications*, vol. 33, pp. 1049–1054, 2012. Times Cited: 17.

[29] B. Le Droumaguet, R. Lacombe, H.-B. Ly, M. Guerrouache, B. Carbonnier, and D. Grande, “Engineering functional doubly porous phema-based materials,” *Polymer*, vol. 55, pp. 373–379, 2014.

[30] B. Le Droumaguet, R. Lacombe, H.-B. Ly, B. Carbonnier, and D. Grande, “Novel polymeric materials with double porosity: Synthesis and characterization,” vol. 340, pp. 18–27, 2014.

[31] O. Okay, "Macroporous copolymer networks," *Progress in Polymer Science*, vol. 25, pp. 711–779, 2000.

[32] H.-B. Ly, B. Le Droumaguet, V. Monchiet, and D. Grande, "Designing and modeling doubly porous polymeric materials," *The European Physical Journal Special Topics*, vol. 224, pp. 1689–1706, 2015.

[33] J. Brandrup, E. H. Immergut, E. A. Grulke, A. Abe, and D. R. Bloch, *Polymer handbook*. Wiley New York, 1999.

[34] E. R.C. Weast, *Handbook of Chemistry and Physics*. Chemical Rubber Co., 1969.

[35] T. Arima, T. Hamada, and J. McCabe, "The effects of cross-linking agents on some properties of hema-based resins," *Journal of dental research*, vol. 74, pp. 1597–1601, 1995.

[36] S. Blacher, V. Maquet, R. Pirard, J.-P. Pirard, and R. Jérôme, "Image analysis, impedance spectroscopy and mercury porosimetry characterisation of freeze-drying porous materials," *Colloids and surfaces A: physicochemical and engineering aspects*, vol. 187, pp. 375–383, 2001.

[37] E. C. Peters, F. Svec, J. M. Fréchet, C. Viklund, and K. Irgum, "Control of porous properties and surface chemistry in âĂIJmoldedâĂİ porous polymer monoliths prepared by polymerization in the presence of tempo," *Macromolecules*, vol. 32, pp. 6377–6379, 1999.

[38] V. Bernabé-Zafón, A. Cantó-Mirapeix, E. F. Simó-Alfonso, G. Ramis-Ramos, and J. M. Herrero-Martínez, "Comparison of thermal-and photo-polymerization of lauryl methacrylate monolithic columns for cec," *Electrophoresis*, vol. 30, pp. 1929–1936, 2009.

[39] S. M. LaNasa, I. T. Hoffecker, and S. J. Bryant, "Presence of pores and hydrogel composition influence tensile properties of scaffolds fabricated from well-defined sphere templates," *Journal of Biomedical Materials Research, Part B: Applied Biomaterials*, vol. 96, pp. 294–302, 2011.

[40] R. B. Diego, M. P. Olmedilla, Á. S. Aroca, J. G. Ribelles, M. M. Pradas, G. G. Ferrer, and M. S. Sánchez, "Acrylic scaffolds with interconnected spherical pores and controlled hydrophilicity for tissue engineering," *Journal of Materials Science*, vol. 40, pp. 4881–4887, 2005.

[41] C. R. Kothapalli, M. T. Shaw, and M. Wei, "Biodegradable ha-pla 3-d porous scaffolds: effect of nano-sized filler content on scaffold properties," *Acta Biomaterialia*, vol. 1, pp. 653–662, 2005.

[42] W. L. Murphy, R. G. Dennis, J. L. Kileny, and D. J. Mooney, "Salt fusion: an approach to improve pore interconnectivity within tissue engineering scaffolds," *Tissue engineering*, vol. 8, pp. 43–52, 2002.

[43] J. Zeltinger, J. K. Sherwood, D. A. Graham, R. Müeller, and L. G. Griffith, "Effect of pore size and void fraction on cellular adhesion, proliferation, and matrix deposition," *Tissue engineering*, vol. 7, pp. 557–572, 2001.

[44] U.-J. Kim, J. Park, H. J. Kim, M. Wada, and D. L. Kaplan, "Three-dimensional aqueous-derived biomaterial scaffolds from silk fibroin," *Biomaterials*, vol. 26, pp. 2775–2785, 2005.

[45] K. K. Aligizaki, *Pore structure of cement-based materials: testing, interpretation and requirements*. Taylor & Francis, 2005.

[46] S. G. Lévesque, R. M. Lim, and M. S. Shoichet, "Macroporous interconnected dextran scaffolds of controlled porosity for tissue-engineering applications," *Biomaterials*, vol. 26, pp. 7436–7446, 2005.

[47] J. Reignier and M. A. Huneault, "Preparation of interconnected poly (ε-caprolactone) porous scaffolds by a combination of polymer and salt particulate leaching," *Polymer*, vol. 47, pp. 4703–4717, 2006.

[48] F. Audouin and A. Heise, “Synthesis of polymer–silica hybrid polyhipes by double in situ polymerization of concentrated water in oil emulsion,” *Polymer*, vol. 55, pp. 403–409, 2014.

Chapter 3

Tailoring doubly porous poly(2-hydroxyethyl methacrylate)-based materials *via* thermally induced phase separation

The work developed in this chapter has been the subject of one paper:

- H.B. Ly, B. Le Droumaguet, V. Monchiet, D. Grande: Tailoring doubly porous PHEMA-based materials via thermally induced phase separation, to be submitted as a regular article to *Polymer*.

3.1 Introduction

Over the last two decades, fundamental research in the field of porous materials has witnessed a tremendous expansion [1]. This widespread interest partly arises from the broad variety of applications related to these materials: indeed, they are as diversified as potential scaffolds for implantable devices [2], membranes for filtration [3] and separation [4], chemical (nano)reactors for (bio)catalysis [4, 5], as well as devices for biomedical applications [6]. Compared to their inorganic counterparts, porous polymeric materials possess some undeniable advantages. Their tunable mechanical properties are useful for various specific applications. Additionally, easy modification of their pore surface by simple organic reactions is certainly of great interest. Last but not least, their low production/fabrication cost is also an important factor if one considers future potential industrial scale-up. Finally, different porous structures and morphologies can be designed depending on the targeted application, including porous polymeric particles [7], polymer monoliths [8], thin films [2], membranes [9], and nanofibrous scaffolds [10].

Recently, doubly porous polymeric materials have attracted much interest as they offer new promising perspectives for diverse specific applications. Such biporous materials possess two different porosity levels, namely macroporosity and nanoporosity. In tissue engineering applications for instance, an interconnected macroporous network could facilitate cell seeding, profileration and differentiation, and thus guide tissue regeneration, while nanoporosity within macropore walls may modulate cell adhesion and functions in the biomaterials [11–13]. An additional lower porosity level could also improve or enhance the interconnectivity of the porous frameworks [14]. Moreover, one such nanoporosity level could significantly increase the specific surface area of the materials, like in the case of polyHIPEs [15, 16]. The specific surface area is an important parameter in such materials and plays a critical role in surface chemistry [17, 18].

In this context, different approaches to structure design and production have hitherto been reported in the literature for such biporous materials. The double porogen approach for the fabrication of poly(L-lactic acid) (PLLA) has been previously reported [14]. In this study, the authors typically used inorganic particles (NaCl) as macroporogens, and a polymer, *i.e.* poly(ethylene oxide) (PEO), as a nanoporogen, in order to improve scaffold interconnectivity. Different groups have also focused their attention on diverse porogenic solvents, such as the cyclohexanol/dodecan-1-ol solvent system [19, 20], methanol, ethanol [21], THF or hexane [22], or cyclohexanol and toluene [23–25]. Such a method provides a large range of porous polymeric scaffolds but it may have a limitation arising from particle size. Another elegant approach to producing hierarchically porous materials have recently been developed *via* High Internal Phase Emulsion (HIPE) templating [26–29]. In such a methodology, a porogenic solvent, either organic or aqueous, contributes to the formation of the macroporosity level, while interconnections between macropores (the so-called "windows") could be considered as a second porosity level. Last but not least, the combination of particle leaching and thermally induced phase separation (TIPS) can allow for the preparation of different doubly porous materials. Poly(L-lactide-*co*-glycolide)- (PLGA) [30], gelatin- [31] or PLLA- [32] based scaffolds were obtained by using either organic or inorganic particles to generate the higher porosity, while dioxane, ethanol/water or chloroform, respectively, were used as porogenic agents for the formation of a lower porosity *via* the TIPS process.

While TIPS has been applied to a limited number of bio-based polymers, manifold synthetic polymers can still be used to produce porous frameworks with unique properties *via* this methodology. In this paper, we thoroughly describe an unprecedented TIPS route for the preparation of doubly porous poly(2-hydroxyethyl methacrylate) (PHEMA)-based biocompatible materials. A co-solvent mixture constituted of dioxane and water is used to solubilize previously prepared linear PHEMA, following a solidification process by freezing the solvents/PHEMA mixture, and subsequent sublimation of the solvents to generate the corresponding porous PHEMA materials. The obtained porous PHEMA display different morphologies: either monoporous or biporous materials can thus be prepared. Our interest mainly focuses on materials with a bimodal porosity. The macroporosity with pores having a cylindrical shape lies in the 10-100 μm range while various nanoporous structures are found within the macropore walls. Pore size and morphology of the porous structures can be finely controlled by varying the cooling rate, by varying the co-solvent mixture ratio, or by adjusting the polymer concentration of the solvents/PHEMA mixture. The porosity of the as-obtained porous frameworks is carefully examined by means of scanning electron microscopy (SEM), and mercury intrusion porosimetry (MIP) so as to clearly determine the crucial parameters affecting the porous characteristics of the resulting doubly porous PHEMA-based materials.

3.2 Experimental

3.2.1 Materials

2-hydroxyethyl methacrylate (HEMA, 97%), 2,2'-azobis(2-methylpropionitrile) (AIBN, 98%), glutaryl chloride (97 %), terephthaloyl chloride(>99 %), and dodecanedioyl dichloride(98 %) were purchased from Aldrich. Absolute ethanol (EtOH, 99%, SDS), cyclohexane (99.8%), 1-4 dioxane (99.9%), dichloromethane (CH_2Cl_2) were supplied by Carlo Erba. All chemicals and solvents were used without any further purification procedure, except for AIBN that was recrystallized from methanol and stored at 4°C prior to use.

3.2.2 Preparation of linear PHEMA

0.1 g AIBN (1% wt/wt with respect to the monomer) was added to a solution of HEMA (10 g) in 100mL of EtOH. The resulting mixture was homogeneously stirred. Following a thermally-induced conventional free-radical polymerization conducted at 70°C overnight, the resulting slightly viscous solution was added dropwise in an important amount of dichloromethane (CH_2Cl_2) so as to precipitate linear PHEMA. After filtration and drying under vacuum, the pure product was obtained as a colorless powder. Linear PHEMA was then stored in moisture-free conditions prior to the generation of porous materials. The sample was characterized by SEC with DMF as the eluent: M_n=100.000 g.mol^{-1} and $M_w/M_n = 2.3$.

3.2.3 Polymer-solvent phase diagram by turbidimetry

The temperature-composition phase diagrams of PHEMA solutions in a water/1,4-dioxane mixture were determined by visual turbidimetry. A test tube was filled with the polymer solution at different concentrations and sealed under vacuum in order to keep the composition constant over the whole temperature range. The test tube was then immersed in an acetone bath, the temperature of which was decreased at a cooling rate of 1°C.min^{-1}. Solutions of linear PHEMA in a water/1,4-dioxane mixture were prepared depending on the polymer concentration (0.5, 1, 1.5, 2.5, and 5% (wt/v) and immediately analyzed. The water/1,4-dioxane volume ratio was also varied from 78/22 to 10/90 vol.%, respectively. The phase diagram was plotted as a function of temperature and of the volume ratio of the solvents with different concentrations of PHEMA.

3.2.4 Preparation of porous PHEMA

Linear PHEMA (with increasing mass/volume ratios: 0.5, 1, 1.5, 2.5, and 5% (wt/v), respectively) was homogeneously mixed with the co-solvent mixture constituted of water/1,4-dioxane (78/22, 50/50, or 10/90 vol.%) at room temperature, before being transferred into glass vials. The latters were immediately quenched at different temperatures, either in a freezer at -18°C, in an acetone/ice bath (-80°C) or in liquid nitrogen (-196°C) to induce the phase separation. This phase separation technique followed by a subsequent solvent sublimation process allowed for the generation of porous PHEMA frameworks. The phase separated polymer frameworks were freeze-dried under vacuum (1 mm Hg) at room temperature for 2 days to completely remove the porogenic solvents. Gravimetric analysis of each sample, after freeze-drying, was used to confirm the complete removal of the solvents.

3.2.5 Chemical cross-linking reaction of PHEMA

In a glass vial, 2 mL of cyclohexane in which were dissolved 5 equiv. of desired acyl dichloride with respect to the total hydroxyl groups were stirred until a transparent solution was obtained. 10 mg of PHEMA were then added to the previously prepared solution containing the selected acyl dichloride cross-linking agent. The vial was gently agitated on an orbital shaking plate overnight at 150 rpm. The sample was then washed with cyclohexane several times and dried under vacuum. IR spectroscopy was used to confirm the effectiveness of the covalent cross-linking of porous PHEMA.

3.2.6 Instrumentation

SEM investigations of the materials was performed on a MERLIN microscope from Zeiss equipped with InLens and SE2 detectors using a low accelerating tension (2-3 kV) with a diaphragm aperture of 30 μm. The samples were first cryofractured and coated with a 4-nm layer of palladium/platinum alloy in a Cressington 208 HR sputter-coater. Average pore diameters were determined using the ImageJ 1.47v software.

The porosity ratios, pore volumes, and pore size distributions of the materials were determined by mercury intrusion porosimetry (MIP) using an AutoPore IV 9500 porosimeter from Micromeritics. The determination of the porosity features was based on the Washburn equation between the applied pressure (from 1.03 to 206.8 MPa) and the pore diameter into which mercury intruded.

FTIR spectra were recorded using a Bruker Tensor 27 DTGS spectrometer in attenuated total reflection (ATR) mode between 4000 and 450 cm^{-1} with an average of 32 consecutive scans and a resolution of 4 cm^{-1}.

3.3 Results and discussion

The present studies thoroughly describe an unprecedented route to generate biporous PHEMA materials *via* thermally induced phase separation, as depicted in Figure 3.1. Although this process is complicated to understand, hierarchical biporous PHEMA can successfully be generated with high porosity and controllable pore architecture, depending on the thermodynamic and kinetic behaviors of precursor polymeric solution under various experimental conditions [33, 34]. Thermally-induced phase separation can generally be divided into two main processes: solid-liquid phase separation and liquid-liquid phase separation. For a polymer/solvent(s) mixture in which the solvent(s) crystallization temperature is higher than the liquid-liquid phase separation temperature, the system can phase separate when lowering the temperature, and should be called solid-liquid phase separation [35]. On the contrary, if the crystallization temperature of the solvent(s) is lower than the phase separation temperature, a liquid-liquid phase separation process takes place when the temperature of the polymer/solvent(s) decreases [35].

2-hydroxyethyl methacrylate (HEMA) is considered as a monomer of choice for biomedical applications, not only due to its intrinsic biocompatible properties but also because of its ability to be further functionalized with (bio)molecules of interest to promote cell adhesion, proliferation, and differentiation in tissue engineering or drug delivery applications [36–40]. 1,4-dioxane and water are solvents commonly used in TIPS processes. An interesting behavior of linear PHEMA in the water/1,4-dioxane co-solvent system is observed: the polymer is insoluble in each of the two liquids individually, but it has been shown that co-solvency exists. Linear PHEMA is thus soluble in the mixture of water/1,4-dioxane with a water proportion ranging from 10 to 78 vol.% [41, 42]. Like water, 1,4-dioxane is a relatively high melting point solvent (about 11.8°C), thus it can facilitate the freeze-drying step during the TIPS process.

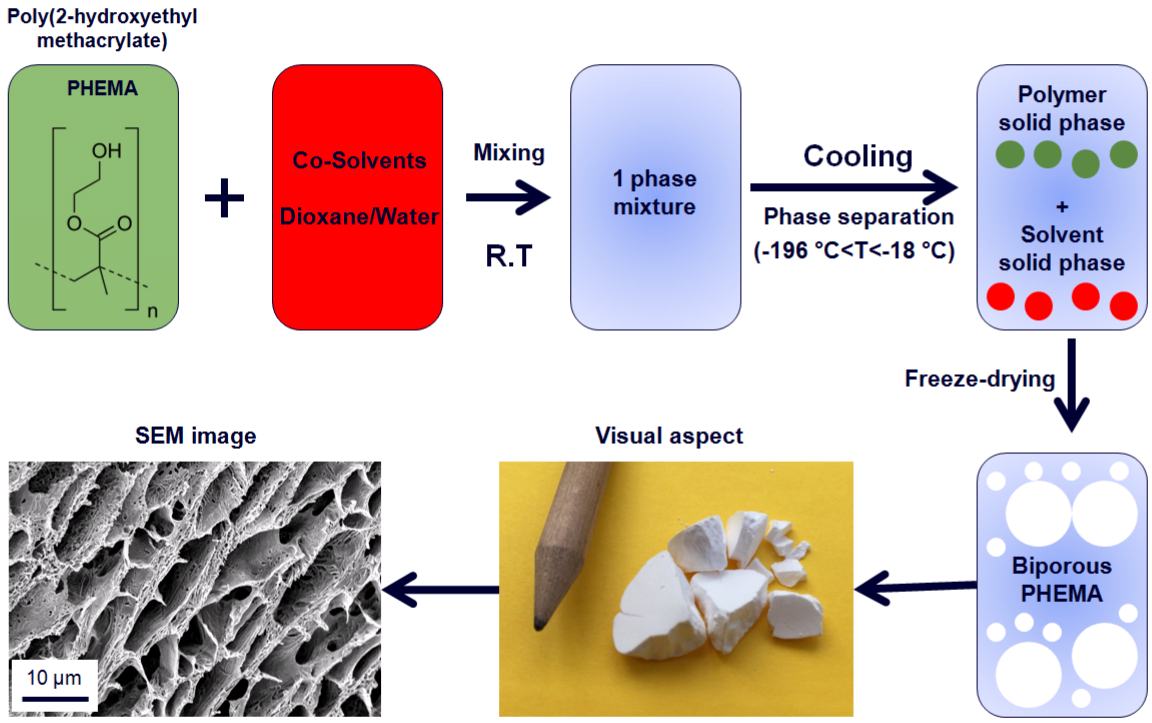

Figure 3.1: Sequence for the fabrication of porous PHEMA by thermally induced phase separation.

3.3.1 Polymer-solvent phase diagram

First, it is crucial to determine the phase separation mechanism when cooling down the temperature of the PHEMA/co-solvents (water/dioxane) mixture. Generally, a system consisting of a polymer in its solvent generates a solid-liquid phase separation [43]. When a non-solvent of this polymer is introduced in the solvent mixture, this likely induces a liquid-liquid phase separation [44]. Water or 1,4-dioxane were non-solvents for linear PHEMA, but some mixtures of both solvents could solubilize the polymer.

It was thus important to analyze the melting points of each system constituted of PHEMA and water/1,4-dioxane co-solvent mixture to verify whether the solvents were crystallized before, or on the contrary, to determine the critical point of the liquid-liquid phase separation. A phase diagram of the water/1,4-dioxane co-solvent system was determined after investigation of the different systems studied (Table 3.1). In all cases, it was demonstrated that the cloud points of the polymer/co-solvent system corresponded to the melting point of the corresponding co-solvent mixture, and did not depend on the PHEMA concentration in the polymer/co-solvents mixture systems. This process was determined by visual turbidimetry with a cooling rate of 1°C.min^{-1}. However, a cooling rate of 0.1°C.min^{-1} might be ideal for a clear visual detection of cloud points [45]. As a conclusion, the TIPS process herein investigated took place according to a solid-liquid phase separation.

Table 3.1: Cloud point values associated with different volume ratios of the water/dioxane co-solvent mixture.

Water/dioxane ratio (vol.%)	100/0	78/22	50/50	10/90	0/100
Cloud point (°C)	0	-6.5	-12	3	11.5

3.3.2 Preliminary results

Some preliminary results were first achieved when the polymer-solvents mixtures were slightly cooled down to -18°C in a freezer before freeze-drying. Two different polymer concentrations were used in this case in order to observe the influence on the morphology of the resulting porous structures. When 1% (wt/v) polymer concentration (1 g of polymer/100 mL water/dioxane: 78/22 vol.%, respectively) was used, no mechanically stable framework was obtained (Figures 3.2.a and 3.2.b). The obtained structure was likely in chain folded lamellae shape, with average diameter of 3 μm, as observed by SEM (Figure 3.2). This structure was unstable, due to precipitation of individual polymer chains after solvent sublimation. Some different areas in these materials also displayed different distinct morphologies, with irregular structures (data not shown), likely due to relatively low cooling rate (*i.e.* at -18°C). Indeed, when the phase separation occurred, the heat flow and thus the flow rate was rather more pronounced on the exterior part of the vial than in the center of the sample. It was shown that the 78/22 vol.% of water/dioxane mixture crystallized at about -7°C. Therefore, the applied temperature gradient was not low enough to instantly freeze the sample, thus giving rise to an inhomogeneous porous PHEMA structure.

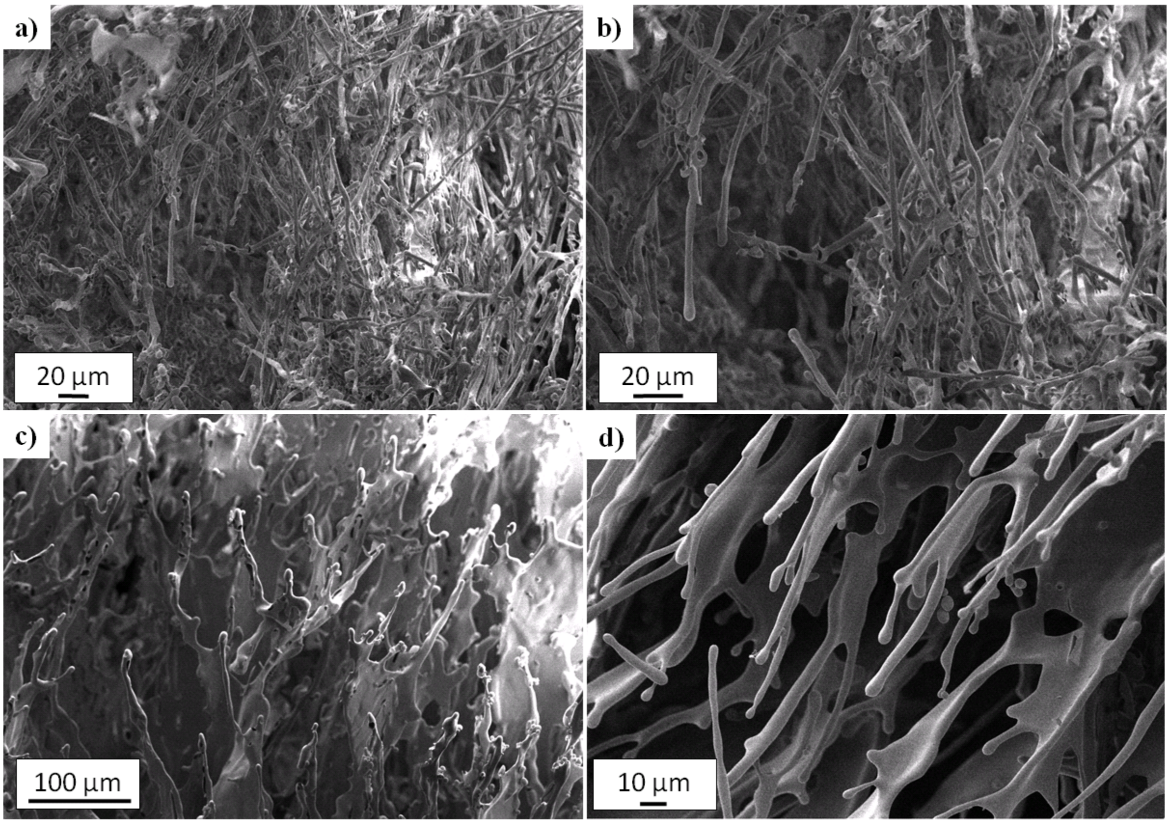

Figure 3.2: SEM micrographs of porous PHEMA prepared by TIPS at -18°C: (a), (b) 1% (wt/v) of polymer concentration; (c), (d) 2.5% (wt/v) of polymer concentration. The co-solvent mixture contained 78/22 vol.% of water/dioxane.

The exterior part of the sample located on the edge of the vial presented a kind of lamellar shape framework while the structure of the interior part was rather inhomogeneous and dense, thus less porous. A similar structure was also displayed with a polymer concentration of 2.5% (wt/v) (Figure 3.2.c and 3.2.d). In this case, a higher polymer concentration resulted in a connected polymer phase with basically the same morphology as that of the previous case. An inhomogeneous structure in the interior part compared to the exterior part of the sample was also observed, thus confirming our suggestion mainly based on the too slow cooling rate of the polymer/porogenic solvents mixture. Furthermore, when decreasing the temperature of the polymer/solvents system, the solvents were crystallized before the solid-liquid phase separation took place. During this process, the polymer phase was expelled from the crystallization front as impurities [46]. This could be another reason accounting for an inhomogeneous structure between the exterior part of the sample and the interior part: due to the slow cooling rate of the precursor polymer/porogenic solvent mixture, PHEMA was slowly expelled out of the crystallized solvents phase, and became denser inside the sample. It is noteworthy that these obtained morphologies had similarities to those of materials resulting from the phase separation process involved in polymer crystallization, with semi-crystalline polymers consisting of molecules with sufficient regularity in the chains [34]. The morphologies obtained in the latter case strongly depended on the polymer concentration: at very low concentration, some single crystals could be obtained, while at higher concentration, the morphology looked like lamellar stacks (similar to morphologies obtained in Figure 3.2).

3.3.3 Effect of quenching temperature

The quenching temperature is an important factor that may influence the porous structure obtained by the TIPS methodology. It is worth mentioning that the term ”quenching temperature” in our case represented the phase separation temperature, when the PHEMA/water/dioxane mixtures were cooled down. In other words, the cooling rate applied by plunging the mixtures into cryogenic medium allowed for the crystallization of the polymer/co-solvents mixtures. The lower the quenching temperature, the higher the cooling rate. In order to analyze the cooling rate effect on the phase separation process, the quenching temperature was set to -80°C and -196°C. Thus, PHEMA samples with a 2.5% (wt/v) concentration in a water/1,4-dioxane mixture (78/22 vol.%) were rapidly quenched in an acetone/ice bath (with measured temperature of -80°C), or in liquid nitrogen. SEM images of the resulting samples at a -80°C quenching temperature are gathered in Figure 3.3.a and 3.3.b. It is interesting to notice that homogeneous and stable porous PHEMA frameworks were obtained, contrary to the case at -18°C. Additionally, two distinct porosities appeared in these samples: the larger one was found between 10 and 100 μm, while the lower one lied in a 100-1000 nm range within the macropore walls. According to the SEM micrographs, the porous structures seemed highly interconnected. The larger porosity had a tubular morphology and an internal ladder-like structure, mainly based on the solvent crystallization (Figure 3.3.a), while the lower porosity had a fiber-like structure (Figure 3.3.b). A similar structure was also displayed with the same polymer concentration of 2.5% (wt/v) in liquid nitrogen (Figures 3.3.c and 3.3.d). There was no significant difference between the macroporosity of samples obtained from a 2.5% (wt/v) PHEMA concentration in 78/22 vol.% water/dioxane after cooling in liquid nitrogen or acetone ice bath. The macroporosity of both frameworks were anisotropic and tubular-shaped. This typical morphology was also well-documented in the literature [44, 46–50]. In the case of quenching temperature at -80°C, macropore diameters were in the range of 5-10 μm, while in the case of -196°C as a quenching temperature, they were in the range of 2-6 μm. At the lower porosity level, the nanopores of the as-obtained material at -196°C were larger than those of the corresponding materials at -80°C (*i.e.* around 800 nm and 400 nm, respectively). MIP profiles, plotted in Figure 3.4, also confirmed this observation: the nanoporosity of PHEMA at -80°C with a 2.5% (wt/v) of polymer concentration was close to 500 nm, and that of the corresponding PHEMA obtained with liquid nitrogen was centered on 1 μm.

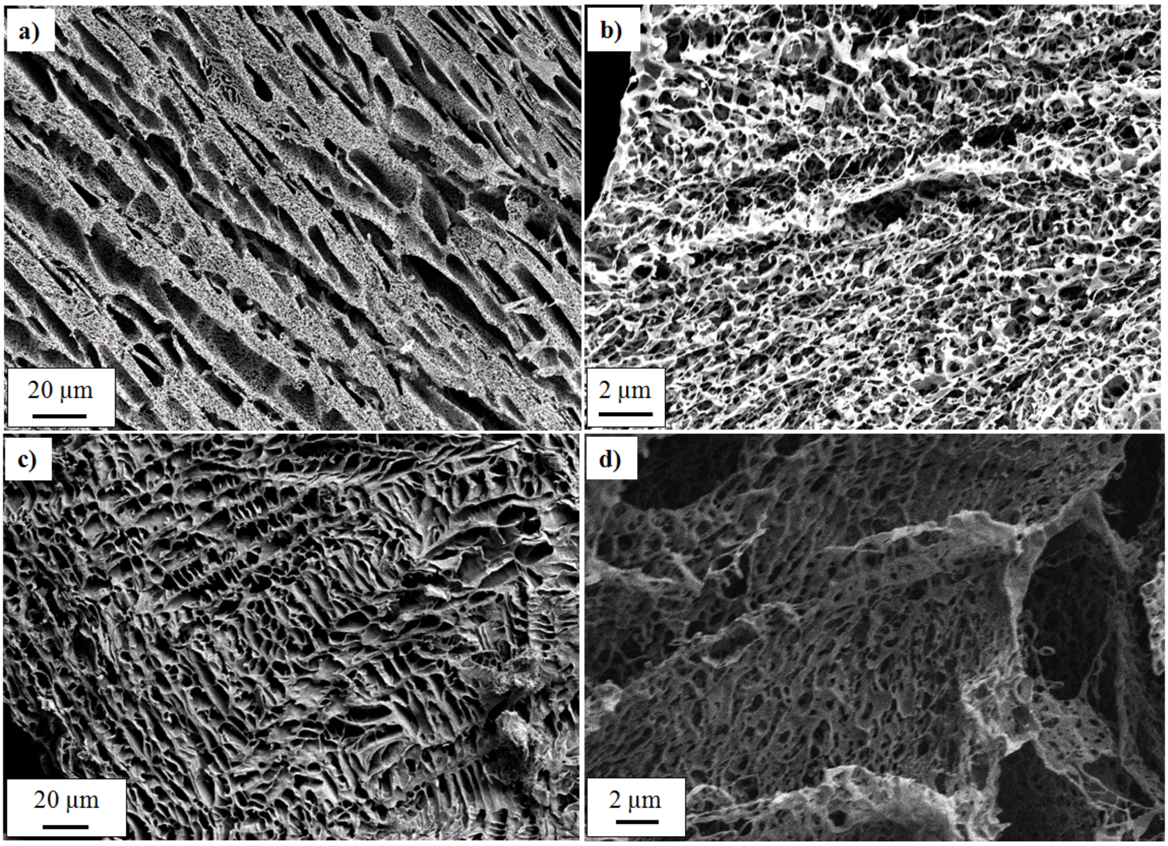

Figure 3.3: SEM micrographs of porous PHEMA samples prepared by TIPS at 2.5% (wt/v) of polymer concentration: (a), (b) cooling to -80°C; (c), (d) cooling to -196°C. The co-solvent mixture contained 78/22 vol.% of water/dioxane.

The macropore size distribution was rather broad, ranging from 10-100 μm, even if different polymer concentrations were assessed (data not shown). This could be likely explained by the basic principle of mercury intrusion porosimetry, and especially by the Washburn equation [51]. This mathematical equation estimates the diameters of pores based on a longitudinal penetration of mercury into cylindrical tubes. Macropores observed from SEM images had cylindrical shapes of $\sim$100 μm length and $\sim$10 μm diameter, strongly depending on the solvent solidification direction. Figure 3.3.a could illustrate the pore size of about 100 μm, observed from MIP profiles, when mercury penetrated *via* a transversal direction through cylindrical pores. Figure 3.3.d depicted the cross-section of macropores, whose diameters lied in the 10 μm range. In this case, longitudinal mercury penetration accounted for several peaks around 10 μm obtained from MIP measurements. Due to the highly anisotropic morphology of the porous PHEMA structures, MIP profiles resulted in a rather broad macroporosity. In addition, it should be stressed that the as-obtained materials had a very high porosity ratio around 85%–90%.

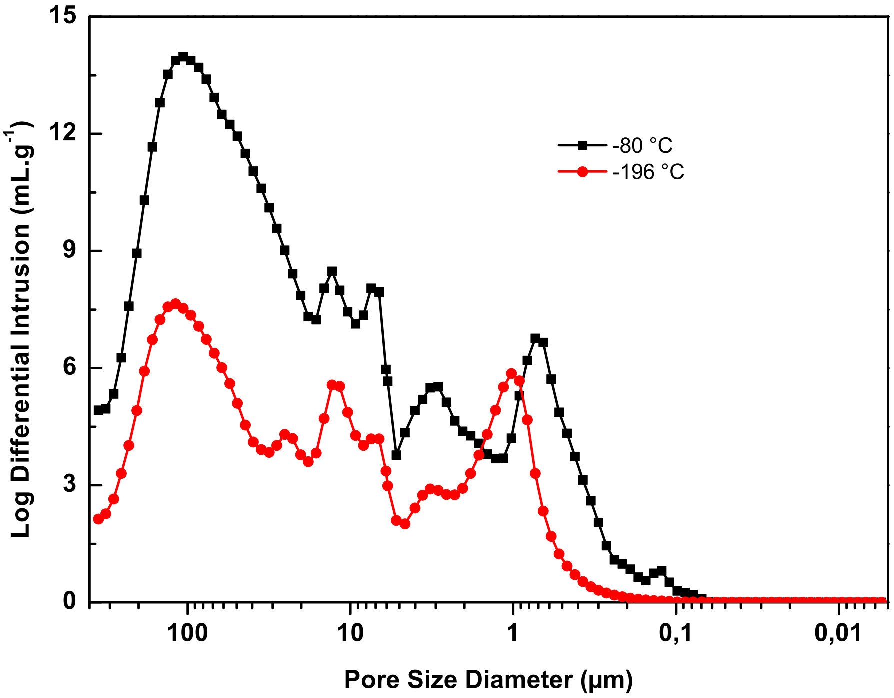

Figure 3.4: Mercury intrusion porosimetry profiles of porous PHEMA material prepared using 2.5% (wt/v) of polymer concentration at different quenching temperatures. The co-solvent mixture contained 78/22 vol.% of water/dioxane.

As a conclusion, stable biporous frameworks can only be prepared when the quenching temperature is low enough to instantly freeze the polymer/co-solvents mixture. A lower quenching temperature was generally associated with a lower macroporosity and a higher nanoporosity.

3.3.4 Effect of co-solvent mixture ratio

The lower porosity structure within the macropore walls of the as-obtained biporous materials were not fully understood at this stage. Nam et al. [52] notably reported on a nanoporous array observed at the surface of macropores in PLLA, PLGA or poly(D,L-lactide)(PLA) systems with dioxane/water. The authors suggested that this particular morphology was derived from the coarsening process after a liquid-liquid phase separation of the polymer/solvents system. With a hybrid system based on PLLA with dioxane/water, Wei et al. [44] also found out that the coarsening effect might contribute to the formation of a nanoporous phase in addition to the macropores. However, to the best of our knowledge, no systematic investigation has hitherto been studied for the formation of a double porous structure.

In order to fully understand the role of each solvent in the co-solvent system, three different water/dioxane volume ratios were used, namely 78/22, 50/50, and 10/90 vol.%, respectively. The polymer concentration was kept constant at 1% (wt/v) and the quenching temperature was set to -196°C (in liquid nitrogen). As expected, the macroporous phase of porous PHEMA kept its tubular shape or ladder-like structure in all the cases (Figure 3.5).

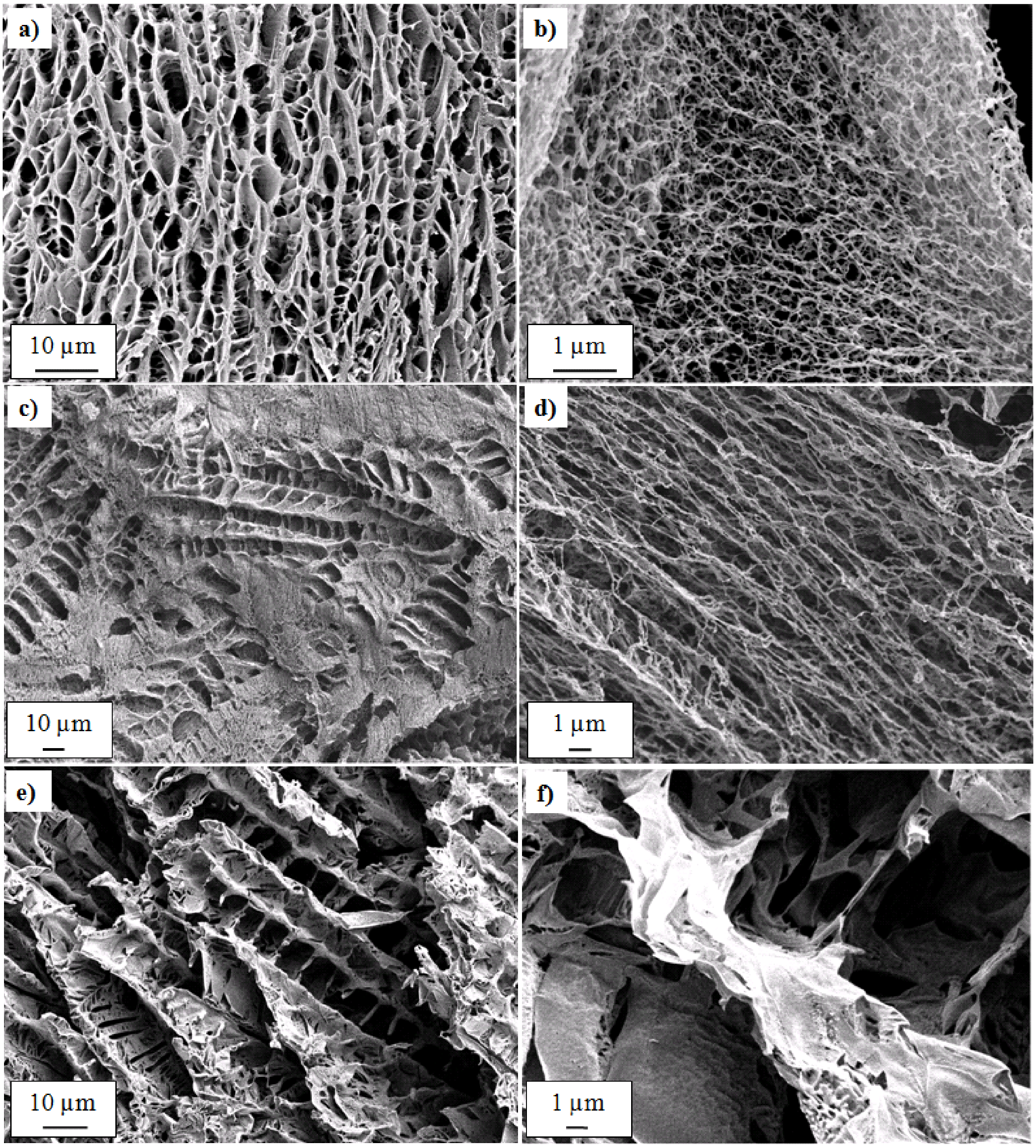

Figure 3.5: SEM micrographs of porous PHEMA prepared at 1% (wt/v) of polymer concentration by TIPS at -196°C with different water/dioxane volume ratios: (a), (b) 78/22 vol.%; (c), (d) 50/50 vol.%; (e), (f) 10/90 vol.%.

The porous PHEMA framework obtained with 78/22 vol.% water/dioxane exhibited a nanofibrous structure within macropore walls, with nanofibers diameters ranging from

50 to 100 nm (Figures 3.5.a and 3.5.b). When comparing to the PHEMA framework obtained with 50/50 vol.% water/dioxane, the macroporous structure appeared more compact in the latter case (Figure 3.5.c). Nevertheless, a regular nanofibrous structure was also observed in this case (Figure 3.5.d). Such a nanofibrous structure seemed also well-oriented, with nanofiber diameters ranging from 200 to 250 nm. The porous PHEMA framework obtained with 10/90 vol.% water/dioxane showed a highly regular ladder-like macroporous structure (Figures 3.5.e and 3.5.f), while only a very small amount of nanopores were observed in this case. According to MIP measurements, porosity ratios around 85–90% was determined in all the samples, along with broad macropore size distributions (Figure 3.6).

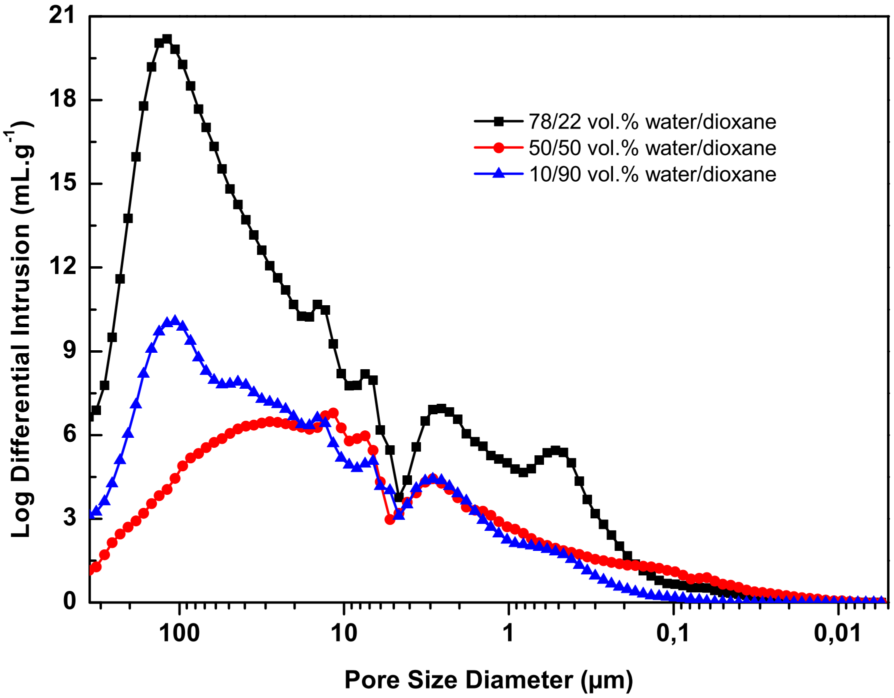

Figure 3.6: Mercury intrusion porosimetry profiles of porous PHEMA materials prepared using 1% (wt/v) of polymer concentration in different mixtures of water and dioxane. The quenching temperature was set to -196°C.

Samples with 78/22 and 10/90 vol.% water/dioxane presented a macroporosity centered around 100 μm, while it was around 30 μm with the specimen derived from 50/50 vol.% water/dioxane. Interestingly, the samples with 10/90 vol.% water/dioxane possessed nanopores of diameters higher than 100 nm, while the homologue samples with 78/22 and 50/50 vol.% water/dioxane displayed much smaller nanopores with diameters down to about 40 nm. These observations clearly demonstrated that water in the co-solvent mixture played a major role in the generation of the nanoporous phase in PHEMA frameworks synthesized by TIPS. A higher water volume proportion in the water/dioxane ratio favored the formation of nanopores, thus introducing a second porosity level in addition to the macroporosity level associated with PHEMA materials. On the other hand, the 1,4-dioxane contribution to the co-solvent mixture was important regarding macropore morphology. It is noteworthy that a similar system of polymer/co-solvents (*i.e.*, PMMA using a co-solvent mixture of water/EtOH) was recently disclosed [53]. Nonetheless, the authors reported on porous monoliths with a sole porosity level. As a conclusion, the interactions between the co-solvents and the polymer, so in turn the co-solvent volume ratio, were critical to produce well-defined biporous PHEMA structures.

3.3.5 Effect of polymer concentration

In this section, we analyzed the effect of polymer concentration on biporous PHEMA materials. Firstly, it was observed that the use of a low quenching temperature led to a stable porous structure (*i.e.*, either in acetone ice bath or in liquid nitrogen). Secondly, the use of liquid nitrogen led to a more controllable porosity framework, due to a shorter time of solidification of the polymer/co-solvent mixture. We thus used -196°C as a reference quenching temperature. Various PHEMA samples of different concentrations (0.5, 1.5, and 5% (wt/v)) with 78/22 vol.% co-solvent mixture of water/1,4-dioxane were rapidly quenched into liquid nitrogen. Following a second step of co-solvent sublimation, the as-obtained porous samples were then investigated. SEM micrographs of the biporous samples generated with different polymer concentrations are presented in Figure 3.7. Obviously enough, the macroporosity of the porous frameworks was anisotropic (Figures 3.7.a, 3.7.c, and 3.7.e). The temperature gradient along the solidification direction (from sample surface to sample center) might have led to such highly anisotropic porous structures. However, as mentioned above, the macroporous morphology only depended on the solvent crystallization, and was suggested to be attributed to 1,4-dioxane. Along with 1,4-dioxane gelation, the PHEMA solution was expelled to the outside of the crystallites, thus forming highly reproducible ladder-like 3-D regular porous structures. A second porosity level was observed within the polymer walls. We suggested that the use of an easily freeze-dried co-solvent system had a non-negligible influence on the final morphology of the porous PHEMA structures. After the expulsion of PHEMA solutions from dioxane crystallites, water left from the mixture created a second porosity level.

The nanoporous PHEMA framework prepared from 5% (wt/v) of polymer concentration possessed a small amount of nanopores within the macropore walls (Figure 3.7.b), with sizes around several μm. In contrast, the sample prepared from 2.5% (wt/v) of PHEMA concentration contained a well-defined nanoporous phase whose size ranged from 500 nm to 1 μm (see Figure 3.3.d).

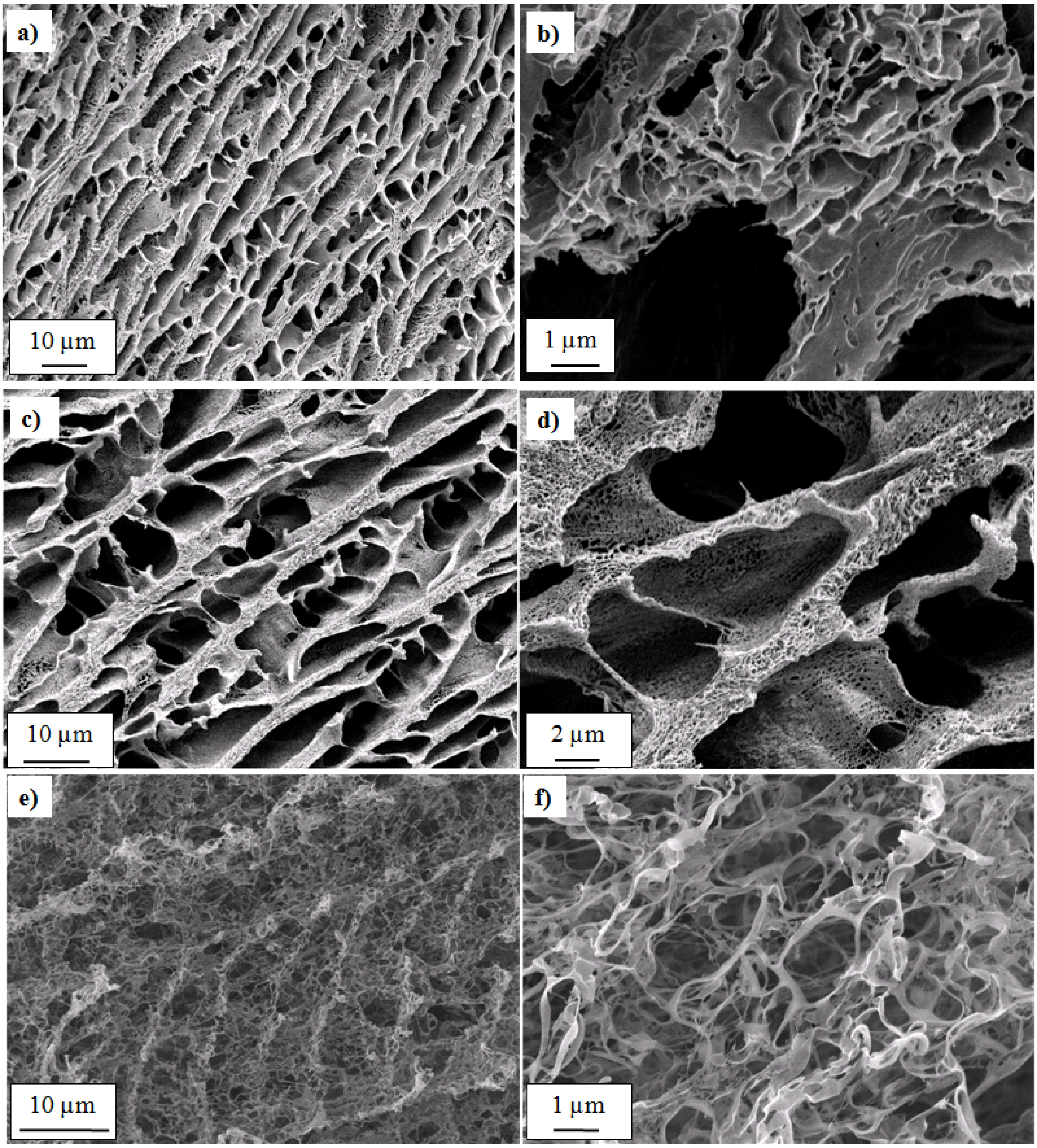

Figure 3.7: SEM micrographs of porous PHEMA prepared by TIPS at -196°C with a co-solvent mixture ratio of water/dioxane equal to 78/22 vol.%: (a), (b) 5% (wt/v) of polymer concentration; (c), (d) 1.5% (wt/v) of polymer concentration; (e), (f) 0.5% (wt/v) of polymer concentration.

When the PHEMA concentration was decreased to 1.5% (wt/v), the nanoporosity within the macropore walls was smaller than that associated with higher polymer concentrations. The nanopores ranged from 100 to 200 nm. These observations were confirmed by MIP analysis of the PHEMA porous frameworks obtained by using different polymer concentrations (Figure 3.8). Pores of a few tens of nanometers (down to 30 nm) were indeed evidenced when a PHEMA concentration of 1.5% (wt/v) was used. Such observations were also made when a quenching temperature of

-80°C was used (data not shown).

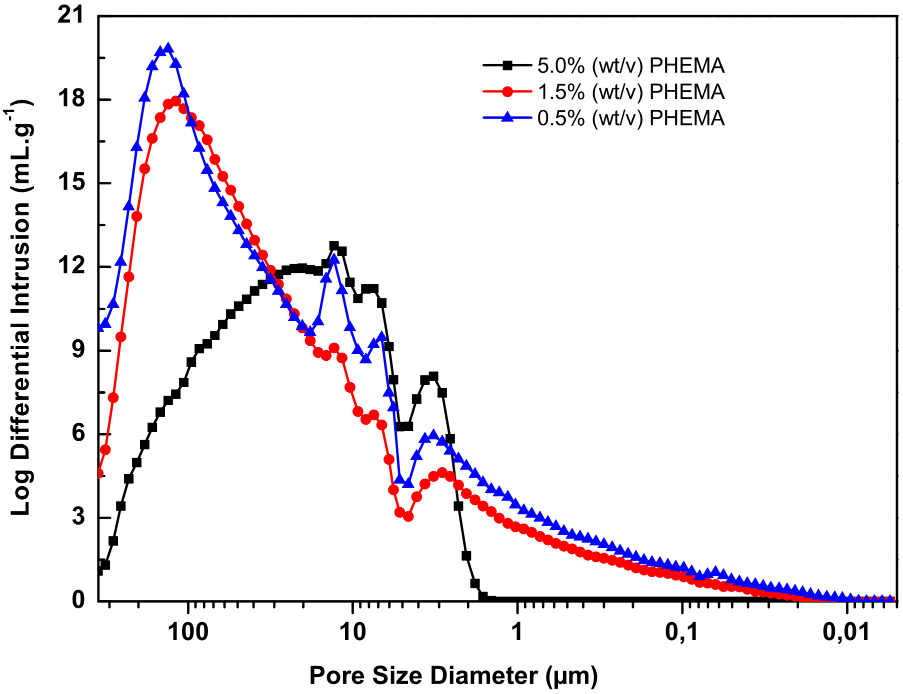

Figure 3.8: Mercury intrusion porosimetry profiles of porous PHEMA materials prepared using different polymer concentrations with a 78/22 vol.% co-solvent mixture of water/dioxane. The quenching temperature was set to -196°C.

Again, the biporous materials synthesized from TIPS presented very high porosity ratio values (from 85 up to 95%), according to MIP measurements. Such values were in excellent agreement with the total volume ratios of co-solvents used in the co-solvent/polymer systems. Figures 3.7.e and 3.7.f illustrate the porous PHEMA framework obtained from a 0.5% (wt/v) polymer concentration. Interestingly, a mechanically unstable nanofibrous structure was formed, mainly due to the high dilution related to the co-solvent/polymer system used.

As a conclusion, the polymer concentration also had a significant influence on the morphology of biporous PHEMA frameworks, essentially on the nanoporosity level. A lower polymer concentration was associated with lower nanopore sizes. When the PHEMA concentration was lower than 1% (wt/v), a nanofibrous structure with fiber diameters ranging from several nanometers to several hundreds of nanometers was produced.

3.3.6 Chemical cross-linking of PHEMA structure

Since porous PHEMA frameworks engineered by TIPS had really poor mechanical stability, it seemed necessary to cross-link them for further potential applications. As linear PHEMA was rather hydrophilic, the solvent choice was critical: too polar solvents might induce swelling of the as-formed PHEMA porous matrices, and thus led to porosity collapse. A few solvents, including dichloromethane, tetrahydrofuran (THF), toluene, and cyclohexane, were used to investigate the possibility of chemical cross-linking of such PHEMA porous frameworks. The obtained fibrous structures collapsed in the case of CH_2Cl_2, THF, toluene after chemical cross-linking. To maintain the porous structures, especially the nanofibrous features, cyclohexane was chosen as a solvent of choice as its polarity was relatively low and should in principle avoid any porous framework collapse. The reaction media were cooled down to 5°C (working in ice bath), taking into account that reactions between hydroxyl groups of PHEMA and acyl chloride were exothermic. The reaction scheme is depicted in Figure 3.9.

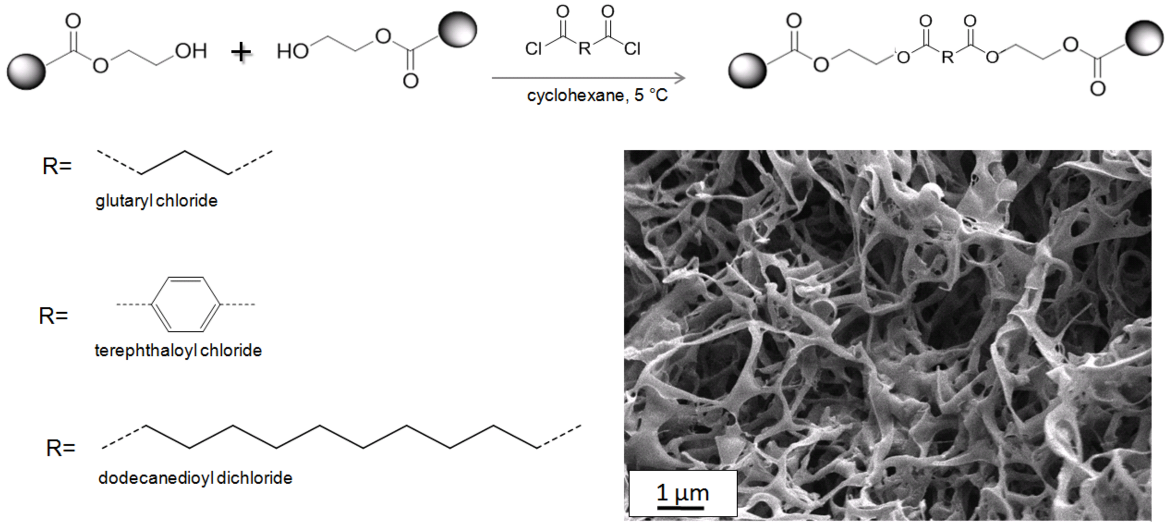

Figure 3.9: Chemical reaction associated with cross-linking of porous PHEMA structure prepared by TIPS. The inset displays a typical SEM micrograph of a cross-linked porous PHEMA-based structure.

Successful chemical cross-linking of PHEMA was demonstrated by SEM analysis. The porous PHEMA sample prepared from 0.5% (wt/v) of polymer concentration was examined before (Figure 3.7.f) and after cross-linking reaction with terephthaloyl chloride (Figure 3.9). Obviously, the nanofibrous structure was successfully retained after chemical cross-linking. FT-IR spectroscopy clearly highlighted the efficiency of the cross-linking reactions, as the characteristic ν(OH) stretching band from hydroxyl groups of PHEMA around 3400 cm^{-1} completely disappeared after reactions with acyl dichlorides (Figure 3.10).

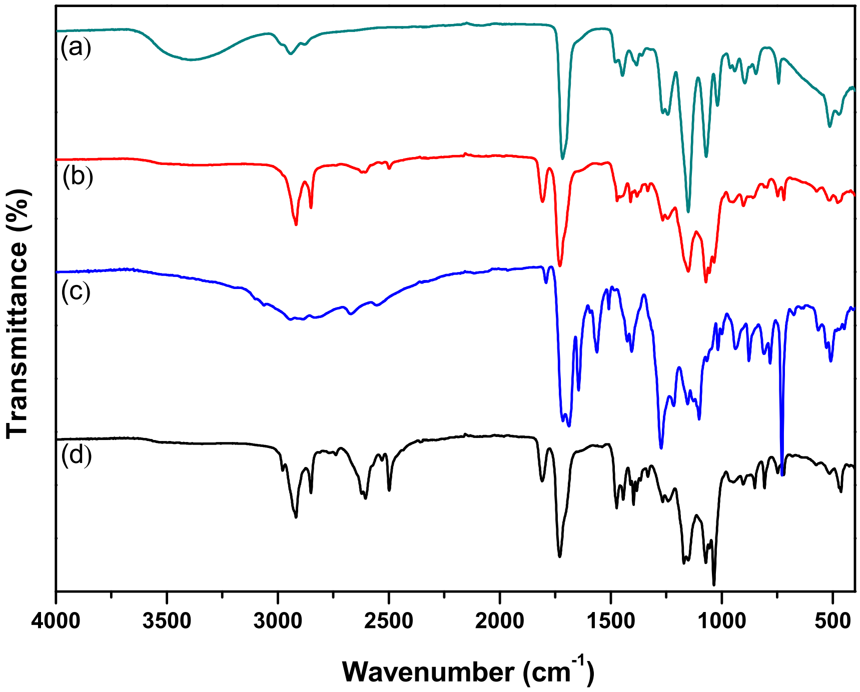

Figure 3.10: ATR-FTIR spectra of PHEMA-based materials before (a) and after chemical cross-linking with glutaryl chloride (b), terephthaloyl chloride (c), and dodecanedioyl dichloride (d).

By using terephthaloyl chloride as a crosslinker, it was also observed the appearance of a weak stretching band associated with the aromatic CH bonds at 3060 cm^{-1}, along with three ν(C=C) bands at 1500, 1560 and 1640 cm^{-1}. Moreover, the δ(CH) out-of-plane deformation band was also observed at 730 cm^{-1}. These results strengthened the proof of successful cross-linking reaction with terephthaloyl chloride. For glutaryl chloride and dodecanedioyl dichloride as cross-linkers, in addition to the complete disappearance of ν(OH) after the reactions, we observed the appearance of a weak ν(C=O) band at 1810 cm^{-1}.

3.4 Conclusions

This chapter has demonstrated the versatility and effectiveness of an unprecedented route to doubly porous PHEMA-based materials *via* Thermally Induced Phase Separation (TIPS). Such biporous materials could successfully be obtained through the use of a co-solvent mixture of water/dioxane to solubilize pre-synthesized linear PHEMA, and subsequent sublimation of the co-solvents. Thanks to this novel approach, it is thus possible to achieve a highly regular macroporosity in conjunction with a tunable nanoporosity. SEM and MIP characterizations gave evidence of the occurrence of a bimodal porosity within the porous structures.

The possibility to functionalize them has also been investigated *via* chemical cross-linking reactions so that the resulting materials might possess a higher mechanical stability. Further possibilities of functionalization of these innovative materials could be envisioned so that they might be used as potential bioreactors or scaffolds in miscellaneous biomedical applications, such as tissue engineering or drug delivery.

References

[1] D. Wu, F. Xu, B. Sun, R. Fu, H. He, and K. Matyjaszewski, “Design and preparation of porous polymers,” *Chemical Reviews*, vol. 112, pp. 3959–4015, 2012.

[2] C. J. Buchko, L. C. Chen, Y. Shen, and D. C. Martin, “Processing and microstructural characterization of porous biocompatible protein polymer thin films,” *Polymer*, vol. 40, pp. 7397–7407, 1999.

[3] I. Tokarev and S. Minko, “Stimuli-responsive porous hydrogels at interfaces for molecular filtration, separation, controlled release, and gating in capsules and membranes,” *Advanced Materials*, vol. 22, pp. 3446–3462, 2010.

[4] F. Svec and J. M. Fréchet, “New designs of macroporous polymers and supports: from separation to biocatalysis,” *Science*, vol. 273, pp. 205–211, 1996.

[5] C. Viklund, F. Svec, J. M. Fréchet, and K. Irgum, “Monolithic, ”molded”, porous materials with high flow characteristics for separations, catalysis, or solid-phase chemistry: control of porous properties during polymerization,” *Chemistry of Materials*, vol. 8, pp. 744–750, 1996.

[6] K. Rezwan, Q. Chen, J. Blaker, and A. R. Boccaccini, “Biodegradable and bioactive porous polymer/inorganic composite scaffolds for bone tissue engineering,” *Biomaterials*, vol. 27, pp. 3413–3431, 2006.

[7] M. T. Gokmen and F. E. Du Prez, “Porous polymer particles - a comprehensive guide to synthesis, characterization, functionalization and applications,” *Progress in Polymer Science*, vol. 37, pp. 365–405, 2012.

[8] F. Svec, “Porous polymer monoliths: amazingly wide variety of techniques enabling their preparation,” *Journal of Chromatography A*, vol. 1217, pp. 902–924, 2010.

[9] A. G. Mikos, A. J. Thorsen, L. A. Czerwonka, Y. Bao, R. Langer, D. N. Winslow, and J. P. Vacanti, “Preparation and characterization of poly (l-lactic acid) foams,” *Polymer*, vol. 35, pp. 1068–1077, 1994.

[10] K. Whang, C. Thomas, K. Healy, and G. Nuber, “A novel method to fabricate bioabsorbable scaffolds,” *Polymer*, vol. 36, pp. 837–842, 1995.

[11] K. M. Woo, V. J. Chen, and P. X. Ma, “Nano-fibrous scaffolding architecture selectively enhances protein adsorption contributing to cell attachment,” *Journal of Biomedical Materials Research Part A*, vol. 67, pp. 531–537, 2003.

[12] V. J. Chen, L. A. Smith, and P. X. Ma, “Bone regeneration on computer-designed nano-fibrous scaffolds,” *Biomaterials*, vol. 27, pp. 3973–3979, 2006.

[13] J. Hu, X. Liu, and P. X. Ma, “Induction of osteoblast differentiation phenotype on poly (l-lactic acid) nanofibrous matrix,” *Biomaterials*, vol. 29, pp. 3815–3821, 2008.

[14] S. Ghosh, J. Viana, R. Reis, and J. Mano, “The double porogen approach as a new technique for the fabrication of interconnected poly (l-lactic acid) and starch based biodegradable scaffolds,” *Journal of Materials Science: Materials in Medicine*, vol. 18, pp. 185–193, 2007.

[15] A. Barbetta and N. R. Cameron, “Morphology and surface area of emulsion-derived (polyhipe) solid foams prepared with oil-phase soluble porogenic solvents: Three-component surfactant system,” *Macromolecules*, vol. 37, pp. 3202–3213, 2004.

[16] A. Barbetta and N. R. Cameron, “Morphology and surface area of emulsion-derived (polyhipe) solid foams prepared with oil-phase soluble porogenic solvents: Span 80 as surfactant,” *Macromolecules*, vol. 37, pp. 3188–3201, 2004.

[17] J. Deitzel, W. Kosik, S. McKnight, N. B. Tan, J. DeSimone, and S. Crette, “Electrospinning of polymer nanofibers with specific surface chemistry,” *Polymer*, vol. 43, pp. 1025–1029, 2002.

[18] D. Laura, H. Keskkula, J. Barlow, and D. Paul, “Effect of glass fiber surface chemistry on the mechanical properties of glass fiber reinforced, rubber-toughened nylon 6,” *Polymer*, vol. 43, pp. 4673–4687, 2002.

[19] D. Horák, H. Hlídková, J. Hradil, M. Lapčíková, and M. Šlouf, “Superporous poly (2-hydroxyethyl methacrylate) based scaffolds: preparation and characterization,” *Polymer*, vol. 49, pp. 2046–2054, 2008.

[20] J. Hradil and D. Horák, “Characterization of pore structure of phema-based slabs,” *Reactive and Functional Polymers*, vol. 62, pp. 1–9, 2005.

[21] H.-B. Ly, B. Le Droumaguet, V. Monchiet, and D. Grande, “Designing and modeling doubly porous polymeric materials,” *The European Physical Journal Special Topics*, vol. 224, pp. 1689–1706, 2015.

[22] C. Yu, M. Xu, F. Svec, and J. M. Fréchet, “Preparation of monolithic polymers with controlled porous properties for microfluidic chip applications using photoinitiated free-radical polymerization,” *Journal of Polymer Science Part A: Polymer Chemistry*, vol. 40, pp. 755–769, 2002.

[23] O. Okay and Ç. Gürün, “Synthesis and formation mechanism of porous 2-hydroxyethyl methacrylate–ethylene glycol dimethacrylate copolymer beads,” *Journal of Applied Polymer Science*, vol. 46, pp. 401–410, 1992.

[24] B. Le Droumaguet, R. Lacombe, H.-B. Ly, M. Guerrouache, B. Carbonnier, and D. Grande, “Engineering functional doubly porous phema-based materials,” *Polymer*, vol. 55, pp. 373–379, 2014.

[25] B. Le Droumaguet, R. Lacombe, H.-B. Ly, B. Carbonnier, and D. Grande, “Novel polymeric materials with double porosity: Synthesis and characterization,” vol. 340, pp. 18–27, 2014.

[26] S. Kovacic, D. Štefanec, and P. Krajnc, “Highly porous open-cellular monoliths from 2-hydroxyethyl methacrylate based high internal phase emulsions (hipes): preparation and void size tuning,” *Macromolecules*, vol. 40, pp. 8056–8060, 2007.

[27] O. Kulygin and M. S. Silverstein, “Porous poly (2-hydroxyethyl methacrylate) hydrogels synthesized within high internal phase emulsions,” *Soft Matter*, vol. 3, pp. 1525–1529, 2007.

[28] N. R. Cameron, “High internal phase emulsion templating as a route to well-defined porous polymers,” *Polymer*, vol. 46, pp. 1439–1449, 2005.

[29] M. S. Silverstein, “Emulsion-templated porous polymers: a retrospective perspective,” *Polymer*, vol. 55, pp. 304–320, 2014.

[30] Y. Yang, J. Zhao, Y. Zhao, L. Wen, X. Yuan, and Y. Fan, “Formation of porous plga scaffolds by a combining method of thermally induced phase separation and porogen leaching,” *Journal of Applied Polymer Science*, vol. 109, pp. 1232–1241, 2008.

[31] X. Liu and P. X. Ma, “Phase separation, pore structure, and properties of nanofibrous gelatin scaffolds,” *Biomaterials*, vol. 30, pp. 4094–4103, 2009.

[32] V. A. Santamaría, H. Deplaine, D. Mariggió, A. Villanueva-Molines, J. García-Aznar, J. G. Ribelles, M. Doblaré, G. G. Ferrer, and I. Ochoa, “Influence of the macro and micro-porous structure on the mechanical behavior of poly (l-lactic acid) scaffolds,” *Journal of Non-Crystalline Solids*, vol. 358, pp. 3141–3149, 2012.

[33] A. Atala and R. P. Lanza, *Methods of tissue engineering.* San Diego, CA: Academic Press, 2002.

[34] P. Van de Witte, P. Dijkstra, J. Van den Berg, and J. Feijen, “Phase separation processes in polymer solutions in relation to membrane formation,” *Journal of Membrane Science*, vol. 117, pp. 1–31, 1996.

[35] P. X. Ma and J. Elisseeff, *Scaffolding in tissue engineering.* Boca Raton, FL: CRC press - Taylor and Francis Group, 2006.

[36] S. L. McArthur, M. W. Halter, V. Vogel, and D. G. Castner, “Covalent coupling and characterization of supported lipid layers,” *Langmuir*, vol. 19, pp. 8316–8324, 2003.

[37] K. Yamada, Y. Iizawa, J.-i. Yamada, and M. Hirata, “Retention of activity of urease immobilized on grafted polymer films,” *Journal of Applied Polymer Science*, vol. 102, pp. 4886–4896, 2006.

[38] J. Yang, P. Zhang, L. Tang, P. Sun, W. Liu, P. Sun, A. Zuo, and D. Liang, “Temperature-tuned dna condensation and gene transfection by pei-g-(pmeo 2 ma-b-phema) copolymer-based nonviral vectors,” *Biomaterials*, vol. 31, pp. 144–155, 2010.

[39] R. Langer and J. P. Vacanti, “Tissue engineering,” *Science*, vol. 260, pp. 920–926, 1993.

[40] L. S. Nair and C. T. Laurencin, “Biodegradable polymers as biomaterials,” *Progress in Polymer Science*, vol. 32, pp. 762–798, 2007.

[41] Z. Tuzar and M. Bohdanecky, “The properties of diluted solutions of poly(ethylene glycol monomethacrylate),” *Coll. Czech. Chem. Com.*, vol. 34, p. 289, 1969.

[42] T. P. Davis and M. B. Huglin, “Some mechanical properties of poly (2-hydroxyethyl methacrylate) gels swollen in water/1, 4-dioxane mixtures,” *Die Makromolekulare Chemie, Rapid Communications*, vol. 9, pp. 39–43, 1988.

[43] D. R. Lloyd, K. E. Kinzer, and H. Tseng, “Microporous membrane formation via thermally induced phase separation. i. solid-liquid phase separation,” *Journal of Membrane Science*, vol. 52, pp. 239–261, 1990.

[44] G. Wei and P. X. Ma, “Structure and properties of nano-hydroxyapatite/polymer composite scaffolds for bone tissue engineering,” *Biomaterials*, vol. 25, pp. 4749–4757, 2004.

[45] C. Jackson and M. Shaw, “The phase behaviour and gelation of a rod-like polymer in solution and implications for microcellular foam morphology,” *Polymer*, vol. 31, pp. 1070–1084, 1990.

[46] R. Zhang and P. X. Ma, “Poly (a-hydroxyl acids)/hydroxyapatite porous composites for bone-tissue engineering. i. preparation and morphology,” *Journal of Biomedical Materials Research*, vol. 44, pp. 446–455, 1999.

[47] C. Schugens, V. Maquet, C. Grandfils, R. Jérome, and P. Teyssie, “Biodegradable and macroporous polylactide implants for cell transplantation: 1. preparation of macroporous polylactide supports by solid-liquid phase separation,” *Polymer*, vol. 37, pp. 1027–1038, 1996.

[48] Y. Q. Goh and C. P. Ooi, “Fabrication and characterization of porous poly (l-lactide) scaffolds using solidâĂŞliquid phase separation,” *Journal of Materials Science: Materials in Medicine*, vol. 19, pp. 2445–2452, 2008.

[49] C. Tu, Q. Cai, J. Yang, Y. Wan, J. Bei, and S. Wang, “The fabrication and characterization of poly(lactic acid) scaffolds for tissue engineering by improved solid-liquid phase separation,” *Polymers for Advanced Technologies*, vol. 14, pp. 565–573, 2003.

[50] P. X. Ma, R. Zhang, G. Xiao, and R. Franceschi, “Engineering new bone tissue in vitro on highly porous poly (a-hydroxyl acids)/hydroxyapatite composite scaffolds,” *Journal of Biomedical Materials Research*, vol. 54, pp. 284–293, 2001.

[51] H. Giesche, “Mercury porosimetry: a general (practical) overview,” *Particle & Particle Systems Characterization*, vol. 23, pp. 9–19, 2006.

[52] Y. S. Nam and T. G. Park, “Porous biodegradable polymeric scaffolds prepared by thermally induced phase separation,” *Journal of Biomedical Materials Research*, vol. 47, pp. 8–17, 1999.

[53] S. Yoneda, W. Han, U. Hasegawa, and H. Uyama, “Facile fabrication of poly (methyl methacrylate) monolith via thermally induced phase separation by utilizing unique cosolvency,” *Polymer*, vol. 55, pp. 3212–3216, 2014.

Chapter 4

Versatile functionalization platform of biporous poly(2-hydroxyethyl methacrylate)-based materials: application in supported catalysis

The work developed in this chapter has been the subject of one paper:

- H.B. Ly, R. Poupart, B. Le Droumaguet, D. Grande, Versatile functionalization platform of biporous poly(2-hydroxyethyl methacrylate)-based materials: Application in supported catalysis, to be submitted as a regular article to *Langmuir*.

4.1 Introduction

Surface chemistry plays an important role in the field of porous polymer materials. Over the past decades, investigation in this area has received much attention and has been oriented toward various applications [1]. In this regard, the surface modification of porous scaffolds to promote interactions with cells has been considerably reported, due to the possibility of affecting the ability of cellular response or influencing the rate of tissue regeneration [2, 3]. On the other hand, the conversion of non-polar, hydrophobic surfaces to polar, hydrophilic, water-wettable surfaces by plasma techniques [4–6], electrochemical processes [7], or *in-situ* polymerization of hydrophilic monomers [8], are also attractive examples of surface modification. Moreover, polymer modification by grafting chemistry is one of the interesting methods that has widely been used in the literature for separation science [9, 10], for instance. Last but not least, the use of proper chemical moieties to anchor metallic nanoparticles has allowed for the formation of (nano)reactors that can advantageously be used as supported catalysts.

In the past years, the immobilization of metallic nanoparticles on the surface of porous polymers has undergone significant development for a wide range of applications [11], among which heterogeneous catalysis is of crucial importance [12–14]. In addition to the nanometals frequently reported in the literature, including silver [15], palladium [16], or platinum [17], gold appears to be the most attractive candidate [18]. It is well-known that gold nanoparticles (GNPs) can be covalently attached to pore surfaces which bear amino or thiol groups [19]. Miscellaneous catalytic supports have been used in the literature, such as capillary systems [20–22], monoliths [23], carbon nanotubes [24, 25], graphene [26], and silica-based materials [27].

In our previous papers, we have developed the fabrication of doubly porous materials based on poly(2-hydroxyethyl methacrylate) (PHEMA) [28–30]. Such original materials with multiple porosity may hold relevance in the areas of civil engineering, soils mechanics or tissue engineering, for instance. The larger porosity level would allow macromolecules to flow through the materials, while the smaller porosity level would be dedicated to the passage of smaller molecules or play an important role regarding filtration applications.

In the present paper, we describe the synthesis and application of a new type of catalytic support derived from a doubly porous cross-linked poly(2-hydroxyethyl methacrylate) (PHEMA)-based matrix. Various surface modifications of the matrix are first addressed through the use of carbonydiimidazole chemistry or ”click” chemistry *via* either thiol-ene or thiol-yne additions of functional organic molecules. In selected cases, the catalytic responses of the resulting functionalized biporous materials is then examined. As a matter of fact, gold nanoparticles (GNPs) are generated by *in situ* reduction of corresponding salts and immobilized on the amino- or thiol- modified surface of PHEMA-based frameworks. Through hydride-mediated reduction of *p*-nitrophenol, we demonstrate the higher efficiency of these newly synthesized catalytic supports compared to that associated with their monoporous analogues possessing only either the upper porosity level or the lower porosity level. Finally, tethering a tripeptide, *i.e.* glutathione (GSH), to the surface of doubly porous materials may pave the way to promising perspectives for biomedical applications.

4.2 Experimental

4.2.1 Materials

2-hydroxyethyl methacrylate (HEMA, 97%), ethylene glycol dimethacrylate (EGDMA, 98%), 2,2'-azobisisobutyronitrile (AIBN, 98%), ethylene diamine (EDA, ≥99%), sodium borohydride ($NaBH_4$, ≥99%), 2,2-dimethoxy-2-phenylacetophenone (DMPA, 99%), D,L-dithiothreitol (DTT, ≥98%), and L-glutathione (GSH, ≥99% powder) were purchased from Sigma Aldrich. 4-nitrophenol (*p*-nitrophenol, 99%), 1,1'-carbonyldiimidazole (CDI, 97%), mercaptoacetic acid (thioglycolic acid) (97%+), allylamine (98%+), propargylamine (98%) and hydrogen tetrachloroaurate (III) hydrate ($HAuCl_4$, 99.9%) were obtained from Alfa Aesar. Cysteamine (≥98%) was supplied by Fluka. Sodium chloride (NaCl) particles with diameters ranging from 50 to 500 μm were purchased from Prolabo, and were stored under moisture-free conditions. Prior to use, they were sieved to isolate the particle fraction with average diameters between 125 and 200 μm. All reagents and solvents were used without further purification, except for AIBN that was recrystallized from methanol and stored at 4°C, prior to use. 18.2 MΩ deionized water was filtered through a Milli-Q Plus purification pack.

4.2.2 Preparation of porous PHEMA-based materials

Initially, sieved NaCl particles were submitted to a Spark Plasma Sintering (SPS) treatment so as to obtain a fused NaCl particle phase. A Sumitomo Dr. Sinter Lab 515S SPS machine from Fuji Electronic Industrial was used. Experimentally, NaCl particles were introduced into a graphite die and heated from room temperature to 150 °C at a heating rate of 50 $°C.min^{-1}$, while applying a 3 kN force onto the sample under inert atmosphere. After 20 min at 150 °C, the sintered sample was cooled to room temperature at a rate of 50 $°C.min^{-1}$. The mixture consisting of HEMA, EGDMA (molar ratios: 70/30 mol. %), DMPA (2 wt.% with respect to the comonomers), and isopropanol (*i*-PrOH) as the porogenic solvent (85 vol.% with respect to the total volume of the comonomers) were added to the fused NaCl particle template, and the polymerization was conducted in a UV oven for 4 h at 365 nm. NaCl macro-sized particles removal by water extraction took 1 day. After this step, the samples were washed abundantly with deionized water, and dried at room temperature under vacuum. Gravimetric analysis confirmed the complete removal of both porogens.

The generation of monoporous analogues was similar to that of doubly porous materials. In the case of PHEMA-based macro porous materials, NaCl particles were solely used and no porogenic solvent was used. In the case of porous materials possessing only the lower porosity, the polymerization mixtures were directly introduced in glass vials, without previously forming the NaCl particle template.

4.2.3 Functionalization of biporous poly(HEMA-*co*-EGDMA) materials

The different functionalization reactions applied to porous PHEMA-based networks are depicted in Figure 4.1.

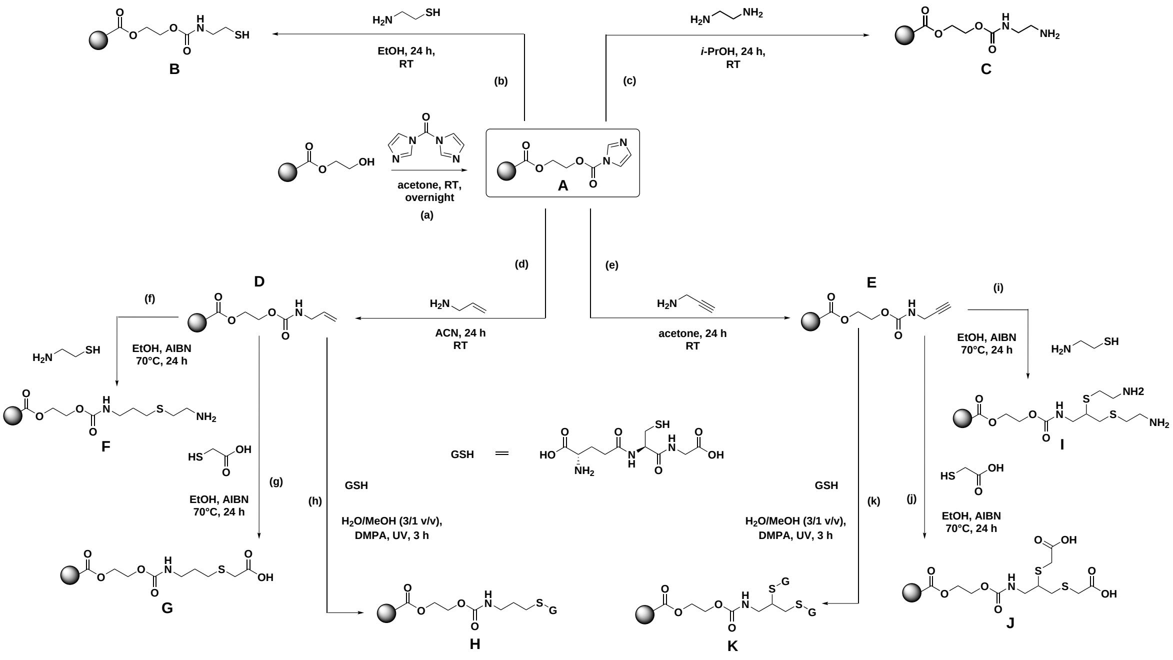

Figure 4.1: Miscellaneous synthetic routes for functionalization of porous PHEMA-based networks.

4.2.3.1 Activation of PHEMA with CDI

100 mg of porous poly(HEMA-*co*-EGDMA) (~0.66 mmol of hydroxyl groups) were immersed in 2 mL of acetone. 2 equiv. of CDI (compared to hydroxyl groups in the porous materials, *i.e.* 214 mg) were added, and the reaction medium was gently stirred on an orbital shaking plate overnight. The solid was then filtered off, washed abundantly with acetone, and dried under vacuum. The as-obtained material was denoted as polymer A, and was characterized by Raman spectroscopy.

4.2.3.2 Functionalization of polymer A with cysteamine

A sample of polymer A (100 mg) was immersed in 2 mL of absolute ethanol. Cysteamine (102 mg, 2 equiv. compared to hydroxyl groups in the porous precursor) was then added. The solution was gently shaken for 24 h at room temperature. After washing with an abundant quantity of absolute ethanol, the resulting porous PHEMA-based material was dried under vacuum for 24 h, and analyzed by Raman spectroscopy. Such a functionalized PHEMA-based material was denoted as B. For the sake of comparison, we also referred to B1, B2, and B3, respectively, the material possessing a double porosity, the macroporous analogue with a porosity similar to the upper porosity level of the latter, and the monoporous analogue with a porosity similar to the lower porosity level of the former.

4.2.3.3 Functionalization of polymer A with ethylenediamine

A sample of polymer A (100 mg) was immersed in 2 mL of propan-2-ol (*i*-PrOH). Ethylenediamine (79 mg, 2 equiv. compared to hydroxyl groups in the porous precursor) was added. The solution was then gently shaken for 24 h at room temperature. After washing with an abundant quantity of *i*-PrOH, the resulting porous PHEMA-based material was dried under vacuum for 24 h, and analyzed by Raman spectroscopy. The functionalized porous PHEMA-based materials was denoted as C. For the sake of comparison, we used the terminology C1, C2, and C3 to refer to the analogues of B1, B2, and B3, as mentioned above.

4.2.3.4 Functionalization of polymer A with allylamine

A sample of polymer A (100 mg) was immersed in 2 mL of acetonitrile (ACN). Allylamine (75 mg, 2 equiv. compared to hydroxyl groups in the porous precursor) was added, and the solution was gently shaken for 24 h at room temperature. The resulting porous PHEMA-based materials was washed with an abundant quantity of acetonitrile, then acetone, and dried under vacuum for 24 h before Raman spectroscopy measurements. The functionalized material was denoted as D.

4.2.3.5 Functionalization of polymer A with propargylamine

A sample of polymer A (100 mg) was immersed in 2 mL of acetone. Propargylamine (73 mg, 2 equiv. compared to hydroxyl groups in the porous precursor) was added, and the solution was gently shaken for 24 h at room temperature. The resulting porous PHEMA-based material was washed with an abundant quantity of acetone, and dried under vacuum for 24 h before being analyzed by Raman spectroscopy. The functionalized material was denoted as E.

4.2.3.6 Functionalization of polymers D and E with cysteamine

A sample of polymer D or E (100 mg) was immersed in 2 mL of absolute ethanol. Cysteamine (153 mg, 3 equiv. compared to hydroxyl groups in the porous precursor) was added and solubilized. The thiol-ene reaction (or thiol-yne in case of polymer E) was conducted at 70 °C in the presence of AIBN (2 wt.% with respect to the polymer) for 24 h. The samples were then washed with an abundant quantity of absolute ethanol, and dried under vacuum for 24 h before Raman spectroscopy analysis. The resulting materials were denoted as F and I, respectively.

4.2.3.7 Functionalization of polymers D and E with thioglycolic acid

A sample of polymer D or E (100 mg) was immersed in 2 mL of absolute ethanol in presence of thioglycolic acid (182 mg, 3 equiv. compared to hydroxyl groups in the porous precursor). The thiol-ene reaction (or thiol-yne in case of polymer E) was conducted at 70 °C in the presence of AIBN (2 wt.% with respect to the polymer) for 24 h. The samples were then washed with an abundant quantity of absolute ethanol, and dried under vacuum for 24 h before Raman spectroscopy analysis. The resulting materials were denoted as G and J, respectively.

4.2.3.8 Functionalization of polymers D and E with glutathione

A sample of polymer E (100 mg) was immersed in 3 mL of a mixture of water/methanol (75/25 vol.%) with DMPA (2 mg, 2 wt.% with respect to the polymer). GSH (609 mg, 3 equiv. compared to hydroxyl groups in the porous precursor) was then added into glass vials. The latters were placed in a UV oven for 3 h under irradiation at 365 nm. After being carefully washed, the resulting porous materials were dried under vacuum, and then analyzed by Raman spectroscopy. The resulting materials were denoted as H and K, respectively.

4.2.4 *In-situ* formation of gold nanoparticles within functionalized PHEMA-based networks

35 mg of the porous polymeric materials (B1, C1, C2, C3, I) were introduced separately into different vials containing 2 mL of a freshly pre-prepared 10 wt.% of $HAuCl_4$ aqueous solution, and let to react overnight. The polymers were then washed several times with deionized water in order to remove the Au^{3+} ions that were non-specifically adsorbed on the surface of the materials. The samples were then transferred into 2 mL of an aqueous solution of $NaBH_4$ (7 mg in 2 mL water) for 2 h in order to generate the gold nanoparticles (GNPs). The hybrid samples based on GNP@PHEMA were washed several times with deionized water and dried under vacuum.

4.2.5 Supported catalytic reduction of *p*-nitrophenol

10 mg of the gold functionalized monoporous samples with a simple amine function (GNP@C2, GNP@C3) were separately placed in a freshly pre-prepared solution containing 20 μL of a *p*-nitrophenol solution (4 mg in 10 mL deionized water), 20 μL of a $NaBH_4$ solution (114 mg in 10 mL water), and 4 mL of water. UV-Vis spectra were recorded before the adjunction of catalyst and 1 h after the addition of the gold functionalized samples in the solution.

On the other hand, other samples (GNP@B1, GNP@C1, GNP@I) were separately placed in a solution of 20 μL of *p*-nitrophenol, 60 μL of $NaBH_4$, and 4 mL of water. Comparisons were carried out during five successive cycles of 1 h in the same experimental conditions. A blank experiment (without GNPs) was also recorded for a 1 h cycle.

4.2.6 Instrumentation

Scanning Electron Microscopy (SEM) analyses of the materials were performed with a MERLIN microscope from Zeiss equipped with InLens, EBSD and SE2 detectors using a low accelerating tension (2-3 kV) with a diaphragm aperture of 30 μm. Prior to analyses, the samples were coated with a 4-nm thin layer of palladium in a Cressington 208 HR sputter-coater. Energy-dispersive X-ray spectroscopy (EDX) was performed using a SSD X-Max detector of 50 mm^2 from Oxford Instruments (127 eV for the Kα of Mn).

The porosity ratios, pore volumes, and pore size distributions of the materials were determined by mercury intrusion porosimetry (MIP) using an AutoPore IV 9500 porosimeter from Micromeritics. The determination of the porosity features was based on the Washburn equation between the applied pressure (from 1.03 to 206.8 MPa) and the pore diameter into which mercury intruded.

The chemical structure of the polymeric materials was examined using an XPlora One Raman spectrometer from Horiba Jobin Yvon equipped with a laser emitting at 638 nm. The acquisition time was fixed at 1 min.

UV-Vis spectra were recorded on a Cary 60 UV-Vis spectrophotometer from Agilent Technologies from 200 to 800 nm.

Inductively-coupled plasma optical emission spectrometry (ICP-OES) analyses were performed using a Varian Vista-PRO CCD Simultaneous ICP-OES spectrometer.

4.3 Results and discussion

4.3.1 Characterization of porous PHEMA frameworks

The doubly porous material obtained after extraction of NaCl macro-sized particles and the porogenic solvent (*i*-PrOH) presented a 92% porosity, with a macropore to nanopore volume ratio of about 85/15 vol.%. The MIP profile associated with this porous PHEMA framework indicated a bimodal porosity with a macroporosity centered around 40 μm and a lower porosity with pore size ranging around 8 μm (Figure 4.2).

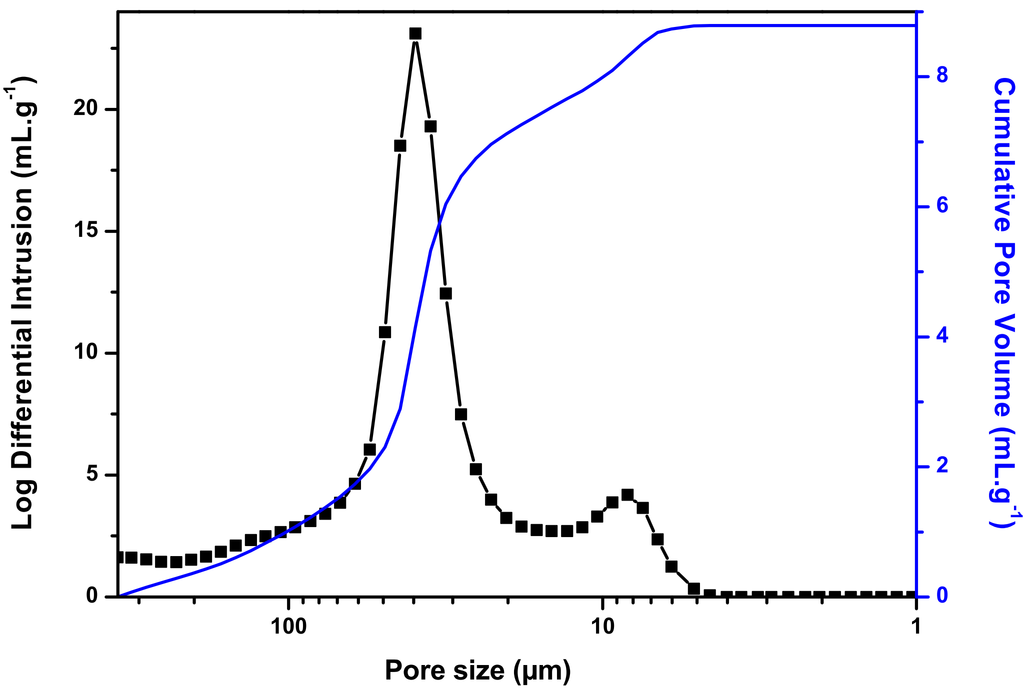

Figure 4.2: Mercury intrusion porosimetry profile of biporous PHEMA material with interconnected macropores prepared using fused NaCl particle template resulting from SPS. The polymerization mixture was constituted of 70/30 mol. % HEMA/EGDMA and 85 vol. % *i*-PrOH (with respect to the total volume of co-monomers). The porous distribution profile curve associated with the biporous material was plotted (black squares and black line) along with the cumulative pore volume curve (continue blue curve).

It is noteworthy that the pore size distribution curve presented a bimodal distribution with an interconnected macroporosity, as previously reported elsewhere [28, 29]. The use of SPS for sintering NaCl particles constitute an unprecedented methodology. This novel route could thus generate materials with controlled macropore interconnectivity. Indeed, the threshold (or interconnectivity window) average diameter could be equal to 85, 65 or 40 μm depending on the NaCl particle size, *i.e.* 250-400, 200-250, or 125-200 μm, respectively (data not shown).

Similar MIP profiles were also observed with polyHIPE-based porous materials in which average pore diameters were usually lower than those measured from SEM images [31]. SEM micrographs of the biporous polymer showed macropores with an average diameter ranging from 120 to 200 μm, *i.e.* similar to NaCl particle imprints. For the sake of comparison, two monoporous analogues were also fabricated. The monoporous analogue with only the lower porosity level possessed an average pore size ranging around 9 μm with a porosity of 72 %. The latter with only the upper porosity level possessed an average pore diameter of 42 μm and a porosity of 74% (data not shown). These results demonstrated an undeniable advantage of the double porogen approach to generate doubly porous materials: pore size and interconnectivity of each porosity level could be distinctly controlled *via* particle size and degree of sintering for the upper porosity level, and through the use of different porogenic solvents along with their volume ratios, for the lower porosity level.

4.3.2 Functionalization and characterization of mono- and biporous poly(HEMA-*co*-EGDMA) materials

The first modification of the porous PHEMA-based polymer consisted in the activation of hydroxyl groups with carbonyldiimidazole (CDI). By Raman spectroscopy, characteristic bands of CDI were found at 1760 cm^{-1} corresponding to the carbamate function, and at 3130 and 3160 cm^{-1} corresponding to the C-H bonds from the imidazole ring. This modification was also reported by our previous work [29], as a preliminary result for various functionalization reactions herein proposed.

The Raman spectra of resulting functionalized polymers are presented in Figure 4.3. Chemical reactions with the CDI-modified polymer (polymer A) were accomplished by nucleophilic substitution with miscellaneous amino (-NH$_2$) compounds, *i.e.* cysteamine, ethylenediamine, allylamine, and propargylamine. The success of all these reactions was testified by Raman spectroscopy (see Figure 4.3.a), with the total disappearance of characteristic bands of CDI. Moreover, specific Raman signatures corresponding to the employed amino compounds could be noticed:

- for polymer B obtained from reaction of polymer A with cysteamine, the appearance of a thiol (-SH) stretching band was observed at 2570 cm^{-1};

- for polymer C derived from reaction of polymer A with ethylenediamine, a weak stretching band of -NH$_2$ was found at 3310 cm^{-1};

- for polymer D resulting from reacting polymer A with allylamine, the appearance of a stretching ν(C=C) band at 1640 cm^{-1} was detected;

- and for polymer E after subsequent coupling of polymer A with propargylamine, the spectrum showed a characteristic intense band at 2120 cm^{-1} ascribed to alkyne stretching vibrations ν(C$\equiv$C-H).

The addition of allylamine afforded an alkene-modified PHEMA-based porous material (polymer D). Raman spectroscopy was used to monitor the thiol-ene "click" reactions of the alkene-modified framework with cysteamine, thioglycolic acid, and glytathione (see Figure 4.3.b). As expected, it was observed that C=C double bonds were completely consumed through the disappearance of the corresponding band at 1640 cm^{-1}. A specific Raman signal corresponding to the amino groups was observed at $\sim$3310 cm^{-1} in the case of the reaction with cysteamine (polymer F), whereas no further band corresponding to the mercaptoacetic acid was found when reacting polymer D with one such compound (polymer G). The thiol-ene reaction with GSH (polymer H) was not complete, as the (C=C) band did not totally disappeared, probably due to steric hindrance effects.

Further, the addition of propargylamine allowed for formation of an alkyne-functionalized PHEMA-based porous material (polymer E). Again, Raman spectroscopy permitted to assess the completion of the thiol-yne 'click" reactions of the alkyne-modified frameworks with cysteamine and thioglycolic acid (see Figure 4.3.c). As expected, it was observed that the ν(C$\equiv$C) band at 2120 cm^{-1} completely disappeared [20]. A specific Raman signal corresponding to the amino group was observed at $\sim$3310 cm^{-1}, in the case of the reaction with cysteamine [20] (polymer I). In the case of the reaction with thioglycolic acid (polymer J), no further peak corresponding to one such acid was found. The thiol-yne reaction with GSH (polymer K) was success with GSH well grafted to the surface of the porous frameworks (*i.e.* total disappearance of the ν(C$\equiv$C) band). It should be stressed that in both thiol-yne and thiol-ene reactions with GSH, we observed the occurrence of an amide II band at 1600 cm^{-1} specific to GSH.

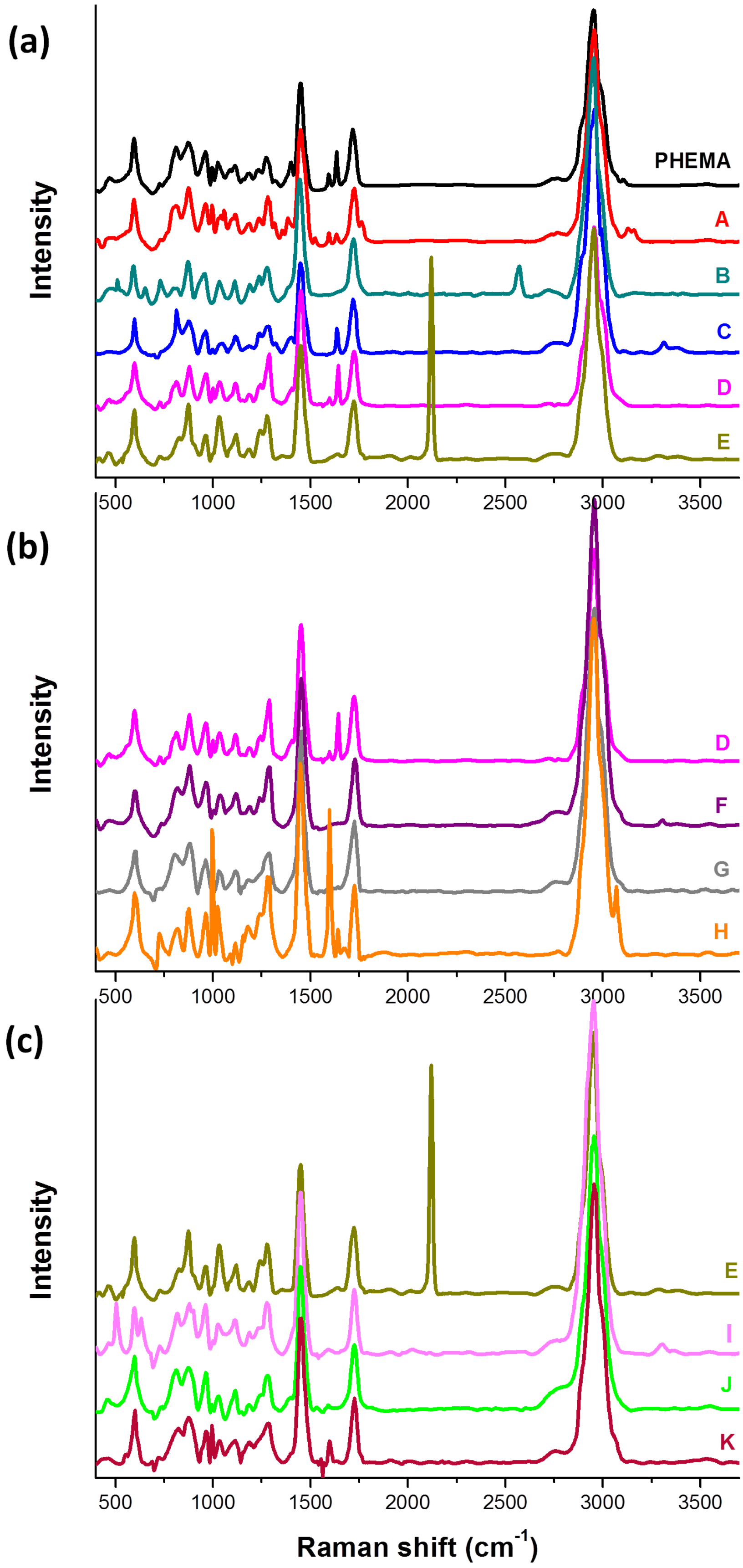

Figure 4.3: Raman spectra of the PHEMA-based porous frameworks in the case of (a) activation with CDI and subsequent functionalization with amino compounds, (b) thiol-ene reactions of polymer D with thiol compounds, and (c) thiol-yne reactions of polymer E with thiol compounds.

4.3.3 Gold nanoparticle immobilization and reduction of *p*-nitrophenol

Gold nanoparticles (GNPs) are widely known for being able to catalyze different organic reactions, especially the reduction of nitro-containing compounds. To this purpose, GNPs were *in-situ* generated and immobilized on the surface of the functionalized porous PHEMA-based materials.

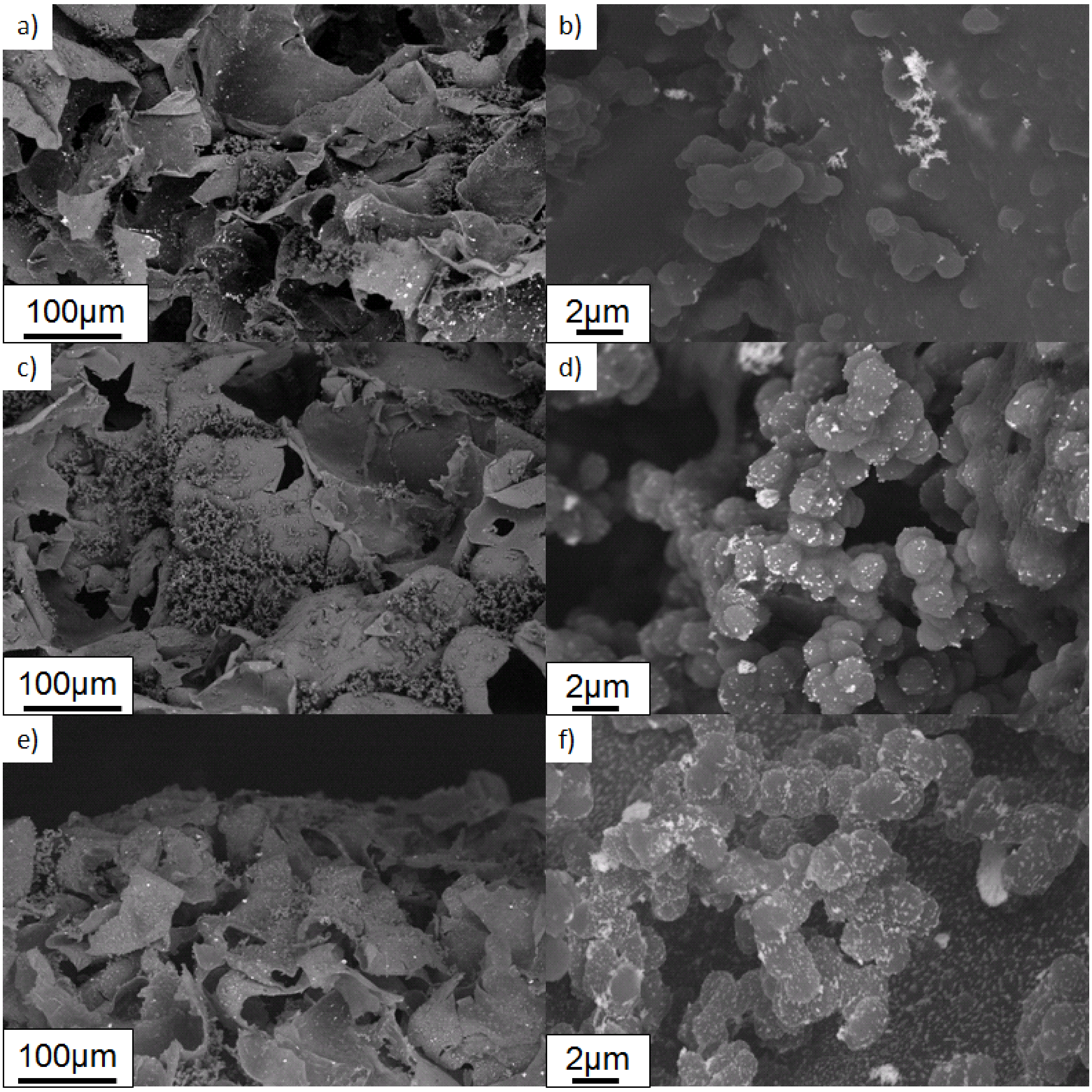

Figure 4.4: SEM micrographs of doubly porous GNP@PHEMA-based materials functionalized with different organic molecules: (a), (b) cysteamine (sample B1); (c),(d) ethylenediamine (sample C1); and (e), (f) propargylamine followed by a thiol-yne addition of cysteamine (sample I).

Different porous structures containing three types of chelating groups, *i.e.* -SH (polymer B), -NH_2 (polymer C), and two adjacent -NH_2 groups (polymer I), were investigated in order to compare their effect on the GNP morphology and catalytic efficiency. The presence of GNPs in the as-obtained hybrid porous materials was evidenced by SEM (Figure 4.4) and EDX (Figure 4.5), while quantification of gold was achieved by ICP-OES. According to SEM micrographs, doubly porous polymers B and I possessed two populations of GNPs: macro-particles whose diameter ranged from 3 to 5 μm, and nanoparticles of around 100 nm diameter, with many particle aggregates. Sample C did not show any macro-sized gold particles, and solely possessed GNPs with sizes between 100 and 150 nm.

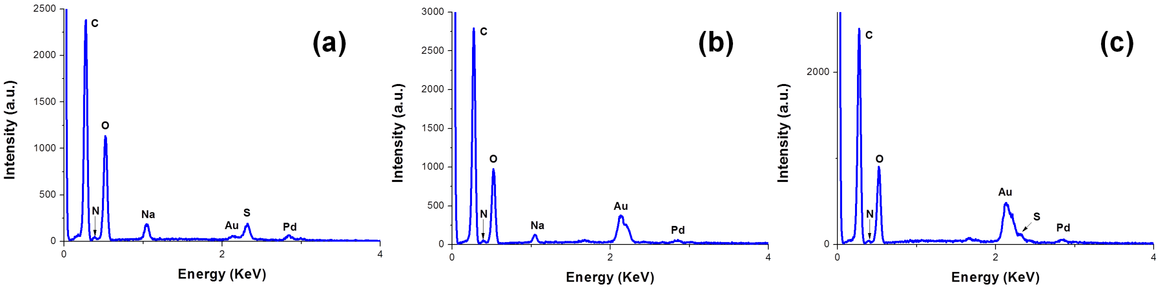

Figure 4.5: EDX spectra of polymer B (a), polymer C (b), and polymer I (c), after immobilization of GNPs.

The catalytic behavior was then investigated *via* NaBH$_4$-mediated reduction of *p*-nitrophenol. Three different types of porosity features were investigated with the PHEMA-based porous samples, as defined next: type 1: doubly porous structure; type 2: monoporous analogue containing only the upper porosity level; and type 3: monoporous analogue containing only the lower porosity level. The catalytic activities of mono porous samples C2 and C3 were first examined. These materials were shown to display approximately the same activity (27 % and 25 % of yield corresponding to polymer C2 and polymer C3, respectively) (Table 4.1).

Nevertheless, according to ICP analysis, the monoporous material with an upper porosity level (C2) contained much fewer GNPs than that with a lower porosity level (C3) (*i.e.* 1.3 wt.% and 4.6 wt.% of GNPs for samples C2 and C3, respectively). The similar catalytic activities of these materials with different pore sizes might be explained by a better GNP accessibility in the porous material with larger pore sizes, as fluid flow was probably much higher in one such material.

Table 4.1: Porous characteristics of porous PHEMA-based samples and corresponding yields of *p*-nitrophenol reduction after GNP immobilization.

Samples	D_p^c (μm)	Porosity ratio ^{c} (%)	Time (min)	Yield (%)
C2	42	74	60	27
C3	9	72	60	25
C3	9	72	60	90
C1	40 & 8.3	92	40	91

^{a} with 20 μL *p*-nitrophenol + 20 μL $NaBH_4$.
^{b} with 20 μL *p*-nitrophenol + 60 μL $NaBH_4$.
^{c} Values as determined by MIP.

Due to the low reactivity of the catalytic systems, likely due to decomposition of $NaBH_4$ in water, the quantity of $NaBH_4$ was tripled in order to increase the catalytic activity (*i.e.* from 20 μL to 60 μL of $NaBH_4$). Indeed, various reports indicated that there was a linear dependence of the catalysis rate on the $NaBH_4$ concentration [32, 33]. Due to the similar activities between samples C2 and C3, we then proposed the comparison between samples C1 and C3 only. It was shown that the doubly porous material (C1) was more efficient to catalyze the reduction of the *p*-nitrophenol, achieving 91 % reduction within 40 min, while the hybrid material C3 achieved 90 % reduction in 1 h (Table 4.1). Regarding these results, we particularly focused our attention on doubly porous materials, and decided to investigate the effect of chelating functions on the catalysis yield of the hydride-mediated reduction of *p*-nitrophenol.

Experiments were conducted to compare thiol-functionalized (B1), and amino-functionalized (C1) PHEMA-based porous materials as well as the polymer resulting from thiol-yne addition reaction with cysteamine (I). The thiol-containing sample (B1) exhibited the fastest reduction rate, achieving 86 % yield in only 15 min during the first cycle. However, a significant leaching of GNPs was observed as the expected transparent solution turned into black during the course of the catalytic reaction. This observation was confirmed by Dynamic Light Scaterring (DLS) experiments on the resulting solution. The results showed the presence of GNPs with average diameter of about 100 nm and above 1 μm, as observed by SEM (data not shown). The leaching of GNPs led to a dramatic decrease in the GNP-catalyzed reaction rate for the second investigated cycle: an 87% yield was indeed observed after one extra hour.

Additionally, subsequent runs did not show any occurrence of catalytic reaction (Figure 4.6).

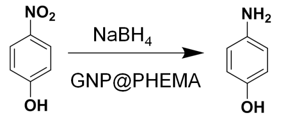

Sample	Yield cycle 1 (%)	Yield cycle 2 (%)	Yield cycle 3 (%)	Yield cycle 4 (%)	Yield cycle 5 (%)
B1	86[a]	87	1	1	1
C1	91	92	92	90	93
I	87	91	90	93	94

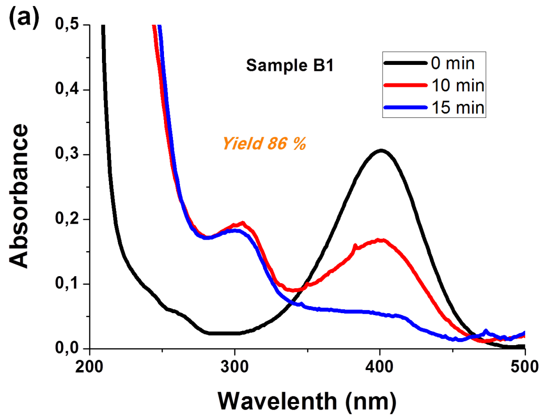

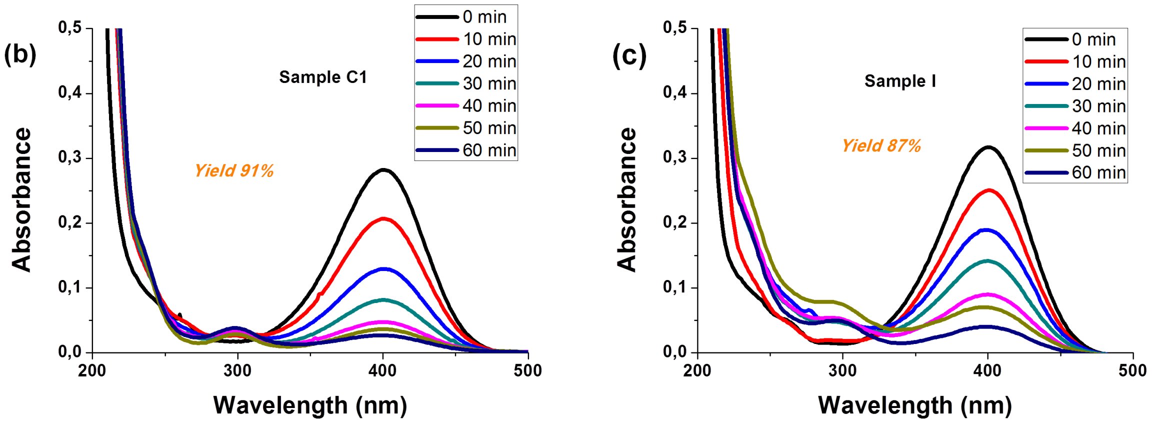

Figure 4.6: UV-Visible investigation of reduction of *p*-nitrophenol into the corresponding *p*-aminophenol catalyzed by the doubly porous GNP@PHEMA-based materials: (a) UV spectra for $NaBH_4$/*p*-nitrophenol solutions before (black trace) and after (blue trace) reaction with sample B1, (b) UV spectra for $NaBH_4$/*p*-nitrophenol solutions before (black trace) and after (dark blue trace) reaction with sample C1, and (c) UV spectra for $NaBH_4$/*p*-nitrophenol solutions before (black trace) and after (dark blue trace) reaction with sample I. The Inset table showed the reusability of the supported catalyst after five runs of the same reduction reaction. ^{a} Yield reached in 15 min.

On the opposite, amino-bearing doubly porous PHEMA-based polymers (C1 and I) displayed excellent reusability and very satisfying yield (around 90% for both in 60 min, Figure 4.6). Furthermore, no traces of gold nanoparticles in the solution were found after catalytic reaction, thus demonstrating that no leaching occurred. The amine function, were better suited to chelate Au^{3+} ions than thiol functions. Moreover, it is noteworthy that sample C1 possessed 9.2 wt.% of GNPs, and sample I contained 12.5 wt.% of GNPs, according to ICP analyses. These results were quite logical as polymer I theoretically possessed a double quantity of groups able to immobilize GNPs.

4.4 Conclusions

In this work, we reported on the preparation of mono- and biporous PHEMA-based materials, and their subsequent functionalization with different organic compounds of interest, namely ethylenediamine (EDA), cysteamine, and propargylamine, among others. In the latter case, a subsequent thiol-yne addition of cysteamine allowed for the preparation of amino-functionalized materials with a higher density of -NH_2 groups at the pore surface than in the case of ethylenediamine-modified materials. Consecutive generation of GNPs through an *in-situ* methodology allowed for the preparation of hybrid materials consisting of amino-functionalized porous PHEMA-based materials on which were adsorbed GNPs. The efficiency of such hybrid systems as catalytic supports was proven *via* hydride-mediated reduction of *p*-nitrophenol that was monitored by UV-Vis spectrometry. Experimentally, better efficiency of amino-bearing hybrid systems was observed when compared to thiol-functionalized ones. More interestingly, biporous systems showed much better efficiency than their monoporous counterparts containing either the upper porosity level or the lower porosity level.

This investigation has paved the way to the design of innovative doubly porous hybrid materials that could find advantage in heterogeneous catalysis.

References

[1] Y. Uyama, K. Kato, and Y. Ikada, “Surface modification of polymers by grafting,” vol. 137, pp. 1–39, 1998.

[2] X. Liu and P. X. Ma, “Polymeric scaffolds for bone tissue engineering,” *Annals of Biomedical Engineering*, vol. 32, pp. 477–486, 2004.

[3] X. Liu, Y. Won, and P. X. Ma, “Surface modification of interconnected porous scaffolds,” *Journal of Biomedical Materials Research Part A*, vol. 74, pp. 84–91, 2005.

[4] H. Yasuda, *Plasma polymerization.* Orlando, Florida: Academic Press, 2012.

[5] N. Inagaki, *Plasma surface modification and plasma polymerization.* Lancaster, Pennsylvania: CRC Press, 1996.

[6] J. G. Terlingen, G. A. Takens, F. J. Van Der Gaag, A. S. Hoffman, and J. Feijen, “On the effect of treating poly (acrylic acid) with argon and tetrafluoromethane plasmas: Kinetics and degradation mechanism,” *Journal of Applied Polymer Science*, vol. 52, pp. 39–53, 1994.

[7] L. Xu, W. Chen, A. Mulchandani, and Y. Yan, “Reversible conversion of conducting polymer films from superhydrophobic to superhydrophilic,” *Angewandte Chemie International Edition*, vol. 44, pp. 6009–6012, 2005.

[8] P. A. Levkin, F. Svec, and J. M. Fréchet, “Porous polymer coatings: a versatile approach to superhydrophobic surfaces,” *Advanced Functional Materials*, vol. 19, pp. 1993–1998, 2009.

[9] C.-D. Ihm and S.-K. Ihm, “Pervaporation of water-ethanol mixtures through sulfonated polystyrene membranes prepared by plasma graft-polymerization,” *Journal of Membrane Science*, vol. 98, pp. 89–96, 1995.

[10] X. Feng and R. Y. Huang, “Liquid separation by membrane pervaporation: a review,” *Industrial & Engineering Chemistry Research*, vol. 36, pp. 1048–1066, 1997.

[11] M. A. El-Sayed, “Some interesting properties of metals confined in time and nanometer space of different shapes,” *Accounts of Chemical Research*, vol. 34, pp. 257–264, 2001.

[12] N. Mizuno and M. Misono, “Heterogeneous catalysis,” *Chemical Reviews*, vol. 98, pp. 199–218, 1998.

[13] A. T. Bell, “The impact of nanoscience on heterogeneous catalysis,” *Science*, vol. 299, pp. 1688–1691, 2003.

[14] R. J. White, R. Luque, V. L. Budarin, J. H. Clark, and D. J. Macquarrie, “Supported metal nanoparticles on porous materials. methods and applications,” *Chemical Society Reviews*, vol. 38, pp. 481–494, 2009.

[15] P. Christopher and S. Linic, “Engineering selectivity in heterogeneous catalysis: Ag nanowires as selective ethylene epoxidation catalysts,” *Journal of the American Chemical Society*, vol. 130, pp. 11264–11265, 2008.

[16] N. T. Phan, M. Van Der Sluys, and C. W. Jones, “On the nature of the active species in palladium catalyzed mizoroki–heck and suzuki–miyaura couplings–homogeneous or heterogeneous catalysis, a critical review,” *Advanced Synthesis & Catalysis*, vol. 348, pp. 609–679, 2006.

[17] A. Baiker, “Progress in asymmetric heterogeneous catalysis: Design of novel chirally modified platinum metal catalysts,” *Journal of Molecular Catalysis A: Chemical*, vol. 115, pp. 473–493, 1997.

[18] E. C. Dreaden, A. M. Alkilany, X. Huang, C. J. Murphy, and M. A. El-Sayed, “The golden age: gold nanoparticles for biomedicine,” *Chemical Society Reviews*, vol. 41, pp. 2740–2779, 2012.

[19] K. C. Grabar, R. G. Freeman, M. B. Hommer, and M. J. Natan, “Preparation and characterization of au colloid monolayers,” *Analytical Chemistry*, vol. 67, pp. 735–743, 1995.

[20] M. Guerrouache, S. Mahouche-Chergui, M. M. Chehimi, and B. Carbonnier, “Site-specific immobilisation of gold nanoparticles on a porous monolith surface by using a thiol–yne click photopatterning approach,” *Chemical Communications*, vol. 48, pp. 7486–7488, 2012.

[21] D. Connolly, B. Twamley, and B. Paull, “High-capacity gold nanoparticle functionalised polymer monoliths,” *Chemical Communications*, vol. 46, pp. 2109–2111, 2010.

[22] Y. Lv, F. M. Alejandro, J. M. Fréchet, and F. Svec, “Preparation of porous polymer monoliths featuring enhanced surface coverage with gold nanoparticles,” *Journal of Chromatography A*, vol. 1261, pp. 121–128, 2012.

[23] C. Féral-Martin, M. Birot, H. Deleuze, A. Desforges, and R. Backov, “Integrative chemistry toward the first spontaneous generation of gold nanoparticles within macrocellular polyhipe supports (au@ polyhipe) and their application to eosin reduction,” *Reactive and Functional Polymers*, vol. 67, pp. 1072–1082, 2007.

[24] S. Mahouche Chergui, A. Ledebt, F. Mammeri, F. Herbst, B. Carbonnier, H. Ben Romdhane, M. Delamar, and M. M. Chehimi, “Hairy carbon nanotube@ nano-pd heterostructures: design, characterization, and application in suzuki c- c coupling reaction,” *Langmuir*, vol. 26, pp. 16115–16121, 2010.

[25] K. Jiang, A. Eitan, L. S. Schadler, P. M. Ajayan, R. W. Siegel, N. Grobert, M. Mayne, M. Reyes-Reyes, H. Terrones, and M. Terrones, “Selective attachment of gold nanoparticles to nitrogen-doped carbon nanotubes,” *Nano Letters*, vol. 3, pp. 275–277, 2003.

[26] Y. Li, X. Fan, J. Qi, J. Ji, S. Wang, G. Zhang, and F. Zhang, “Gold nanoparticles–graphene hybrids as active catalysts for suzuki reaction,” *Materials Research Bulletin*, vol. 45, pp. 1413–1418, 2010.

[27] S. L. Westcott, S. J. Oldenburg, T. R. Lee, and N. J. Halas, “Formation and adsorption of clusters of gold nanoparticles onto functionalized silica nanoparticle surfaces,” *Langmuir*, vol. 14, pp. 5396–5401, 1998.

[28] H.-B. Ly, B. Le Droumaguet, V. Monchiet, and D. Grande, “Designing and modeling doubly porous polymeric materials,” *The European Physical Journal Special Topics*, vol. 224, pp. 1689–1706, 2015.

[29] B. Le Droumaguet, R. Lacombe, H.-B. Ly, M. Guerrouache, B. Carbonnier, and D. Grande, “Engineering functional doubly porous phema-based materials,” *Polymer*, vol. 55, pp. 373–379, 2014.

[30] B. Le Droumaguet, R. Lacombe, H.-B. Ly, B. Carbonnier, and D. Grande, “Novel polymeric materials with double porosity: Synthesis and characterization,” vol. 340, pp. 18–27, 2014.

[31] F. Audouin and A. Heise, “Synthesis of polymer–silica hybrid polyhipes by double in situ polymerization of concentrated water in oil emulsion,” *Polymer*, vol. 55, no. 1, pp. 403–409, 2014.

[32] S. Wunder, F. Polzer, Y. Lu, Y. Mei, and M. Ballauff, “Kinetic analysis of catalytic reduction of 4-nitrophenol by metallic nanoparticles immobilized in spherical polyelectrolyte brushes,” *The Journal of Physical Chemistry C*, vol. 114, pp. 8814–8820, 2010.

[33] M. M. Raju and D. K. Pattanayak, “A platinum supported reduced graphene catalyst to enhance the hydrogenation of nitro compound activity,” *RSC Advances*, vol. 5, pp. 59541–59549, 2015.

Chapter 5

Computation of permeability at the lower porosity level in doubly porous materials

The work developed in this chapter has been published in two papers:

- H.B. Ly, V. Monchiet, D. Grande: Computation of permeability with Fast Fourier Transform from 3-D digital images of porous microstructures, *International Journal of Numerical Methods for Heat and Fluid Flow* , accepted (2015).
- H.B. Ly, B. Le Droumaguet, V. Monchiet, D. Grande: Designing and modeling doubly porous polymeric materials, *Eur. Phys. J. Special Topics* 224, 1689-1706 (2015).

In this chapter, we determine the first permeability by solving the Stokes problem at the nanoscale. This permeability will be used at the intermediate scale to determine the macroscopic permeability, this is the subject of chapter six. The permeability is obtained in the periodic homogenization framework. The unit cell problem consists in solving the Stokes equations with an adherence condition at the solid-fluid interface and the periodic boundary conditions. Two numerical methods are considered: the Finite Element Method (FEM) or iterative scheme based on Fast Fourier Transform (FFT). Various 3-D examples of increasing complexity are considered to show the capacity of the two implemented numerical tools to handle the problem of porous polymers. First, the case of flow through regular arrays of aligned cylinders or spheres are considered as benchmark problems for which comparisons with available results coming from the literature is possible. Next, the method is applied to some more complex and realistic porous solids obtained with assemblies of overlapping spherical pores which are regularly distributed in the volume. In order to determine the permeability of porous polymers at the nanoscale, a unit cell containing a population of randomly distributed spherical and overlapping spherical pores is considered. The case of porous media with different distribution in size is also investigated.

5.1 Introduction

The determination of permeability of porous media in connection with microstructure morphology has been addressed with homogenization techniques based on asymptotic series expansion methods [1–3] or on energy principle and volume averaging [4, 5].
At the nanoscopic level, we consider a porous medium fulfilled by a newtonian viscous fluid with the dynamic viscosity μ. The periodic medium can be represented by a parallelepiped (rectangle for 2D problems) unit cell and three vectors (2 vectors for 2D problems) of spatial invariance. We define by Ω_f the volume of the fluid, Ω_s the volume of the solid phase, and Ω=$\Omega_s \cup \Omega_f$ the total volume of the unit cell. The surface between the fluid and the polymer is denoted by Γ. The flow is assumed to be incompressible and obeys to the Stokes equations:

$$\begin{aligned} \mu\Delta\boldsymbol{v} - \nabla p - \boldsymbol{G} &= 0 \quad x \in \Omega_f \\ \operatorname{div}\boldsymbol{v} &= 0 \quad x \in \Omega_f \\ \boldsymbol{v} &= 0 \quad x \in \Gamma \end{aligned} \tag{5.1}$$

with the periodicity conditions for the velocity and the pressure.
In the above relations, $\boldsymbol{v}$ and p are respectively the local velocity and pressure fields. The flow of the fluid is generated by a prescribed macroscopic pressure gradient, denoted by $\boldsymbol{G}$. In (5.1), p denotes the periodic pressure. At the local scale, the components of the velocity field $\boldsymbol{v}$ linearly depends on the components of the

macroscopic pressure gradient:

$$\boldsymbol{v} = \boldsymbol{A}(x).\boldsymbol{G} \tag{5.2}$$

where $\boldsymbol{A}$ is the localisation tensor which depends on the position vector. As shown in the framework of the homogenization applied to porous media [1–3], the average of the velocity field over the volume of the unit cell is the Darcy law:

$$< \boldsymbol{v} >_V = -\frac{1}{\mu}\boldsymbol{K}_{\text{meso}}.\boldsymbol{G} \tag{5.3}$$

which involves the permeability tensor $\boldsymbol{K}_{\text{meso}}$ that will be used at the mesoscopic scale (or intermediate scale) to describe the fluid flow in the nanopores.

Analytic methods have been first developed in the literature for solving the associated unit cell problem. For instance, some works use expansions along eigenfunctions [6–9], however such approaches are limited to some simple geometries corresponding to the flow through regular arrays of cylinders or spheres. The use of high-performance computers open number of possibilities for considering more realistic geometries, based on reconstructed porous cell or directly based on digital images obtained from X-ray microtomography. This also encourages the development of robust and efficient numerical tools for computing the effective permeability. For instance, standard numerical methods based on Finite Elements (FEM) or Finite Volumes have been often considered for computing the permeability of porous media [10–18]. The computation of permeability by means of the Boundary Element Method (BEM) has has been also proposed [19] or using the Lattice Boltzmann method [20–22]. When the microstructure is defined by voxels, the FEM can be used by considering a regular mesh with cubic elements. However the use of FFT type algorithms is more adapted for reducing the memory saving. Indeed, the method do not need the storage of stiffness or interaction matrices but only the storage of the nodal variables and the Fourier coefficients of the Green tensors. Moreover, the case of incompressible constituents (the fluid) does not requires specific treatments while, the FEM uses more sophisticated interpolation (for instance the "MINI" elements [23–25]) which generally increases the size of the system. In this chapter, we aim to determine the permeability tensor of a porous medium constituted of a random distribution of spherical pores and which can mimic realistically the porous polymer designed and depicted in the first part of this work. The method based on Fast Fourier Transform is privileged since it is possible to be applied to high dimension problems. Besides, some comparisons between FFT and FEM capacities are provided in this chapter. Note also that particular attention is paid to the description of the Finite Element implementation of the Stokes problem which will serves for the resolution of the Darcy-Stokes problems presented in chapter 5.

5.2 Solving Stokes equations by Finite Element method

5.2.1 Variational formulation of Stokes problem

The suitable variational form of the Stokes problem is provided by taking two test functions $\boldsymbol{w} \in \mathcal{W}$ and $q \in \mathcal{Q}$ where $\mathcal{W}$ and $\mathcal{Q}$ are two admissible spaces. $\mathcal{W}$ is the space of continuous, square integrable, periodic, derivable velocity fields and which are null on Γ. On the other hand, $\mathcal{Q}$ is the space of square integrable and periodic fields but not necessary continuous. As shown in the next, the pressure can be also assimilated as Lagrange multiplier associated with the incompressibility for the velocity field. Obviously, by taking continuous fields, a better approximation is derived for the pressure distribution. However, if we only interested with the determination of the velocity field, for computing the intrinsic permeability, it is not necessary to use continuous fields for the pressure.

By multiplying the first equation in (5.1) by $\boldsymbol{w}$, the second equation in (5.1) by q and by integrating over the volume of fluid Ω_f we obtain:

$$\int_{\Omega_f} \mu(\Delta \boldsymbol{v}).\boldsymbol{w} dx - \int_{\Omega_f} (\nabla p).\boldsymbol{w} dx - \int_{\Omega_f} \boldsymbol{G}.\boldsymbol{w} dx = 0 \tag{5.4}$$

$$\int_{\Omega_f} q \operatorname{div}(\boldsymbol{v}) dx = 0 \tag{5.5}$$

Note that, due to the incompressibility, it is possible, in the first equation in (5.4), to replace $\mu\Delta\boldsymbol{v}$ by $\operatorname{div}(2\mu\boldsymbol{d}(\boldsymbol{v}))$ where $\boldsymbol{d}(\boldsymbol{v})$ is the strain rate tensor associated to the velocity $\boldsymbol{v}$:

$$\boldsymbol{d}(\boldsymbol{v}) = \frac{1}{2}(\nabla \boldsymbol{v} + \nabla^t \boldsymbol{v}) \tag{5.6}$$

Making use of the divergence theorem in the two equations in (5.4), it gives:

$$\begin{aligned} \int_{\partial\Omega_f \cup \Gamma} [2\mu\boldsymbol{d}(\boldsymbol{v}).\boldsymbol{n}].\boldsymbol{w} dx - \int_{\Omega_f} 2\mu\boldsymbol{d}(\boldsymbol{v}) : \nabla\boldsymbol{w} dx - \int_{\partial\Omega_f \cup \Gamma} p\boldsymbol{w}.\boldsymbol{n} dx \\ + \int_{\Omega_f} p \operatorname{div}(\boldsymbol{w}) dx - \int_{\Omega_f} \boldsymbol{G}.\boldsymbol{w} dx = 0 \end{aligned} \tag{5.7}$$

$$\int_{\Omega_f} q \operatorname{div}(\boldsymbol{v}) dx = 0 \tag{5.8}$$

where $\partial\Omega_f$ is the portion of the cell boundary $\partial\Omega$ crossed by the fluid. The first integral in (5.7) is null. The integral over Γ is null since $\boldsymbol{w} = 0$ on Γ. The integral over $\partial\Omega_f$ is null since the term $2\mu\boldsymbol{d}(\boldsymbol{v}).\boldsymbol{n}$ is antiperiodic while $\boldsymbol{w}$ is periodic.

For the same reason, the third integral in (5.7) is null. Indeed, $\boldsymbol{w}$ is null on Γ while p is periodic and $\boldsymbol{w}.\boldsymbol{n}$ is antiperiodic.

Note also that, in the second integral in (5.7), $\nabla\boldsymbol{w}$ can be replaced by $\boldsymbol{d}(\boldsymbol{w})$ since $\boldsymbol{d}(\boldsymbol{v})$

is a symmetric two order tensor.
It then remains:

$$-\int_{\Omega_f} 2\mu \boldsymbol{d}(\boldsymbol{v}) : \boldsymbol{d}(\boldsymbol{w}) dx + \int_{\Omega_f} p \,\mathrm{div}(\boldsymbol{w}) dx - \int_{\Omega_f} \boldsymbol{G}.\boldsymbol{w} dx = 0 \tag{5.9}$$

$$\int_{\Omega_f} q \,\mathrm{div}(\boldsymbol{v}) dx = 0 \tag{5.10}$$

Introducing $(\cdot,\cdot)$ the inner product or duality pairing to simplify the expressions, we obtain:

$$\begin{cases} 2\mu(\boldsymbol{d}(\boldsymbol{v}), \boldsymbol{d}(\boldsymbol{w})) - (p, \mathrm{div}(\boldsymbol{w})) = -(\boldsymbol{G}, \boldsymbol{w}) \\ (\mathrm{div}(\boldsymbol{v}), q) = (0, q) \end{cases} \tag{5.11}$$

By replacing $\boldsymbol{w}$ and q by $\delta\boldsymbol{v}$ and δp respectively, the above two equations are equivalently given by $\delta\Phi(\boldsymbol{v}, p) = 0$ where $\Phi(\boldsymbol{v}, p)$ is given by:

$$\Phi(\boldsymbol{v}, p) = \mu(\boldsymbol{d}(\boldsymbol{v}), \boldsymbol{d}(\boldsymbol{v})) - (p, \mathrm{div}(\boldsymbol{v})) + (\boldsymbol{G}, \boldsymbol{v}) \tag{5.12}$$

The solution then appears as the stationarity point (saddle-point) of the functional $\Phi(\boldsymbol{v}, p)$.

5.2.2 Choice of elements

The domain Ω_f is meshed and different approximations for the velocity and pressure field are used in the elements:

$$\boldsymbol{v} = \sum_{i=1}^{i=r} \boldsymbol{v}^i N_i(\boldsymbol{x}), \quad p = \sum_{i=1}^{i=s} p^i N_i(\boldsymbol{x}) \tag{5.13}$$

where $\boldsymbol{v}^i$ and p^i are the Degrees Of Freedom (DOFs) and $N_i(\boldsymbol{x})$ for $i = 1, 2, 3...$ are the basis functions. Note that, in each element, the velocity field and the pressure are not necessary interpolated with the same number of basis functions, that is the reason why, in equation (5.13), the sum is made for i from 1 to r while the second sum is made for i from 1 to s.

For the numerical integration wich will be presented in the newt of this chapter, it is convenient to put the relations (5.13) into the following matricial form:

$$\left\{\begin{matrix} v_x(\boldsymbol{x}) \\ v_y(\boldsymbol{x}) \\ v_z(\boldsymbol{x}) \end{matrix}\right\} = \underbrace{\begin{bmatrix} N_1 & 0 & 0 & N_2 & 0 & 0 & \dots \\ 0 & N_1 & 0 & 0 & N_2 & 0 & \dots \\ 0 & 0 & N_1 & 0 & 0 & N_2 & \dots \end{bmatrix}}_{=[D(\boldsymbol{x})]} \underbrace{\left\{\begin{matrix} v_x^1 \\ v_y^1 \\ v_z^1 \\ v_x^2 \\ v_y^2 \\ v_z^2 \\ \vdots \end{matrix}\right\}}_{=\{v_e\}} \tag{5.14}$$

$$p(\boldsymbol{x}) = \underbrace{\begin{bmatrix} N_1 & N_2 & N_3 & \dots \end{bmatrix}}_{=[F(\boldsymbol{x})]} \underbrace{\left\{\begin{matrix} p^1 \\ p^2 \\ p^3 \\ \vdots \end{matrix}\right\}}_{=\{p_e\}} \tag{5.15}$$

In the next, are provided various possible interpolation, which are used in the chapter and which respect the LBB condition.

5.2.2.1 Rectangular/cuboidal elements

We consider a discretization of 2D porous microstructures with rectangular elements. It is convenient to use the local basis (ξ, η) instead of the components (x, y) of the vector position $\boldsymbol{x}$. These variables being related by:

$$x = x_1N_1 + x_2N_2 + x_3N_3 + x_4N_4 \tag{5.16}$$

$$y = y_1N_1 + y_2N_2 + y_3N_3 + y_4N_4 \tag{5.17}$$

where N_i for $i = 1, 2, 3, 4$ are the basis function defined by:

$$N_1 = (1-\xi)(1-\eta),\ N_2 = \xi(1-\eta),\quad N_3 = \eta(1-\xi),\quad N_4 = \xi\eta \tag{5.18}$$

and where (x_1, y_1), (x_2, y_2), ... represents the position of the corner of the rectangular element as defined in Figure 5.1. In (5.18), the dimensionless variables ξ and η vary from 0 to 1.

Both the velocity and the pressure are interpolated with the polynomials N_i for $i = 1, 2, 3, 4$:

$$\boldsymbol{v} = \sum_{i=1}^{i=4} \boldsymbol{v}^i N_i,\quad p = \sum_{i=1}^{i=4} p^i N_i \tag{5.19}$$

where $\boldsymbol{v}^i$ and p^i are the values of the velocity and pressure at the corner of the rectangular element.

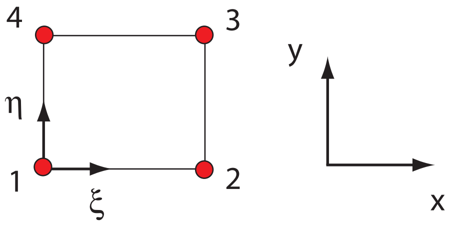

Figure 5.1: Rectangular element.

In the 3D case, cuboidal elements (see Figure 5.2) are used with the following basis functions:

$$\begin{aligned} &N_1 = (1-\xi)(1-\eta)(1-\zeta), \quad &&N_2 = \xi(1-\eta)(1-\zeta), \quad &&N_3 = \xi\eta(1-\zeta) \\ &N_4 = (1-\xi)\eta(1-\zeta), &&N_5 = (1-\xi)(1-\eta)\zeta, &&N_6 = \xi(1-\eta)\zeta \\ &N_7 = \xi\eta\zeta, &&N_8 = (1-\xi)\eta\zeta \end{aligned} \tag{5.20}$$

The velocity and pressure in the cuboidal element are given by:

$$\boldsymbol{v} = \sum_{i=1}^{i=8} \boldsymbol{v}^i N_i, \quad p = \sum_{i=1}^{i=8} p^i N_i \tag{5.21}$$

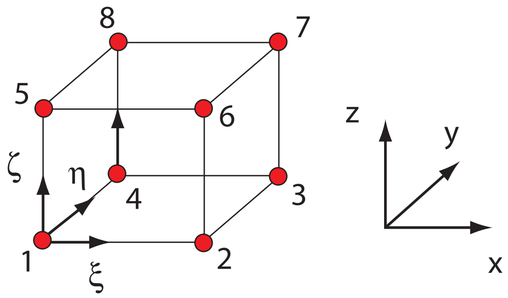

Figure 5.2: Cuboidal element.

For 2D case, the total Degree Of Freedom (DOF) is 12: two components of the velocity at each corner + the one pressure at each corner. For 3D case, the total DOF is 32: three components of the velocity at each corner + the one pressure at each corner.

5.2.2.2 The MINI elements

In the 2D case, triangular elements are considered (see Figure (6.5)). In the coordinate system (ξ, η) related to the reference triangular element, the basis functions have the following form:

$$N_1 = 1 - \xi - \eta, \quad N_2 = \xi, \quad N_3 = \eta, \quad N_4 = N_1 N_2 N_3 \tag{5.22}$$

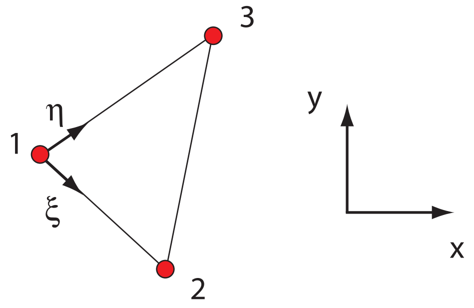

Figure 5.3: Triangular MINI element

N_4 is the bubble function, it is null everywhere on the boundary of the element. In 3D case, tetrahedra elements are used. and the basis functions are:

$$N_1 = 1 - \xi - \eta - \zeta, \quad N_2 = \xi, \quad N_3 = \eta, \quad N_4 = \zeta, \quad N_5 = N_1 N_2 N_3 N_4 \tag{5.23}$$

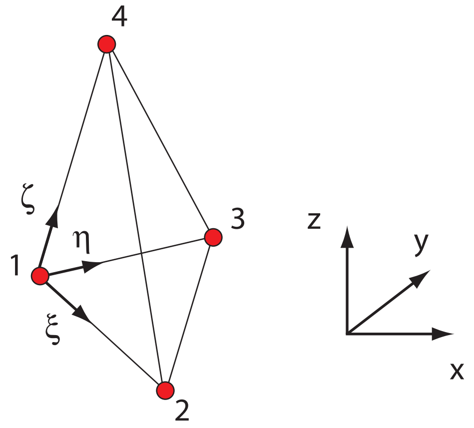

Figure 5.4: Tetrahedral MINI element

N_5 is the bubble function for 3D element.
The local basis (ξ, η, ζ) is related to (x, y, z) by:

$$\left\{ \begin{aligned} x &= x_1 N_1 + x_2 N_2 + x_3 N_3 \\ y &= y_1 N_1 + y_2 N_2 + y_3 N_3 \end{aligned} \right. \text{(2D)}, \quad \left\{ \begin{aligned} x &= x_1 N_1 + x_2 N_2 + x_3 N_3 + x_4 N_4 \\ y &= y_1 N_1 + y_2 N_2 + y_3 N_3 + y_4 N_4 \\ z &= z_1 N_1 + z_2 N_2 + z_3 N_3 + z_4 N_4 \end{aligned} \right. \text{(3D)} \tag{5.24}$$

The velocity in the triangular element is taken into the form:

$$\boldsymbol{v} = \sum_{i=1}^{i=r} N_i \boldsymbol{v}^i \tag{5.25}$$

where $r = 4$ for the 2D case but $r = 5$ for 3D case. $\boldsymbol{v}^i$ for $i = 1, 2, 3$ are the velocities at the corner of the element. For the pressure, a linear interpolation is used:

$$p = \sum_{i=1}^{i=s} p^i N_i \tag{5.26}$$

with $s = 3$ for the 2D case and $s = 4$ for the 3D case.

The bubble function is used only for the velocity field and is considered in order to comply with the BBL stability condition. In the 2D case, each element has 11 degrees of freedom: two components of the velocity at each corner + two components of the bubble function + one pressure at each corner. In the 3D case, each element has 19 degrees of freedom: three components of the velocity at each corner + three components of the bubble function + one pressure at each corner.

5.2.2.3 Taylor-Hood elements

The Taylor-Hood elements had 6 interpolation points (3 each corners and 3 at each edge),

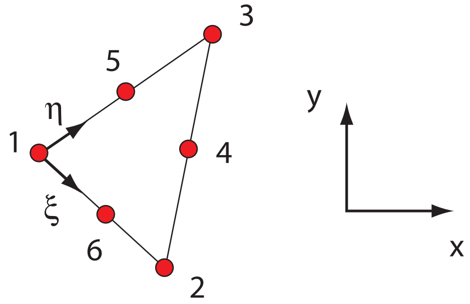

Figure 5.5: Taylor-Hood triangular element.

The basis functions are (in 2D case):

$$\begin{cases} N_1 = (2\xi - 1 + 2\eta)(\xi - 1 + \eta), & N_2 = \xi(-1 + 2\xi), \qquad N_3 = \eta(-1 + 2\eta) \\ N_4 = -4\eta(\xi - 1 + \eta), & N_5 = -4\xi(\xi - 1 + \eta), \qquad N_6 = 4\xi\eta \end{cases} \tag{5.27}$$

and in 3-D case:

$$\begin{cases} S = 1 - \xi - \eta - \zeta, \\ N_1 = S(2S - 1), \quad N_2 = \xi(2\xi - 1), \quad N_3 = \eta(2\eta - 1), \\ N_4 = \zeta(2\zeta - 1), \quad N_5 = 4\xi S, \quad N_6 = 4\xi\eta, \\ N_7 = 4\eta S, \quad N_8 = 4\zeta S, \quad N_9 = 4\xi\zeta, \\ N_{10} = 4\eta\zeta, \end{cases} \tag{5.28}$$

The velocity field is:

$$\boldsymbol{v} = \sum_{i=1}^{i=r} \boldsymbol{v}^i N_i \tag{5.29}$$

where $r = 6$ for the 2D case and $r = 10$ for the 3D one.

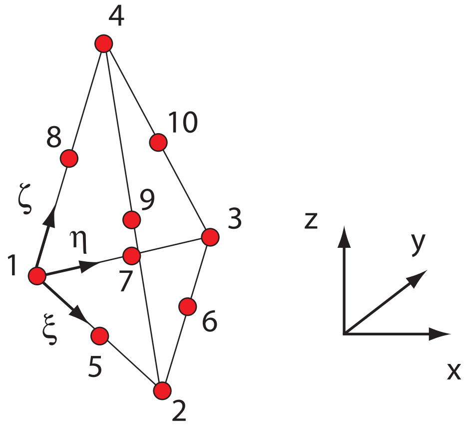

Figure 5.6: Taylor-Hood tetrahedral element.

The linear interpolation (5.26) is still considered for the pressure. In the 2D case, the number of DOFs is 15: two components of the velocity a each corner + two components of the velocity at each edge + the pressure at each corner. For 3-D computations, the Taylor-Hood elements have 34 DOFs: 3 components of the velocity field at each corner + 3 components of the velocity field at each edge + the pressure at each corner.

5.2.3 Finite Element discretization

By considering the trial fields (5.13) in (5.12), it leads to the following expression for Φ:

$$\Phi = \frac{1}{2} \sum_{\text{elements}} \{v\}^t [K] \{v\} - \{p^t\} [B] \{v\} + \{v\}^t \{b\} \tag{5.30}$$

which involves the computation of the matrices $[K]$ and $[B]$ and the vector $\{b\}$. Vectors $\{v\}$ and $\{p\}$ contain all the DOFs for the velocity and the pressure.

The determination of the stationarity point of Φ involves the resolution of the linear system:

$$\begin{bmatrix} K & -B^t \\ -B & 0 \end{bmatrix} \begin{Bmatrix} v \\ p \end{Bmatrix} = \begin{Bmatrix} b \\ 0 \end{Bmatrix} \tag{5.31}$$

Below we describe the method for computing $[K]$, $[B]$ and $\{b\}$. For simplicity, only the discretization in the 3D case is provided in the next of this section. The 2D case could be obtained by eliminating all the row and the columns corresponding to the components associated with the Oz direction.

The computation of the components of the strain rate tensor with the expressions (5.13) leads to the following relations:

$$\left\{\begin{array}{c} d_{xx} \\ d_{yy} \\ d_{zz} \\ 2d_{yz} \\ 2d_{xz} \\ 2d_{xy} \end{array}\right\} = \left[\quad E(\boldsymbol{x}) \quad\right] \underbrace{\left\{\begin{array}{c} v_x^1 \\ v_y^1 \\ v_z^1 \\ v_x^2 \\ v_y^2 \\ v_z^2 \\ \vdots \\ \\ \end{array}\right\}}_{=\{v_e\}} \tag{5.32}$$

in which the matrix $[E(\boldsymbol{x})]$ is function of the coordinates and on the choice of the element : cuboidal, tetrahedral MINI element or tetrahedral Taylor-Hood element. The components of $[E(\boldsymbol{x})]$ are:

$$[E(\boldsymbol{x})] = \left[\begin{array}{ccc|ccc|c} N_{1,x} & 0 & 0 & N_{2,x} & 0 & 0 & \dots \\ 0 & N_{1,y} & 0 & 0 & N_{2,y} & 0 & \dots \\ 0 & 0 & N_{1,z} & 0 & 0 & N_{2,z} & \dots \\ 0 & N_{1,z} & N_{1,y} & 0 & N_{2,z} & N_{2,y} & \dots \\ N_{1,z} & 0 & N_{1,x} & N_{2,z} & 0 & N_{2,x} & \dots \\ N_{1,y} & N_{1,x} & 0 & N_{2,y} & N_{2,x} & 0 & \dots \end{array}\right] \tag{5.33}$$

The basis functions being defined with the coordinates (ξ, η, ζ), the computation of the jacobian matrix is involved:

$$J_{ij} = \begin{bmatrix} \xi_{,x} & \xi_{,y} & \xi_{,z} \\ \eta_{,x} & \eta_{,y} & \eta_{,z} \\ \zeta_{,x} & \zeta_{,y} & \zeta_{,z} \end{bmatrix} \tag{5.34}$$

The inverse of J_{ij} is given by:

$$J_{ij}^{-1} = \begin{bmatrix} x_{,\xi} & x_{,\eta} & x_{,\zeta} \\ y_{,\xi} & y_{,\eta} & y_{,\zeta} \\ z_{,\xi} & z_{,\eta} & z_{,\zeta} \end{bmatrix} = \begin{bmatrix} x_2 - x_1 & x_3 - x_1 & x_4 - x_1 \\ y_2 - y_1 & y_3 - y_1 & y_4 - y_1 \\ z_2 - z_1 & z_3 - z_1 & z_4 - z_1 \end{bmatrix} \tag{5.35}$$

Owing to relation (5.32), the first term in (5.11) is:

$$\mu(\boldsymbol{d}(\underline{v}), \boldsymbol{d}(\underline{v})) = \frac{1}{2} \sum_{\text{elements}} \{v_e\}^t [K_e] \{v_e\} = \frac{1}{2} \sum_{\text{elements}} \{v\}^t [K] \{v\} \tag{5.36}$$

where the elementary matrix $[K_e]$ is given by:

$$[K_e] = \int_{\text{element}} [E(\overline{\boldsymbol{x}})]^t [L][E(\overline{\boldsymbol{x}})] dx \tag{5.37}$$

and the matrix $[L]$ is given by:

$$[L] = \begin{bmatrix} 2\mu & 0 & 0 & 0 & 0 & 0 \\ 0 & 2\mu & 0 & 0 & 0 & 0 \\ 0 & 0 & 2\mu & 0 & 0 & 0 \\ 0 & 0 & 0 & \mu & 0 & 0 \\ 0 & 0 & 0 & 0 & \mu & 0 \\ 0 & 0 & 0 & 0 & 0 & \mu \end{bmatrix} \tag{5.38}$$

The full calculation of matrix $[K_e]$ is performed on Maple. The second term in (5.11) reads:

$$(p, \operatorname{div}(\underline{v})) = \sum_{\text{elements}} \{p\}^t [B_e] \{v_e\} = \{p\}^t [B] \{v\} \tag{5.39}$$

with:

$$[B_e] = \int_{\text{element}} [F(\boldsymbol{x})]^t [T][E(\boldsymbol{x})] dx \tag{5.40}$$

with:

$$[T] = \begin{bmatrix} 1 & 1 & 1 & 0 & 0 & 0 \end{bmatrix} \tag{5.41}$$

The last term in (5.11) is:

$$(\boldsymbol{G}, \underline{v}) = \sum_{\text{elements}} \{v_e\}^t \{b_e\} = \{v\}^t \{b\} \tag{5.42}$$

with:

$$\{b_e\} = \int_{\text{elements}} [D(\boldsymbol{x})]^T \{G\} dx \tag{5.43}$$

and:

$$\{G\} = \begin{Bmatrix} G_x \\ G_y \\ G_z \end{Bmatrix} \tag{5.44}$$

matrices $[K]$, $[B]$ and $\{b\}$ are fully determined by the elementary matrices $[K_e]$, $[B_e]$ and elementary vector $\{b_e\}$. Obviously, all the components of these matrices depends on the choice of element : cuboidal, tetrahedral MINI element or tetrahedral Taylor-Hood element. The computation $[K_e]$, $[B_e]$, $\{b_e\}$ has been made analytically on Maple and stored in Matlab to construct the global matrices $[K]$, $[B]$ and vector $\{b\}$.

5.2.4 Integration of the boundary conditions

Two kind of boundary conditions must be considered in the linear system: the adherence conditions at the fluid-solid interface, the periodic conditions.

5.2.4.1 Adherence

At the interface between the solid and the fluid the velocity field must be taken as zero. This condition is accounted by removing, in the linear system (6.88), all the nodal DOF at the interface. The reduced linear system is:

$$\begin{bmatrix} \widetilde{K} & -\widetilde{B}^t \\ -\widetilde{B} & 0 \end{bmatrix} \begin{Bmatrix} \widetilde{v} \\ \widetilde{p} \end{Bmatrix} = \begin{Bmatrix} \widetilde{b} \\ 0 \end{Bmatrix} \tag{5.45}$$

The vector

$$\begin{Bmatrix} \widetilde{v} \\ \widetilde{p} \end{Bmatrix} \tag{5.46}$$

is computed from

$$\begin{Bmatrix} v \\ p \end{Bmatrix} \tag{5.47}$$

by eliminating all the nodal DOFs which are at the interface.

5.2.4.2 Periodic conditions

The periodic conditions are verified if the velocity and the pressure take the same values on the opposite side of the unit cell. This formally reads for the velocity field:

$$\begin{cases} \boldsymbol{v}(x=-h/2,y,z) = \boldsymbol{v}(x=h/2,y,z) \\ \boldsymbol{v}(x,y=-h/2,z) = \boldsymbol{v}(x,y=h/2,z) \\ \boldsymbol{v}(x,y,z=-h/2) = \boldsymbol{v}(x,y,z=h/2) \end{cases} \tag{5.48}$$

and for the pressure

$$\begin{cases} p(x=-h/2,y,z) = p(x=h/2,y,z) \\ p(x,y=-h/2,z) = p(x,y=h/2,z) \\ p(x,y,z=-h/2) = p(x,y,z=h/2) \end{cases} \tag{5.49}$$

In the discretized form, the periodic boundary conditions can be read:

$$[C_v]\left\{ \widetilde{v} \right\} = \left\{ 0 \right\}, \quad [C_p]\left\{ \widetilde{p} \right\} = \left\{ 0 \right\} \tag{5.50}$$

These conditions are taken into account in the linear system by introducing Lagrange multipliers, λ_v and λ_p:

$$\begin{bmatrix} \widetilde{K} & -\widetilde{B}^t & C_v^T & 0 \\ -\widetilde{B} & 0 & 0 & C_p^t \\ C_v & 0 & 0 & 0 \\ 0 & C_p & 0 & 0 \end{bmatrix} \begin{Bmatrix} \widetilde{v} \\ \widetilde{p} \\ \lambda_v \\ \lambda_p \end{Bmatrix} = \begin{Bmatrix} \widetilde{b} \\ 0 \\ 0 \\ 0 \end{Bmatrix} \tag{5.51}$$

This linear system is solved by means of the conjugate gradient iterative scheme.

5.3 Solving Stokes equations by Fast Fourier Transform

The FFT methods has been first introduced by Moulinec *et al.* [26, 27] to handle the problem of elastic composites and to determine the effective stiffness. The principle of this approach consists to rewrite the local problem into an integral equation well known as "Lippmann-Schwinger equation". This equation introduces the Green tensor and is solved by expanding the solution along Neummann series. This method has been thereafter extended to the resolution of the Stokes problem for 2D porous solid [28]. In this section, we recall the main results of this approach.

5.3.1 Reformulation of Stokes equations for FFT implementation

In order to apply the FFT method to the resolution of Stokes equations (5.1), it is rewritten in a more suitable form. First of all, let us introduce the pseudo compliance tensor $\mathbb{S}$ by

$$\mathbb{S} = \frac{1}{2\mu(\boldsymbol{x})}\mathbb{K} \quad \text{with:} \quad \mu(\boldsymbol{x}) = \begin{cases} \mu & \text{in } \Omega \\ h\mu & \text{in } \Omega \end{cases} \tag{5.52}$$

where the tensor $\mathbb{K}$ is a projector defined by

$$\boldsymbol{K} = \mathbb{I} - \mathbb{J}, \quad \mathbb{J} = \frac{1}{3}\boldsymbol{I} \otimes \boldsymbol{I} \tag{5.53}$$

where $\boldsymbol{I}$ and $\mathbb{I}$ are the two order and fourth order identity tensors respectively and having the components δ_{ij} and $(\delta_{ik}\delta_{jl} + \delta_{il}\delta_{jk})/2$ where δ_{ij} is the Kronecker symbol. For any two order tensor $\boldsymbol{\sigma}$,

$$\overline{\boldsymbol{\sigma}} = \boldsymbol{K} : \boldsymbol{\sigma} \tag{5.54}$$

represents the deviatoric part of $\boldsymbol{\sigma}$. In equation (5.52), we have introduced the viscosity $h\mu$ in the solid part. This coefficient h is chosen very large so that we retrieve the

condition $\boldsymbol{v} = 0$ in the solid part. Classically, when solving the Stokes equations by the FEM, only the fluid domain is discretized, the adherence at the interface between the fluid and the solid domain is then just considered as a boundary condition for the velocity field. This condition is generally obtained with Lagrange multipliers or by a penalized terms. The FFT method use a discretization of the problem by means of Fourier series and use the discrete Fourier transform (this is more precisely explained in the next of the paper). By doing so, the method use a discretization of the problem with a regular grid and each point lie within the fluid phase or within the solid phase. Consequently, in order to retrieve the condition $\boldsymbol{v} = 0$ within the solid phase, we replace it by a viscous fluid of viscosity $h\mu$ where h is a constant which is chosen sufficiently large. This coefficient can then be interpreted as a penalty coefficient as used in the FEM for obtaining the adherence on the fluid/solid interface.
With these definitions, the Stokes problem (5.1) can be rewritten into the form:

$$\begin{cases} \boldsymbol{d} = \frac{1}{2}(\nabla \boldsymbol{v} + \nabla^t \boldsymbol{v}) & \text{in} \quad \Omega \\ \boldsymbol{d} = \mathbb{S} : \boldsymbol{\sigma} & \text{in} \quad \Omega \\ \operatorname{div}(\boldsymbol{\sigma}) + \boldsymbol{f} = 0 & \text{in} \quad \Omega \\ \boldsymbol{\sigma}.\boldsymbol{n} & \text{antiperiodic} \\ \boldsymbol{v} & \text{periodic} \end{cases} \tag{5.55}$$

In these equations, a continuation by continuity of the velocity field $\boldsymbol{v}$, the strain rate $\boldsymbol{d}$ and the stress $\boldsymbol{\sigma}$ is made in the solid phase. The condition $\boldsymbol{v} = 0$ in Ω_s is verified when h tends to infinity in the expression of $\mathbb{S}$. The problem depicted in equation (5.55) is equivalent to a composite, however, the loading is not given by an applied macroscopic strain or stress but a body force $\boldsymbol{f}$ which equal to $\boldsymbol{G}$ in the fluid phase. In the solid phase, $\boldsymbol{f}$ is assumed to be constant and is determined as function of the applied pressure gradient by using the equilibrium of the cell. This equilibrium reads:

$$\int_{\partial\Omega} \boldsymbol{\sigma}.\boldsymbol{n} dS + \int_{\Omega} \boldsymbol{f} dV = 0 \tag{5.56}$$

Since the stress field is periodic, and so $\boldsymbol{\sigma}.\boldsymbol{n}$ antiperiodic, the first integral is null. By dividing the above relation by the volume of the unit cell, we obtain:

$$< \boldsymbol{f} >_{\Omega} = 0 \tag{5.57}$$

In order to comply with the above condition, the expression of the body force in the solid phase is:

$$\boldsymbol{f} = -\frac{c_f}{c_s} \boldsymbol{G} \tag{5.58}$$

where c_f et c_s are the volume fraction of the fluid phase and the solid phase, respectively. The body force $\boldsymbol{f}$ in the solid phase represents physically the drag force due to the fluid flow. It is then possible to rewrite $\boldsymbol{f}$ into the form:

$$\boldsymbol{f} = \left[\mathrm{I}_f(\boldsymbol{x}) - \frac{c_f}{c_s} \mathrm{I}_s(\boldsymbol{x}) \right] \boldsymbol{G} \tag{5.59}$$

where $\mathrm{I}_f(\boldsymbol{x})$ et $\mathrm{I}_f(\boldsymbol{x})$ are the characteristic functions of the phases:

$$\mathrm{I}_f(\boldsymbol{x}) = \begin{cases} 0 & \text{in } \Omega_s \\ 1 & \text{in } \Omega_f \end{cases} , \quad \mathrm{I}_f(\boldsymbol{x}) = 1 - \mathrm{I}_s(\boldsymbol{x}) \tag{5.60}$$

5.3.2 Integral forms of the homogenization problem

The system of equations (5.55) is similar to the problems of an elastic two-phase composite. Indeed, the fluid can be assimilated to a linear viscous and incompressible elastic solid while the skeleton is considered as a rigid phase. The equations in (5.55) only differs by the loading: a macroscopic deformation is considered for the elastic composite while a pressure gradient $\boldsymbol{G}$ is applied for the Stokes problem. Thus, it is possible to rewrite the Stokes equations as Lippmann-Schwinger equations.

In order to formulate the integral equation for the Stokes problem, let us introduce a fictitious compressibility k such that the pseudo-compliance tensor $\mathbb{S}$ can be written as:

$$\mathbb{S} = \frac{1}{3k}\mathbb{J} + \frac{1}{2\mu(x)}\mathbb{K} \tag{5.61}$$

the Stokes problem is then recovered by taking the value $+\infty$ for k. Obviously, the fourth order tensor $\mathbb{S}$ is not invertible since k takes the values $+\infty$ in the solid phase, however, by keeping k finite, the inversion of $\mathbb{S}$, giving $\mathbb{C}$, leads to

$$\mathbb{C} = (\mathbb{S})^{-1} = 3k\mathbb{J} + 2\mu(x)\mathbb{K} \tag{5.62}$$

Considering now these notations, and introducing a reference medium of constant stiffness $\mathbb{C}^0$, the Stokes equations (5.55) can then reformulated as follows:

$$\begin{cases} \boldsymbol{d} = \frac{1}{2}(\nabla \boldsymbol{v} + \nabla^t \boldsymbol{v}) & \text{in} \quad \Omega \\ \boldsymbol{\sigma} = \mathbb{C}^0 : \boldsymbol{d} + \boldsymbol{\tau} & \text{in} \quad \Omega \\ \operatorname{div}(\boldsymbol{\sigma}) + \boldsymbol{f} = 0 & \text{in} \quad \Omega \\ \boldsymbol{\sigma}.\boldsymbol{n} & \text{antiperiodic} \\ \boldsymbol{v} & \text{periodic} \end{cases} \tag{5.63}$$

where $\boldsymbol{\tau}$ is the polarization tensor, defined by :

$$\boldsymbol{\tau} = (\mathbb{C} - \mathbb{C}^0) : \boldsymbol{d} = \boldsymbol{\sigma} - \mathbb{C}^0 : \boldsymbol{d} \tag{5.64}$$

The solution of the Stokes problem (5.63), for $\boldsymbol{\tau}$ and $\boldsymbol{f}$ imposed, is written (cf. [28]):

$$\boldsymbol{d} = -\boldsymbol{\Gamma}^0 * (\boldsymbol{\tau} + \boldsymbol{\theta}) \tag{5.65}$$

where $\boldsymbol{\Gamma}^0$ is the Green operator whose components, in the Fourier space, are:

$$\widehat{\boldsymbol{\Gamma}}^0 = \frac{1}{\lambda_0 + 2\mu_0} \boldsymbol{P} \otimes \boldsymbol{P} + \frac{1}{2\mu_0} \left[\boldsymbol{Q} \underline{\overline{\otimes}} \boldsymbol{P} + \boldsymbol{P} \underline{\overline{\otimes}} \boldsymbol{Q} \right] \tag{5.66}$$

where $\lambda_0 = k_0 - \frac{2\mu_0}{3}$, k_0 and μ_0 are the compressibility and viscosity of the reference medium respectively. In the expression (5.66), tensors $\boldsymbol{P}$ and $\boldsymbol{Q}$ are defined by:

$$\boldsymbol{P} = \frac{1}{|\boldsymbol{\xi}|^2} \boldsymbol{\xi} \otimes \boldsymbol{\xi}, \qquad \boldsymbol{Q} = \boldsymbol{I} - \boldsymbol{P} \tag{5.67}$$

In equation (5.70), the expression of $\boldsymbol{\theta}$, in the Fourier space, is:

$$\widehat{\boldsymbol{\theta}} = \frac{i}{|\boldsymbol{\xi}|} \left[(\boldsymbol{f}.\boldsymbol{\xi}) \boldsymbol{P} - \boldsymbol{f} \otimes \boldsymbol{\xi} - \boldsymbol{\xi} \otimes \boldsymbol{f} \right] \tag{5.68}$$

where the Fourier transform of function $F(x)$ is defined by:

$$\widehat{F}(\boldsymbol{\xi}) = \frac{1}{V_\Omega} \int_\Omega F(x) \exp(-i\boldsymbol{\xi}.\boldsymbol{x}) dV_\Omega \tag{5.69}$$

Finally, in equation (5.70), the symbol "$*$" denotes the convolution product. By replacing in equation (5.70) the polarization $\boldsymbol{\tau}$ by expression (5.64), an integral equation is then obtained for the strain rate tensor:

$$\boldsymbol{d} = -\boldsymbol{\Gamma}^0 * \left[(\mathbb{C} - \mathbb{C}^0) : \boldsymbol{d} + \boldsymbol{\theta} \right] \tag{5.70}$$

This integral equation is similar to that obtained for elastic composites, the difference comes from the term $\boldsymbol{\theta}$. The equation (5.70) is linear with the strain rate but its resolution is difficult due to the presence of the convolution product. Fast and efficient approach is to develop the solution along Neumann series and to compute each term of the series by means of an iterative scheme. The method was originally proposed by Brown [29], Kroner [30] and by Moulinec *et al.* who have been implemented numerically [26] with the FFT algorithm.

However, this is the dual form (stress based formulation) of the iterative scheme that will be used for the resolution of Stokes problem. Indeed, the iterative scheme associated with equation (5.70) has a slow convergence rate when increasing the value of h (see equation (5.52)). In the other hand, the value of h must be chosen sufficiently large in order to retrieve the condition $\boldsymbol{v} = 0$ in the solid phase.

Let us provide the dual form of the integral equation (5.70). To this end, note that the stress is given by

$$\boldsymbol{\sigma} = \boldsymbol{\tau} + \mathbb{C}^0 : \boldsymbol{d} \tag{5.71}$$

Using now equation (5.70), the stress becomes

$$\boldsymbol{\sigma} = \boldsymbol{\tau} - \mathbb{C}^0 : \boldsymbol{\Gamma}^0 * [\boldsymbol{\tau} + \boldsymbol{\theta}] \tag{5.72}$$

Considering also the relation

$$\boldsymbol{\tau} = \boldsymbol{\sigma} - \mathbb{C}^0 : \boldsymbol{d} = \mathbb{C}^0 : (\mathbb{S}^0 - \mathbb{S}) : \boldsymbol{\sigma}, \tag{5.73}$$

and introducing the Green tensor for the stresses, denoted $\boldsymbol{\Delta}^0$ and defined by

$$\boldsymbol{\Delta}^0 = \mathbb{C}^0 - \mathbb{C}^0 : \boldsymbol{\Gamma}^0 : \mathbb{C}^0, \tag{5.74}$$

we then obtain :

$$\boldsymbol{\sigma} = -\boldsymbol{\Delta}^0 * \left[(\mathbb{S} - \mathbb{S}^0) : \boldsymbol{\sigma}\right] - \mathbb{C}^0 : \boldsymbol{\Gamma}^0 * \boldsymbol{\theta} \tag{5.75}$$

It is convenient to introduce the two order tensor $\boldsymbol{b}$ by

$$\boldsymbol{b} = -\mathbb{C}^0 : \boldsymbol{\Gamma}^0 * \boldsymbol{\theta} \tag{5.76}$$

Note also that the components of the dual Green tensor are given by

$$\widehat{\boldsymbol{\Delta}}^0 = \frac{2\mu_0\lambda_0}{\lambda_0 + 2\mu_0}\boldsymbol{Q} \otimes \boldsymbol{Q} + 2\mu_0 \boldsymbol{Q} \overline{\underline{\otimes}} \boldsymbol{Q} \tag{5.77}$$

where λ_0, μ_0 and $\boldsymbol{Q}$ have been introduced in the last section. Reminded that a fictitious compressibility was introduced to facilitate the calculations, the limit $k_0 \to +\infty$ must now be taken. This could equivalently considered by taking the limit $\lambda_0 \to +\infty$. The Green tensor has then the expression

$$\boldsymbol{\Delta}^0 = 2\mu_0 \left[\boldsymbol{Q} \otimes \boldsymbol{Q} + \boldsymbol{Q} \overline{\underline{\otimes}} \boldsymbol{Q}\right] \tag{5.78}$$

while the stiffness tensor of the reference medium is

$$\mathbb{S}^0 = \frac{1}{2\mu_0}\mathbb{K} \tag{5.79}$$

In the expression of $\boldsymbol{b}$, the limit $\lambda_0 \to +\infty$ gives :

$$\widehat{\boldsymbol{b}} = -\lim_{\lambda \to +\infty} \mathbb{C}^0 : \widehat{\boldsymbol{\Gamma}}^0 : \hat{\boldsymbol{\theta}} = \boldsymbol{\Omega}.\widehat{\boldsymbol{f}} \tag{5.80}$$

where the components of the tensor of order three $\boldsymbol{\Omega}$ are defined by

$$\Omega_{ijk}(\boldsymbol{\xi}) = \frac{i}{|\xi|}[\delta_{ij}\overline{\xi}_k + \delta_{ik}\overline{\xi}_j + \delta_{jk}\overline{\xi}_i - 2\overline{\xi}_i\overline{\xi}_j\overline{\xi}_k], \overline{\boldsymbol{\xi}} = \boldsymbol{\xi}/\left|\xi\right| \tag{5.81}$$

Finally, in the expression of $\mathbb{S}$, we take the limit $k \to +\infty$, that will retrieve the expression (5.52).

5.3.3 Numerical integration by FFT

We now present the iterative scheme based on the FFT algorithm to compute the solution of the Stokes problem and to determine the intrinsic permeability. The general form of the iterative scheme is presented in section 5.3.3.1. The details related to the implementation of the iterative scheme are presented in section 5.3.3.2. Finally, in the last section, we will discuss about the choice of the reference medium and the convergence criterion.

5.3.3.1 The stress based iterative scheme

The Lippmann-Schwinger integral equation (5.75) can be written into the following equivalent and compact form :

$$\boldsymbol{\sigma} + \mathbb{Z} \bullet \boldsymbol{\sigma} = \boldsymbol{b} \tag{5.82}$$

where $\mathbb{Z} \bullet \boldsymbol{\sigma}$ is a linear operator defined such that:

$$\mathbb{Z} \bullet \boldsymbol{\sigma} = \boldsymbol{\Delta}^0 * \left[(\mathbb{S} - \mathbb{S}^0) : \boldsymbol{\sigma} \right] \tag{5.83}$$

The inversion of the linear system (5.82) is computationally to expensive due to the presence of the convolution product. Following [29, 30], the solution is expanded into Neumann series:

$$\boldsymbol{\sigma} = \boldsymbol{b} - \mathbb{Z} \bullet \boldsymbol{b} + \mathbb{Z} \bullet \mathbb{Z} \bullet \boldsymbol{b} - \mathbb{Z} \bullet \mathbb{Z} \bullet \mathbb{Z} \bullet \boldsymbol{b} + ... \tag{5.84}$$

and which converges if the spectral radius of the operator $\mathbb{I} - \mathbb{Z}$ is lower than 1. Each term of this series can be obtained by the following iterative scheme:

$$\boldsymbol{\sigma}^{i+1} = \boldsymbol{b} - \mathbb{Z} \bullet \boldsymbol{\sigma}^i \tag{5.85}$$

in which the value of the first term is $\boldsymbol{\sigma}^{i=1} = \boldsymbol{b}$.
A simplification of the iterative scheme is possible. For any stress fields $\boldsymbol{\sigma}$ in equilibrium with the source term $\boldsymbol{f}$, we have the relation

$$\boldsymbol{\Delta}^0 : \mathbb{S}^0 : \boldsymbol{\sigma} = \boldsymbol{\sigma} - \boldsymbol{b} \tag{5.86}$$

Accounting for (5.86) in (5.85) with the definition (5.83) for $\mathbb{Z}$ leads to the following final expression for the stress based iterative scheme:

$$\boldsymbol{\sigma}^{i+1} = \boldsymbol{\sigma}^i - \boldsymbol{\Delta}^0 * \left[\mathbb{S} : \boldsymbol{\sigma}^i \right] \tag{5.87}$$

The details about the numerical integration of this iterative scheme are presented in the next section.

5.3.3.2 Discretization of the problem

The convolution product between the Green operator $\boldsymbol{\Delta}^0$ and the strain rate $\boldsymbol{d}^i = \mathbb{S} : \boldsymbol{\sigma}^i$ is made in the Fourier space. This has two advantages. First, the components of the Green operator are explicitly determined in the Fourier space by the wave vectors $\boldsymbol{\xi}$ (equation (5.77)). Second, the product between $\boldsymbol{\Delta}^0$ and $\boldsymbol{d}^i$ is local in the Fourier space. In the Fourier domain, the iterative scheme reads

$$\widehat{\boldsymbol{\sigma}}^{i+1} = \widehat{\boldsymbol{\sigma}}^i - \widehat{\boldsymbol{\Delta}}^0 : \widehat{\boldsymbol{d}^i} \tag{5.88}$$

The problem is discretized with $2N$ wave vectors $\boldsymbol{\xi}_n$, defined by

$$\boldsymbol{\xi}_n = 2\pi n \boldsymbol{\zeta}, \quad n = 0, \pm 1, ... \pm \infty, \quad \zeta_i = \frac{1}{h_i} \tag{5.89}$$

where h_1, h_2, h_3 are the dimensions of the unit cell along each space directions. Obviously, for three dimensional problems, three indices n_1, n_2, et n_3 must be used to denote the wave number along each directions. However, to simplify the formula, we will use only one index n. Still for simplicity, we denote by $\widehat{F}_n = \widehat{F}(\boldsymbol{\xi}_n)$, the Fourier transform of the function $F(\boldsymbol{x})$ calculated with the wave vector $\boldsymbol{\xi}_n$. We also denote by

$$F_n = F(\boldsymbol{x}_n) = \mathcal{F}^{-1}(\widehat{F}_n) \tag{5.90}$$

the inverse Fourier transform of $\widehat{F}_n$. The F_n for $n = -N..N-1$ are the values taken by the function $F(\boldsymbol{x})$ at each node of a regular grid. In the discretized form, the iterative scheme (5.88) becomes

$$\widehat{\boldsymbol{\sigma}}_n^{i+1} = \widehat{\boldsymbol{\sigma}}_n^i - \widehat{\boldsymbol{\Delta}}_n^0 : \widehat{\boldsymbol{d}}_n^i \tag{5.91}$$

At each iteration, we have to calculate the strain rate $\widehat{\boldsymbol{d}}_n^i$ from the stress field $\widehat{\boldsymbol{\sigma}}_n^i$. This requires the product between the stress and the stiffness tensor $\mathbb{S}$ which is performed in real space:

$$\boldsymbol{d}_n^i = \mathbb{S}_n : \boldsymbol{\sigma}_n^i \tag{5.92}$$

where $\boldsymbol{d}_n^i$ and $\boldsymbol{\sigma}_n^i$ denote the inverse Fourier transform of $\widehat{\boldsymbol{d}}_n^i$ and $\widehat{\boldsymbol{\sigma}}_n^i$. Tensor $\mathbb{S}_n$ is defined by:

$$\mathbb{S}_n = \left[I_f(\boldsymbol{x}_n) + \frac{1}{h} I_s(\boldsymbol{x}_n) \right] \frac{1}{2\mu} \mathbb{K} \tag{5.93}$$

where $I_f(\boldsymbol{x})$ and $I_s(\boldsymbol{x})$ are the characteristic functions of the fluid an the solid phases, already introduced in (5.60).

At each iteration, the strain rate $\widehat{\boldsymbol{d}}_n^i$ in (5.91) is computed by performing successively :

- the inverse discrete Fourier transform of the stress $\widehat{\boldsymbol{\sigma}}_n^i$,
- the product between tensor $\mathbb{S}_n$ and $\boldsymbol{\sigma}_n^i$ following relation (5.92),
- the discrete Fourier transform of $\boldsymbol{d}_n^i$.

The discrete Fourier transform and the inverse discrete Fourier transform are performed with the FFT algorithm. In our numerical tools, this is performed with a pre-existing module in MATLAB. The tensor $\mathbb{S}_n$ is calculated one time, stored and could be used at each iteration.

Finally, still remains the computation of the first term of the series $\boldsymbol{b}$. The latter is defined by equation (5.80) in which the Fourier transform of $\boldsymbol{f}$ is:

$$\widehat{\boldsymbol{f}}_n = \left[\widehat{\mathrm{I}}_f(\boldsymbol{\xi}_n) - \frac{c_f}{c_s} \widehat{\mathrm{I}}_s(\boldsymbol{\xi}_n) \right] \boldsymbol{G} = \frac{1}{c_s} \widehat{\mathrm{I}}_s(\boldsymbol{\xi}_n) \boldsymbol{G} \tag{5.94}$$

for any $n \neq 0$ and is equal to $\widehat{\boldsymbol{f}}_n = 0$ if $n = 0$. The iterative scheme is summarized in table 5.1. At convergence of the iterative scheme, the strain rate $\widehat{\boldsymbol{d}}_n^{i+1}$ is a compatible, this means that the strain rate derivates from a velocity field. In the Fourier space this condition reads for any $n \neq 0$:

$$\widehat{\boldsymbol{\Delta}}_n^0 : \widehat{\boldsymbol{d}}_n^i = 0 \quad \Leftrightarrow \quad \widehat{\boldsymbol{d}}_n^i = \frac{1}{2} (\widehat{\boldsymbol{v}}_n \otimes \boldsymbol{\xi}_n + \boldsymbol{\xi}_n \otimes \widehat{\boldsymbol{v}}_n) \tag{5.95}$$

Table 5.1: The stress based iterative scheme for solving the Stokes problem.

Step i=1: $\widehat{\boldsymbol{\sigma}}_n^{i=1} = \widehat{\boldsymbol{\Omega}}_n.\widehat{\boldsymbol{f}}_n, \widehat{\boldsymbol{\sigma}}_0^{i=1} = 0$

$\widehat{\boldsymbol{d}}_n^1 = \widehat{\mathbb{S}}_n * \widehat{\boldsymbol{\sigma}}_n^{i=1}$

Step i: $\boldsymbol{d}_n^i$ and $\boldsymbol{\sigma}_n^i$ are known

convergence tests

$\widehat{\boldsymbol{\sigma}}_n^{i+1} = \widehat{\boldsymbol{\sigma}}_n^i - \widehat{\boldsymbol{\Delta}}_n^0 : \widehat{\boldsymbol{d}}_n^i$

$\widehat{\boldsymbol{d}}_n^{i+1} = \widehat{\mathbb{S}}_n * \widehat{\boldsymbol{\sigma}}_n^{i+1}$

Thus, by using the incompressibility condition:

$$\widehat{\boldsymbol{v}}_n.\boldsymbol{\xi}_n = 0, \tag{5.96}$$

we observe that the velocity field can be computed from the strain rate tensor $\widehat{\boldsymbol{d}}_n$ by the relation

$$\widehat{\boldsymbol{v}}_n = -\frac{2i}{|\boldsymbol{\xi}_n|^2}\widehat{\boldsymbol{d}}_n.\boldsymbol{\xi}_n; \forall n \neq 0 \tag{5.97}$$

The velocity field is defined by its Fourier coefficients for all values of $\boldsymbol{\xi}_n$ except at $n = 0$. The velocity field corresponding to $n = 0$ represents the average over the volume of the unit cell:

$$\widehat{\boldsymbol{v}}_0 =< \boldsymbol{v} >_V= \boldsymbol{V} \tag{5.98}$$

The velocity field can be put into the form

$$\boldsymbol{v} = \boldsymbol{V} + \boldsymbol{v}^* \tag{5.99}$$

where $\boldsymbol{v}^*$ is a periodic velocity field having a null volume average. This field can be determined by

$$\begin{cases} \widehat{\boldsymbol{v}}_n^* = -\dfrac{2i}{|\boldsymbol{\xi}_n|^2}\widehat{\boldsymbol{d}}_n.\boldsymbol{\xi}_n & \forall n \neq 0 \\ \widehat{\boldsymbol{v}}_n^* = 0 & n = 0 \end{cases} \tag{5.100}$$

The macroscopic velocity is determined by accounting for the condition $\boldsymbol{v} = 0$ in the solid phase:

$$\boldsymbol{V} = -\boldsymbol{v}^*(\boldsymbol{x}_n \in V_s) \tag{5.101}$$

Practically, we compute $\boldsymbol{V}$ by choosing a point within the solid phase which is not located too close to the solid-fluid interface.

5.4 Numerical results and discussions

5.4.1 Benchmark problems

Stokes flow through arrays of cylinders and spheres has been often considered in many studies in the literature. For instance, the permeability of porous media with cylinders has been investigated by Sparrow and Loeffler [31], Banerjee and Hadaller [32], Sangani and Acrivos [6], Drummond and Tahir [33], Larson and Higdon [34, 35], Wang [9] and Idris [36]. The numerical implementation of the Stokes problem through an array of rigid spheres has been provided by Sangani and Acrivos [7], Barrere *et al.* [10], Chapman and Higdon [37], Kadaksham *et al.* [38]. Note that some works deal with the extension of the self-consistent in the field of periodic homogenization method to derive analytic expressions for the permeability [39, 40] but the formula are restricted to some particular microstructures corresponding to porous media with rigid cylinders or spheres. Obviously, a unit cell containing a rigid cylinder or sphere cannot mimic realistically a porous solid and these two examples are only considered here as benchmark problems. The corresponding unit cell is represented in Figure 5.7.

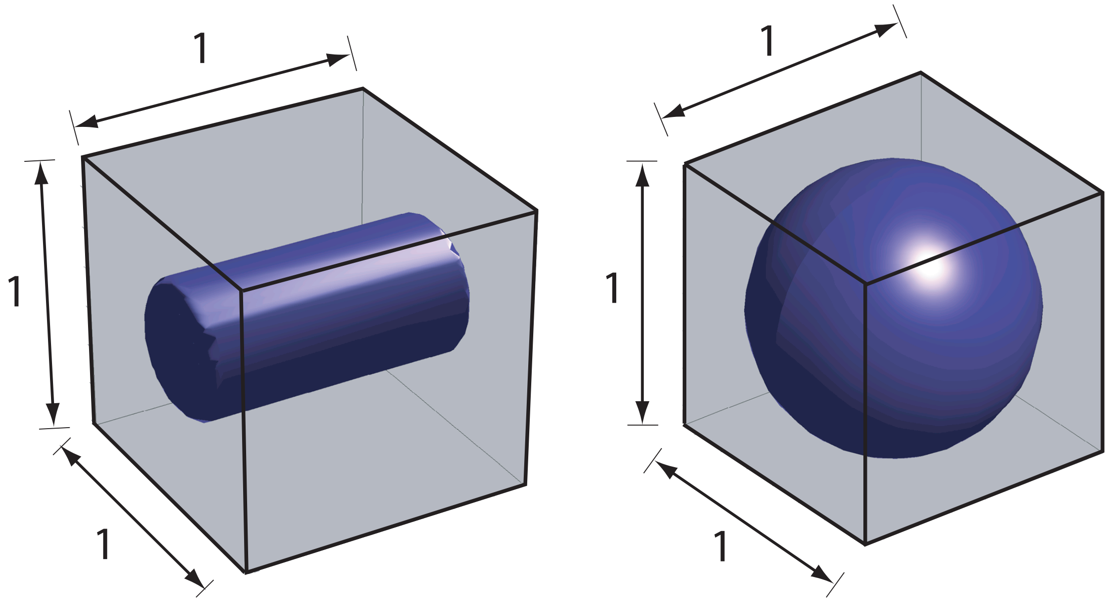

Figure 5.7: Unit cell containing a rigid cylinder or sphere

The solutions obtained with the FFT method are compared with the results obtained by Sparrow and Loeffler [31], Wang [9] for the cylinder and those obtained by Sangani and Acrivos [7] for the sphere. The computations are performed on a dimensionless unit cell (having the dimension 1 along each direction), leading then to the computation of a dimensionless permeability. Cubic elements have been used for the FEM, the cylinder surface is then approximated by a regular mesh. All the DOF related to the node which are in the solid or at the interface between the solid and the fluid are eliminated in the linear system. This advantageously reduce the size of the problem. The total number of voxels considered with the FEM is 192 × 192 × 192 voxels, which corresponds to the maximum possible memory occupancy. A comparison with available data is provided in the case of the flow through an array of rigid cylinders or spheres. The transversal and longitudinal components of the permeability tensor are successively computed by applying a pressure gradient parallel or orthogonal to the cylinder axis. The results for the transversal and longitudinal permeability are shown in Figures 5.8 and 5.9, respectively.

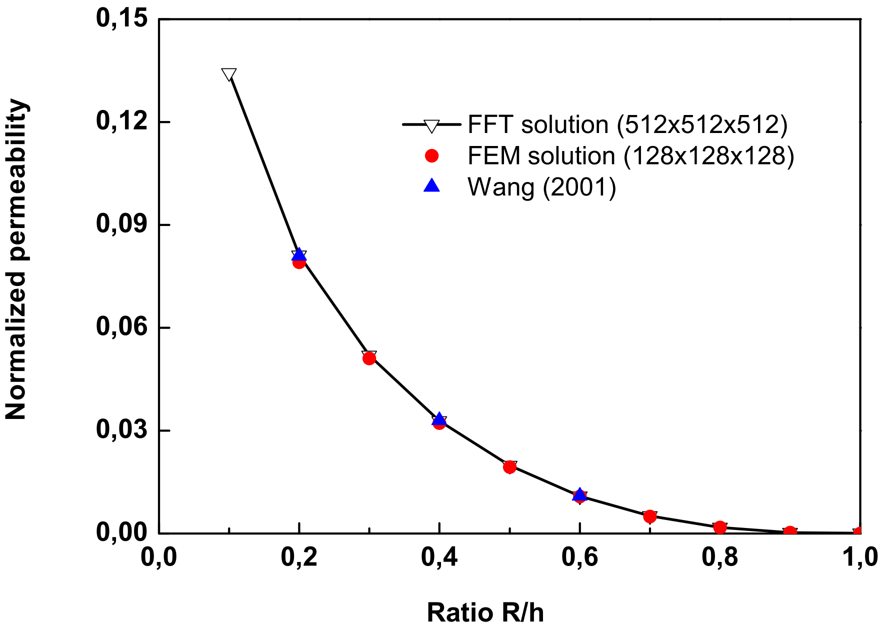

Figure 5.8: Dimensionless transversal permeability for the flow through a regular array of cylinders. Comparison of the FFT solution, the FEM solution and with the results obtained by Wang [9]. R is the radius of the cylinder or the sphere, and h is the half-length of the unit cell.

The FFT solutions are compared with those of Wang [9], Sparrow and Loeffler [31]. A good agreement is observed between our numerical values and those reported in the literature. The results obtained with the FFT method and the FEM are now quantitatively compared in Table 5.2 for the transverse flow through the array of cylinders and for various values of the Radius. The FFT-based data are provided for the resolution 128 × 128 × 128 and for 512 × 512 × 512 while, the results obtained with FEM are given for the resolution 128 × 128 × 128 and for Taylor-Hood elements are with 28000 elements.

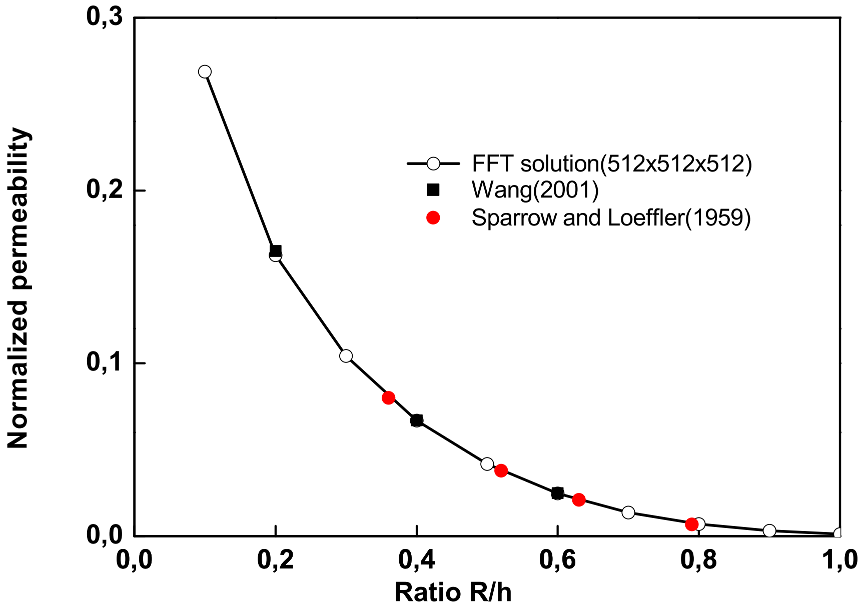

Figure 5.9: Dimensionless longitudinal permeability for the flow through a regular array of cylinders. Comparison of the FFT solution with the results obtained by Sparrow and Loeffler [31], and Wang [9].

Table 5.2: Comparison of the intrinsic permeability of transverse flow through array of cylinders computed with the FFT method and the FEM.

Radius	FFT (512^3)	FFT (128^3)	FEM (cubic 128^3)	FEM Taylor-Hood
0.1	0.134310	0.133383	0.131609	0.133830
0.2	0.081148	0.080984	0.079120	0.081066
0.3	0.051926	0.051386	0.051078	0.051625
0.4	0.032864	0.032476	0.032255	0.032760
0.5	0.019855	0.019600	0.019366	0.019722
0.6	0.010921	0.010692	0.010769	0.010850
0.7	0.005143	0.005049	0.004966	0.005060
0.8	0.001812	0.001699	0.001782	0.001755
0.9	0.000308	0.000279	0.000302	0.000290

We now consider numerical applications in the case of a regular array of rigid spheres. The convergence of the FFT solution with the grid refinement is provided in Figure 5.10 for the radius $R = 0.15$, $R = 0.25$ and $R = 0.35$, and it is also compared with FEM solutions. The FEM solution is obtained with the cubic elements. A good agreement between the FFT and the FEM methods is observed for the largest value of the radius ($R = 0.35$). There is a slight difference for the radius $R = 0.25$, that is more significant for $R = 0.15$. These differences are essentially attributed to the discretization error. Indeed, the sphere being approximated by means of cubic elements, the error is higher for the smaller radius. This is the main limitation of the methods which use a regular grid.

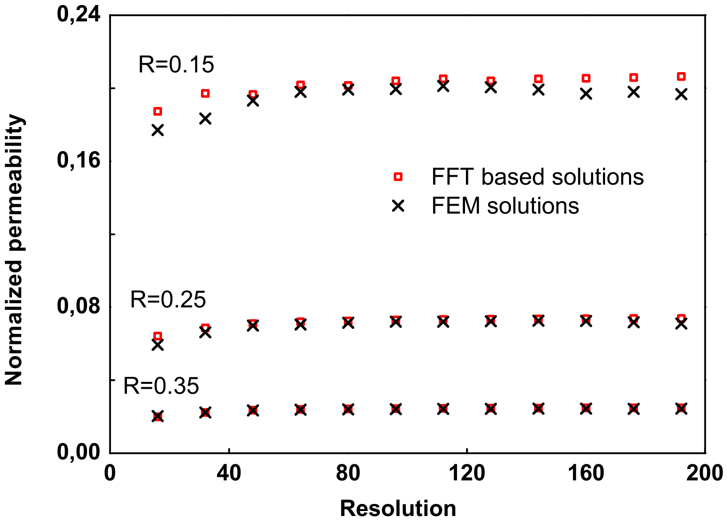

Figure 5.10: Dimensionless permeability for the flow through a regular array of sphere of radius $R = 0.15$, $R = 0.25$ and $R = 0.35$. Comparison between the FFT and the FEM solution.

The FFT solution (with $512 \times 512 \times 512$ voxels), the FEM with cubic elements (with $192 \times 192 \times 192$ voxels), the FEM with the MINI elements with 70.000 elements are compared with the data provided by Sangani and Acrivos [7] in Table 5.3. Various values of the radius of the sphere have been considered in the range $[0.1, 1]$. It is observed that the FFT solutions are in a better agreement with the data of Sangani and Acrivos [7] than the FEM solution. The error between the FFT method and the results of Sangani and Acrivos [7] vary from 0.6% (in the case $R = 0.1$) to 0.13% (in the case $R = 1$). This was expected, since the FFT solution was computed with a more refined grid than the FEM solution. Obviously, the results would be compared with the same discretization, however here we compare the solutions obtained by these two methods and the maximum possible memory occupancy of the computer.

Table 5.3: Dimensionless permeability for the flow through a regular array of sphere with radius lying in the range $[0.1, 1]$. Comparison between the FFT solutions, the FEM solutions and the results of Sangani and Acrivos [7].

R	FFT	FEM (cubic elements)	Sangani & Acrivos from Ref. [7]	FEM (MINI elements)
0.1	0.905109	-	0.911070	0.900804
0.2	0.380631	-	0.382190	0.378258
0.3	0.207387	0.196734	0.208050	0.206626
0.4	0.122899	-	0.123270	0.122561
0.5	0.074448	0.070996	0.074668	0.073559
0.6	0.044340	-	0.044501	0.044399
0.7	0.025136	0.024461	0.025246	0.025263
0.8	0.013121	-	0.013197	0.013362
0.85	0.009098	-	0.009151	-
0.9	0.006140	-	0.006153	0.006290
0.95	0.003980	-	0.004003	-
1	0.002487	-	0.002520	-

The calculation times needed for solving the FFT method are provided in Table 5.4. The calculation time depends on the number of iterations needed to obtain the convergence. Particularly, it must be observed that for the flow around the rigid sphere, the number of iteration increases with the radius of the sphere.

Table 5.4: Computation time (in seconds) with the FFT-based algorithm in the case of the flow around the rigid sphere of R.

Radius	0.1	0.2	0.3	0.4	0.5	0.6	0.7	0.8	0.9
Time(s)	869	1001	1126	1139	1190	1404	1691	2002	2920
Time(min)	∼14	∼17	∼19	∼19	∼20	∼23	∼28	∼33	∼49

5.4.2 Microstructures with overlapping spherical pores

5.4.2.1 Cubic arrays of overlapping spheres

In this section, we consider more realistic porous cells which can mimic for instance metal foams or porous polymer solids. Various configurations are obtained by an assembly of overlapping spherical pores. For most studies on composite materials, the hypothesis of non-overlapping inclusions is considered, while in the present case, it is necessary to consider overlapping spheres in order to obtained a network of interconnected pores. As a first example, we represent, in Figures 5.11 and 5.12, a regular array of spherical overlapping voids arranged along a cubic lattice.

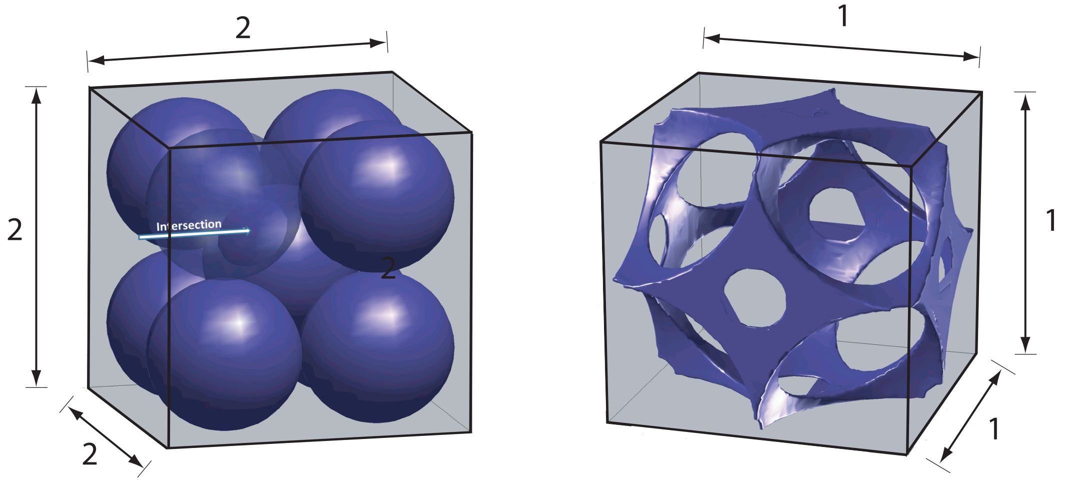

Figure 5.11: Body-centered array of spherical voids. At the left: the voids distribution, at the right: the rigid porous solid.

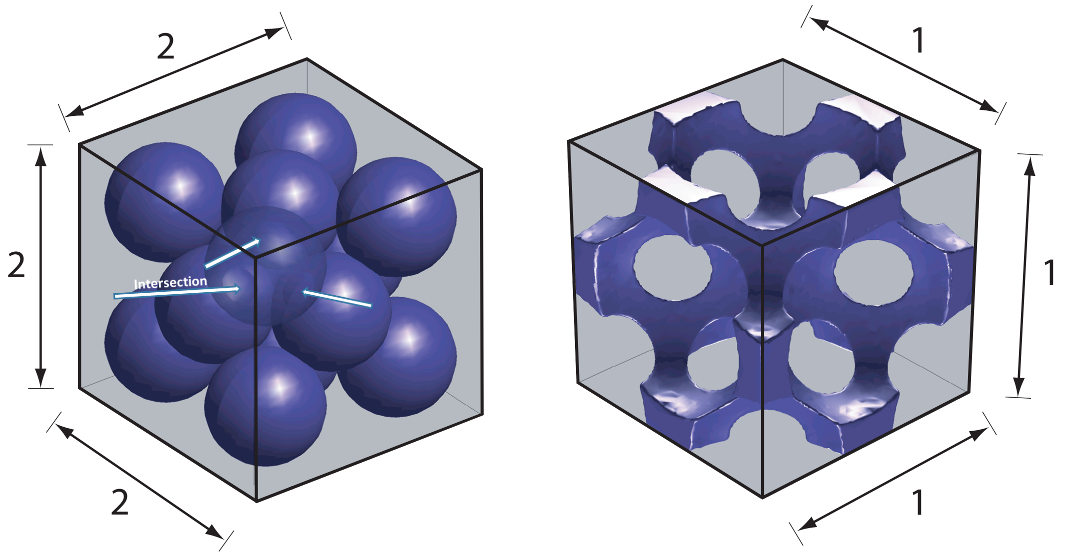

Figure 5.12: Face-centered array of spherical voids. At the left: the voids distribution, at the right: the rigid porous solid.

Figure 5.11 represents, at the left, a unit cell having the dimension 2 and containing a body-centered cubic (BCC) array of spherical cavities with the radius $R = 0.5$. Each spheres intersect another one along the diagonals of the cube. The resulting irreducible unit cell of the porous medium is represented in Figure 5.11, at the right. The porosity for the BCC array is $\phi = 0.939$. Another example is given in Figure 5.12. At the left, we represent a face-centered cubic (FCC) structure of spherical voids. At the right, the irreducible unit cell of the porous medium is represented for the FCC structure. The radius of the spherical voids is $R = 0.375$. The porosity for the FCC array is $\phi = 0.858$. The results for the permeability are shown in Figure 5.13 and 5.14.

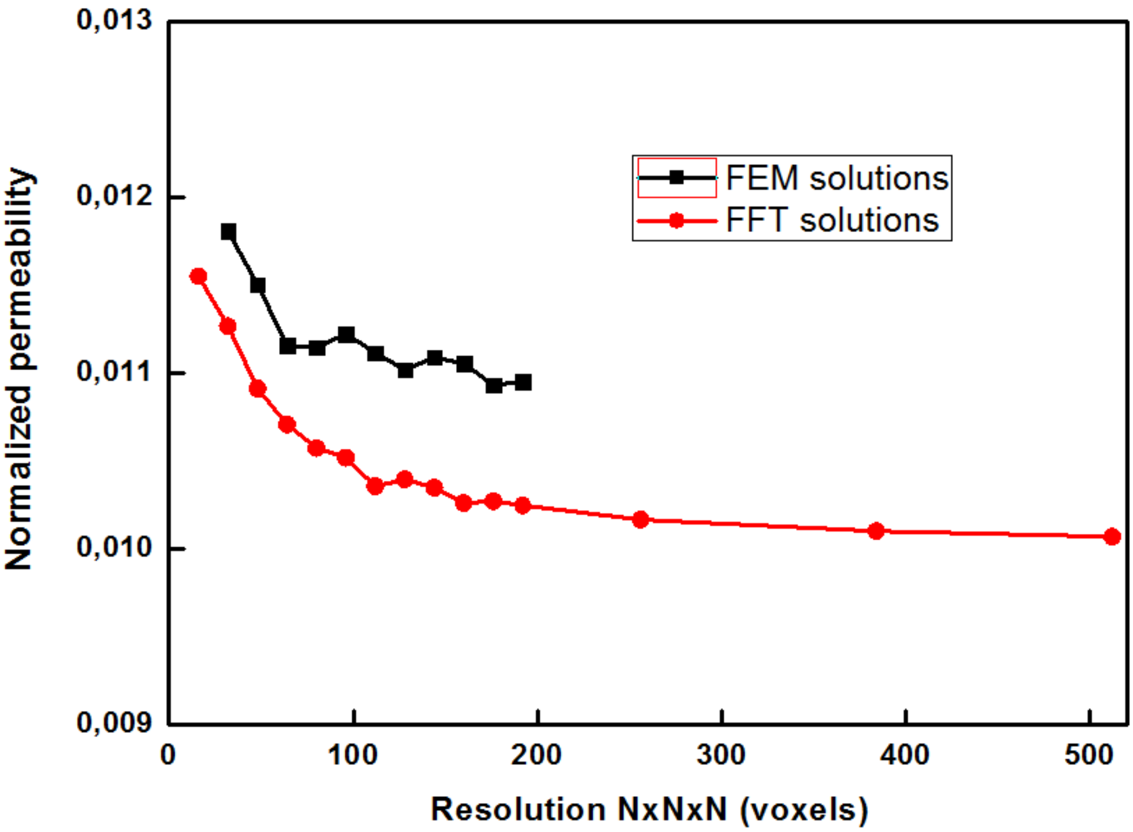

Figure 5.13: Dimensionless permeability for the flow through a body-centered array of spherical voids.

The permeability, computed with the FFT method and the FEM, is plotted as function of the grid refinement. FEM numerical tool using MINI elements was also used for comparison. For a BCC structure, using 156000 tetrahedral elements, the normalized permeability was evaluated at 0.010191 (compared to 0.010072 by using FFT). For a FCC structure, the normalized permeability of the unit cell was 0.002737 by using the FFT-based numerical tool. While using FEM with MINI elements, various results were obtained: 0.002644, 0.002656 and 0.002658 using meshes with 28000, 128000 and 992000 elements, respectively. These results clearly showed a disadvantage of using FEM with regular cubic elements. The use of an adaptive mesh reduces this error, however, a lot of effort in mesh construct is needed.

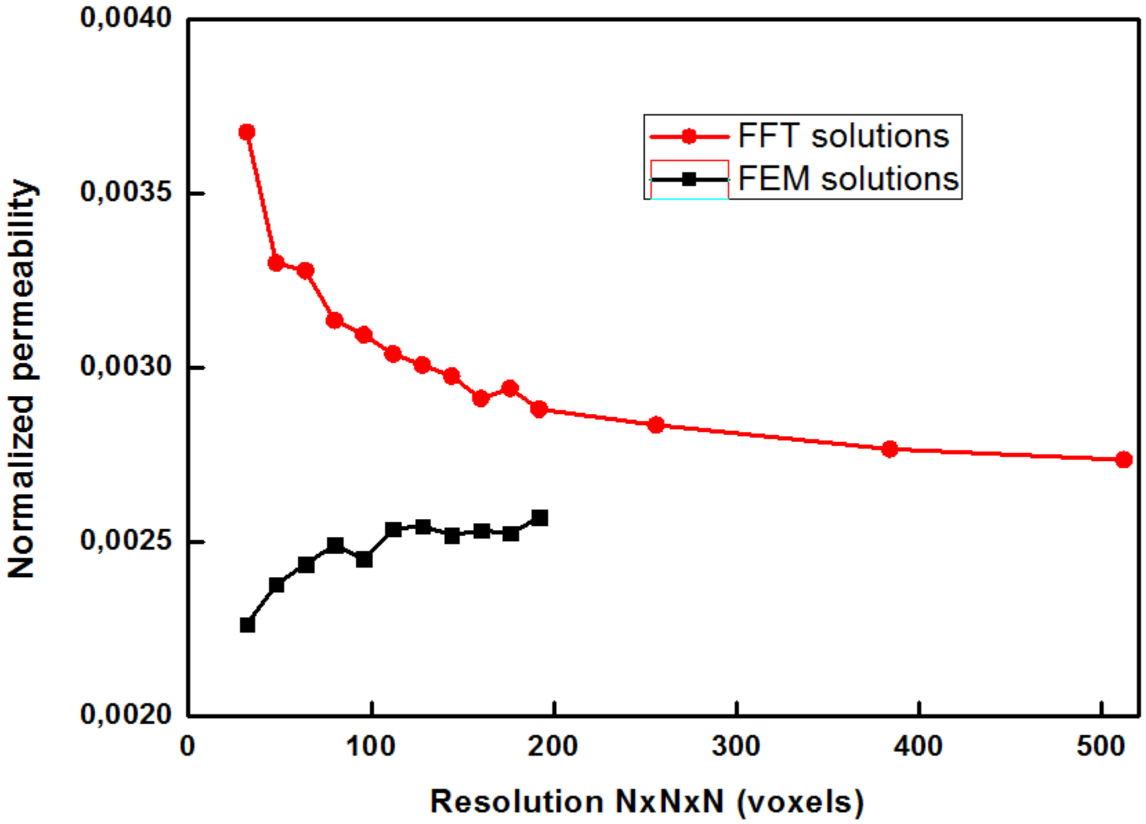

Figure 5.14: Dimensionless permeability for the flow through a face-centered array of spherical voids.

5.4.2.2 Random distribution of spherical pores

Finally, to mimic more realistically the nanoporous polymer, we consider randomly distributed spherical pores (Figure 5.15). The process used to construct the unit cell is the following: We build one eighth of the unit cell that we duplicate by symmetry with respect to three orthogonal planes (Ox1x2, Ox1x3 and Ox2x3 in the cartesian frame). By doing so, the resulting microstructure is then periodic. The radius of each small void is randomly considered in the range $[0.05, 0.08]$ and its position is randomly chosen in the range $[0, 0.5] \times [0, 0.5] \times [0, 0.5]$. Numerical tests are used to ensure that for each occurrence, each void cross at least one other void. This verification is needed in order to obtain an interconnected microstructure. The porous material represented in Figure 5.15 has the porosity $\phi = 0.7914$ and contains 1208 random spheres.

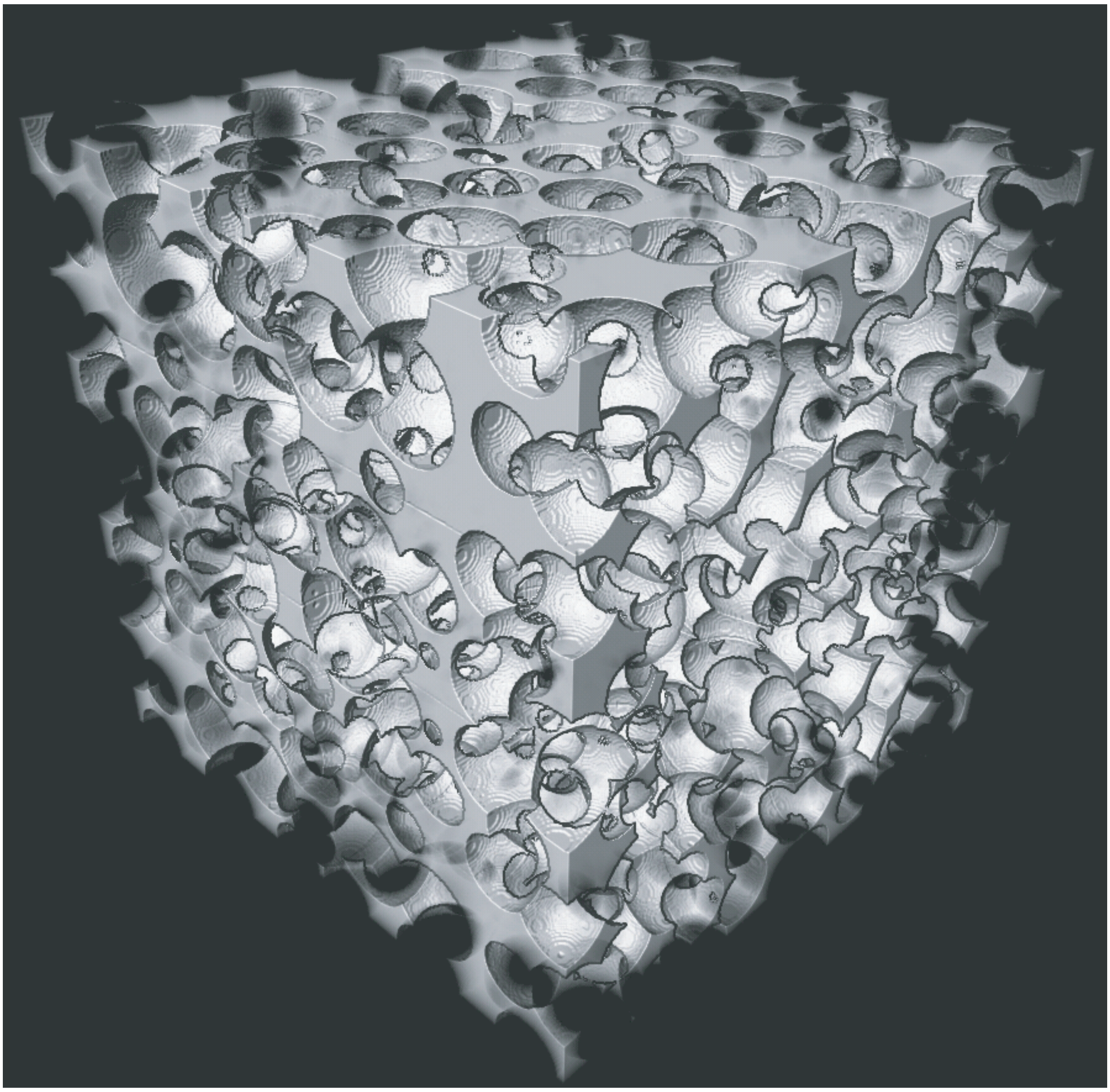

Figure 5.15: Porous material with randomly distributed and overlapping spheres

The unit cell problem is solved with the resolution $512 \times 512 \times 512$. The results are provided below:

$$K_{11}^{*} = 0.000358 \tag{5.102}$$

$$K_{22}^{*} = 0.000234 \tag{5.103}$$

$$K_{33}^{*} = 0.000020 \tag{5.104}$$

The porous material is clearly not isotropic, while the pore positions are randomly generated. Fluid flow along direction Oz is the most tortuous, the permeability K_{33} is very small. The velocity distribution is represented in Figures 5.16, 6.13, and 6.14, corresponding to the pressure gradient $G_1 = 1$, $G_2 = 1$, and $G_3 = 1$, respectively.

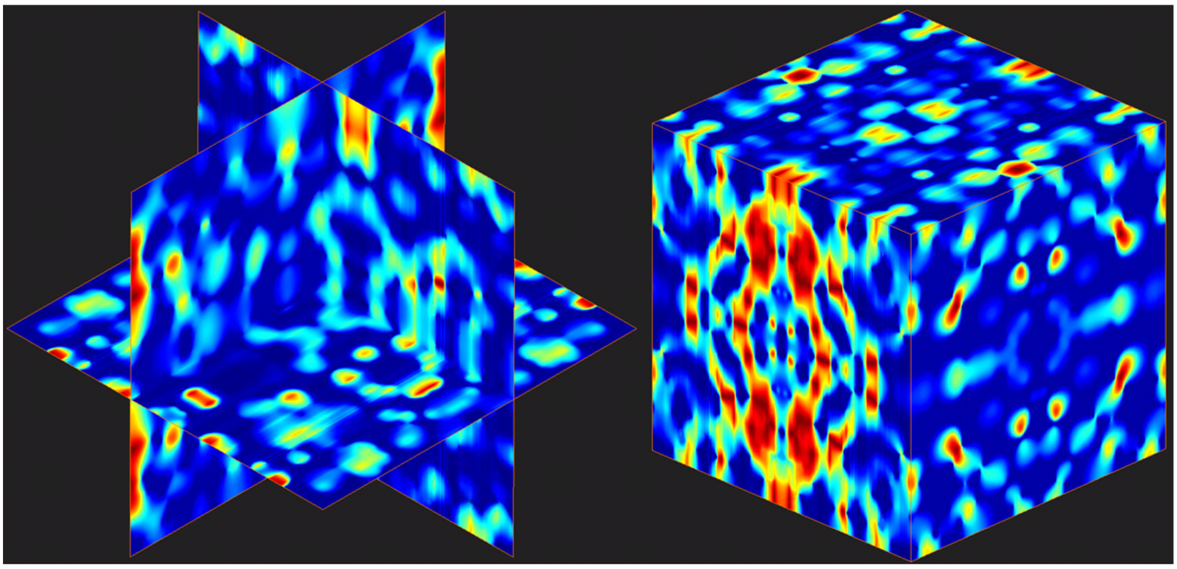

Figure 5.16: Velocity distribution for the component v_1 under the applied gradient of pressure G_1.

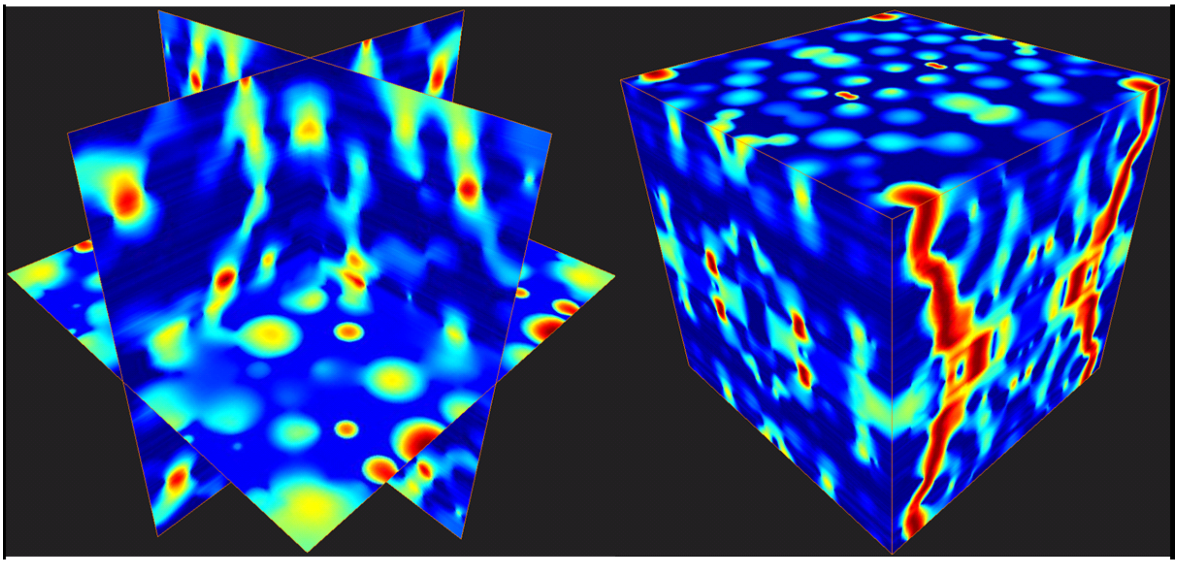

Figure 5.17: Velocity distribution for the component v_2 under the applied gradient of pressure G_2.

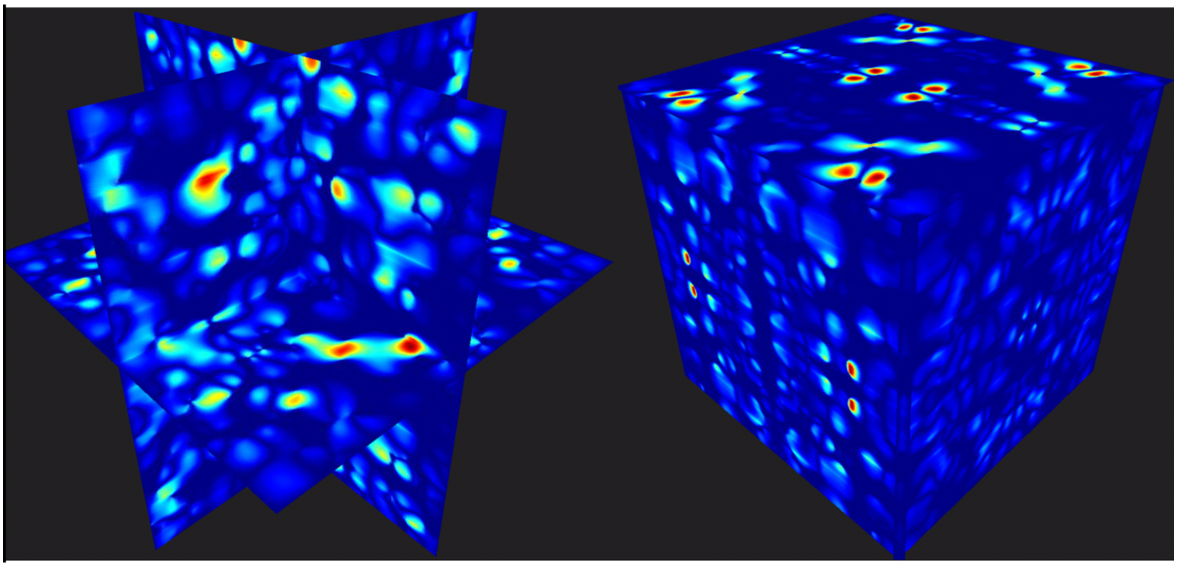

Figure 5.18: Velocity distribution for the component v_3 under the applied gradient of pressure G_3.

5.4.3 Nanoporous solid with two populations of nanocavities

We now consider a more complex nanporous medium (Figure 5.19) defined by two populations of cavities.

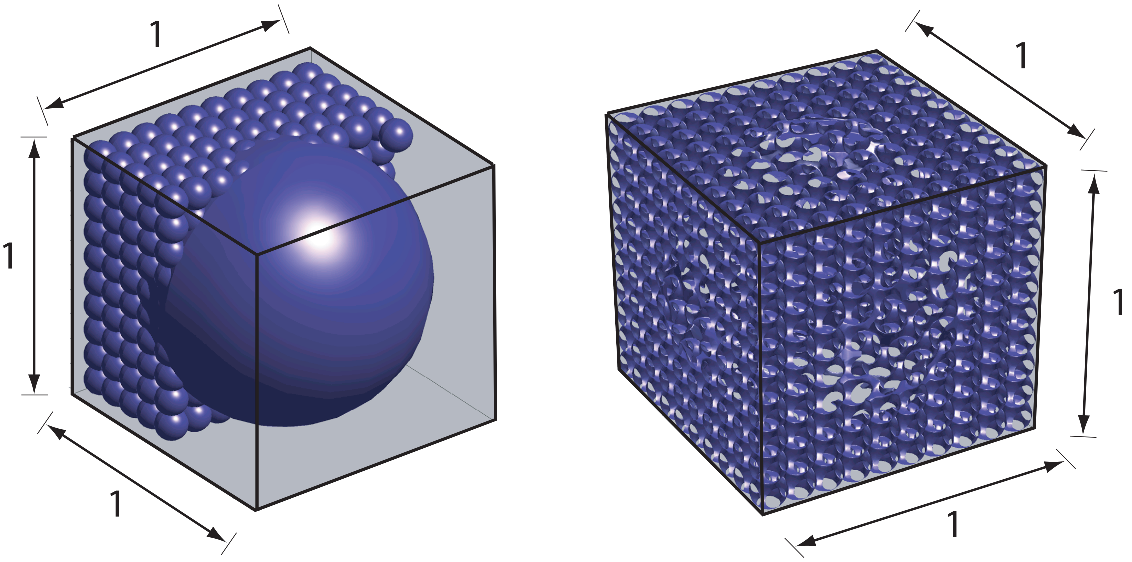

Figure 5.19: Porous material with 376 regularly aligned small voids and one larger void located at the center of the unit cell. At the left: the pore positions, at the right: the rigid porous solid.

A larger void located at the center of the cubic cell having the radius $R_1 = 0.52$ and 376 smaller voids having the radius $R_2 = 0.06$. Each smaller void overlaps with its neighboring void and some small voids also overlaps the larger one. By doing so, the fluid domain is then ensured to be interconnected. The porosity for this microstructure is $\phi = 0.915$. In Figure 5.20, we consider a second example corresponding to a random distribution of the smaller voids. The unit cell contains 536 voids with a radius comprised between 0.06 and 0.08 randomly distributed. A larger void is still located at the center of the cell and has the radius $R = 0.52$. The porosity for this last example is $\phi = 0.871$.

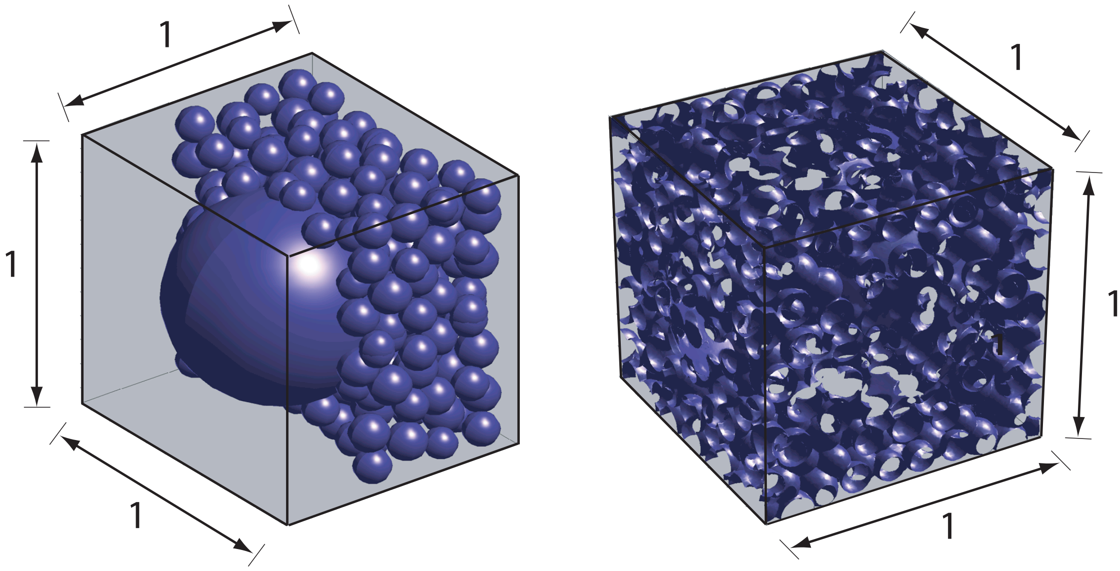

Figure 5.20: Porous material with 536 randomly distributed small voids and one larger void located at the center of the unit cell. At the left: the pore positions, at the right: the rigid porous solid.

The process used to construct the microstructure is the same that used in the last section: we build one eighth of the unit cell that we duplicate by symmetry with respect to three orthogonal planes. The construction of the eighth of the unit cell is made in two steps. In the first one, we put the larger sphere of radius $R = 0.52$ at the center of the unit cell. In the second step we put all the smaller voids and we use numerical tests. The radius of each small void is randomly considered in the range $[0.06, 0.08]$ and its position is randomly chosen in the range $[0, 0.5] \times [0, 0.5] \times [0, 0.5]$.

The dimensionless permeability for these two microstructures is represented in Figures 5.21 and 5.22. In the case of the regular arrangement of smaller voids (and also for the BCC and the FCC arrays), the permeability is isotropic and is defined by only one coefficient. However, in the particular case corresponding to random distribution of smaller voids, the permeability tensor is anisotropic. In fact, in Figure 5.22, we only represent the component K_{11} by applying a pressure gradient along the direction Ox_1. The microstructure is however quasi-isotropic, due to the effect of the central cavity, the off-diagonal coefficients of the permeability tensor are close to 0 and the terms on the diagonal take very close values.

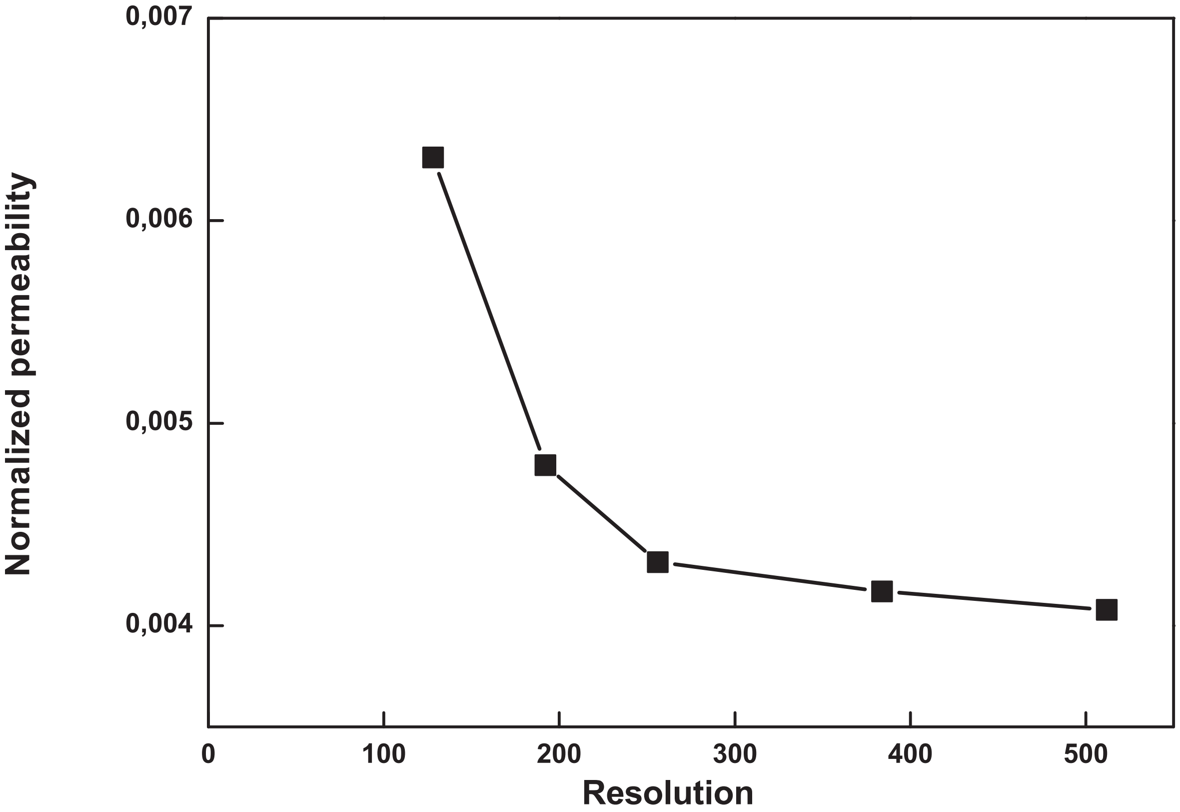

Figure 5.21: Dimensionless permeability for the flow through the microstructure given in Figure 5.19

The lower convergence observed in Figure 5.22 will probably be attributed to the tortuosity of the porous medium with random pores compared to the case of regularly aligned pores. This tortuosity would introduce some complexity in the local field distribution that an accurate description would require higher order Fourier series expansions (that is obtained by increasing of the resolution of the image). The application of the FEM to the case of random distributions of overlapping sphere fails due to the voxelization of the image. Indeed, for such microstructure the smaller voids must contain a sufficient number of voxels such that the problem would be numerically solved. If a least the number of voxels is not sufficient, the fluid flow circulation is blocked in the smaller voids. When the FFT method is used, the results are only provided for a resolution equal or higher than 128^3. When the FEM is used the resolution of the linear system is made with an iterative method whose convergence greatly depends on the geometry of the porous medium. Particularly, for the porous cell with a random distribution of spherical voids, the time computation has found to be prohibitive.

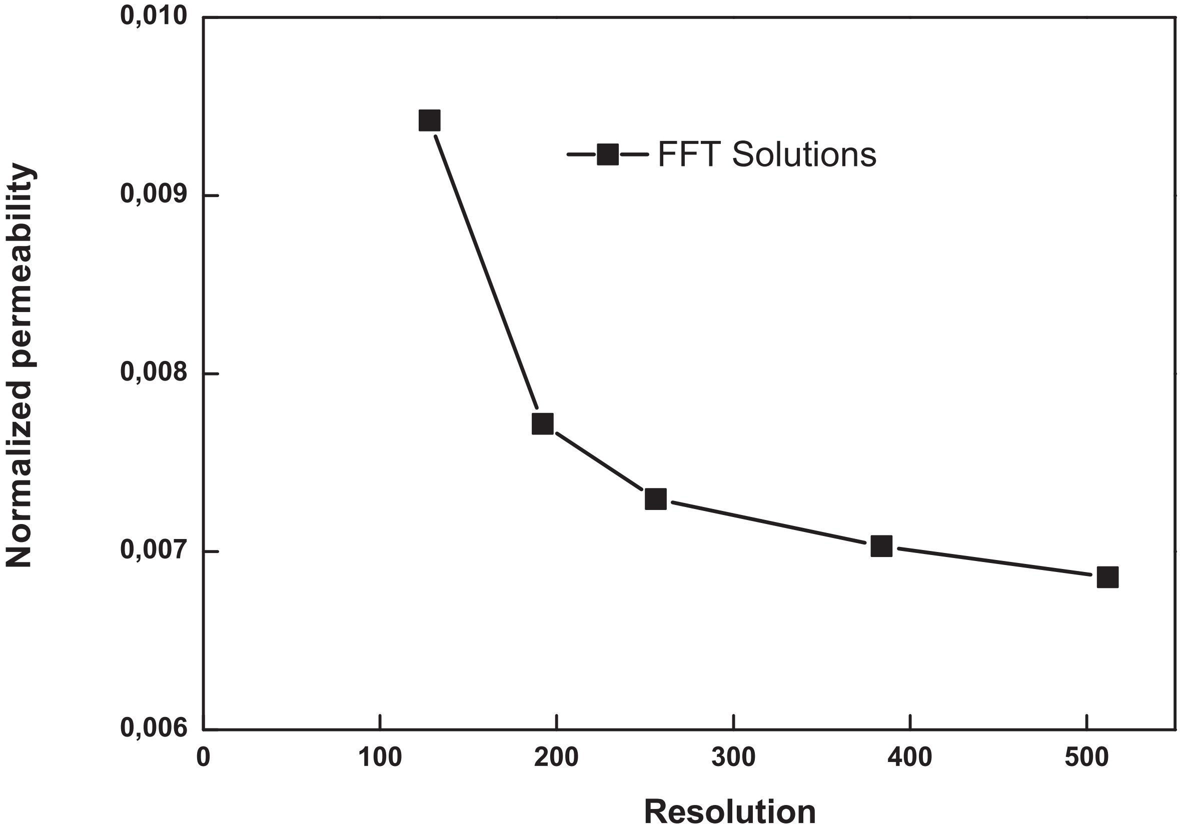

Figure 5.22: Dimensionless permeability for the flow through the microstructure given in Figure 5.20

5.4.4 Comparative analysis and discussion of the results

For completeness, in Tables 5.5, 5.6, 5.7, 5.8, and we also provide the values of the permeability for the flow through different microstructures depicted in Figures 5.11, 5.12, 5.19 and 5.20 and for the values of resolution 128^3, 256^3, 384^3 and 512^3. Just as indication, we also provide the relative error along formula given in Tables 5.5 and 5.6, to evaluate the accuracy of the solution and the rate of convergence with respect to the resolution. It is observed that the relative error decreases when the resolution increases, that is expected. However, at a given spatial resolution, the error significantly differs from one microstructure to another. In particular, the the relative error is the lowest for the BCC array of pores (see Figure 5.11) that is close to 0.1 % for the spatial resolution of 512^3. The relative error is the highest for the last example corresponding to the random distribution of small voids depicted in Figure 5.20 that is close to 1.2 % for the spatial resolution of 512^3. It is also interesting to note that the relative error given in Tables 5.7 and 5.8 are quite similar, even though the results corresponds to a regular or a random distribution of spherical voids. It seems that the tortuosity, which is more important for the random distribution, do not really affect the rate of convergence with the spatial distribution.

Table 5.5: Values of permeability and relative error as function of the resolution for the BCC array of spherical pores

resolution	permeability	relative error
128^3	0.010398	-
256^3	0.010169	$\frac{K_{64}-K_{128}}{K_{64}+K_{128}} = 0.01113$
384^3	0.010104	$\frac{K_{128}-K_{192}}{K_{128}+K_{192}} = 0.00321$
512^3	0.010072	$\frac{K_{192}-K_{256}}{K_{192}+K_{256}} = 0.00159$

Table 5.6: Values of permeability and relative error as function of the resolution for the FCC array of spherical pores

Resolution	permeability	relative error
128^3	0.003009	-
256^3	0.002837	0.02942
384^3	0.002768	0.01231
512^3	0.002737	0.00563

Table 5.7: Values of permeability and relative error as function of the resolution for the problem with a large pore and smaller aligned pores

Resolution	permeability	relative error
128^3	0.006313	-
256^3	0.004314	0.18811
384^3	0.004170	0.01697
512^3	0.004078	0.01115

Table 5.8: Values of permeability and relative error as function of the resolution for the problem with a large pore and smaller randomly distributed pores

Resolution	permeability	relative error
128^3	0.009423	-
256^3	0.007296	0.12722
384^3	0.007032	0.01842
512^3	0.006856	0.01267

Table 5.9: Computation time (in seconds) with the FFT-based algorithm, for the different porous cells and the resolution 512 × 512 × 512 voxels

Configurations	Time(s)
BCC	144149 ($\sim$ 1.7 day)
FFC	81317 ($\sim$ 0.94 day)
376 regularly aligned	163826 ($\sim$ 1.9 day)
536 randomly distributed	643283 ($\sim$ 7.44 days)

The calculation times needed are provided in Table 5.9 for the resolution 512 × 512 × 512. Finally, it is interesting note that the FFT based algorithm can be applied to a problem with two populations of pores in materials with moderate scale factor (of about 10). But the limit of the method is attained with this example. Indeed, it is not possible to increase the number of pixels due to the computer memory limitation. Obviously, the problem with two populations of cavities with a larger value of the scale factor must be considered with a double scaling approach. This is the subject of chapter 6.

5.5 Conclusion

In the present chapter, we have employed FEM or numerical one based on FFT to compute the permeability of periodic porous media with spherical overlapping spheres. Different configurations have been tested to show the capacity of the method and the accuracy of its solution. The case of the flow around rigid cylinders and spheres have been considered as benchmark problems. The results have been compared to those coming from the literature and show a good accuracy of the FFT-based solution. Advanced numerical results have been then considered. Some microstructures are constructed with an assemblies of overlapping spherical voids that can mimic more realistically the real microstructure of polymer porous materials. First, porous media are obtained by considering regularly distributed spheres along a body-centered cubic (BCC) or face-centered cubic (FCC) structures. More complex microstructure are then studied by considering porous media having different pore size which are regularly or randomly distributed. In each case, the results show a good convergence with the grid refinement used by the FFT algorithm.

References

[1] E. Auriault, Jean-Louis; Sanchez-Palencia, "Etude du comportement macroscopique d'un milieu poreux saturÃľ déformable," *Journal de Mécanique*, vol. 16, pp. 575–603, 1977.

[2] E. Sanchez-Palencia, "Non-homogeneous media and vibration theory," in *Non-homogeneous Media and Vibration Theory*, vol. 127, 1980.

[3] T. Lévy, "Fluid flow through an array of fixed particles," *International Journal of Engineering Science*, vol. 21, pp. 11–23, 1983.

[4] S. Whitaker, "Flow in porous media i: A theoretical derivation of darcy's law," *Transport in Porous Media*, vol. 1, pp. 3–25, 1986.

[5] G. Allaire, "Homogenization of the stokes flow in a connected porous medium," *Asymptotic Analysis*, vol. 2, 1989.

[6] A. Sangani and A. Acrivos, "Slow flow past periodic arrays of cylinders with application to heat transfer," *International Journal of Multiphase Flow*, vol. 8, pp. 193–206, 1982.

[7] A. Sangani and A. Acrivos, "Slow flow through a periodic array of spheres," *International Journal of Multiphase Flow*, vol. 8, pp. 343–360, 1982.

[8] C. Wang, "Stokes flow through an array of rectangular fibers," *International Journal of Multiphase Flow*, vol. 22, pp. 185–194, 1996.

[9] C. Wang, "Stokes flow through a rectangular array of circular cylinders," *Fluid Dynamics Research*, vol. 29, pp. 65–80, 2001.

[10] J. Barrere, J.-P. Caltagirone, and O. Gipouloux, "Détermination numérique de la perméabilité en milieu poreux périodique tridimensionnel," *Comptes Rendus de l'Académie des Sciences. Série 2, Mécanique, Physique, Chimie, Sciences de l'Univers, Sciences de la Terre*, vol. 310, pp. 347–352, 1990.

[11] D. Cioranescu, P. Donato, and H. I. Ene, "Homogenization of the stokes problem with non-homogenous slip boundary conditions," *Mathematical Methods in the Applied Sciences*, vol. 19, pp. 857–881, 1996.

[12] F. Alcocer, V. Kumar, and P. Singh, "Permeability of periodic porous media," *Physical Review E*, vol. 59, p. 711, 1999.

[13] F. Alcocer and P. Singh, "Permeability of periodic arrays of cylinders for viscoelastic flows," *Physics of Fluids*, vol. 14, pp. 2578–2581, 2002.

[14] E. Sawicki, *Numerical investigations of the fluid flow through rotating porous media at both the microscopic scale and the macroscopic scale.* PhD thesis, 2004.

[15] D. Bernard, O. Nielsen, L. Salvo, and P. Cloetens, "Permeability assessment by 3d interdendritic flow simulations on microtomography mappings of al-cu alloys," *Materials Science and Engineering: A*, vol. 392, pp. 112–120, 2005.

[16] T. Stylianopoulos, A. Yeckel, J. J. Derby, X.-J. Luo, M. S. Shephard, E. A. Sander, and V. H. Barocas, "Permeability calculations in three-dimensional isotropic and oriented fiber networks," *Physics of Fluids*, vol. 20, p. 123601, 2008.

[17] I. Malinouskaya, V. Mourzenko, J.-F. Thovert, and P. Adler, "Wave propagation through saturated porous media," *Physical Review E*, vol. 77, p. 066302, 2008.

[18] M. Tahir and H. V. Tafreshi, "Influence of fiber orientation on the transverse permeability of fibrous media," *Physics of Fluids*, vol. 21, p. 083604, 2009.

[19] L. Borne, "Harmonic stokes flow through periodic porous media: a 3d boundary element method," *Journal of Computational Physics*, vol. 99, pp. 214–232, 1992.

[20] V. Koivu, M. Decain, C. Geindreau, K. Mattila, J.-F. Bloch, and M. Kataja, "Transport properties of heterogeneous materials. combining computerised x-ray micro-tomography and direct numerical simulations," *International Journal of Computational Fluid Dynamics*, vol. 23, pp. 713–721, 2009.

[21] M. A. Spaid and F. R. Phelan Jr, "Lattice boltzmann methods for modeling microscale flow in fibrous porous media," *Physics of Fluids*, vol. 9, pp. 2468–2474, 1997.

[22] A. Koponen, D. Kandhai, E. Hellen, M. Alava, A. Hoekstra, M. Kataja, K. Niskanen, P. Sloot, and J. Timonen, "Permeability of three-dimensional random fiber webs," *Physical Review Letters*, vol. 80, p. 716, 1998.

[23] M. Fortin, "Old and new finite elements for incompressible flows," *International Journal for Numerical Methods in Fluids*, vol. 1, pp. 347–364, 1981.

[24] D. N. Arnold, F. Brezzi, and M. Fortin, "A stable finite element for the stokes equations," *Calcolo*, vol. 21, pp. 337–344, 1984.

[25] T. Arbogast and D. S. Brunson, "A computational method for approximating a darcy-stokes system governing a vuggy porous medium," *Computational Geosciences*, vol. 11, pp. 207–218, 2007.

[26] H. Moulinec and P. Suquet, "A fast numerical method for computing the linear and nonlinear mechanical properties of composites," *Comptes Rendus de l'Académie des Sciences. Série II, Mécanique, Physique, Chimie, Astronomie*, vol. 318, pp. 1417–1423, 1994.

[27] H. Moulinec and P. Suquet, "A numerical method for computing the overall response of nonlinear composites with complex microstructure," *Computer Methods in Applied Mechanics and Engineering*, vol. 157, pp. 69–94, 1998.

[28] V. Monchiet, G. Bonnet, and G. Lauriat, "A fft-based method to compute the permeability induced by a stokes slip flow through a porous medium," *Comptes Rendus Mécanique*, vol. 337, pp. 192–197, 2009.

[29] W. F. Brown Jr, "Solid mixture permittivities," *The Journal of Chemical Physics*, vol. 23, pp. 1514–1517, 1955.

[30] K. Ekkehart, "Statistical continuum mechanics," *Springer*, 1972.

[31] E. Sparrow and A. Loeffler, "Longitudinal laminar flow between cylinders arranged in regular array," *AIChE Journal*, vol. 5, pp. 325–330, 1959.

[32] S. Banerjee and G. Hadaller, "Longitudinal laminar flow between cylinders arranged in a triangular array by a variational technique," *Journal of Applied Mechanics*, vol. 40, pp. 1136–1138, 1973.

[33] J. Drummond and M. Tahir, “Laminar viscous flow through regular arrays of parallel solid cylinders,” *International Journal of Multiphase Flow*, vol. 10, pp. 515–540, 1984.

[34] R. Larson and J. Higdon, “Microscopic flow near the surface of two-dimensional porous media. part 1. axial flow,” *Journal of Fluid Mechanics*, vol. 166, pp. 449–472, 1986.

[35] R. Larson and J. Higdon, “Microscopic flow near the surface of two-dimensional porous media. part 2. transverse flow,” *Journal of Fluid Mechanics*, vol. 178, pp. 119–136, 1987.

[36] Z. Idris, L. Orgéas, C. Geindreau, J.-F. Bloch, and J.-L. Auriault, “Microstructural effects on the flow law of power-law fluids through fibrous media,” *Modelling and Simulation in Materials Science and Engineering*, vol. 12, p. 995, 2004.

[37] A. Chapman and J. Higdon, “Oscillatory stokes flow in periodic porous media,” *Physics of Fluids A: Fluid Dynamics (1989-1993)*, vol. 4, pp. 2099–2116, 1992.

[38] A. Kadaksham, S. Pillapakkam, and P. Singh, “Permeability of periodic arrays of spheres,” *Mechanics Research Communications*, vol. 32, pp. 659–665, 2005.

[39] A. L. Berdichevsky and Z. Cai, “Preform permeability predictions by self-onsistent method and finite element simulation,” *Polymer Composites*, vol. 14, pp. 132–143, 1993.

[40] C. Boutin, “Study of permeability by periodic and self-consistent homogenisation,” *European Journal of Mechanics-A/Solids*, vol. 19, pp. 603–632, 2000.

Chapter 6

Computation of macroscopic permeability of doubly porous materials

Part of the work developed in this chapter has been published in one paper:

- H.B. Ly, B. Le Droumaguet, V. Monchiet, D. Grande: Designing and modeling doubly porous polymeric materials, *Eur. Phys. J. Special Topics* 224, 1689-1706 (2015).

In this chapter, we determine the macroscopic permeability of doubly porous materials using the periodic homogenization and the Finite Element Method (FEM). At the "intermediate scale" or "mesoscopic scale" (*i.e.* that of macropores), the problem consists in solving a Darcy-Stokes coupled problem. In the macropores the fluid flow obeys the Stokes equations while, in the permeable solid, the flow obeys the Darcy equation to account for the presence of the nanoscopic pores. This coupled problem is solved by means of a mixed variational formulation with FE discretization. Finally, various illustrations are provided by considering different pore configurations for which the macropores are interconnected, non-interconnected, or having the FCC structure.

6.1 Introduction

Doubly porous media has been the subject of intense researches long ago [1, 2] since the first consideration of a dual-porosity concept and model in the 60s [3–5]. These studies mainly associated with homogenization techniques based on asymptotic series expansion methods [6–8]. Throughout those investigations, acoustics properties [9, 10], acoustic wave propagation [11] or transport properties in doubly porous media [12–14] have been the main issues. A macroscopic response for the fluid flow problems through a dual porosity media is then needed [15]. Modeling fluid flow through doubly porous media turns to a model in which we have to solve the coupling of two equations: the first equation describes fluid flow freely in the larger porous network, and the second deals with the fluid flows through a smaller porous network. The exchange of fluid between two porosity levels is then becomes an important factor for the coupling problem. For the sake of simplicity, the fluid in the higher porosity level is mainly considered as incompressible, obeying the Stokes equation, and Darcy equation for the porous permeable solid, thus the problem of coupling of Stokes and Darcy is then considered.

The nature of the simulation of flow through doubly porous materials leads to the problem of coupling the Stokes and Darcy equations. This is also the main interest of several practical problems related to Earth sciences where surface water percolates through rocks and sand, transport of substances between surface water and groundwater, fluid flow through rock fractures, reservoir problems, flow of oil or magma through geological media [3, 5, 16–20], and many industrials issues [21–30]. The main challenge of such problem is that, we have to find a mathematical formulation to deal with the continuity/discontinuity/conservation of the fields at the interface between free fluid and the porous counterpart. One of the solution can be found in the work of Brinkman [31], which is suitable for high permeability medium [32], or other in the work of Beavers, Joseph [33] and then completed by Saffman [34].

Finite element discretization of such problem, whether analytical or numerical, has been received a considerable attention from the research community. Unified or decoupled finite elements has been mainly discussed in the literature for the implementation. Decoupled approach with all the well-posedness related problems have been analyzed by Layton *et al.* [35]. This strategy devoted on the use of each stable elements for each domain, respectively (*i.e.* Taylor Hood elements or MINI elements for Stokes, coupling with Raviart Thomas or Brezzi-Douglas-Marini in Darcy domain). The second strategy based on the use of one finite element discretization overall the domain Stokes and Darcy, in a main motivation for the simplicity of implementation [36–38].

We propose herein to analyze two different approaches, decoupled and unified approach, *via* the implementation of both type finite elements. We use the robust elements proposed by Arbogast *et al.* [39, 40] for unified approach, and the MINI elements coupling with lowest order of Raviart Thomas elements for the decoupled approach. Some validations of the numerical tools are provided firstly, following by more detailed investigations, mainly on the effect of meshing interface between Stokes Darcy, or the contribution of each domain (whether Stokes or Darcy) to the macroscopic permeability. All the examples are provided in 2D and 3D for the decoupled approach.

6.2 Stokes - Darcy flow problem

6.2.1 The governing equations

At the mesoscopic scale, the unit cell contain two phases: the permeable solid denoted Ω_s containing the nanopores and defined by the permeability $\boldsymbol{K}_{\text{meso}}$, the fluid which occupy the domain Ω_f. The total volume of the unit cell is $\Omega = \Omega_s \cup \Omega_f$. The velocity is denoted by $\boldsymbol{v}$ and the pressure is p. At the interface between the solid and the fluid, the quantities $\boldsymbol{v}$ and p are discontinuous. In order to provide the conditions that hold at the interface Γ, the following notations are used:

$$\boldsymbol{v}^{(s)} = \boldsymbol{v}(\boldsymbol{x} \in \Gamma \cap \Omega_s), \quad \boldsymbol{v}^{(f)} = \boldsymbol{v}(\boldsymbol{x} \in \Gamma \cap \Omega_f), \tag{6.1}$$

$$p^{(s)} = p(\boldsymbol{x} \in \Gamma \cap \Omega_s), \quad p^{(f)} = p(\boldsymbol{x} \in \Gamma \cap \Omega_f) \tag{6.2}$$

By μ, we denote the dynamic viscosity of the fluid. The permeability tensor $\boldsymbol{K}_{\text{meso}}$ is assumed to be positive definite and is determined by solving the Stokes problem at the lower scale, this has been detailed in chapter 4. We denote by $\boldsymbol{\nu}$ the normal unit vector on Γ taken from Ω_s to Ω_f. Also, we denoted by $\boldsymbol{\tau}$ the tangent vector on Γ.

The Darcy-Stokes problem is defined by:

- the Stokes equations in the macropores:

$$\mu \Delta \boldsymbol{v} - \nabla p - \boldsymbol{G} = 0 \quad \boldsymbol{x} \in \Omega_f \tag{6.3}$$

$$\operatorname{div} \boldsymbol{v} = 0 \quad \boldsymbol{x} \in \Omega_f \tag{6.4}$$

- the Darcy equation and incompressibility condition in the permeable solid:

$$-\mu \boldsymbol{K}_{\text{meso}}^{-1}.\boldsymbol{v} - \nabla p - \boldsymbol{G} = 0 \quad \boldsymbol{x} \in \Omega_s \tag{6.5}$$

$$\operatorname{div} \boldsymbol{v} = 0 \quad \boldsymbol{x} \in \Omega_s \tag{6.6}$$

- the periodicity conditions:

$$\boldsymbol{v} \ \text{ periodic } \quad \boldsymbol{x} \in \partial\Omega \tag{6.7}$$

$$p \ \text{ periodic } \quad \boldsymbol{x} \in \partial\Omega \tag{6.8}$$

where $\partial\Omega$ denote the boundary of the unit cell.

- the interface conditions:

$$\boldsymbol{v}^{(s)}.\boldsymbol{\nu} = \boldsymbol{v}^{(f)}.\boldsymbol{\nu} \quad \boldsymbol{x} \in \Gamma \tag{6.9}$$

$$2\mu\boldsymbol{\nu}.\boldsymbol{d}(\boldsymbol{v}^{(f)}).\boldsymbol{\tau} = -\frac{\alpha}{\sqrt{k_{meso}}}\boldsymbol{v}^{(f)}.\boldsymbol{\tau} \quad \boldsymbol{x} \in \Gamma \tag{6.10}$$

$$2\mu\boldsymbol{\nu}.\boldsymbol{d}(\boldsymbol{v}^{(f)}).\boldsymbol{\nu} = p^{(s)} - p^{(f)} \quad \boldsymbol{x} \in \Gamma \tag{6.11}$$

These interface conditions represent the continuity of the mass flux (6.9), the Beaver-Joseph-Saffman (BJS) interface condition for the tangential stress (6.10) and the continuity for the normal stress (6.11). In equations (6.10) and (6.11), $\boldsymbol{d}(\boldsymbol{v}^{(f)})$ represents the strain rate tensor computed in the fluid region. The BJS interface condition involves a coefficient α and the scalar permeability k_{meso}. The BJS interface condition is then only applicable to the case of isotropic porous medium, $\boldsymbol{K}_{\text{meso}} = k_{\text{meso}}\boldsymbol{I}$ where it is recalled that $\boldsymbol{I}$ is the two order identity tensor. The coefficient α cannot be determined from a homogenization procedure. Indeed, homogenization technics only provide the bulk coefficients, not the interface one. Since we do not have any information about this coefficient we put $\alpha = +\infty$ which involves that the tangential part of the velocity at the interface Γ and in the fluid region is null. The Beaver-Joseph-Saffman (BJS) interface condition for the tangential stress (6.10) is then replaced by:

$$\boldsymbol{v}^{(f)}.\boldsymbol{\tau} = 0 \quad \boldsymbol{x} \in \Gamma \tag{6.12}$$

The Stokes-Darcy problem is linear, the local velocity field then linearly depends on the applied pressure gradient $\boldsymbol{G}$. The average of $\boldsymbol{v}$ over the volume of the unit cell is:

$$\boldsymbol{V} = <\boldsymbol{v}>_V = -\frac{1}{\mu}\boldsymbol{K}_{\text{macro}}.\boldsymbol{G} \tag{6.13}$$

which introduces the macroscopic permeability tensor $\boldsymbol{K}_{\text{macro}}$. The permeability $\boldsymbol{K}_{\text{macro}}$ depends on the porous microstructure at the mesoscopic scale and also on the permeability of the solid, $\boldsymbol{K}_{\text{macro}}$. The permeability $\boldsymbol{K}_{\text{meso}}$ then accounts for both porosities.

6.2.2 Variational formulation of Stokes-Darcy problem

Consider two test functions $\boldsymbol{w} \in \partial\mathcal{W}$, $q \in \mathcal{Q}$ where $\mathcal{W}$ is the space of continuous, derivable and square integrable velocity fields in Ω_f and in Ω_s which comply with the interface conditions:

$$\boldsymbol{w}^{(f)}.\boldsymbol{\nu} = \boldsymbol{w}^{(s)}.\boldsymbol{\nu} \qquad \boldsymbol{x} \in \Gamma \tag{6.14}$$

$$\boldsymbol{w}^{(f)}.\boldsymbol{\tau} = 0 \qquad \boldsymbol{x} \in \Gamma \tag{6.15}$$

and which are periodic. $\mathcal{Q}$ is the space of continuous square integrable pressure fields in Ω_f and in Ω_s which are discontinuous on Γ and are periodic.
In the Stokes equations (6.3) and (6.4), we multiply by the test functions $\boldsymbol{w}$ and q respectively and we integrate over the domain Ω_f:

$$\int_{\Omega_f} \mu(\Delta\boldsymbol{v}).\boldsymbol{w}dx - \int_{\Omega_f} (\nabla p).\boldsymbol{w}dx - \int_{\Omega_f} \boldsymbol{G}.\boldsymbol{w}dx = 0 \tag{6.16}$$

$$\int_{\Omega_f} q\,\mathrm{div}(\boldsymbol{v})dx = 0 \tag{6.17}$$

Following the method depicted in chapter 4, section (5.2.1), we can replace $\mu\Delta\boldsymbol{v}$ in the first integral in (6.16) by $\mathrm{div}(2\mu\boldsymbol{d}(\boldsymbol{v}))$ where $\boldsymbol{d}(\boldsymbol{v})$ is the strain rate tensor associated to the velocity $\boldsymbol{v}$. Making use of the divergence theorem, we obtain for this first integral:

$$\int_{\Omega_f} \mu(\Delta\boldsymbol{v}).\boldsymbol{w}dx = \int_{\partial\Omega_f\cup\Gamma} [2\mu\boldsymbol{d}(\boldsymbol{v}^{(f)}).\boldsymbol{n}].\boldsymbol{w}dx - \int_{\Omega_f} 2\mu\boldsymbol{d}(\boldsymbol{v}) : \boldsymbol{d}(\boldsymbol{w})dx \tag{6.18}$$

Where $\partial\Omega_f$ is the portion of $\partial\Omega$ crossed by the fluid (see Figure 6.1).

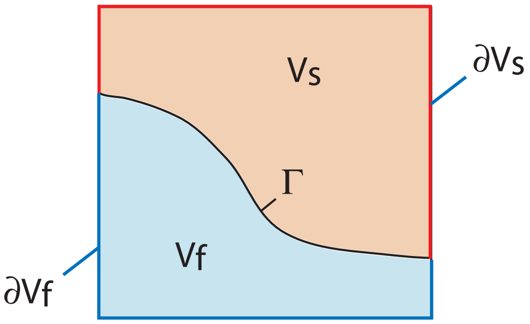

Figure 6.1: Representation of ∂V_f and ∂V_s the two parts of ∂V crossed by the fluid and the solid respectively.

The integral over $\partial\Omega$ is null due to the periodicity condition. However the integral over Γ is non null. On Γ, the tangential part of $\boldsymbol{w}$ is null but the normal component remains non null. On Γ, the velocity $\boldsymbol{w}$ can then be read:

$$\boldsymbol{w}^{(f)} = (\boldsymbol{w}^{(f)}.\boldsymbol{\nu})\boldsymbol{\nu} \tag{6.19}$$

where $\boldsymbol{\nu}$ is the normal unit vector taken on Γ, from Ω_s to Ω_f. Consequently $\boldsymbol{n} = -\boldsymbol{\nu}$ over Γ and (6.18) becomes:

$$\int_{\Omega_f} \mu(\Delta \boldsymbol{v}).\boldsymbol{w} dx = -\int_{\Gamma} 2\mu[\boldsymbol{\nu}.\boldsymbol{d}(\boldsymbol{v}^{(f)}).\boldsymbol{\nu}]\boldsymbol{w}^{(f)}.\boldsymbol{\nu} dx - \int_{\Omega_f} 2\mu \boldsymbol{d}(\boldsymbol{v}) : \boldsymbol{d}(\boldsymbol{w}) dx \tag{6.20}$$

Consider the second integral in (6.16) with the divergence theorem, it leads to:

$$\int_{\Omega_f} (\nabla p).\boldsymbol{w} dx = \int_{\partial\Omega_f \cup \Gamma} p(\boldsymbol{w}.\boldsymbol{n}) dx - \int_{\Omega_f} p \operatorname{div}(\boldsymbol{w}) dx \tag{6.21}$$

The integral over $\partial\Omega_f$ is null due to the periodicity of p and $\boldsymbol{w}$ but the integral over Γ is non null. Equation (6.21) then becomes (accounting again that $\boldsymbol{n} = -\boldsymbol{\nu}$ on Γ):

$$\int_{\Omega_f} (\nabla p).\boldsymbol{w} dx = -\int_{\Gamma} p^{(f)}(\boldsymbol{w}^{(f)}.\boldsymbol{\nu}) dx - \int_{\Omega_f} p \operatorname{div}(\boldsymbol{w}) dx \tag{6.22}$$

Accounting for (6.20) and (6.22) in (6.16), it leads to:

$$-\int_{\Gamma} 2\mu[\boldsymbol{\nu}.\boldsymbol{d}(\boldsymbol{v}^{(f)}).\boldsymbol{\nu}]\boldsymbol{w}^{(f)}.\boldsymbol{\nu} dx - \int_{\Omega_f} 2\mu \boldsymbol{d}(\boldsymbol{v}) : \boldsymbol{d}(\boldsymbol{w}) dx \tag{6.23}$$

$$+\int_{\Gamma} p^{(f)}(\boldsymbol{w}^{(f)}.\boldsymbol{\nu}) dx + \int_{\Omega_f} p \operatorname{div}(\boldsymbol{w}) dx - \int_{\Omega_f} \boldsymbol{G}.\boldsymbol{w} dx = 0 \tag{6.24}$$

Now, we multiply (6.5) and (6.6) by the test functions $\boldsymbol{w}$ and q respectively and we integrate over the volume Ω_s:

$$-\int_{\Omega_s} \mu \boldsymbol{v}.\boldsymbol{K}_{meso}^{-1}.\boldsymbol{w} dx - \int_{\Omega_s} (\nabla p).\boldsymbol{w} dx - \int_{\Omega_s} \boldsymbol{G}.\boldsymbol{w} dx = 0 \tag{6.25}$$

$$\int_{\Omega_s} q \operatorname{div} \boldsymbol{v} dx = 0 \tag{6.26}$$

In the second integral in (6.25), we use the divergence theorem:

$$\int_{\Omega_s} (\nabla p).\boldsymbol{w} dx = \int_{\partial\Omega_s \cup \Gamma} p\boldsymbol{w}.\boldsymbol{n} dx - \int_{\Omega_s} p \operatorname{div}(\boldsymbol{w}) dx \tag{6.27}$$

where $\partial\Omega_s$ is the surface of the boundary $\partial\Omega$ crossed by the porous solid. The integral over $\partial\Omega_s$ is null due to the periodicity and only the integral over Γ remains where $\boldsymbol{n} = \boldsymbol{\nu}$. The above equation then reads:

$$\int_{\Omega_s} (\nabla p).\boldsymbol{w} dx = \int_{\Gamma} p^{(s)}\boldsymbol{w}^{(s)}.\boldsymbol{\nu} dx - \int_{\Omega_s} p \operatorname{div}(\boldsymbol{w}) dx \tag{6.28}$$

Introducing the above result in equation (6.25), it gives:

$$-\int_{\Omega_s} \mu \boldsymbol{v}.\boldsymbol{K}_{meso}^{-1}.\boldsymbol{w} dx - \int_{\Gamma} p^{(s)}\boldsymbol{w}^{(s)}.\boldsymbol{\nu} dx + \int_{\Omega_s} p \operatorname{div}(\boldsymbol{w}) dx - \int_{\Omega_s} \boldsymbol{G}.\boldsymbol{w} dx = 0 \tag{6.29}$$

By adding the results (6.24) and (6.29) and considering that $\boldsymbol{w}^{(s)}.\boldsymbol{\nu} = \boldsymbol{w}^{(f)}.\boldsymbol{\nu}$ (see relation (6.14)), we obtain:

$$\int_{\Gamma} \left\{p^{(f)} - p^{(s)} - 2\mu[\boldsymbol{\nu}.\boldsymbol{d}(\boldsymbol{v}^{(f)}).\boldsymbol{\nu}]\right\} \boldsymbol{w}^{(f)}.\boldsymbol{\nu} dx - \int_{\Omega_f} 2\mu \boldsymbol{d}(\boldsymbol{v}) : \boldsymbol{d}(\boldsymbol{w}) dx \tag{6.30}$$

$$-\int_{\Omega_s} \mu \boldsymbol{v}.\boldsymbol{K}_{meso}^{-1}.\boldsymbol{w} dx + \int_{\Omega} p \operatorname{div}(\boldsymbol{w}) dx - \int_{\Omega} \boldsymbol{G}.\boldsymbol{w} dx = 0 \tag{6.31}$$

Owing to relation (6.11), we deduce that the first integral in the above equation is null and it then remains:

$$-\int_{\Omega_f} 2\mu \boldsymbol{d}(\boldsymbol{v}) : \boldsymbol{d}(\boldsymbol{w}) dx - \int_{\Omega_s} \mu \boldsymbol{v}.\boldsymbol{K}_{meso}^{-1}.\boldsymbol{w} dx \tag{6.32}$$

$$+\int_{\Omega} p \operatorname{div}(\boldsymbol{w}) dx - \int_{\Omega} \boldsymbol{G}.\boldsymbol{w} dx = 0 \tag{6.33}$$

Adding now the results (6.17) and (6.26), we deduce that:

$$\int_{\Omega} q \operatorname{div}(\boldsymbol{v}) dx = 0 \tag{6.34}$$

Introducing $(\cdot,\cdot)$, $(\cdot,\cdot)_f$, $(\cdot,\cdot)_s$ the inner products on the domains Ω, Ω_f and Ω_s respectively, the relations (6.33) and (6.34) can be given into the form:

$$\begin{cases} 2\mu(\boldsymbol{d}(\boldsymbol{v}), \boldsymbol{d}(\boldsymbol{w}))_f + \mu(\boldsymbol{K}_{meso}^{-1}.\boldsymbol{v}, \boldsymbol{w})_s - (p, \operatorname{div}(\boldsymbol{w})) = -(\boldsymbol{G}, \boldsymbol{w}) \\ (\operatorname{div}(\boldsymbol{v}), q) = (0, q) \end{cases} \tag{6.35}$$

It can be observed that the exact solution is a stationarity point of the functional Φ defined by:

$$\Phi(\boldsymbol{v}, p) = \mu(\boldsymbol{d}(\boldsymbol{v}), \boldsymbol{d}(\boldsymbol{v}))_f + \frac{\mu}{2}(\boldsymbol{K}_{meso}^{-1}.\boldsymbol{v}, \boldsymbol{v})_s - (p, \operatorname{div}(\boldsymbol{v})) + (\boldsymbol{G}, \boldsymbol{v}) \tag{6.36}$$

6.2.3 Dimensionless equations

From a practical point of view, a dimensionless version of the Darcy-Stokes equations is used for the implementation. This has the advantage to produce various results which are independent of the choice of the fluid and of the size of the microstructure. This only involves a change of variable in the set of equations constituted of relation (6.3) to relation (6.12). Indeed, let us put in these relations:

$$\boldsymbol{v} = \frac{L^2 \|\boldsymbol{G}\|}{\mu} \boldsymbol{v}^*, \quad p = L\|\boldsymbol{G}\| p^*, \quad \boldsymbol{G} = \|\boldsymbol{G}\| \boldsymbol{J}, \quad \boldsymbol{K}_{\text{meso}} = h^2 \boldsymbol{K}_{\text{meso}}^*, \quad \boldsymbol{x} = L\boldsymbol{x}^* \tag{6.37}$$

where L is the dimension of the unit cell at the mesoscopic scale, h is the dimension of the unit cell at the nanoscopic scale, $\boldsymbol{K}_{\text{meso}}^*$ is the dimensionless mesoscopic permeability, $\boldsymbol{J}$ is a unit vector giving the direction of flow. By doing so, the Darcy-Stokes equations become:

- the Stokes equations in the macropores:

$$\Delta^* \boldsymbol{v}^* - \nabla^* p^* - \boldsymbol{J} = 0 \quad \boldsymbol{x}^* \in \Omega_f^* \tag{6.38}$$

$$\operatorname{div}^* \boldsymbol{v}^* = 0 \quad \boldsymbol{x}^* \in \Omega_f^* \tag{6.39}$$

- the Darcy equation and incompressibility condition in the permeable solid:

$$-(\epsilon^2 \boldsymbol{K}_{\text{meso}}^*)^{-1}.\boldsymbol{v}^* - \nabla^* p^* - \boldsymbol{J} = 0 \quad \boldsymbol{x}^* \in \Omega_s^* \tag{6.40}$$

$$\operatorname{div}^* \boldsymbol{v}^* = 0 \quad \boldsymbol{x}^* \in \Omega_s^* \tag{6.41}$$

- the periodicity conditions:

$$\boldsymbol{v}^* \quad \text{periodic} \quad \boldsymbol{x}^* \in \partial\Omega^* \tag{6.42}$$

$$p^* \quad \text{periodic} \quad \boldsymbol{x}^* \in \partial\Omega^* \tag{6.43}$$

- the interface conditions:

$$\boldsymbol{v}^{*(s)}.\boldsymbol{\nu} = \boldsymbol{v}^{*(f)}.\boldsymbol{\nu} \quad \boldsymbol{x} \in \Gamma^* \tag{6.44}$$

$$\boldsymbol{v}^{*(f)}.\boldsymbol{\tau} \quad \boldsymbol{x}^* \in \Gamma^* \tag{6.45}$$

$$2\boldsymbol{\nu}.\boldsymbol{d}^*(\boldsymbol{v}^{*(f)}).\boldsymbol{\nu} = p^{*(s)} - p^{*(f)} \quad \boldsymbol{x} \in \partial\Gamma^* \tag{6.46}$$

in which we have introduced the scale factor

$$\epsilon = \frac{h}{L} \tag{6.47}$$

which is a small parameter. With the dimensionless variables, the macroscopic Darcy law is:

$$\boldsymbol{V}^* =< \boldsymbol{v}^* >= -\boldsymbol{K}^*_{\text{macro}}.\boldsymbol{J} \tag{6.48}$$

where $\boldsymbol{K}^*_{\text{macro}}$ is the dimensionless macroscopic permeability defined by $\boldsymbol{K}^*_{\text{macro}} = \boldsymbol{K}_{\text{macro}}/L^2$. Practically, the calculations are performed on a unit cell having the dimension 1 in each space directions, with a viscosity $\mu = 1$ and with an applied pressure gradient having the norm $\|\boldsymbol{G}\| = 1$. The components of the permeability tensor $\boldsymbol{K}^*_{\text{macro}}$ are computed by applying successvely $J_1 = 0$, $J_2 = J_3 = 0$, then $J_2 = 0$, $J_1 = J_3 = 0$, and then $J_3 = 0$, $J_1 = J_2 = 0$. If the macroscopic permeability is isotropic, only one loading case is considered for the computation of the macroscopic permeability. When the problem is written with dimensionless variables, the Darcy equation (6.40) uses the apparent permeability $\epsilon^2\boldsymbol{K}^*_{\text{meso}}$. Consider an isotropic porous microstructure at the nanoscale:

$$\boldsymbol{K}^*_{\text{meso}} = k^*_{meso} I \tag{6.49}$$

The apparent isotropic permeability in the dimensionless equation is:

$$\kappa = \frac{k_{meso}}{L^2} = \epsilon^2 k^*_{meso} \tag{6.50}$$

We aim now to give the magnitude of the coefficient κ which will be used in our calculations. This coefficient depends on the nanoporous microstructure but also on the scale factor that exists between the nanoscopic and the mesoscopic scale. In Table 6.1 are provided the values of κ by taking for ϵ the values 2E-1, 1E-2, 2E-4 and various porous microstructures with spherical pores already considered in the last chapter. For each of this microstructure, we give the radius r of the nano-voids and their arrangement along a SC, BCC or FCC packing system.

Table 6.1: Values of κ for different nanoporous structures, radius of inclusion (r) and scale factors (ϵ).

Packing system	κ $\epsilon^2 = 5 \times 10^{-2}$	κ $\epsilon^2=10^{-4}$	κ $\epsilon^2=5\times10^{-8}$
SC structure			
r = 0.3×h	10.36×10^{-3}	20.73×10^{-6}	10.36×10^{-9}
r = 0.5×h	35.60×10^{-4}	7.44×10^{-6}	35.60×10^{-10}
r = 0.7×h	12.55×10^{-4}	2.51×10^{-6}	12.55×10^{-10}
r = 0.9×h	3.05×10^{-4}	0.61×10^{-6}	3.05×10^{-10}
BCC structure			
r = 0.5×h	5.00×10^{-4}	1.00×10^{-6}	5.00×10^{-10}
FCC structure			
r = 0.375×h	1.30×10^{-4}	0.26×10^{-6}	1.30×10^{-10}

It is observed that the apparent isotropic permeability κ varies in the range [1E-10,1E-2]. In some numerical application provided in this chapter, the values of κ in the range [1E-10,1E-2] are considered but we also use the value $\kappa = 1$. Obviously this value may corresponds to a highly permeable microstructure whose existence is not ensure. It is greatly probable that such value of κ is not physically. However, if κ is two small, the Darcy contribution is also too small compared to the Stokes one and it is not really possible to verify/validate the accuracy of the FE numerical tools.

6.3 Finite element numerical integration

6.3.1 Choice of elements

6.3.1.1 Arbogast and Brunson's rectangular element

In Arbogast *et al.* [38, 39], rectangular elements are considered for both the fluid or the solid phase. As in the last chapter, it is convenient to define the basis functions with the dimensionless coordinates (ξ, η) instead of the coordinates (x, y). The origin of (ξ, η) is the center of the rectangle and ξ, η vary from -1 to 1. The positions of the corners are $(-1,1)$, $(1,1)$, $(-1,-1)$ and $(1,-1)$.

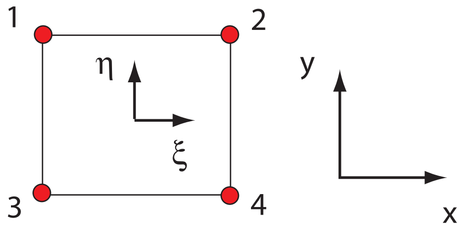

Figure 6.2: Arbogast and Brunson's rectangular element

The relations giving the coordinates (x, y) as function of (ξ, η) are:

$$x = \sum_{i=1}^{i=4} x_i N_i, \quad y = \sum_{i=1}^{i=4} y_i N_i \tag{6.51}$$

where N_1, N_2, N_3 and N_4 are defined by:

$$N_1 = (1-\xi)(1-\eta), \;\; N_2 = \xi(1-\eta), \quad N_3 = \eta(1-\xi), \quad N_4 = \xi\eta \tag{6.52}$$

In the element, the pressure is taken into the form:

$$p = \sum_{i=1}^{i=4} p_i N_i \tag{6.53}$$

where p_1, p_2, p_3 and p_4 are the values of the pressure at each corner. For the velocity field, the following expressions are considered:

$$v_x = v_x^1 P_1 + v_x^2 P_2 + v_x^3 P_3 + v_x^4 P_4 + f_x^1 Q_1 + f_x^2 Q_2 \tag{6.54}$$
$$v_y = v_y^1 P_5 + v_y^2 P_6 + v_y^3 P_7 + v_y^4 P_8 + f_y^1 Q_3 + f_y^2 Q_4 \tag{6.55}$$

with the following expressions for the basis functions P_i and Q_i:

$$\begin{aligned}
&P_1 = (1-\xi)(1+\eta)(3\eta-1)/8, && P_2 = (1+\xi)(1+\eta)(3\eta-1)/8,\\
&P_3 = (1-\xi)(\eta-1)(3\eta+1)/8, && P_4 = (1+\xi)(\eta-1)(3\eta+1)/8,\\
&P_5 = (\xi-1)(1+\eta)(3\xi+1)/8, && P_6 = (1+\xi)(1+\eta)(3\xi-1)/8,\\
&P_7 = (1-\xi)(\eta-1)(3\xi+1)/8, && P_8 = (1+\xi)(1-\eta)(3\xi-1)/8,\\
&Q_1 = 3(1-\xi+\xi\eta^2-\eta^2)/8, && Q_2 = 3(1-\eta^2+\xi-\xi\eta^2)/8\\
&Q_3 = 3(1-\eta+\eta\xi^2-\xi^2)/8, && Q_4 = 3(1-\xi^2+\eta-\eta\xi^2)/8,
\end{aligned} \tag{6.56}$$

In relations (6.54) and (6.55), v_x^i and v_y^i for $i = 1, 2, 3, 4$ represent the components of the velocity field at each corner while f_x^1, f_x^2, f_y^1 and f_y^2 represent the flux on each edge.

These fluxes are defined such that:

$$\begin{aligned}
&\int_{\eta=-1}^{\eta=1} v_x(\xi=-1,\eta)d\eta = f_x^1, \\
&\int_{\eta=-1}^{\eta=1} v_x(\xi=1,\eta)d\eta = f_x^2, \\
&\int_{\eta=-1}^{\eta=1} v_y(\xi,\eta=-1)d\xi = f_y^1, \\
&\int_{\eta=-1}^{\eta=1} v_y(\xi,\eta=1)d\xi = f_y^2
\end{aligned} \tag{6.57}$$

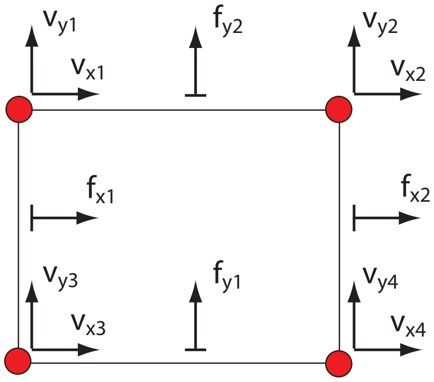

Figure 6.3: Degrees of freedoms of the Arbogast and Brunson rectangular element

The rectangular Arbogast and Brunson's element introduce 16 DOFs: 2 components of the velocity field at each corner + 1 flux at each edge + 1 pressure at each corner. The generalization to the 3D case would introduce 38 DOFs: 8 corners × 3 components of the velocity field + 8 corners × 1 pressure + 6 faces × 1 flux. The Arbogast and Brunson elements has various disadvantages: the porous cell is discretized with a regular array, this involve a large number of elements, moreover the interface between the solid and the fluid is approximated by horizontal or vertical edges which would reduces the accuracy of the finite element solution.

An alternative method is presented in the next section, it uses triangular element which has two advantages: first, adaptive meshes can be used to reduce the total number of elements and then then the total number of DOFs, second the interface is approximated with polygonal curves which would considerably improve the solution.

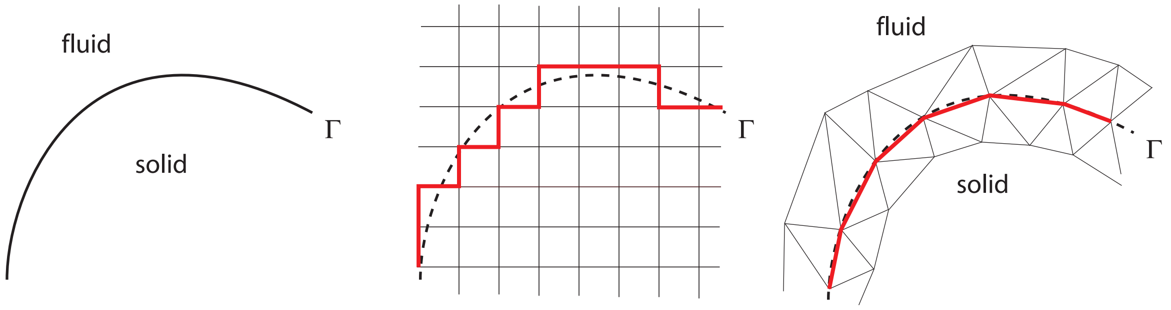

Discretization with rectangular elements

Discretization with triangular elements

Figure 6.4: Discretization of the interface between the solid and the fluid when using triangular or rectangular elements

6.3.1.2 Discretization with triangular elements

Obviously, a generalization of the Arbogast and Brunson rectangular element to arbitrary quadrangle is possible, however the use of triangular elements is more advantageous since we can use the MINI element for the fluid domain already introduced in the last chapter. For the solid part we propose to use the Raviart-Thomas elements which only introduce 4 degrees of freedom by element: 3 flux and 1 pressure. This corresponds to the better choice for reducing the total DOFs.

The notations used in chapter 4 are still considered in this section: we denoted by (x_1, y_1), (x_2, y_2), (x_3, y_3) the positions of the corners of the triangles. In the local basis (ξ, η), the positions of the corners are $(0, 0)$, $(0, 1)$, $(1, 0)$. The triangular element is represented in Figure 6.5.

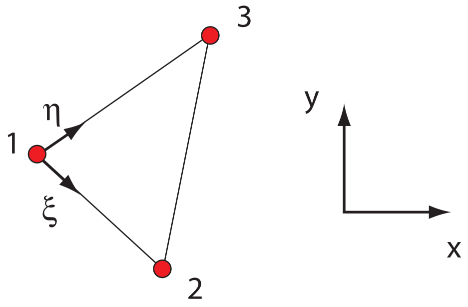

Figure 6.5: Triangular element

In this section we provide an alternative form for the velocity field. In [41], the velocity field is provided in the local basis $(\boldsymbol{e}_\xi, \boldsymbol{e}_\eta)$ associated with coordinates (ξ, η) and which is not appropriate for the computation of the integrals of the weak form. In the present section the velocity field is expressed in an arbitrary frame $(\boldsymbol{e}_x, \boldsymbol{e}_y)$ associated with the

coordinates (x, y).
In the triangular Raviart-Thomas element, the velocity field is approximated by:

$$\boldsymbol{v} = \sum_{i=1}^{i=3} N_i \boldsymbol{g}_i \tag{6.58}$$

where the N_1, N_2 and N_3 are the basis functions:

$$N_1 = 1 - \xi - \eta, \quad N_2 = \xi, \quad N_3 = \eta \tag{6.59}$$

and $\boldsymbol{g}_i$ for $i = 1, 2, 3$ are three vectors which have to be determined.

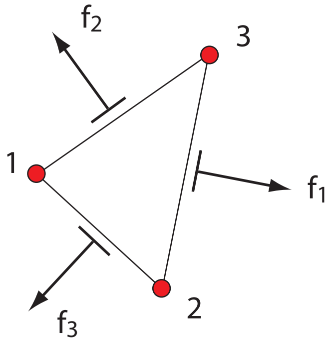

Figure 6.6: Raviart-Thomas triangular element

Let us denote by f_1, f_2 and f_3 the flux on each edges (see Figure 6.6) defined by:

$$f_1 = \boldsymbol{v}\Big|_{A_2A_3} .\boldsymbol{n}_1 dx, \quad f_2 = \boldsymbol{v}\Big|_{A_2A_3} .\boldsymbol{n}_2 dx, \quad f_3 = \boldsymbol{v}\Big|_{A_2A_3} .\boldsymbol{n}_3 dx \tag{6.60}$$

in which

$$\boldsymbol{v}\Big|_{A_2A_3}, \quad \boldsymbol{v}\Big|_{A_2A_3}, \quad \boldsymbol{v}\Big|_{A_2A_3} \tag{6.61}$$

represent the values taken by the velocity field $\boldsymbol{v}$ on each edges A_2A_3, A_3A_1 and A_1A_2 where A_1, A_2 and A_3 represent the points with the coordinates (x_1, y_1), (x_2, y_2), (x_3, y_3) respectively. In (6.60), $\boldsymbol{n}_1$, $\boldsymbol{n}_2$ and $\boldsymbol{n}_3$ denote the normal unit vectors to the edges A_2A_3, A_3A_1 and A_1A_2 taken from inside to outside the element. We introduce the velocity (6.58) in the formula (6.60) to determine the vectors $\boldsymbol{g}_i$ for $i = 1, 2, 3$ as function of the constant flux f_i for $i = 1, 2, 3$. Consider the equation in (6.60). On the edge A_2A_3 we have $\eta = 1 - \xi$, $N_1 = 0$, $N_3 = 1 - N_2$, this leads to:

$$f_1 = [\xi \boldsymbol{g}_2 + (1 - \xi)\boldsymbol{g}_3] .\boldsymbol{n}_1 \tag{6.62}$$

This equation being verified for arbitrary value of ξ, we deduce that:

$$f_1 = \boldsymbol{g}_3.\boldsymbol{n}_1, \quad [\boldsymbol{g}_3 - \boldsymbol{g}_2] .\boldsymbol{n}_1 = 0 \tag{6.63}$$

By doing the same with the two other equations in (6.60), we obtain:

$$f_2 = \boldsymbol{g}_1.\boldsymbol{n}_2, \quad [\boldsymbol{g}_3 - \boldsymbol{g}_1].\boldsymbol{n}_2 = 0 \tag{6.64}$$

$$f_3 = \boldsymbol{g}_1.\boldsymbol{n}_3, \quad [\boldsymbol{g}_2 - \boldsymbol{g}_1].\boldsymbol{n}_3 = 0 \tag{6.65}$$

Owing to:

$$A = \frac{1}{2}\overrightarrow{A_1A_3}.\boldsymbol{n}_1 = \frac{1}{2}\overrightarrow{A_2A_1}.\boldsymbol{n}_2 = \frac{1}{2}\overrightarrow{A_2A_1}.\boldsymbol{n}_3 \tag{6.66}$$

where A is the area of the triangle, we deduce that the solution of (6.63), (6.64) and (6.65) is:

$$\boldsymbol{g}_1 = \frac{1}{2A}(f_2\overrightarrow{A_2A_1} + f_3\overrightarrow{A_3A_1}) \tag{6.67}$$

$$\boldsymbol{g}_2 = \frac{1}{2A}(f_1\overrightarrow{A_1A_2} + f_3\overrightarrow{A_3A_2}) \tag{6.68}$$

$$\boldsymbol{g}_3 = \frac{1}{2A}(f_1\overrightarrow{A_1A_3} + f_2\overrightarrow{A_2A_3}) \tag{6.69}$$

6.3.1.3 Extension to the 3D case

In the 3D case, tetrahedral elements are used. The MINI-element is still considered in the fluid region and, in the solid region, we use a generalization of the Raviart-Thomas interpolation. Let us define by A_1, A_2, A_3 and A_4 the points having the coordinates (x_1, y_1, z_1), (x_2, y_2, z_2), (x_3, y_3, z_3), (x_4, y_4, z_4) of the four corners such that:

$$V = \frac{1}{6}(\overrightarrow{A_1A_2}, \overrightarrow{A_1A_3}, \overrightarrow{A_1A_4}) = (\overrightarrow{A_1A_2} \wedge \overrightarrow{A_1A_3}).\overrightarrow{A_1A_4} > 0 \tag{6.70}$$

where $(\boldsymbol{u}, \boldsymbol{v}, \boldsymbol{w})$ is the scalar triple product defined by $(\boldsymbol{u} \wedge \boldsymbol{v}).\boldsymbol{w}$. Following the approach depicted in the 2D case (the details are not provided) we obtain the formula given below.

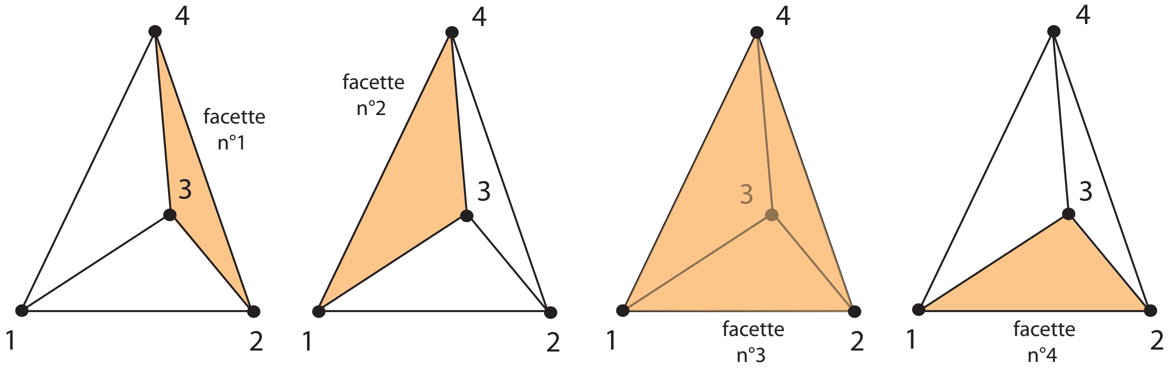

Let us denote $\boldsymbol{n}_1$, $\boldsymbol{n}_2$, $\boldsymbol{n}_3$ and $\boldsymbol{n}_4$ the normal flux on the faces $A_2A_3A_4$, $A_1A_3A_4$,

$A_1A_2A_4$, and $A_1A_2A_3$, respectively which can be computed with the formula:

$$\boldsymbol{n}_1 = \frac{1}{2S_1}\overrightarrow{A_2A_4} \wedge \overrightarrow{A_2A_3} \tag{6.71}$$

$$\boldsymbol{n}_2 = \frac{1}{2S_2}\overrightarrow{A_3A_4} \wedge \overrightarrow{A_3A_1} \tag{6.72}$$

$$\boldsymbol{n}_3 = \frac{1}{2S_3}\overrightarrow{A_4A_2} \wedge \overrightarrow{A_4A_1} \tag{6.73}$$

$$\boldsymbol{n}_4 = \frac{1}{2S_4}\overrightarrow{A_1A_2} \wedge \overrightarrow{A_1A_3} \tag{6.74}$$

and in which S_1, S_2, S_3, S_4 are the surface area of the corresponding faces:

$$S_1 = \frac{1}{2}\|\overrightarrow{A_2A_4} \wedge \overrightarrow{A_2A_3}\| \tag{6.75}$$

$$S_2 = \frac{1}{2}\|\overrightarrow{A_3A_4} \wedge \overrightarrow{A_3A_1}\| \tag{6.76}$$

$$S_3 = \frac{1}{2}\|\overrightarrow{A_4A_2} \wedge \overrightarrow{A_4A_1}\| \tag{6.77}$$

$$S_4 = \frac{1}{2}\|\overrightarrow{A_1A_2} \wedge \overrightarrow{A_1A_3}\| \tag{6.78}$$

The velocity is given by

$$\boldsymbol{v} = \sum_{i=1}^{i=4} \boldsymbol{g}^i N_i \tag{6.79}$$

where N_i are the basis functions defined by :

$$N_1 = 1 - \xi - \eta - \zeta, \quad N_2 = \xi, \quad N_3 = \eta, \quad N_4 = \zeta \tag{6.80}$$

and the vectors $\boldsymbol{g}^i$ for $i = 1, 2, 3, 4$ are defined by

$$\boldsymbol{g}_1 = \frac{1}{6V}(f_2\overrightarrow{A_2A_1} + f_3\overrightarrow{A_3A_1} + f_4\overrightarrow{A_4A_1}) \tag{6.81}$$

$$\boldsymbol{g}_2 = \frac{1}{6V}(f_1\overrightarrow{A_1A_2} + f_3\overrightarrow{A_3A_2} + f_4\overrightarrow{A_4A_2}) \tag{6.82}$$

$$\boldsymbol{g}_3 = \frac{1}{6V}(f_1\overrightarrow{A_1A_3} + f_2\overrightarrow{A_2A_3} + f_4\overrightarrow{A_4A_3}) \tag{6.83}$$

$$\boldsymbol{g}_4 = \frac{1}{6V}(f_1\overrightarrow{A_1A_4} + f_2\overrightarrow{A_2A_4} + f_3\overrightarrow{A_3A_4}) \tag{6.84}$$

Note that all the components of $\boldsymbol{g}_i$ for $i = 1, 2, 3, 4$ can be given in the following matrical form:

$$\begin{Bmatrix} g_{1x} \\ g_{1y} \\ g_{1z} \\ \vdots \\ g_{4x} \\ g_{4y} \\ g_{4z} \end{Bmatrix} = [P] \begin{Bmatrix} f_1 \\ f_2 \\ f_3 \\ f_4 \end{Bmatrix} \tag{6.85}$$

where the components of $[P]$ are:

$$[P] = \frac{1}{6V}\begin{bmatrix} 0 & x_1 - x_2 & x_1 - x_3 & x_1 - x_4 \\ 0 & y_1 - y_2 & y_1 - y_3 & y_1 - y_4 \\ 0 & z_1 - z_2 & z_1 - z_3 & z_1 - z_4 \\ x_2 - x_1 & 0 & x_2 - x_3 & x_2 - x_4 \\ y_2 - y_1 & 0 & y_2 - y_3 & y_2 - y_4 \\ z_2 - z_1 & 0 & z_2 - z_3 & z_2 - z_4 \\ x_3 - x_1 & x_3 - x_2 & 0 & x_3 - x_4 \\ y_3 - y_1 & y_3 - y_2 & 0 & y_3 - y_4 \\ z_3 - z_1 & z_3 - z_2 & 0 & z_3 - z_4 \\ x_4 - x_1 & x_4 - x_2 & x_4 - x_3 & 0 \\ y_4 - y_1 & y_4 - y_2 & y_4 - y_3 & 0 \\ z_4 - z_1 & z_4 - z_2 & z_4 - z_3 & 0 \end{bmatrix} \tag{6.86}$$

6.3.2 Finite Element discretization

6.3.2.1 The linear system

Following the same approached described in the last chapter, the discretized expression of Φ, given by relation (6.94), is:

$$\Phi = \tfrac{1}{2}\left\{v\right\}^t[K]\left\{v\right\} - \left\{p^t\right\}[B]\left\{v\right\} + \left\{v\right\}^t\left\{b\right\} \tag{6.87}$$

which involves the matrix $[K]$, $[B]$ and the vector $\{b\}$. In $\{v\}$ and $\{p\}$ are regrouped all the DOFs. The stationary point of Φ is obtained by solving the linear system:

$$\begin{bmatrix} K & -B^t \\ -B & 0 \end{bmatrix}\begin{Bmatrix} v \\ p \end{Bmatrix} = \begin{Bmatrix} b \\ 0 \end{Bmatrix} \tag{6.88}$$

• When the Arobogast rectangular elements are used, it must be recalled that the same elements are taken in for both region, the fluid and the solid. In $\{v\}$ are regrouped all the nodal velocities and the flux at each edge. In $\{p\}$ are collected all the nodal pressure.

• When the triangular or tetrahedral elements are used, we have different elements in the fluid and the solid region. In the fluid, the MINI-elements are used and the Raviart-Thomas elements are considered in the solid. In the vector $\{v\}$, are regrouped all the nodal velocities and the DOF associated with the bubble function for the elements which are in the fluid region. For the element in the solid region, the fluxes on each edge are regrouped in $\{v\}$. Concerning the vector $\{p\}$, it contains the nodal pressure in the fluid region and one pressure by element in the solid region.

The Arbogast and Brunson elements are only applicable to 2D problems and have been considered just to check the accuracy of the method based on MINI-elements coupled with Raviart-Thomas elements. For this reason we only provide the details about the computation $[K]$, $[B]$ and $\{b\}$ for the MINI-elements/Raviart-Thomas approach. Moreover all the formula are given for the 3D problems, the 2D case could be obtain by eliminating all the components corresponding to the Oz direction.

In each element, the velocity and the pressure could be still written in the form given by (5.14) in which $\{v_e\}$ and $\{p_e\}$ must be replaced by $\left\{v_e^{(f)}\right\}$ and $\left\{p_e^{(f)}\right\}$ which are given by:

$$\{v_e^{(f)}\} = \left\{ \begin{array}{c} v_x^1 \\ v_y^1 \\ v_z^1 \\ \vdots \\ v_x^5 \\ v_y^5 \\ v_z^5 \end{array} \right\}, \quad \{p_e^{(f)}\} = \left\{ \begin{array}{c} p^1 \\ p^2 \\ p^3 \\ p^4 \end{array} \right\} \tag{6.89}$$

v_x^1, v_y^1, v_z^1, ... v_x^4, v_y^4, v_z^4 are the nodal velocities and v_x^5, v_y^5, v_z^5 are the DOF corresponding to the bubble functions. In the Raviart-Thomas element, $\{v_e\}$ and $\{p_e\}$ are given by:

$$\{v_e^{(s)}\} = \left\{ \begin{array}{c} F^1 \\ F^2 \\ F^3 \end{array} \right\}, \quad \{p_e^{(s)}\} = \left\{ \begin{array}{c} p \end{array} \right\} \tag{6.90}$$

where F^1, F^2, F^3 are the edge flux in the global frame. Indeed, in the reference element, the normal unit vectors $\boldsymbol{n}_1$, $\boldsymbol{n}_2$, $\boldsymbol{n}_3$ are unambiguously definite: they are oriented from inside to outside the triangular element. However, in the global frame, an edge belong to two triangular elements. A normal vector $\boldsymbol{N}_i$ must be affected to each edges which are in the solid region. For this reason, we must distinguish the normal unit vectors $\boldsymbol{N}_1$, $\boldsymbol{N}_2$, $\boldsymbol{N}_3$ in the global frame from the normal unit vector $\boldsymbol{n}_1$, $\boldsymbol{n}_2$, $\boldsymbol{n}_3$ in the local frame. The flux F^1, F^2, F^3 in the global frame are related to f^1, f^2, f^3 by:

$$F_1 = \boldsymbol{N}_1.\boldsymbol{n}_1 f_1, \quad F_2 = \boldsymbol{N}_2.\boldsymbol{n}_2 f_2, \quad F_3 = \boldsymbol{N}_3.\boldsymbol{n}_3 f_3 \tag{6.91}$$

in which $\boldsymbol{N}_1.\boldsymbol{n}_1$, $\boldsymbol{N}_2.\boldsymbol{n}_2$ and $\boldsymbol{N}_3.\boldsymbol{n}_3$ take the values 1 or -1.

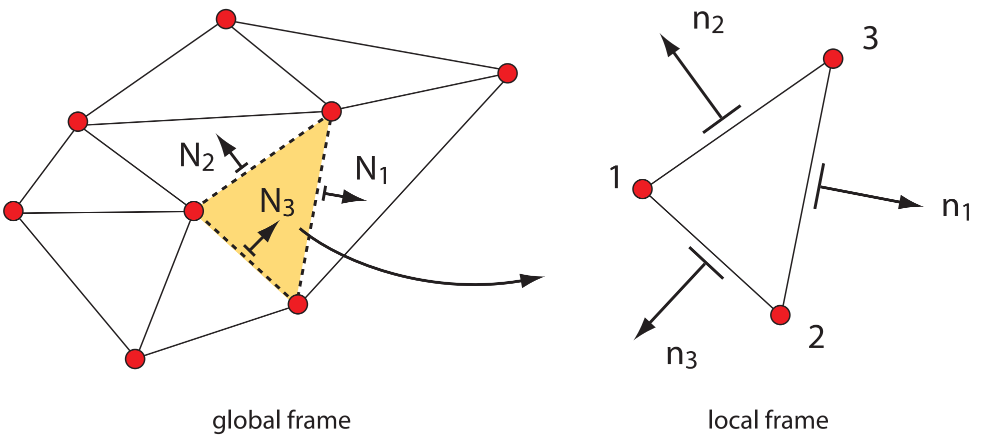

Figure 6.7: Orientation of the normal unit vectors in the global and local frame

The computation of $[K]$ involves the integration of:

$$\mu(\boldsymbol{d}(\boldsymbol{v}),\boldsymbol{d}(\boldsymbol{v}))_f=\frac{1}{2}\sum_{\text{fluid elements}}\left\{v_e^{(f)}\right\}^t\left[K_e^{(f)}\right]\left\{v_e^{(f)}\right\} \tag{6.92}$$

and the integration of:

$$\frac{\mu}{2}(\boldsymbol{K}_{\text{meso}}^{-1}.\boldsymbol{v}),\boldsymbol{v})_s=\frac{1}{2}\sum_{\text{solid elements}}\left\{v_e^{(s)}\right\}^t\left[K_e^{(s)}\right]\left\{v_e^{(s)}\right\} \tag{6.93}$$

Which leads to two elementary matrices $[K_e^{(f)}]$ and $[K_e^{(s)}]$ for the fluid or the solid elements. The integration of the third term in Φ,

$$(p,\operatorname{div}(\boldsymbol{v}))=\sum_{\text{fluid elements}}\left\{p_e^{(f)}\right\}^t\left[B_e^{(f)}\right]\left\{v_e^{(f)}\right\}+\sum_{\text{solid elements}}\left\{p_e^{(s)}\right\}^t\left[B_e^{(s)}\right]\left\{v_e^{(s)}\right\} \tag{6.94}$$

also involves two elementary matrices $[B_e^{(f)}]$ and $[B_e^{(s)}]$ depending on either the element is in the fluid or the solid region. The integration of the last term gives:

$$(\boldsymbol{G},\boldsymbol{v})=\sum_{\text{fluid elements}}\left\{b_e^{(f)}\right\}^t\left\{v_e^{(f)}\right\}+\sum_{\text{solid elements}}\left\{b_e^{(s)}\right\}^t\left\{v_e^{(s)}\right\} \tag{6.95}$$

The expressions of $[K_e^{(f)}]$, $[B_e^{(f)}]$ and $\left\{b_e^{(f)}\right\}$ have been already provided for the MINI-element. The expressions of $[K_e^{(s)}]$, $[B_e^{(s)}]$ and $\left\{b_e^{(s)}\right\}$ are given in appendix, for the Raviart-Thomas elements.

6.3.3 Interface and boundary conditions

6.3.3.1 Interface conditions

Consider two elements at the junction between the solid and fluid the fluid. These elements have three mutual nodes "i", "j" and "k" on the interface Γ. Let us denote by A_i, A_j, A_k the points with the coordinates (x_i, y_i), (x_j, y_j) and (x_k, y_k) defining the positions of the nodes "i", "j" and "k" respectively. The normal unit vector in the global frame is $\boldsymbol{N}$ and the tangential vector is denoted $\boldsymbol{T}$ and lies in the plane orthogonal to $\boldsymbol{N}$. For the MINI-element in the fluid phase, the velocity on Γ is denoted by $\boldsymbol{v}^{(f)}$ and the velocities at the nodes are denoted $\boldsymbol{v}^{i(f)}$, $\boldsymbol{v}^{j(f)}$ and $\boldsymbol{v}^{k(f)}$. For the Raviart-Thomas element in the solid phase, the flux on the face (A_i, A_j, A_k) is denoted F_{ijk}.

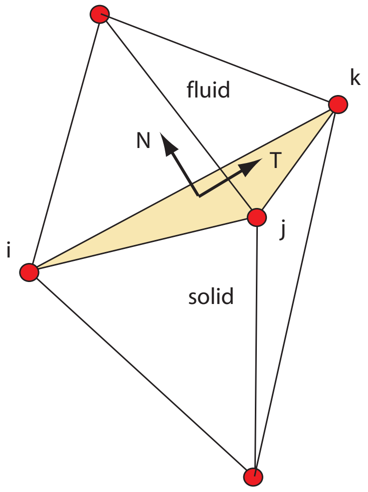

Figure 6.8: Interface between the fluid and the solid region.

- Condition for the tangential velocity.

A weak form of the interface condition (6.12) is applied to the edge:

$$\int_{\text{edge i,j}} \boldsymbol{v}^{(f)}.\boldsymbol{T}dx = \frac{1}{2}(\boldsymbol{v}^{i(f)} + \boldsymbol{v}^{j(f)}).\boldsymbol{T} = 0 \tag{6.96}$$

For a 2D problem the interface is defined by and edge and two nodes i, j. In this case $\boldsymbol{T} = \overrightarrow{A_iA_j}$ is considered in the above equation. For the 3D problem, the above conditions is written by considering $\boldsymbol{T} = \overrightarrow{A_iA_j}$ and $\boldsymbol{T} = \overrightarrow{A_iA_k}$ successively.

- Condition for the normal velocity.

A weak form of the interface condition (6.9) is also considered:

$$\int_{\text{edge i,j}} [\boldsymbol{v}^{(f)} - \boldsymbol{v}^{(s)}].\boldsymbol{N}dx = \frac{1}{2}(\boldsymbol{v}^{i(f)} + \boldsymbol{v}^{j(f)}).\boldsymbol{N} - F_{ijk} = 0 \tag{6.97}$$

Also the conditions at interface are put into the form:

$$[C_\Gamma]\,\{v\} = 0 \tag{6.98}$$

6.3.3.2 Periodic conditions on the boundary of the cell

The periodic conditions remains unchanged from the previous chapter, and are written into the form:

$$[C_v]\left\{\ v\ \right\} = \left\{\ 0\ \right\},\quad [C_p]\left\{\ p\ \right\} = \left\{\ 0\ \right\} \tag{6.99}$$

6.3.4 Integration of the interface and boundary conditions

The conditions (6.96), (6.98) and (6.99) are introduced in the linear system by means of Lagrange multipliers:

$$\begin{bmatrix} K + h\,[C_v]^t\,[C_v] + h\,[C_\Gamma]^t\,[C_\Gamma] & -B^t \\ -B & h\,[C_p]^t\,[C_p] \end{bmatrix} \begin{Bmatrix} v \\ p \end{Bmatrix} = \begin{Bmatrix} b \\ 0 \end{Bmatrix} \tag{6.100}$$

This linear system is solved by means of the conjugate gradient iterative scheme.

6.4 Results and discussions

6.4.1 Benchmark problems: the layered bi-porous material

6.4.1.1 Description of the problem

In this section we check the accuracy of the FEM solution with analytical solutions for a layered bi-porous material. The latter is constituted of a fluid layer with the thickness a and a porous material with the thickness b. The two layers periodically alternate in the Ox_2 direction. The nano-porous material is assumed to be isotropic, $\boldsymbol{K}_{\text{meso}} = k_{\text{meso}}\boldsymbol{I}$. The unit cell used for the FEM calculations is represented in Figure 6.9. The unit cell is a square with the dimension L along each direction. The porous layer is centered at $x_2 = 0$. The porosity is denoted $\varphi = a/L$.

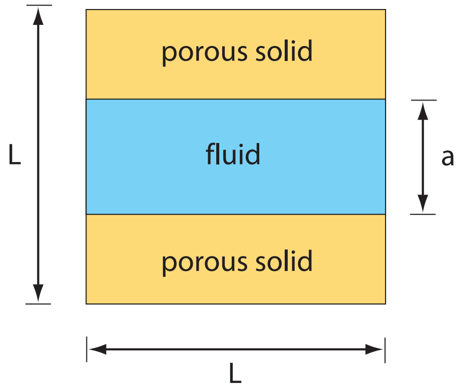

Figure 6.9: 2D unit cell of the layered bi-porous material.

Due to the orientation of the layers, the macroscopic permeability is not anisotropic but transversely isotropic and involves two distinct components $K_{\text{macro},11} = K_{\text{macro},33}$ and

$K_{\text{macro},22}$. The permeability $K_{\text{macro},11}$ is computed by applying the pressure gradient along the direction Ox_1 (longitudinal flow), the permeability $K_{\text{macro},22}$ is computed by applying the pressure gradient along the direction Ox_2 (transverse flow). The problem are studied in 2D or 3D to check the capacity of our 2D/3D finite element codes.
The off-diagonal components are null of the macroscopic permeability are null. By applying the pressure gradient along the direction Ox_1, we determine the component $K_{\text{macro},11}$ which reads:

$$K_{\text{macro},11} = K_S + K_D \tag{6.101}$$

where K_S represents the Stokes contribution (obtained by averaging the velocity over the volume Ω_f) and K_D is the Darcy contribution (obtained by averaging the velocity over the volume Ω_s). The analytic expressions of K_S and K_D are:

$$K_S = \frac{\varphi^3}{12} L^2, \quad K_D = (1-\varphi) k_{\text{meso}} \tag{6.102}$$

It must be noted that K_S is the permeability obtained from the Poiseuille solution and corresponding to the flow between two impervious layers. K_D is obtained by multiplying the nanoporous permeability k_{meso} by a factor $1-\varphi$. By applying the pressure gradient along the direction Ox_2, the solution is:

$$K_{\text{macro},22} = \frac{L-a}{L} k_{\text{meso}} \tag{6.103}$$

It must be noted that in (6.102) when the mesoscopic permeability is null $k_{\text{meso}} = 0$ we have $K_{\text{macro},11} = K_S$ and in (6.103) we have $K_{\text{macro},22} = 0$. Following the notation already introduced in section 6.2.3 we put $k_{\text{meso}} = h^2 k^*_{\text{meso}}$ where k^*_{meso} is a dimensionless permeability computed on a unit cell at nanoscopic scale having the dimension 1 in each direction and h in the characteristic length of the nanoscopic porous microstructure. It is convenient to introduce the dimensionless permeability:

$$\kappa = \frac{k_{\text{meso}}}{L^2} = \epsilon^2 k^*_{\text{meso}} \tag{6.104}$$

where it is recalled that $\epsilon = h/L$ is the scale factor between the nanoscopic and the mesoscopic scale. Due to the scale separation, the parameter ϵ is small and the contribution of K_S is small behind K_D as long as the thickness of the layer $b = L - a$ is not too small. The contributions of each dimensionless permeabilities $K^*_S = K_S/L^2$ and $K^*_D = K_D/L^2$ as well as the total dimensionless permeability $K^*_S + K^*_D$ are represented in Figure 6.10 as function of the porosity φ. When φ is large enough,the contribution of K_D is negligible while for the small values of the ratio φ, the contribution of K_S is negligible.

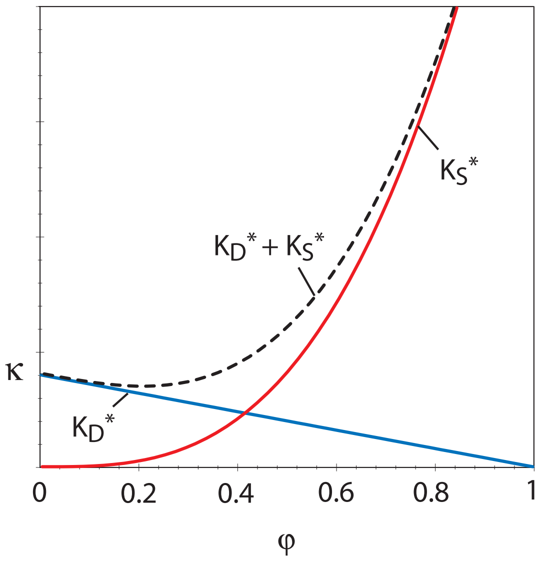

Figure 6.10: Variations of the permeabilities $K_S^* = K_S/L^2$, K_D^* and $K_S^* + K_D^*$ with φ.

The condition $K_S = K_D$ provides an equation of the third degree giving porosity φ for which the Stokes and the Darcy contribution is the same. In Figure 6.11 is given the value of the porosity φ as function of κ corresponding to $K_S = K_D$. The values of (κ, φ) which are above the curve corresponds to the situation for which $K_D > K_S$, below this curve, we have $K_S > K_D$.

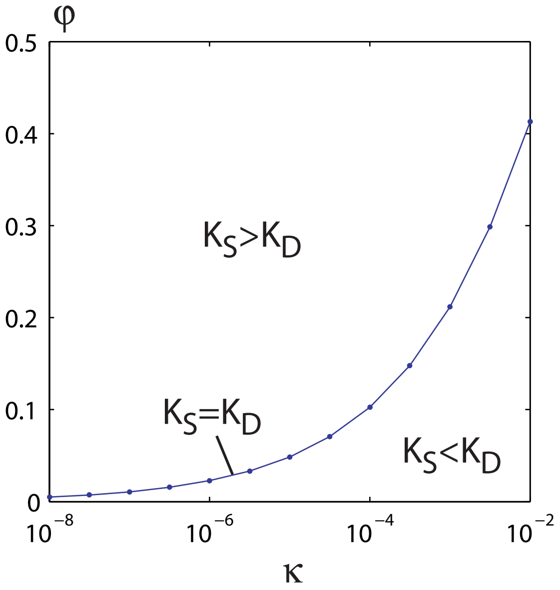

Figure 6.11: Value of the ratio a/L corresponding to $K_S = K_D$ as function of k_{meso}/L^2.

6.4.1.2 2D validations: case of longitudinal flow

Comparisons of the analytical solutions with the FEM ones are now provided. The two kind of elements are considered: (i) the Arbogast and Brunson rectangular elements, (ii) the MINI/RT (for Raviart-Thomas) elements. The Arbogast and Brunson rectangular elements are expected to provide the better solution since the discretization with the regular array is exact for the layered bi-porous material and these elements have a higher number of DOFs than the triangular elements. The results for the MINI/RT triangular elements are provided in Table 6.2.

Table 6.2: Permeabilities K_S^* and K_D^* for the longitudinal flow in the a layered bi-porous material. Comparison between the FEM solution which uses the MINI/RT elements and the exact solution.

κ	K_S^* (MINI/RT)	K_D^* (MINI/RT)	K_S^* (Exact)	K_D^* (Exact)
1E-01	1.041641E-2	5.004128E-02	1.041667E-02	5.000000E-02
1E-02	1.041641E-2	5.004128E-03		5.000000E-03
1E-03	1.041641E-2	5.004127E-04		5.000000E-04
1E-04	1.041641E-2	5.004127E-05		5.000000E-05
1E-05	1.041641E-2	5.004126E-06		5.000000E-06
1E-06	1.041641E-2	5.004125E-07		5.000000E-07
1E-07	1.041641E-2	5.004124E-08		5.000000E-08
1E-08	1.041641E-2	5.004123E-09		5.000000E-09
1E-09	1.041641E-2	5.004122E-10		5.000000E-10
1E-10	1.041641E-2	5.004122E-11		5.000000E-11
1E-11	1.041641E-2	5.004121E-12		5.000000E-12
1E-12	1.041641E-2	5.004111E-13		5.000000E-13

The second and third columns give the permeabilities K_S^* and K_D^* obtained by the FEM for various values of κ while the two last columns give the exact values of K_S^* and K_D^*. The calculations are performed with 700.000 DOFs. For the numerical results we choose $\varphi = 0.5$ and various values of κ in the range $[10^{-12}, 10^{-2}]$ are used. The permeability K_S^* is independent of κ that's why in the fourth column only one value is given for the exact solution of K_S^*. The comparison with the exact solution shows a very good agreement of the FE solution. The comparison for K_S^* shows an error of 0.0024%, while for K_D^*, the relative error is 0.082%.

As a comparison purpose, the 2D problem is now solved with the regular element of Arbogast and Brunson. The unit cell is meshed with a regular grid containing 40×40 to 640×640 rectangular elements. The results are provided in Table 6.3.

Table 6.3: Permeabilities K_S^* and K_D^* for the longitudinal flow in a layered bi-porous material. Comparison between the FEM solution which uses the rectangular elements of Arbogast and Brunson and the exact solution. $\kappa = 1$ in this case.

Nb of elements	$\boldsymbol{K}_S^*$	$\boldsymbol{K}_D^*$	$\boldsymbol{K}_S^*$ (Exact)	$\boldsymbol{K}_D^*$ (Exact)
40×40	1.041667E-02	5.000001E-01	1.041667E-02	5.000000E-01
80×80			1.041667E-02	5.000000E-01
160×160			1.041667E-02	5.000000E-01
320×320			1.041667E-02	5.000000E-01
640×640			1.041667E-02	5.000000E-01

The first column give the total number of element used for the computation of the FEM solution. The two next columns give the exact values of permeabilities K_S^* and K_D^*. The last two columns give the FEM solutions. As expected the numerical solution with the rectangular elements are in a very good agreement with the exact solution. Particularly, the convergence of the FEM solution is already attained with 40 rectangular elements.

6.4.1.3 2D validations: case of transversal flow

We now compare the FEM element solutions in the case of a transverse flow in the bi-porous layered material. First, Table 6.4 provides the values of the permeabilities K_S^* and K_D^* computed with various values of κ in the range $[10^{-12}, 10^{-2}]$ and for a porosity $\varphi = 0.5$.

It is must be noted that for $\kappa > 10^{-8}$, the relative errors can be found acceptable (i.e. error $< 0.63\%$) compared to the analytical problem. However by decreasing the value of κ the relative error increases. This must be attributed to an inadequate choice of the penalty coefficient h. Indeed, the value $h = 10^6$ has been chosen for this penalty coefficient and appears to be acceptable when the macroscopic permeability of the biporous material is small behind 10^{-6}. In other cases, the value of h must be adjusted to increase the accuracy of the FEM solution. In Table 6.5, we provide corrected values of the FEM solution by choosing $h = 10^{12}$

Table 6.4: Permeabilities K_S^* and K_D^* for the transversal flow in the a layered bi-porous material. Comparison between the FEM solution which uses the MINI/RT elements and the exact solution.

κ	K_S^* (MINI/RT)	K_D^* (MINI/RT)	K_S^* (Exact)	K_D^* (Exact)
1E-01	1.000000E-01	1.000826E-01	1.000000E-01	1.000000E-01
1E-02	1.000000E-02	1.000825E-02	1.000000E-02	1.000000E-02
1E-03	1.000000E-03	1.000826E-03	1.000000E-03	1.000000E-03
1E-04	1.000001E-04	1.000826E-04	1.000000E-04	1.000000E-04
1E-05	1.000006E-05	1.000826E-05	1.000000E-05	1.000000E-05
1E-06	1.000064E-06	1.000826E-06	1.000000E-06	1.000000E-06
1E-07	1.000645E-07	1.000827E-07	1.000000E-07	1.000000E-07
1E-08	1.006420E-08	1.000843E-08	1.000000E-08	1.000000E-08
1E-09	1.061830E-09	1.000988E-09	1.000000E-09	1.000000E-09
1E-10	1.501609E-10	1.001685E-10	1.000000E-10	1.000000E-10
1E-11	4.684015E-11	1.002450E-11	1.000000E-11	1.000000E-11
1E-12	3.367775E-11	1.002678E-12	1.000000E-12	1.000000E-12

Table 6.5: Permeabilities K_S^* and K_D^* for the transversal flow in the a layered bi-porous material. Comparison between the FEM solution which uses the MINI/RT elements and the exact solution. Correction with an adjusted penalty coefficient h.

κ	K_S^* (MINI/RT)	K_D^* (MINI/RT)	K_S^* (Exact)	K_D^* (Exact)
1E-09	1.000000E-09	1.000088E-09	1.000000E-09	1.000000E-09
1E-10	1.000000E-10	1.000085E-10	1.000000E-10	1.000000E-10
1E-11	1.000000E-11	1.000090E-11	1.000000E-11	1.000000E-11
1E-12	1.000000E-12	1.000092E-12	1.000000E-12	1.000000E-12

6.4.1.4 Validation of the 3D FEM code

The 3D FEM element code which uses the MINI/RT tetrahedral elements is now considered to compute the solution of the layered bi-porous material. The value $\varphi = 0.5$ is still considered with $\kappa = 1$. The mesh contained 750 000 DOFs. The results are provided in Table 6.6. For the longitudinal permeabilities ($K_{\text{macro},11}$ and $K_{\text{macro},33}$), the relative error for the Stokes and Darcy contributions are 0.5% and 0.08% respectively. For the transverse permeability $K_{\text{macro},22}$, the relative error for the Stokes and Darcy contributions are 0.8% and 0% respectively. The results demonstrated that to increase the accuracy of the solutions would need a mesh refinement in the Stokes region but not for the Darcy one.

Table 6.6: Permeabilities K_S^* and K_D^* for the longitudinal flow in the a layered bi-porous material. Comparison between the 3D-FEM solution which uses the MINI/RT elements and the exact solution.

	K_S^* (MINI/RT)	K_D^* (MINI/RT)	K_S^* (Exact)	K_D^* (Exact)
$K_{\text{macro},11}$	1.036281E-02	4.995859E+0	1.041667E-02	5.000000E-01
$K_{\text{macro},33}$	1.036232E-02	4.992429E+0	1.041667E-02	5.000000E-01
$K_{\text{macro},22}$	1.008054E+00	1.000000E+0	1.000000E+00	1.000000E+00

6.4.2 2D examples with rectangular/circular domains

The interface between macropores and nanopores may take different morphologies: spherical interface (in case of using PMMA beads as macroporogens), cubic form interface (case of using NaCl particles as macroporogens). The surface geometry of the fluid-solid interface would be an important factor for phases fluid exchange. Mention must be made that Darcy-Stokes problems considered in the Literature concerns problems with straight interfaces. Obviously, the interface in doubly porous materials are not straight but has cubic or spherical geometry. In this section, we investigate the effect of the interface morphology by various 2D problems : (i) the flow through porous solids containing squared or circular pores, (ii) the flow around porous circular or squared solids.

6.4.2.1 Flow in porous solids with rectangular/circular pores

- **Case of squared cross section**

We first consider the case of a flow through a regular array of aligned porous cylinders with squared cross section. The case of the flow around a porous cylinder with a circular cross section is studied in the second part of this section.

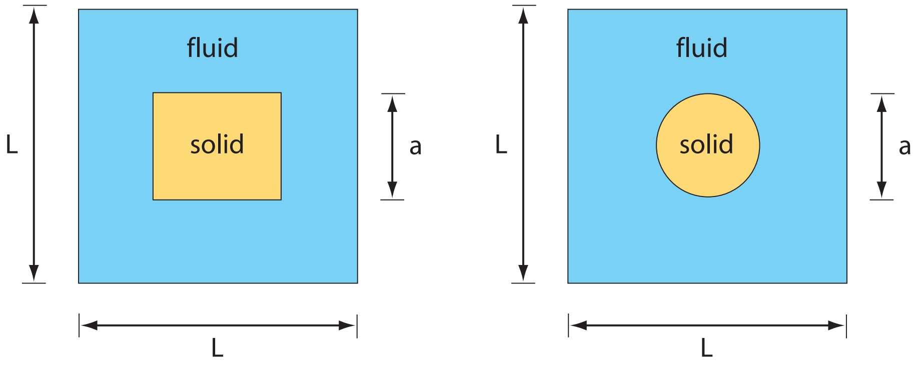

Figure 6.12: Definition of the unit cells for the flow through an a regular array of cylinder with squared and circular cross sections.

The different meshes used are illustrated in Figure 6.13. In the case A, the unit cell is meshed with a regular array and the Arbogast and Brunson elements are used. In the case B, an adaptive mesh with the MINI/RT triangular elements are considered. In the case C, the MINI/RT triangular elements are still considered but the triangles are regularly arranged.

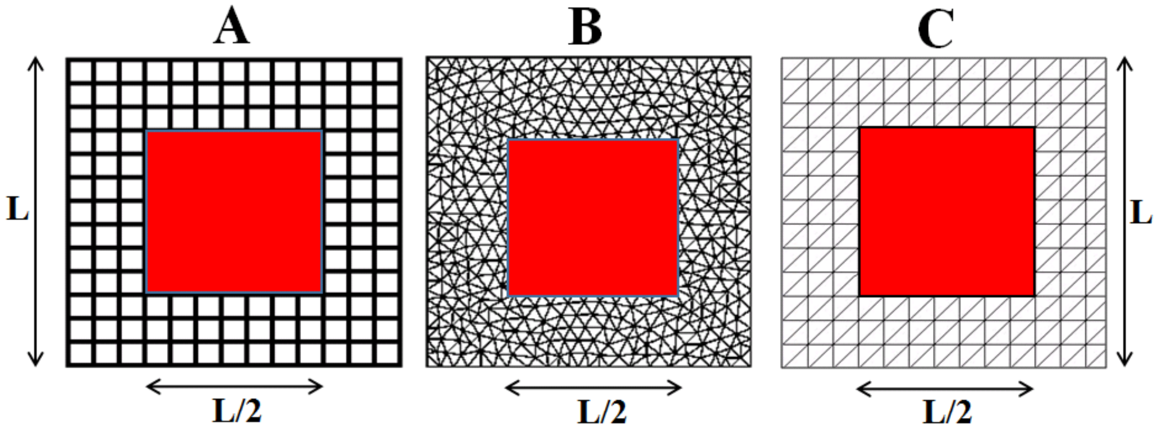

Figure 6.13: 2-D meshes for the flow around a squared inclusion porous solid.

The transverse macroscopic permeability is computed by considering a pressure gradient applied along the Ox direction. The permeability of the squared inclusion is assumed to be isotropic and, following the notation already introduce in the last section, we put $\kappa = k_{\text{meso}}/L^2 = \epsilon^2 k^*_{\text{meso}}$. For the numerical results provided in Table 6.7, 6.8, 6.9 we put $\kappa = 1$. Also, we still denote by K^*_S and K^*_D the Stokes and Darcy contributions to the dimensionless macroscopic permeability.

In Table 6.7, are provided the values of K^*_S and K^*_D computed with the Arbogast and Brunson elements (case A in Figure 6.13) with various grid refinements. As for information, the grid 640 × 640 introduces 1.6 millions DOFs. The relative errors between the permeabilities obtained with the grid 40 × 40 and the grid 640 × 640 is of 3.7-3.8%.

Table 6.7: Permeabilities K^*_S and K^*_D for the transverse flow around porous cylinders with squared cross section. 2D-FEM solutions which uses Arbogast and Brunson's squared elements for various values of the mesh refinement.

Nb elements	K^*_S	K^*_D
40 × 40	4.697146E-02	2.522973E-02
80 × 80	4.762186E-02	2.556591E-02
160 × 160	4.815683E-02	2.584157E-02
320 × 320	4.853731E-02	2.603775E-02
640 × 640	4.879162E-02	2.616898E-02

As for comparison, the values of permeabilities computed with the MINI/RT triangular elements are provided in Table 6.8 for various values of the mesh refinement and using the adaptive mesh or the regular one (see Figure 6.13, cases B and C).

Table 6.8: Permeabilities K_S^* and K_D^* for the transverse flow around porous cylinders with squared cross section. 2D-FEM solutions which uses MINI/RT triangular elements for various values of the mesh refinement.

Nb elements	K_S^*	K_D^*
Adaptive mesh		
∼4000	4.200545E-02	2.173171E-02
∼24000	4.487051E-02	2.338617E-02
∼95000	4.658964E-02	2.469858E-02
Regular mesh		
40 × 40	4.088680E-02	1.964314E-02
100 × 100	4.466737E-02	2.328320E-02
200 × 200	4.626120E-02	2.470475E-02

It is observed in Table 6.7 and 6.8, that the results obtained with the Arbogast and Brunson squared elements give a better estimation of the effective permeabilities than that provided by the MINI/RT triangular elements since the results in Table 6.7 has a better convergence with the grid refinement. This was expected since, as for the case of the layered bi-porous material, in this example the interface is defined by straight lines and the Arbogast and Brunson elements has a great number of degrees of freedom in the element. The relative error in the results obtained with the Arbogast and Brunson squared elements (with 640 × 640 elements) and the MINI/RT is 4.5% (for type B mesh) and 5.1% (for type C mesh). It is noted that the mesh with 640 × 640 squared elements introduces 1.6 millions DOFs while the mesh with triangles has only 300.000 DOFs.

- **Case of a circular cross section**

We now consider the flow through an array of porous cylinders with circular crossed section. A squared unit cell containing a circular porous inclusion is used for the calculations. The diameter a of the solid is equal to 0.5 (see Figure 6.12), the dimension of the unit cell being still given by 1 along each directions. The computation of the macroscopic transverse permeability is performed by choosing $\kappa = 1$ in the Darcy region. The numerical results are provided in Table 6.9.

Table 6.9: Permeabilities K_S^* and K_D^* for the transverse flow around porous cylinders with squared cross section. 2D-FEM solutions obtained with Arbogast and Brunson squared elements and with MINI/RT triangular elements.

Nb elements	K_S^*	K_D^*
Arbogast and Brunson squared elements		
40×40	2.531509E-02	3.356882E-03
80×80	2.305971E-02	1.988509E-03
160×160	2.175161E-02	1.127919E-03
320×320	2.096621E-02	6.650344E-04
640×640	2.050720E-02	3.877717E-04
MINI/RT elements		
$\sim$ 240.000	5.787047E-02	1.845088E-02

We first compute the Stokes and Darcy velocity fields (see Figure 6.14), then their contributions to the dimensionless macroscopic permeability with the Arbogast and Brunson squared elements and for various mesh refinement. Also, in the last line, we provide the numerical solutions obtained with MINI/RT elements on an adaptive mesh with $\sim$240.000 elements.

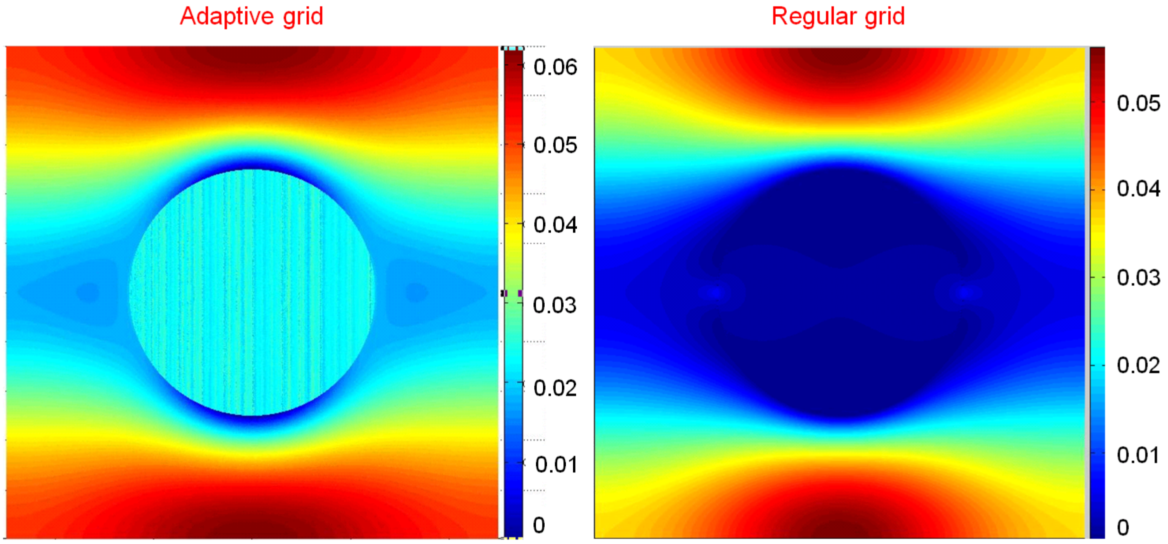

Figure 6.14: Velocity fields between the two cases corresponded to the circular inclusion in a unit cell for the coupling Stokes and Darcy problem.

Interestingly, we observe that the results obtained with the squared elements converge for K_S^* but seems to do not converge for the Darcy contribution K_S^*. Moreover the values obtained with the different grid refinement are very low compared to the values obtained the MINI/RT elements. The differences must be attributed to the approximation of the circular interface by a regular mesh. Indeed, if we consider the Arbogast and Brunson squared elements, the tangential velocity is null on each edge which are at the interface between the solid and the fluid region. Consequently, at each corner which are surrounded by the fluid pixels (black circles in Figure 6.15), the two components of the velocity are null. It follows that the fluid only pass through the nodes which are on three aligned nodes (red stars in Figure 6.15). Since the majority of the nodes are at a corner, the solid seems to be nearly impervious. This explain why the Darcy contribution tends to zero by increasing the mesh refinement. The use of the Arbogast and Brunson squared elements is not adapted to such geometry which must be handled with adaptive meshes.

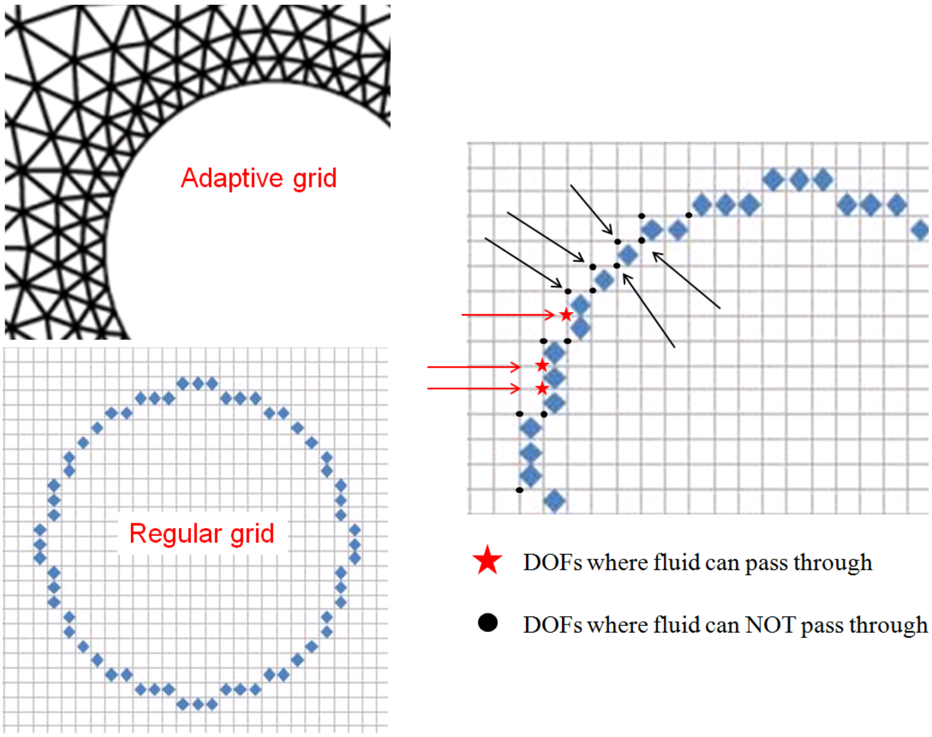

Figure 6.15: Discretization of the fluid region with an adaptive mesh or with a regular array (at the left). The figure at the left show the nodes which allows the fluid circulation.

We proposed to analyze the contribution K_S^* and K_D^* for the case with an adaptive mesh. The computations are performed with the MINI/RT triangular elements with 240.000 elements in the mesh. The variations of K_S^* and K_D^* with the radius of the cylinders are provided in Figure 6.16. It is observed that for the small values of the diameter a (see Figure 6.12), the contribution of Darcy region is negligible. By increasing radius, the Darcy contribution increases while K_S^* decreases and for a value of a/L close to 0.48 the Stokes contribution becomes lower than Darcy one.

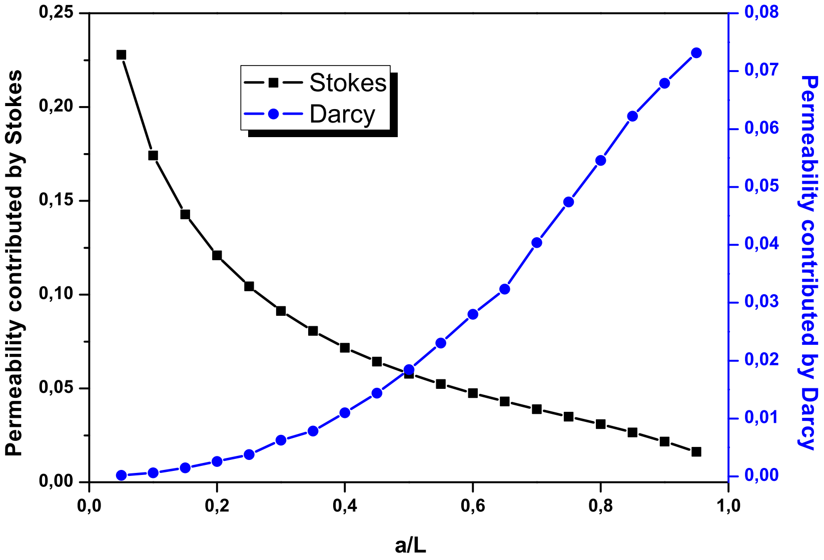

Figure 6.16: Case of interconnected macropores, contribution to the effective permeability of Stokes and Darcy domains. κ=1 in this case.

6.4.2.2 Flow in porous solid containing squared/circular macropores

We now consider the fluid flow in a nano-porous medium with non interconnected squared or circular macropores (see Figure 6.17). The unit cell is made up of a solid with the isotropic permeability k_{meso} and we still denote $\kappa = k_{\text{meso}}/L^2$. The unit cell contain a squared macropore having the dimension 0.5 (the size of the square unit cell being 1). For the applications provided in Table 6.10, 6.11 and 6.12 we consider the value $\kappa = 1$.

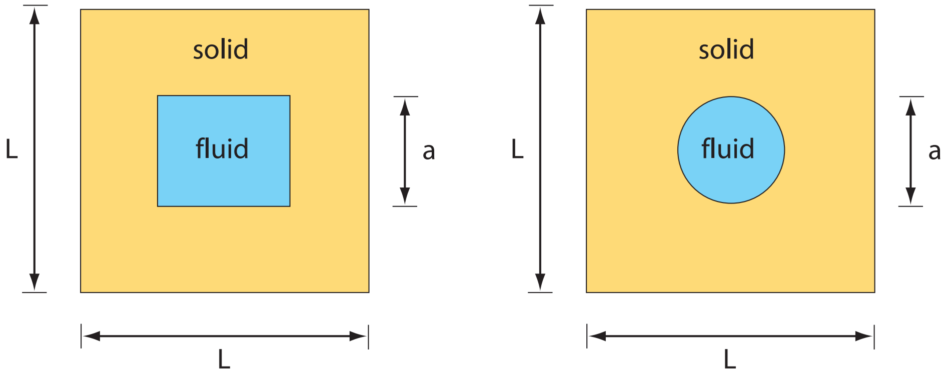

Figure 6.17: Definition of the unit cells for the flow through in a nano-porous solid containing squared or circular macropores.

In Table 6.10 are given the values of K_S^* and K_D^* computed with the Arbogast and Brunson squared elements and for various values of the mesh refinement. The relative error computed with the grid 40 × 40 and 640 × 640 is 0.2-0.3%. It observed that the Darcy contribution, K_D^*, is more significant in the case of non interconnected macropores. Within the macropores the velocity field is very low and the the contribution of K_S^* is negligible for the computation of the macroscopic permeability.

Table 6.10: Permeabilities K_S^* and K_D^* for the transverse flow in a nano-porous solid with a squared macropore. 2D-FEM solutions which uses Arbogast and Brunson's squared elements for various values of the mesh refinement.

Nb elements	K_S^*	K_D^*
40×40	8.929840E-03	5.822408E-01
80×80	8.916746E-03	5.833557E-01
160×160	8.911711E-03	5.838002E-01
320×320	8.909759E-03	5.839769E-01
640×640	8.908999E-03	5.840473E-01

Table 6.11: Permeabilities K_S^* and K_D^* for the flow in a nano-porous solid with a squared macropore. 2D-FEM solutions which use MINI/RT triangular elements for various values of the mesh refinement.

Nb elements	K_S^*	K_D^*
Adaptive mesh		
4000	8.929840E-03	5.822408E-01
∼24000	8.916746E-03	5.833557E-01
∼95000	8.911711E-03	5.838002E-01
Regular mesh		
40 × 40	8.929840E-03	5.822408E-01
100 × 100	8.916746E-03	5.833557E-01
200 × 200	8.911711E-03	5.838002E-01

As for comparison, the permeability is computed with the MINI/RT elements using a regular and adaptive grid (see Figure 6.13) and the results are given in Table 6.11.

As for the case of flow around a porous cylinder with a crossed section, we observe that the Arbogast and Brunson squared elements provide a better estimation of the permeability. The results for the case of a circular macropore are provided in Table 6.12. The calculation are performed with a macropores having a diameter $a = 0.5$. Again, it observed that the Arbogast and Brunson squared elements are not adapted since the convergence is not achieved for K_S^*

Table 6.12: Permeabilities K_S^* and K_D^* for the transverse flow in a nano-porous solid with a circular macropore. 2D-FEM solutions obtained with Arbogast and Brunson squared elements and with MINI/RT triangular elements.

Nb elements	K_S^*	K_D^*
Arbogast and Brunson squared elements		
40×40	1.512643E-03	6.599476E-01
80×80	1.019277E-03	6.651803E-01
160×160	6.273204E-04	6.694020E-01
320×320	3.903897E-04	6.704366E-01
640×640	2.364016E-04	6.709832E-01
1280×1280	1.372364E-04	6.713664E-01
MINI+RT triangular elements		
~ 240.000	1.004945E-02	6.781832E-01

Figure 6.18 shows the variations of the Darcy and Stokes contributions, K_D^* and K_S^*, with the radius of the macropore. The value $\kappa = 1$ has been considered. The computations are performed with the MINI/RT triangular elements. It is observed, in Figure 6.18, that for the small values of the pore radius, the Darcy contribution is prominent and the Stokes contribution could be neglected for the computation of the macroscopic permeability. However, by increasing the radius of the macropore, the Darcy contribution decreases and the Stokes one increases. When the ratio a/L attains a value close to 0.72, the Darcy contribution becomes smaller that the Stokes one.

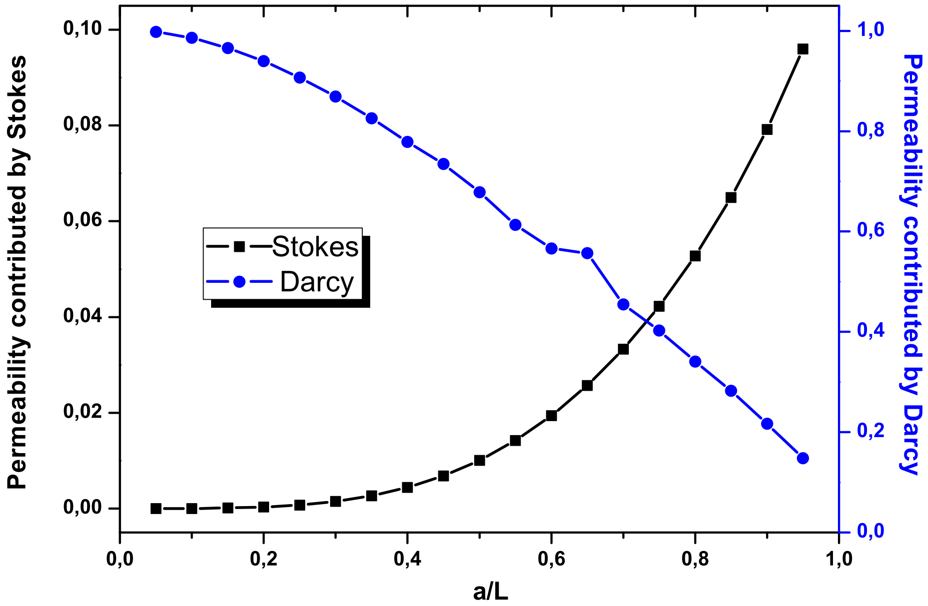

Figure 6.18: Case of non-interconnected macropores, contribution to the effective permeability of Stokes and Darcy domain.

6.4.3 3D problems

In this section, the results obtained on 3D microstructures are computed with the 3D-FEM code which uses the MINI/RT tetrahedral elements.

- Fluid flow around a porous sphere.

The flow in this case is through an array of porous spheres of radius R. The spheres are arranged along a cubic lattice, the corresponding unit cell is a cube which contains one spheres located at its center. The sphere is porous and its permeability is assumed to be isotropic and, as in the last examples, we put $\kappa = \epsilon^2 k^*_{\text{meso}} = 1$ for simplicity. Due to symmetries, the macroscopic permeability is also isotropic and we denote K^*_S and K^*_D the Stokes and Darcy contribution to the dimensionless isotropic macroscopic permeability. In Table 6.13, we provide the values of K^*_S and K^*_D for various values of the radius R. In the last column is given the total number of elements. As for the flow through the array of cylinders, it is observed that the Darcy contribution is negligible for the small values of the radius. When 2R/L>0.6, the contribution of K^*_D become more significative and is equivalent to K^*_S for almost touching spheres.

Table 6.13: Permeabilities K_S^* and K_D^* for the flow through the array of porous spheres.

2R/L	K_S^*	K_D^*	Nb elements
0.1	9.939982E+00	1.694304E-04	70480
0.2	4.223626E-01	6.573289E-04	46744
0.3	2.333533E-01	1.459325E-03	34928
0.4	1.465485E-01	2.886602E-03	28384
0.5	9.209452E-02	4.552294E-03	19240
0.6	6.137987E-02	7.325114E-03	18336
0.7	4.162221E-02	1.135972E-02	15728
0.8	3.047495E-02	1.789287E-02	23424
0.9	2.242646E-02	2.533299E-02	45280

- Fluid flow in a nano-porous solid with non interconnected spherical macropores.

In this second example, the cell is constituted of a nano-porous solid with spherical non-interconnected macropores. The values $\kappa = 1$, $\kappa = 1E-6$ and $\kappa = 1E-12$ are considered for the applications. The macroscopic permeability is still isotropic and we compute the Darcy and Stokes contributions K_D^*, K_S^*. In Table 6.14, we present the results corresponding to $\kappa = 1$ while, in Table 6.15, are given the results obtained with $\kappa = 1E-6$ and $\kappa = 1E-12$. When $\kappa = 1$, it is observed that K_D^* decreases by increasing the value of R. We note also that the Stokes contribution is negligible in each case which suggests that the velocity is quasi null in the macropore. Regarding the results obtained with $\kappa = 1E-6$ and $\kappa = 1E-12$ we observe that the Stokes contribution is negligible for the small values of R. However, by increasing the value of R, the Stokes contribution become larger that the Darcy one. It follows that in this situations both contributions must be considered to compute accurately the value of the macroscopic permeability.

Table 6.14: Permeabilities K_S^* and K_D^* for the flow through a nano-porous medium containing spherical macropores. Case $\kappa = 1$

$2R/L$	K_S^*	K_D^*
	$\kappa = 1$	
0.1	3.059035E-7	9.969337E-1
0.2	9.612623E-6	9.914090E-1
0.3	7.225231E-5	9.775301E-1
0.4	3.063682E-4	9.486712E-1
0.5	9.113460E-4	9.042677E-1
0.6	2.239477E-3	8.398064E-1
0.7	4.685748E-3	7.550611E-1
0.8	9.088341E-3	6.470595E-1
0.9	1.570522E-2	5.570522E-1

Table 6.15: Permeabilities K_S^* and K_D^* for the flow through a nano-porous medium containing spherical macropores. Cases $\kappa = 1E-6$ and $\kappa = 1E-12$

2R/L	K_S^*	K_D^*	K_S^*	K_D^*
	$\kappa = 1E-6$		$\kappa = 1E-12$	
0.1	1.514104E-9	9.976996E-7	1.522022E-15	9.977199E-13
0.3	4.147599E-8	9.983293E-7	4.148656E-14	9.983516E-13
0.5	2.015498E-7	9.973359E-7	2.017093E-13	9.973817E-13
0.7	6.364288E-7	9.967109E-7	6.373380E-13	9.967824E-13
0.9	2.023927E-6	9.922135E-7	2.026785E-12	9.923390E-13

- Macroscopic permeability of a doubly porous polymeric material.

In this last section, we proposed to evaluate the macroscopic permeability of a porous polymer presented in the first part of this work. To this end, we approximate the real microstructure by reconstructed images as illustrated in Figure 6.19. The porous microstructure of the polymer has been synthesized by a double porogen approach, where PMMA beads are used. The configuration of the PMMA beads after sintering is replaced by a FCC structure with spherical pores. At the nanoscopic level, we consider the nanoporous structure synthesized by a phase separation between i-PrOH and PHEMA, where the nanopores are assumed to be spherical with the diameter 400 nm. At the nanoscopic scale the pores are assumed to be randomly distributed within the RVE and we use, for the components of the dimensionless mesoscopic permeability $\boldsymbol{K}^*_{\text{meso}}$ the values computed in the previous chapter. The macropore diameter is 120 μm. The dimensions of the unit cell at the nanoscopic and mesoscopic scale are $h = 6.15\mu m$ and $L = 320\mu m$ respectively. This lead to the following value for the scale factor: $\epsilon \simeq 0.02$.

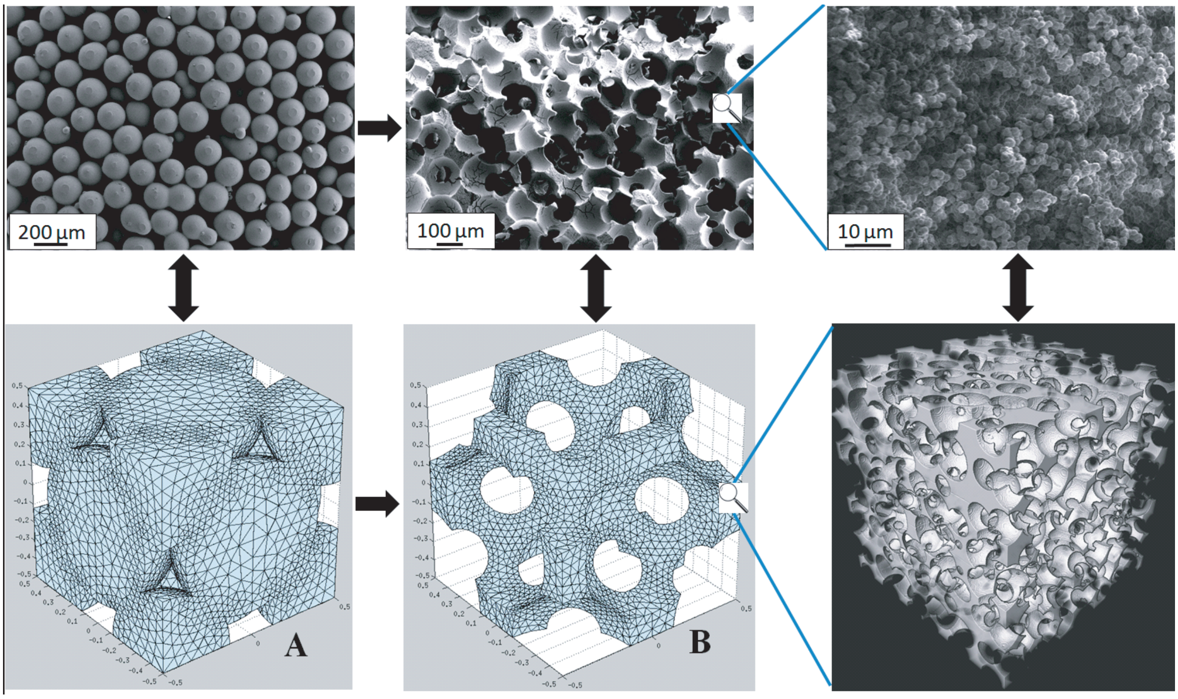

Figure 6.19: Reconstruction of the unit cells by idealized periodic microstructures.

The value of the components of the macroscopic permeability are given below.

$$\boldsymbol{K}^{11}_{macro} = 2.192348E - 03, \quad \boldsymbol{K}^{22}_{macro} = 2.192207E - 03, \quad \boldsymbol{K}^{33}_{macro} = 2.140064E - 03 \tag{6.105}$$

6.5 Conclusion

In the present chapter, we have developed 2D and 3D FEM codes for solving the Darcy-Stokes coupled equations and for computing the macroscopic permeability of doubly porous material. Various examples have been provided to check the accuracy and to show the limitation of the methods. First, the flow through a layered bi-porous solid has been considered as a Benchmark problem. The FEM solutions have been compared to the exact solution and show a very good agreement. 2D examples are then considered: the flow through an array of porous cylinders and the flow in a porous solid with macropores. Circular and squared geometries have been used for the solid cylinders/ macropores to evaluate the precision of the solutions. The use of regular mesh with squared elements appear to be not adapted for curved interface and adaptive mesh based on triangular elements must be used for this situation. The contribution of each phase, Darcy and Stokes one, on the macroscopic permeability has been also investigated. Finally, a 3D calculation on unit cells which hat mimic more realistically the doubly porous polymers has been proposed in the last section.

References

[1] J. Auriault and C. Boutin, “Deformable porous media with double porosity. quasi-statics. i: Coupling effects,” *Transport in Porous Media*, vol. 7, pp. 63–82, 1992.

[2] J. Auriault and C. Boutin, “Deformable porous media with double porosity. quasi-statics. ii: Memory effects,” *Transport in Porous Media*, vol. 10, pp. 153–169, 1993.

[3] G. Barenblatt, I. P. Zheltov, and I. Kochina, “Basic concepts in the theory of seepage of homogeneous liquids in fissured rocks [strata],” *Journal of Applied Mathematics and Mechanics*, vol. 24, pp. 1286–1303, 1960.

[4] G. Barenblatt, “On certain boundary-value problems for the equations of seepage of a liquid in fissured rocks,” *Journal of Applied Mathematics and Mechanics*, vol. 27, pp. 513–518, 1963.

[5] J. Warren, P. J. Root, *et al.*, “The behavior of naturally fractured reservoirs,” *Society of Petroleum Engineers Journal*, vol. 3, pp. 245–255, 1963.

[6] J.-L. Auriault and E. Sanchez-Palencia, “Etude du comportement macroscopique d’un milieu poreux saturé déformable,” *Journal de Mécanique*, vol. 16, pp. 575–603, 1977.

[7] E. Sanchez-Palencia, “Non-homogeneous media and vibration theory,” in *Non-homogeneous media and vibration theory*, vol. 127, 1980.

[8] T. Lévy, “Fluid flow through an array of fixed particles,” *International Journal of Engineering Science*, vol. 21, pp. 11–23, 1983.

[9] J. Auriault and C. Boutin, “Deformable porous media with double porosity iii: Acoustics,” *Transport in Porous Media*, vol. 14, pp. 143–162, 1994.

[10] C. Boutin, P. Royer, and J. Auriault, “Acoustic absorption of porous surfacing with dual porosity,” *International Journal of Solids and Structures*, vol. 35, pp. 4709–4737, 1998.

[11] X. Olny and C. Boutin, “Acoustic wave propagation in double porosity media,” *The Journal of the Acoustical Society of America*, vol. 114, pp. 73–89, 2003.

[12] M. Quintard and S. Whitaker, “Ecoulement monophasique en milieu poreux: Effet des hétérogénéités locales,” *Journal of Theoretical and Applied Mechanics*, pp. 691–726.

[13] K. Lewallen and H. Wang, “Consolidation of a double-porosity medium,” *International journal of solids and structures*, vol. 35, pp. 4845–4867, 1998.

[14] P. Royer and C. Boutin, “Time analysis of the three characteristic behaviours of dual-porosity media. i: fluid flow and solute transport,” *Transport in Porous Media*, vol. 95, pp. 603–626, 2012.

[15] P. Royer, J. Auriault, and C. Boutin, “Macroscopic modeling of double-porosity reservoirs,” *Journal of Petroleum Science and Engineering*, vol. 16, pp. 187–202, 1996.

[16] P. Royer, J.-L. Auriault, J. Lewandowska, and C. Serres, “Continuum modelling of contaminant transport in fractured porous media,” *Transport in Porous Media*, vol. 49, pp. 333–359, 2002.

[17] P. Cheng, “Heat transfer in geothermal systems,” *Advances in Heat Transfer*, vol. 14, pp. 1–105, 1978.

[18] J. Wang, C. Tsang, and R. Sterbentz, “The state of the art of numerical modeling of thermohydrologic flow in fractured rock masses,” *Environmental Geology*, vol. 4, pp. 133–199, 1982.

[19] P. Royer and J.-L. Auriault, “Transient quasi-static gas flow through a rigid porous medium with double porosity,” *Transport in Porous Media*, vol. 17, pp. 33–57, 1994.

[20] P. S. Huyakorn, B. H. Lester, and J. W. Mercer, “An efficient finite element technique for modeling transport in fractured porous media: 1. single species transport,” *Water Resources Research*, vol. 19, pp. 841–854, 1983.

[21] A. G. Salinger, R. Aris, and J. J. Derby, “Modeling the spontaneous ignition of coal stockpiles,” *AIChE journal*, vol. 40, pp. 991–1004, 1994.

[22] T. Masuoka, “Convective currents in a horizontal layer divided by a permeable wall,” *Bulletin of JSME*, vol. 17, pp. 225–232, 1974.

[23] D. D. Joseph and L. Tao, “Lubrication of a porous bearingâĂŤstokes’ solution,” *Journal of Applied Mechanics*, vol. 33, pp. 753–760, 1966.

[24] I. Jones, “Low reynolds number flow past a porous spherical shell,” vol. 73, pp. 231–238, 1973.

[25] T. S. Lundgren, “Slow flow through stationary random beds and suspensions of spheres,” *Journal of Fluid Mechanics*, vol. 51, pp. 273–299, 1972.

[26] G. Neale, N. Epstein, and W. Nader, “Creeping flow relative to permeable spheres,” *Chemical Engineering Science*, vol. 28, pp. 1865–1874, 1973.

[27] G. H. Neale and W. K. Nader, “Prediction of transport processes within porous media: creeping flow relative to a fixed swarm of spherical particles,” *AIChE Journal*, vol. 20, pp. 530–538, 1974.

[28] C. Beckermann, S. Ramadhyani, and R. Viskanta, “Natural convection flow and heat transfer between a fluid layer and a porous layer inside a rectangular enclosure,” *Journal of Heat Transfer*, vol. 109, pp. 363–370, 1987.

[29] D. Poulikakos and M. Kazmierczak, “Forced convection in a duct partially filled with a porous material,” *ASME J. Heat Transfer*, vol. 109, pp. 653–662, 1987.

[30] C. Beckermann, R. Viskanta, and S. Ramadhyani, “Natural convection in vertical enclosures containing simultaneously fluid and porous layers,” *Journal of Fluid Mechanics*, vol. 186, pp. 257–284, 1988.

[31] H. Brinkman, “A calculation of the viscous force exerted by a flowing fluid on a dense swarm of particles,” *Applied Scientific Research*, vol. 1, pp. 27–34, 1947.

[32] S. Kim and W. B. Russel, “Modelling of porous media by renormalization of the stokes equations,” *Journal of Fluid Mechanics*, vol. 154, pp. 269–286, 1985.

[33] G. S. Beavers and D. D. Joseph, “Boundary conditions at a naturally permeable wall,” *Journal of Fluid Mechanics*, vol. 30, pp. 197–207, 1967.

[34] P. G. Saffman, “Boundary condition at surface of a porous medium,” *Studies in Applied Mathematics*, vol. 50, p. 93, 1971.

[35] W. J. Layton, F. Schieweck, and I. Yotov, “Coupling fluid flow with porous media flow,” *SIAM Journal on Numerical Analysis*, vol. 40, pp. 2195–2218, 2003.

[36] X. Xie, J. Xu, and G. Xue, “Uniformly-stable finite element methods for darcy-stokes-brinkman models,” *Journal of Computational Mathematics-International Edition*, vol. 26, p. 437, 2008.

[37] M. Correa and A. Loula, “A unified mixed formulation naturally coupling stokes and darcy flows,” *Computer Methods in Applied Mechanics and Engineering*, vol. 198, pp. 2710–2722, 2009.

[38] T. Arbogast and D. S. Brunson, “A computational method for approximating a darcy-stokes system governing a vuggy porous medium,” *Computational Geosciences*, vol. 11, pp. 207–218, 2007.

[39] T. Arbogast and M. F. Wheeler, “A family of rectangular mixed elements with a continuous flux for second order elliptic problems,” *SIAM Journal on Numerical Analysis*, vol. 42, pp. 1914–1931, 2005.

[40] T. Arbogast and H. L. Lehr, “Homogenization of a darcy-stokes system modeling vuggy porous media,” *Computational Geosciences*, vol. 10, pp. 291–302, 2006.

[41] P.-A. Raviart and J.-M. Thomas, “A mixed finite element method for 2-nd order elliptic problems,” in *Mathematical aspects of finite element methods*, pp. 292–315, Springer, 1977.

General conclusion and perspectives

Doubly porous polymeric materials constitute an interesting class of materials with controlled pore size and connectivity. This Ph.D. thesis has demonstrated a synergy between chemical engineering and mechanical modeling.

In the first part, wa have designed and synthesized miscellaneous doubly porous polymeric materials based on poly(2-hydroxyethyl methacrylate-*co*-ethylene glycol dimethacrylate) (poly(HEMA-*co*-EGDMA)) by two versatile major routes. A critical overview of the different parameters affecting the porous features of doubly porous polymers designed *via* a double porogen templating approach was presented. A thorough investigation was accomplished so as to highlight the main advantages of the proposed double porogen approach which relied on the distinct and independent control of both porosity levels, *i.e.* nano- and macro-porosity. The nanoporosity level was produced *via* a phase separation phenomenon that occurred during the polymerization of the comonomers in the presence of various porogenic solvents. To generate the macroporosity, three straightforward and versatile strategies were implemented through the use of sodium chloride (NaCl) macro-sized particles or PMMA beads. The first one implied the use of non-sintered NaCl particles that allowed for the creation of non-interconnected macropores. The other two strategies involved the sintering of NaCl particles or PMMA beads prior to the generation of the poly(HEMA-*co*-EGDMA) network. In the former case, NaCl particles were fused through two different methods, either through sintering at 730°C or by Spark Plasma Sintering. On the other hand, PMMA beads were fused at 140°C for 4 h. Upon porogen removal, doubly porous PHEMA-based materials were obtained with macropores having particle imprints in the 100 μm order of magnitude, while the second porosity level laid within the 10 nm to 10 μm order of magnitude, as evidenced by mercury intrusion porosimetry and scanning electron microscopy, depending on the solvent structure, its volume proportion and the cross-linker concentration in the polymerization feed.

Furthermore, we have reported a straightforward and unprecedented approach for fabricating doubly porous PHEMA-based materials *via* Thermally Induced Phase Separation (TIPS). Such biporous materials could successfully be obtained through the use of a co-solvent mixture of water/dioxane to solubilize pre-synthesized linear PHEMA, and subsequent sublimation of the co-solvents. Through this novel approach, it is thus possible to achieve highly regular macroporosity features, in conjunction with a tunable nanoporosity. The nanoporous structure could have different morphologies, *i.e.* nanopores within the macropore walls or a nanofiber-like structure. SEM and MIP characterizations confirmed the existence of a bimodal porosity within the porous structures. The possibility to functionalize them has also been investigated *via* chemical cross-linking reactions so that the resulting materials might possess a higher mechanical stability.

In the second part, a modeling and simulation investigation of doubly porous materials has been developed. Firstly, we have employed the FFT-based method and the FEM for computing the permeability of periodic mono-porous media. Different configurations have been tested to show the accuracy of the metods and their capacity to handle 3D porous microstructures. First, benchmark problems, consisting of regular arrays of rigid cylinders or spheres have been considered. The results have been compared to those coming from the literature or by FEM, and show a good accuracy of the FFT-based solutions. Advanced numerical results have been then considered. More realistic porous microstructures are constructed with an assemblies of overlapping spherical voids. The case of spherical pores regularly distributed along a body-centered cubic (BCC) or face-centered cubic (FCC) structures are first considered. More complex microstructure are then studied by considering porous media having different pore size which are regularly or randomly distributed. In all cases, the results showed a good convergence of the FFT algorithm with the grid refinement.

Secondly, we have employed the FEM for solving the coupled Darcy-Stokes equations and to compute the macroscopic permeability of doubly porous materials. The method is based on a mixed variational formulation of the problem and its discretization using a unified or decoupled approach. In the unified approach, the squared elements of Arbogast are used for both the Darcy and Stokes regions. The decoupled approach uses the MINI elements in Stokes domain and the Raviart-Thomas elements in the Darcy one. Various 2D and 3D examples have been considered. First, the problem of fluid flow in layered doubly porous materials has been solved and compared to exact solutions in order to validate the FEM codes. Various 2D and 3D examples are then considered to show the contribution of each phase on the macroscopic permeability. In the case of flow around porous cylinders or spheres, it has been shown that the Darcy contribution is generally negligible excepted in the case of almost touching cylinders or spheres. For the problem of flow in nanoporous solids containing non-interconnected macropores, it has been shown that, the Darcy and the Stokes contributions must be taken into account for the calculation of the macroscopic permeability. A 3D example which can mimic realistically the doubly porous polymer has been finally considered.

As the scale factor between the two porosity levels considered is important, there is a crucial need for tailoring the structure for fluid flow optimization or other applications. By adding a third porosity level (*via* salt templating for instance) intermediate between the lower and upper porosity levels, hierarchical porous materials may be designed.

Doubly porous polymeric materials herein developed have demonstrated some undeniable advantages in controlling pore size, morphology, and connectivity of the as-obtained frameworks. Further applications as biomaterials should ne envisioned: cell seeding tests in such scaffolds would concrete the main advantage of such biporous materials over their monoporous counterparts.

The generation of PHEMA-based materials *via* the TIPS technique could also be extended to the use of a non-solvent in the system of polymer/co-solvents. This could induce a liquid-liquid phase separation and pore interconnectivity could thus be finely controlled *via* the use of a third solvent. The coupling of particle leaching and TIPS can also be applied to this system. Moreover, various surface modifications could be envisioned for the biporous materials engineered by TIPS.

Last but not least, this work paves the way to future developments of modeling and simulation in multi-porous media. First of all, the use of FFT-based method has demonstrated real advantage over FEM to handle the problems of very high dimensions. The simulation of flow using some 3D digital images obtained from X-ray microtomography probably constitutes an important perspective. However, no investigation of the influence of the pores distribution and the size of the unit cell has been reported so far. The identification and reconstruction of a unit cell which fully represents the microstructure should be thoroughly investigated. Along with the morphology of the nano-structures in the unit cell, the experimental measurements of fluid flow through the doubly porous materials would also be important in order to provide a complete comparison between modeling and simulations, and experimental results. Moreover, the development of the FFT-based algorithm to handle the coupled Darcy-Stokes problem would be interesting for reducing the computation time and memory occupancy. A possible approach would be to consider the Brinkman equation to describe the fluid flow at the intermediate scale. Finally, the numerical tools developed in this thesis could be useful for various applications, such as transport problems of surface water with rocks and sands or the quantification of damage on the permeability of fractured porous media.

Annex

[K$_e$] for MINI elements in 2D:

$$\begin{bmatrix}
2A1B1+A2B2+B1^2+A1^2+\frac{1}{2}A2^2+\frac{1}{2}B2^2, & \frac{1}{2}A2B1+\frac{1}{2}A2A1+\frac{1}{2}B2A1+\frac{1}{2}B2B1, & -A1^2-A1B1-\frac{1}{2}A2^2-\frac{1}{2}A2B2, & -\frac{1}{2}A2A1-\frac{1}{2}B2A1, & -B1^2-A1B1-\frac{1}{2}A2B2-\frac{1}{2}B2^2, & -\frac{1}{2}A2B1-\frac{1}{2}B2B1, & 0, & 0 \\
\frac{1}{2}A2B1+\frac{1}{2}A2A1+\frac{1}{2}B2A1+\frac{1}{2}B2B1, & 2A2B2+\frac{1}{2}A1^2+\frac{1}{2}B1^2+B2^2+A2^2+A1B1, & -\frac{1}{2}A2A1-\frac{1}{2}A2B1, & -\frac{1}{2}A1^2-\frac{1}{2}A1B1-A2B2-A2^2, & -\frac{1}{2}B2B1-\frac{1}{2}B2A1, & -\frac{1}{2}A1B1-\frac{1}{2}B1^2-B2^2-A2B2, & 0, & 0 \\
-A1^2-A1B1-\frac{1}{2}A2^2-\frac{1}{2}A2B2, & -\frac{1}{2}A2A1-\frac{1}{2}A2B1, & A1^2+\frac{1}{2}A2^2, & \frac{1}{2}A2A1, & A1B1+\frac{1}{2}A2B2, & \frac{1}{2}A2B1, & 0, & 0 \\
-\frac{1}{2}A2A1-\frac{1}{2}B2A1, & -\frac{1}{2}A1^2-\frac{1}{2}A1B1-A2B2-A2^2, & \frac{1}{2}A2A1, & \frac{1}{2}A1^2+A2^2, & \frac{1}{2}B2A1, & \frac{1}{2}A1B1+A2B2, & 0, & 0 \\
-B1^2-A1B1-\frac{1}{2}A2B2-\frac{1}{2}B2^2, & -\frac{1}{2}B2B1-\frac{1}{2}B2A1, & A1B1+\frac{1}{2}A2B2, & \frac{1}{2}B2A1, & B1^2+\frac{1}{2}B2^2, & \frac{1}{2}B2B1, & 0, & 0 \\
-\frac{1}{2}A2B1-\frac{1}{2}B2B1, & -\frac{1}{2}A1B1-\frac{1}{2}B1^2-B2^2-A2B2, & \frac{1}{2}A2B1, & \frac{1}{2}A1B1+A2B2, & \frac{1}{2}B2B1, & \frac{1}{2}B1^2+B2^2, & 0, & 0 \\
0, & 0, & 0, & 0, & 0, & 0, & \frac{1}{90}A1^2+\frac{1}{180}A2^2+\frac{1}{180}B2^2+\frac{1}{90}B1^2+\frac{1}{180}A2B2+\frac{1}{90}A1B1, & \frac{1}{180}A2A1+\frac{1}{360}A2B1+\frac{1}{360}B2A1+\frac{1}{180}B2B1 \\
0, & 0, & 0, & 0, & 0, & 0, & \frac{1}{180}A2A1+\frac{1}{360}A2B1+\frac{1}{360}B2A1+\frac{1}{180}B2B1, & \frac{1}{90}A2^2+\frac{1}{180}A1^2+\frac{1}{90}B2^2+\frac{1}{180}B1^2+\frac{1}{90}A2B2+\frac{1}{180}A1B1
\end{bmatrix}$$

[B$_e$] for MINI elements in 2D:

$$\begin{bmatrix}
-\frac{1}{6}A1-\frac{1}{6}B1 & -\frac{1}{6}A2-\frac{1}{6}B2 & \frac{1}{6}A1 & \frac{1}{6}A2 & \frac{1}{6}B1 & \frac{1}{6}B2 & \frac{1}{120}A1+\frac{1}{120}B1 & \frac{1}{120}A2+\frac{1}{120}B2 \\
-\frac{1}{6}A1-\frac{1}{6}B1 & -\frac{1}{6}A2-\frac{1}{6}B2 & \frac{1}{6}A1 & \frac{1}{6}A2 & \frac{1}{6}B1 & \frac{1}{6}B2 & -\frac{1}{120}A1 & -\frac{1}{120}A2 \\
-\frac{1}{6}A1-\frac{1}{6}B1 & -\frac{1}{6}A2-\frac{1}{6}B2 & \frac{1}{6}A1 & \frac{1}{6}A2 & \frac{1}{6}B1 & \frac{1}{6}B2 & -\frac{1}{120}B1 & -\frac{1}{120}B2
\end{bmatrix}$$

[K$_e$] for Raviart-Thomas elements in 2D:

$$\left[-\frac{1}{12}\frac{\mu h(-3p1^2y3y1-3p1^2x1x3+3p1^2x1^2+p1^2x2^2+p1^2x3^2+3p1^2y1^2+p1^2y3^2+p1^2y2^2+p1^2x2x3+p1^2y2y3-3p1^2x2x1-3p1^2y2y1)}{\%1},\right.$$

$$-\frac{1}{24}\frac{\mu h(2p2y3^2p1-2y2p2p1y3-2p2y3p1y1-2p2x1^2p1+6x2p2p1x1-2p2x1p1x3+6y2p2p1y1+2p2x3^2p1-2x2p2p1x3-2p2y1^2p1-2p2x2^2p1-2p2y2^2p1)}{\%1},$$

$$\left.-\frac{1}{24}\frac{\mu h(6p3x1p1x3+6p3y3p1y1-2p3x1^2p1-2p3y3^2p1-2p3y1^2p1-2p3x3^2p1-2p3y2p1y1+2p3y2^2p1-2p3y3p1y2-2p3x2p1x1-2x3p3p1x2+2p3x2^2p1)}{\%1}\right]$$

$$\left[-\frac{1}{24}\frac{\mu h(2p2y3^2p1-2y2p2p1y3-2p2y3p1y1-2p2x1^2p1+6x2p2p1x1-2p2x1p1x3+6y2p2p1y1+2p2x3^2p1-2x2p2p1x3-2p2y1^2p1-2p2x2^2p1-2p2y2^2p1)}{\%1},\right.$$

$$-\frac{1}{12}\frac{\mu h(3x2^2p2^2-3x2p2^2x1+p2^2x1^2+3y2^2p2^2-3y2p2^2y1+p2^2y1^2+p2^2x1x3+p2^2y3y1-3x2p2^2x3+p2^2x3^2-3y2p2^2y3+p2^2y3^2)}{\%1},$$

$$\left.-\frac{1}{24}\frac{\mu h(6x3p3x2p2+2p2x1^2p3-2x3p3p2x1-2x2p2p3x1-2y2p2p3y1+2p2y1^2p3+6p3y3y2p2-2p3y3p2y1-2p2y3^2p3-2p2x3^2p3-2p2y2^2p3-2p2x2^2p3)}{\%1}\right]$$

$$\left[-\frac{1}{24}\frac{\mu h(6p3x1p1x3+6p3y3p1y1-2p3x1^2p1-2p3y3^2p1-2p3y1^2p1-2p3x3^2p1-2p3y2p1y1+2p3y2^2p1-2p3y3p1y2-2p3x2p1x1-2x3p3p1x2+2p3x2^2p1)}{\%1},\right.$$

$$-\frac{1}{24}\frac{\mu h(6x3p3x2p2+2p2x1^2p3-2x3p3p2x1-2x2p2p3x1-2y2p2p3y1+2p2y1^2p3+6p3y3y2p2-2p3y3p2y1-2p2y3^2p3-2p2x3^2p3-2p2y2^2p3-2p2x2^2p3)}{\%1},$$

$$\left.-\frac{1}{12}\frac{\mu h(3x3^2p3^2-3x3p3^2x1+p3^2x1^2-3p3^2y3y1+3p3^2y3^2+p3^2y1^2+p3^2y2^2+p3^2x2^2+p3^2y2y1+p3^2x2x1-3x3p3^2x2-3p3^2y3y2)}{\%1}\right]$$

$\%1 := y3x1-x1y2+y2x3-x3y1-x2y3+y1x2$

[B$_e$] for MINI elements in 3D:

$$\left[\begin{array}{ccccccccccccccc}
\%1 & \%2 & \%3 & \frac{1}{24}A1 & \frac{1}{24}A2 & \frac{1}{24}A3 & \frac{1}{24}B1 & \frac{1}{24}B2 & \frac{1}{24}B3 & \frac{1}{24}C1 & \frac{1}{24}C2 & \frac{1}{24}C3 & \frac{3}{560}B1+\frac{3}{560}A1+\frac{3}{560}C1 & \frac{3}{560}A2+\frac{3}{560}C2+\frac{3}{560}B2 & \frac{3}{560}A3+\frac{3}{560}B3+\frac{3}{560}C3 \\
\%1 & \%2 & \%3 & \frac{1}{24}A1 & \frac{1}{24}A2 & \frac{1}{24}A3 & \frac{1}{24}B1 & \frac{1}{24}B2 & \frac{1}{24}B3 & \frac{1}{24}C1 & \frac{1}{24}C2 & \frac{1}{24}C3 & -\frac{3}{560}A1 & -\frac{3}{560}A2 & -\frac{3}{560}A3 \\
\%1 & \%2 & \%3 & \frac{1}{24}A1 & \frac{1}{24}A2 & \frac{1}{24}A3 & \frac{1}{24}B1 & \frac{1}{24}B2 & \frac{1}{24}B3 & \frac{1}{24}C1 & \frac{1}{24}C2 & \frac{1}{24}C3 & -\frac{3}{560}B1 & -\frac{3}{560}B2 & -\frac{3}{560}B3 \\
\%1 & \%2 & \%3 & \frac{1}{24}A1 & \frac{1}{24}A2 & \frac{1}{24}A3 & \frac{1}{24}B1 & \frac{1}{24}B2 & \frac{1}{24}B3 & \frac{1}{24}C1 & \frac{1}{24}C2 & \frac{1}{24}C3 & -\frac{3}{560}C1 & -\frac{3}{560}C2 & -\frac{3}{560}C3
\end{array}\right]$$

$$\%1 := -\frac{1}{24}B1-\frac{1}{24}C1-\frac{1}{24}A1$$

$$\%2 := -\frac{1}{24}B2-\frac{1}{24}A2-\frac{1}{24}C2$$

$$\%3 := -\frac{1}{24}B3-\frac{1}{24}C3-\frac{1}{24}A3$$

[B$_e$] for Raviart-Thomas elements in 3D:

$$\left[-\frac{1}{18}\frac{p\,(A2\,S1\,y2-A2\,S1\,y1-B3\,S1\,z1+B3\,S1\,z3+B2\,S1\,y3+C2\,S1\,y4-C2\,S1\,y1-B2\,S1\,y1-C3\,S1\,z1+C1\,S1\,x4+C3\,S1\,z4-B1\,S1\,x1+B1\,S1\,x3-A1\,S1\,x1+A1\,S1\,x2+A3\,S1\,z2-C1\,S1\,x1-A3\,S1\,z1)}{vol},\right.$$
$$-\frac{1}{18}\frac{p\,(B1\,S2\,x3-C1\,S2\,x1+A2\,S2\,y2-C3\,S2\,z1+B3\,S2\,z3-A3\,S2\,z1+A3\,S2\,z2+C2\,S2\,y4-C2\,S2\,y1+B2\,S2\,y3+C3\,S2\,z4-A1\,S2\,x1+A1\,S2\,x2-B2\,S2\,y1-A2\,S2\,y1-B1\,S2\,x1-B3\,S2\,z1+C1\,S2\,x4)}{vol},$$
$$-\frac{1}{18}\frac{p\,(B1\,S3\,x3-C1\,S3\,x1-C2\,S3\,y1-C3\,S3\,z1+C2\,S3\,y4+C3\,S3\,z4-B3\,S3\,z1+A3\,S3\,z2-B1\,S3\,x1+B2\,S3\,y3-A2\,S3\,y1+C1\,S3\,x4-B2\,S3\,y1+A1\,S3\,x2+A2\,S3\,y2-A1\,S3\,x1-A3\,S3\,z1+B3\,S3\,z3)}{vol},$$
$$\left.-\frac{1}{18}\frac{p\,(-A2\,S4\,y1+B3\,S4\,z3-B3\,S4\,z1+C3\,S4\,z4+B2\,S4\,y3-C2\,S4\,y1+C2\,S4\,y4-C3\,S4\,z1+B1\,S4\,x3-B1\,S4\,x1-C1\,S4\,x1+A2\,S4\,y2+A3\,S4\,z2-B2\,S4\,y1+A1\,S4\,x2+C1\,S4\,x4-A1\,S4\,x1-A3\,S4\,z1)}{vol}\right]$$

Résumé

Les matériaux polymères poreux font l'objet d'intenses recherches depuis de nombreuses années et présentent certains avantages importants par rapport à leurs homologues inorganiques, comme des propriétés mécaniques modulables, une fonctionnalisation aisée et surtout un coût de production plus faible. Au cours de la dernière décennie, les matériaux à double porosité ont attiré une attention particulière de la communauté scientifique car ces matériaux offrent de nouvelles perspectives intéressantes pour l'élaboration de matériaux durables. Le rôle de chaque niveau de porosité est différent et associé à des processus de transfert de masse distincts. Les macropores (100 μm) permettraient l'écoulement de macromolécules ou de cellules à travers le matériau, tandis qu'un réseau nanoporeux (10-100 nm) serait dédié au passage de molécules plus petites, agissant ainsi comme un deuxième mécanisme de transport, en particulier lorsque des macropores sont totalement obstrués.

La première partie de ce travail porte sur le développement d'approches polyvalentes et efficaces pour la préparation de matériaux à double porosité biocompatibles à base de poly(méthacrylate de 2-hydroxyéthyle) (PHEMA). La première approche a reposé sur l'utilisation de deux types distincts de gabarits porogènes, à savoir un macroporogène et un nanoporogène. Pour générer la macroporosité, soit des particules de NaCl ou des billes de PMMA, pouvant être fusionnées ou non, ont été utilisées afin de contrôler la morphologie l'interconnectivité des pores. Le nanoporosité a été obtenue en utilisant diverses quantités de différents solvants porogènes, générant ainsi une large gamme de distributions de tailles de pores pour ce second niveau de porosité. La seconde méthodologie a été fondée sur le procédé de séparation de phases induite thermiquement. Un mélange de co-solvants constitué de dioxane et d'eau a été utilisé pour solubiliser le PHEMA linéaire préalablement préparé, suivi par un processus de solidification par congélation du mélange de co-solvants / PHEMA, et sublimation consécutive des co-solvants pour produire les matériaux de PHEMA biporeux correspondants. Enfin, les matériaux à double porosité ont été valorisés à travers différentes réactions de fonctionnalisation en utilisant la chimie du carbonyldiimidazole, et l'immobilisation postérieure de nanoparticules d'or générées in-situ. De tels matériaux hybrides à double porosité se sont avérés être des supports catalytiques efficaces.

Dans la deuxième partie, nous avons déterminé numériquement la perméabilité des matériaux à double porosité. La méthodologie a été fondée sur une approche à double changement d'échelle dans le cadre des théories d'homogénéisation périodique et sur des calculs de cellules élémentaires. Le premier changement d'échelle a consisté à déterminer une première perméabilité associée au réseau de nanopores. A cette échelle, les pores ont été saturés par un fluide visqueux obéissant aux équations de Stokes et le problème a été résolu par une approche classiques d'éléments finis ou en utilisant des techniques plus récentes à base de la transformée de Fourier rapide. À l'échelle mésoscopique, l'écoulement du fluide a obéi aux équations de Stokes dans les macropores et aux équations de Darcy dans le solide perméable. Le problème de cellules élémentaires couplant les équations de Darcy et Stokes a été résolu par la méthode des éléments finis afin de calculer la perméabilité macroscopique finale. Dans cette optique, nous avons développé une méthode fondée sur une formulation variationnelle mixte qui a été mise en œuvre en prenant différents éléments dans les domaines de solide et fluide. Divers exemples 2D et 3D sont fournis pour illustrer la précision et la capacité des méthodes numériques proposées pour calculer la perméabilité macroscopique des matériaux biporeux.

Mots clés: matériaux poreux à double porosité ; approche à deux porogènes ; séparation de phases induite thermiquement ; perméabilité ; homogénéisation ; méthode des éléments finis.

Abstract

Polymer-based porous materials have been the subject of intense research for many years and present some important advantages over their inorganic counterparts, such as tunable mechanical properties, ease to be functionalized, and especially lower production cost. Over the last decade, materials with dual porosity have attracted a particular attention from the scientific community, as these peculiar materials offer new interesting perspectives for engineering sustainable materials. The role of each porosity level is different and associated with distinct mass transfer processes. Macropores (100 μm) would allow macromolecules and cells flow through the material, while a nanoporous network (10-100 nm) would be dedicated to the passage of smaller molecules, thus acting as a second transport mechanism, especially when macropores are totally clogged.

The first part of this work addresses the development of versatile and effective approaches to biocompatible doubly porous poly(2-hydroxyethyl methacrylate) (PHEMA)-based materials. The first approach relied on the use of two distinct types of porogen templates, i.e. a macroporogen and a nanoporogen. To generate the macroporosity, either NaCl particles or PMMA beads that could be fused or not, were used in order to control the pore morphology and interconnectivity of the materials. The nanoporosity was obtained by using various amounts of different porogenic solvents, thus generating a wide range of pore size distributions for this second porosity level. The second methodology was based on the thermally-induced phase separation process. A co-solvent mixture constituted of dioxane and water was used to solubilize previously prepared linear PHEMA, followed by a solidification process by freezing the co-solvents/PHEMA mixture, and subsequent sublimation of the co-solvents to generate the corresponding biporous PHEMA materials. Finally, advantage of doubly porous materials was taken through different functionalization reactions using carbonyldiimidazole chemistry, and further immobilization of in-situ generated gold nanoparticles. Such hybrid doubly porous materials proved to act as efficient catalytic supports.

In the second part, we numerically determined the permeability of doubly porous materials. The methodology was based on a double upscaling approach in the field of periodic homogenization theories and on unit cell calculations. The first upscaling consisted in the determination of a first permeability associated with the array of nanoscopic pores. At this scale, the pores were saturated by a viscous fluid obeying the Stokes equations and the problem was solved by means of standard Finite-Element approaches or using more recent techniques based on Fast Fourier Transform. At the mesoscopic scale, the fluid flow obeyed the Stokes equations in the macropores and the Darcy equations in the permeable solid. The unit cell problem coupling Darcy and Stokes equations was solved by the Finite Element method in order to compute the final macroscopic permeability. To this purpose, we developed a method based on a mixed variational formulation which was implemented by taking different elements in the solid and fluid regions. Various 2D and 3D examples were provided to illustrate the accuracy and the capacity of the proposed numerical methods to compute the macroscopic permeability of biporous materials.

Keywords: doubly porous polymeric materials; double porogen approach; thermally-induced phase separation; permeability; homogenization; Finite Element method.